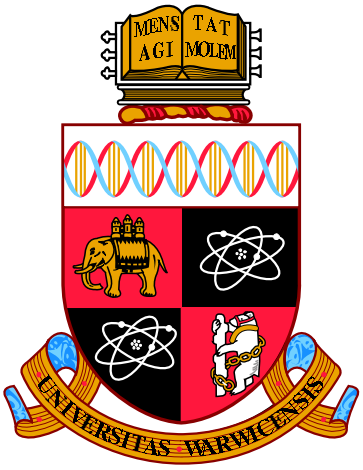

The performance and properties of novel desiccant coated heat exchange surfaces for solar air conditioning

by

Thorsten S. Spillmann

Thesis

Submitted to the University of Warwick

for the degree of

Doctor of Philosophy

School of Engineering

December 2014

THE UNIVERSITY OF WARWICK

Acknowledgments

During the course of this PhD I have had the opportunity to meet and collaborate with a number of people, that have helped make this experience enjoyable and memorable.

Firstly, I would like to thank Prof. Dr. Bob Critoph from the University of Warwick for his supervision of this work, the numerous long early morning discussions during my time abroad and while back in the UK, and for his faith in the success of this work.

Secondly, I would like to thank Dr. Stephen White from CSIRO in Newcastle for making me aware of the opportunity of this project, the constant support, and guidance during this work. I am also thankful for the help and suggestions I have received from Dr. Mark Goldsworthy, especially with the mathematical setup of the model.

Thirdly, I would like thank Dr. Niall Finn from CSIRO in Geelong, where the experimental work of this thesis was conducted, for his many suggestions and help with commissioning the experimental rigs, useful discussions, and for his part in creating a truly enjoyable working environment during my time in Australia. The same goes for the rest of the project team in Geelong, particularly Debbie Hamilton, who was a great help with the coating preparations, Lucy Vuckovic, who helped with the preparation of the flocked inserts, and Lee King, who have made me feel at home and my time at CSIRO a great experience.

Finally, I would like to thank my family for their absolute support during my studies.

Abstract

This work deals with the preparation, thermo-hydraulic characterisation, and performance analysis of silica gel coated highly conductive surface enhancing structures to be used as tube inserts in a prototype of an innovative water-cooled sorption rotor. The candidate inserts under investigation comprise highly porous aluminium foam inserts, twisted-in wire brushes, and flocked structures, that are investigated for their flow impedance, heat transfer performance, and cyclic dehumidification performance. The conducted analysis comprises experimental testing of insert specific pressure drop and heat transfer performance in a purpose built test rig, that led to the preselection of the foam structures and a twisted-in aluminium wire brush insert for desiccant coating and further investigation. Cyclic heat and mass transfer tests were performed in a purpose-built small-scale test rig, that simulated the dehumidification process of a desiccant rotor with and without employing water-cooling. The experimental analysis is complemented by a numerical investigation of the cyclic heat and mass transfer performance of the brush and metal foam type structures, modelled as two-dimensionally axis-symmetric porous media. The geometry based functions of the insert specific flow characteristics are derived from two- and three-dimensional pore scale computational fluid dynamics models, that are calibrated against experimental data. The validity of fundamental modelling assumptions was confirmed by a decent agreement between numerical and experimental steady-state heat transfer results. The heat and mass transfer investigation showed that the investigated structures were capable of effectively removing heat during the dehumidification half-cycle. The thermal mass was shown to be a critical design parameter in achieving acceptable dehumidification performance.

Contents

List of Tables

List of Figures

Nomenclature

Roman Letters

(r, ϕ, z)	radial coordinates	[m]
(u, v, w)	directional velocity components	[m/s]
(x, y, z)	cartesian coordinates	[m]
$\dot{m}$	mass flow rate	[kg/s]
$\dot{Q}$	heat flow rate	[W]
$\dot{q}$	heat flux	[W/m^2]
$\overline{R}$	universal gas constant	[$J/(mol \cdot K)$]
$\overrightarrow{a}$	acceleration	[m/s^2]
$\overrightarrow{F}$	force	[N]
$\overrightarrow{n}$	normal vector	[−]
$\overrightarrow{V}$	velocity	[m/s]
A	area	[m^2]
a	specific area	[m^2/m^3]
a_s	specific surface area	[m^2/m^3]
C	concentration	[mol/m^3]
C_F	form drag factor	[1/m]
c_F	form drag coefficient	[−]
c_p	specific heat capacity at constant pressure	[$J/(kg \cdot K)$]

D	diffusion coefficient	$[\mathrm{m}^2/\mathrm{s}]$
d	diametre	[m]
e	internal energy	[J/kg]
f_a	fraction of active material in coating	[−]
f_D	Darcy friction factor	[−]
f_F	Fanning friction factor	[−]
H	enthalpy	[J]
h	specific enthalpy	[J/kg]
h_h	convective heat transfer coefficient	$[\mathrm{W}/(\mathrm{m}^2 \cdot \mathrm{K})]$
h_m	convective mass transfer coefficient	$[\mathrm{kg}/(\mathrm{m}^2 \cdot \mathrm{s})]$
h_p	half-size of big foam pore	[m]
h_{sp}	half-size of small foam pore	[m]
j	molar flux	$[\mathrm{mol}/(\mathrm{m}^2 \cdot \mathrm{s})]$
j^*	mass flux	$[\mathrm{kg}/(\mathrm{m}^2 \cdot \mathrm{s})]$
j_{hm}	j-factor for heat and mass	[−]
K	permeability	$[\mathrm{m}^2]$
k	thermal conductivity	$[\mathrm{W}/(\mathrm{m} \cdot \mathrm{K})]$
l	length	[m]
Le	Lewis number	[−]
M	molar mass	[g/mol]
m	mass	[kg]
N_{lig}	overall number of ligaments	[−]
N^*_{lig}	number of ligaments per turn	[−]
Nu	Nusselt number	[−]
p	Pressure	[Pa]

Pr	Prandtl number	[−]
q	specific heat	[kJ/kg]
r	radius	[m]
Re	Reynolds number	[−]
s	size, spacing	[m]
Sc	Schmidt number	[−]
Sh	Sherwood number	[−]
T	temperature	[K]
t	time	[s]
U	overall heat transfer coefficient	$[\mathrm{W}/(\mathrm{m}^2 \cdot \mathrm{K})]$
V	volume	$[\mathrm{m}^3]$
W	desiccant moisture content	[kg/kg]
Y	absolute humidity ratio	[kg/kg]

Greek Letters

α_h	thermal diffusivity	$[\mathrm{m}^2/\mathrm{s}]$
$\dot{\omega}$	power density	$[\mathrm{W}/\mathrm{m}^2]$
ϵ	porosity	[−]
μ	dynamic viscosity	$[\mathrm{Pa} \cdot \mathrm{s}]$
ν	kinematic viscosity	$[\mathrm{m}^2/\mathrm{s}]$
ϕ	Relative humidity	[−]
Π	Thermo-hydraulic enhancement ratio	[−]
ρ	density	$[\mathrm{kg}/\mathrm{m}^3]$
ρ_{rel}	relative density	[−]
τ	shear stress	[Pa]
τ_{resp}	time constant	$[s]$

ε	effectiveness	[–]
ζ	tortuosity factor	[–]

Subscripts and Superscripts

(x, y, z)	(x,y,z)-component
0	empty channel
ads	adsorption
br	brush
c	cell
ch	channel
d	dew point
des	desorption
eff	effective
f	fluid
h	hydraulic
in	inlet
lig	ligament
lm	logarithmic mean
loc	local
mat	porous matrix
out	outlet
p	process, pore
pi	process inlet
po	process outlet
r	regeneration
ref	reference

ri	regeneration inlet
ro	regeneration outlet
s	solid, surface
sat	saturated
sp	small pore
tot	total
v	vapour
vap	vaporisation
w	wall,water

Chapter 1

Introduction

Traditional mechanical air conditioning systems are one of the major consumers of electrical energy worldwide. Furthermore, they contribute to environmental pollution involved in the production of the electrical power the systems require and their use of greenhouse gases such as most refrigerants. The ongoing discussion over an energy crisis in the near future and increased environmental awareness have fortified the incentive to investigate alternative solutions, particularly solar and waste heat powered systems. The electrical power consumption of these systems is greatly reduced as they require mainly thermal energy for the air conditioning. Among these, desiccant cooling systems can provide an environmentally attractive and cost effective alternative, as they use solely water as a refrigerant and rely mainly on low temperature heat to operate [Goldsworthy and White, 2011].

The term desiccant cooling usually refers to the desiccant aided evaporative cooling, where the process air is first super-dried in a desiccant dehumidifier and finally conditioned inside an evaporative cooler. Desiccant dehumidifiers are available in solid and liquid form and are commonly used in industrial applications for the drying of process air. While liquid systems tend to have lower regeneration temperature requirements and a lower pressure drop on the process air side, solid systems are less subject to corrosion and carry-over than their liquid counterparts. Most importantly, they tend to be more compact because they allow for a continuous operation as opposed to the batch-wise method of liquid-desiccant systems [Daou et al., 2006].

The first application of a desiccant rotor in a desiccant cooling system was patented by Pennington in 1955 [Jia et al., 2007] and is hence used as the reference desiccant cooling cycle. It is shown schematically in figure 1.1 and consists of a solid desiccant rotor (D), a rotary heat exchanger (HX), a regeneration heat exchanger

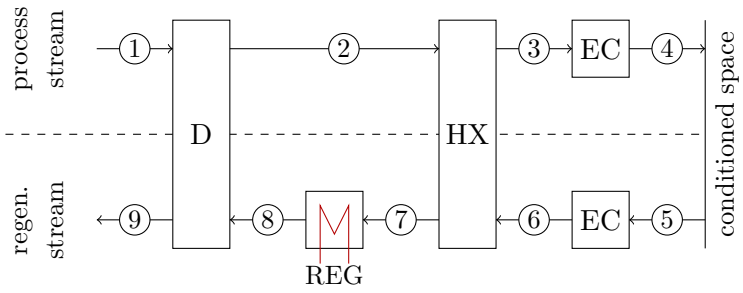

Figure 1.1: Schematic of the Pennignton cycle

(REG), and two evaporative coolers (EC).

The system handles two air streams, namely the "regeneration air stream" dedicated to the regeneration of the desiccant wheel, and the "process air stream" for the actual space conditioning. The dehumidification of the process stream is achieved by forcing the air through a desiccant wheel (D) which adsorbs the water contained in the air stream, as shown in step (1)→(2). In this step, the latent heat held by the air in form of moisture is reduced through adsorption while its sensible heat increases due to the exothermic nature of the process. Subsequently sensible heat of the process air stream is transferred to the regeneration air stream via a sensible heat exchanger (HX). Thus, the process air temperature decreases in step (2)→(3). Finally, the process air is conditioned to the desired level by passing it through an evaporative cooler (EC). In the associated step (3)→(4), the air temperature is further reduced while its moisture content is increased. In order to maintain its moisture removal capacity, the desiccant has to be regenerated continuously by heating it to a critical temperature that is dependent upon the nature of the material used. Therefore air from the conditioned space is first cooled in an evaporative cooler from (5)→(6), so that it can be used to cool the supply air stream in the heat exchanger. Consequently, the regeneration air temperature rises in step (6)→(7). The air is then heated up in step (7)→(8) inside the regeneration heat exchanger (REG) to the desired regeneration temperature. It is then used for the regeneration of the desiccant material. While it is sent through the desiccant wheel in step (8)→(9), the air temperature is reduced and its absolute moisture content increased.

Many attempts of improving desiccant systems focus on the performance enhancement of the desiccant rotor. As will be shown in the course of this thesis, the simultaneous removal of sensible heat during the adsorption process has high potential for not only reducing the temperature level at the outlet of the component,

but also to increasing its dehumidification performance.

1.1 Water-cooled desiccant wheel prototype

A prototype of an innovative desiccant wheel was developed by the Commonwealth Scientific Industrial Research Organisation (CSIRO), consisting of numerous air channels, that are in direct contact with cooling water, allowing for the removal of sensible heat during the adsorption half-cycle.

A sketch of the prototype is given in figure 1.2. The air channels of the

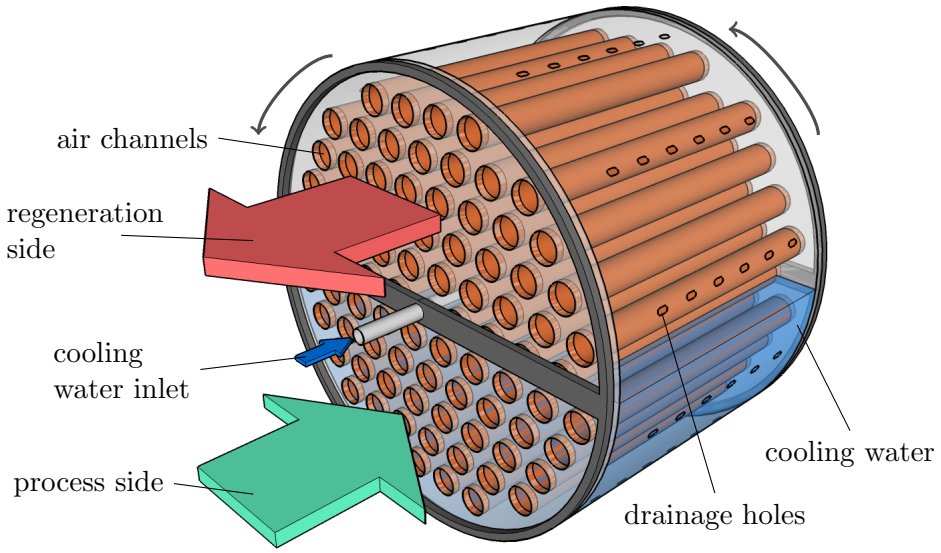

Figure 1.2: Sketch of the water-cooled desiccant wheel prototype

prototype consist of metal tubes that are evenly spaced inside a hollow cylindrical chassis, that has perforations on its side acting as drainage holes. The cooling water is injected into the chassis through the stationary base-rod, simultaneously acting as the rotation axis of the wheel. The cooling water flow rate can be adjusted so that the lower half of the wheel, corresponding to the dehumidification side, is filled with continuously replenished cooling water. As the wheel rotates, channels that were in the upper half of the wheel, corresponding to the regeneration side, are submerged in the cooling water bath as they reach the lower dehumidification side of the wheel.

In order to increase the amount of active surface area available for moisture transfer, the channels are envisaged as being equipped with desiccant coated tube inserts, that possess the following attributes:

- high surface area for desiccant coating

- high thermal conductivity for the effective transport of heat from the core of the respective channels to the cooling water
- a low thermal mass to reduce carry-over of regeneration heat into the adsorption half-cycle
- a small flow resistance to limit the overall pressure drop across the wheel.

The first-generation prototype consists of 306 copper tubes commonly used in heat exchangers, with an inner diameter of $d_{t,i} = 19$mm and a length of $l_t = 200$mm.

1.2 Scope and structure of this work

The focus of this work is the preparation, characterisation and performance analysis of surface enhancing structures that serve as tube inserts for the novel water-cooled desiccant wheel prototype developed at the CSIRO laboratories. The direct contact of cooling fluid and channel walls can be expected to overcome limitations faced by a previous realisation of a directly cooled continuously operating dehumidification component and therefore has the potential of further exploiting the potentials of isothermal adsorption, that has been demonstrated in the pertinent literature.

The current work focusses on metal foam structures, twisted-in wire brushes and flocked structures as potential inserts, because they provide a high specific surface area, indicating a large increase in surface area for fluid interaction at a limited increase in solid volume attributed thermal mass and have a high intrinsic thermal conductivity that allows them to transport the heat generated during the exothermic adsorption process efficiently to the water-cooled channel walls.

The characterisation of the inserts under investigation is carried out by analysing their geometrical composition, their influence on the flow impedance and stationary heat transfer through the air channels, and their cyclic heat and mass transfer performance.

In order to introduce the fundamental nomenclature for this work, the following chapter 2 summarises the underlying thermodynamic principles of the desiccant wheel process and introduces the basic mathematical relations used in the numerical analysis of this work.

Subsequently an overview of the pertinent literature is given in chapter 3, highlighting the limitations of the conventional solid desiccant dehumidification process and summarising important works focussing on systems approaching isothermal dehumidification. Finally an overview of works focussing on the thermo-hydraulic analysis of structures similar to the ones employed in this work is given.

A detailed description of the inserts under investigation is given in chapter 4. Here, three-dimensional geometrical models of the foam- and brush-type structures are developed that are the bases for the subsequent micro-scale flow analysis carried out in this work. Finally, the preparation of the desiccant coating mixture and its application are discussed.

Chapter 5 focusses on the measurements of flow impedance attributed to the respective channel inserts, which are used to calibrate the developed flow models, that are introduced in the subsequent chapter.

The numerical pressure drop analysis is carried out for the metal foam and metal brush structures and discussed in chapter 6. It consists of three steps: First, the pore-scale flow is calculated numerically using the three-dimensional foam-cell model and a simplified two-dimensional representation of the brush-type structures. The modelling results are consolidated in a subsequent step into porous medium flow characteristics by fitting a porous medium flow model to the flow impedance data of a characteristic family of unit cells. Finally, the derived characteristics are utilised in a macro-scale tube flow model that is calibrated against the experimental pressure drop data.

The experimental investigation of the heat transfer of the test pieces was carried out in a purpose built experimental test rig described in chapter 7, where their heat transfer performance is compared by means of thermal and thermal-hydraulic numbers of merit.

The experimental results are utilised to validate the numerical model described in subsequent chapter 8, that builds upon the previously established tube flow model.

Chapter 9 describes the experimental investigation of the cyclic heat and mass transfer performance of the coated test pieces with and without water-cooling in a purpose built test rig.

Finally, the numerical investigation of the transient heat and mass transfer performance is described in chapter 10, that gives insight into the performance limiting factors of the test pieces under investigation.

The findings of this work are summarised in the final chapter 11 and an outlook with recommendations for future work is given.

Chapter 2

Fundamental Theory

In the current chapter, the underlying thermodynamic principles of the desiccant wheel process will be described. For this, the basic heat and mass transfer nomenclature will be introduced and the transport equations required for describing the transient transport processes inside a desiccant wheel derived in general form. Subsequently, the basic relations of psychrometry will be recapitulated briefly and the principles of solid sorption described.

2.1 Principles of heat and mass transfer

The physical principles of the conductive and convective heat and mass transfer are well understood and the transport equations relevant for this work are regularly derived in pertinent textbooks. The following derivations are mainly based on discussions found in [Wendt et al., 2009], [Baehr and Stephan, 2011], [VDI, 2010], and [Incropera and DeWitt, 2002].

The following introduction of basic heat and mass transfer principles and terminology is divided into sections focusing on the fundamental heat transfer process, the mass transfer process, a summary of relevant dimensionless numbers, and related boundary layer analogies.

2.1.1 Heat transfer

Heat can be transferred to a system either through radiation or by contact with another medium. Here, it can be distinguished between conductive and convective heat transfer. The former is the result of energy transport between neighbouring molecules that takes place in all matter. It is governed by Fourier's law that states

that the heat flux is proportional to the temperature gradient:

$$\frac{\mathrm{d}\dot{Q}}{\mathrm{d}A} = \dot{q} = -k \cdot \nabla T \tag{2.1}$$

where in its most general form k is a (3×3)-matrix of the directional material intrinsic thermal conductivity values:

$$k = \begin{pmatrix} k_{xx} & k_{xy} & k_{xz} \\ k_{yx} & k_{yy} & k_{yz} \\ k_{zx} & k_{zy} & k_{zz} \end{pmatrix} \tag{2.2}$$

In a moving fluid, the conductive heat transfer process is superposed by the movement of the molecules themselves. This process is called convection and is of special importance when describing the heat transfer between a moving fluid and a solid wall. The local temperature of the fluid exhibits a strong gradient in a thin region near the wall, called the boundary layer, where it approaches the temperature level of the wall. In the boundary layer theory it is assumed that the fluid is stationary and in thermal equilibrium with the wall at the solid-fluid-interface. The local flux of heat transferred from the fluid to the wall is proportional to the difference between the free-stream temperature of the fluid and the wall temperature:

$$\frac{\mathrm{d}\dot{Q}}{\mathrm{d}A} = \dot{q} = h_{h,loc} \cdot (T_w - T_f) \Leftrightarrow h_{h,loc} = \frac{\mathrm{d}\dot{Q}}{\mathrm{d}A \cdot \Delta T_{loc}} \tag{2.3}$$

While the equation above describes the local heat transfer through an infinitesimally small area $\mathrm{d}A$, the same relation can be applied in an averaged sense to describe the heat transfer over a wall of finite area A:

$$\dot{Q} = h_h \cdot A \cdot \Delta\overline{T} \tag{2.4}$$

where h_h is the mean convective heat transfer coefficient and ΔT is the mean process driving temperature difference between fluid and solid wall.

For the case of a fluid flow parallel to the wall, it follows from the first law of thermodynamics that the difference in mean fluid temperature is linked to the heat transfer with the solid wall as:

$$\dot{Q} = h_h \cdot A \cdot \Delta\overline{T} = \dot{m} \cdot c_p \cdot (T_{f,out} - T_{f,in}) \tag{2.5}$$

It is common practice for in-line heat exchangers to define $\Delta\overline{T}$ as the logarithmic

mean of the temperature differences at system in- and outlet:

$$\Delta\overline{T} = \Delta\overline{T}_{lm} = \frac{(T_w - T_f)_{in} - (T_w - T_f)_{out}}{\ln(T_w - T_f)_{in} - \ln(T_w - T_f)_{out}} \tag{2.6}$$

Observing equations 2.1 and 2.3 it can be seen that both conductive and convective heat fluxes are linear functions of the prevailing temperature difference. As a result, it is possible to combine both coefficients into one overall heat transfer coefficient, when the two processes occur in series. A typical example for this is the heat transfer between two fluids separated by a solid wall. In the steady state system the heat flow rates in and out of the three domains are equal and one can write for every point along the wall

$$\begin{aligned} d\dot{Q} =& d\dot{Q}_1 = d\dot{Q}_2 = d\dot{Q}_3 \\ =& h_{h,loc,1} \cdot dA_1 \cdot (T_{f,1} - T_{w,1}) && \text{(2.7a)} \\ =& k_m \cdot dA_m \cdot \frac{(T_{w,1} - T_{w,2})}{\mathrm{d}x} && \text{(2.7b)} \\ =& h_{h,loc,2} \cdot dA_2 \cdot (T_{w,2} - T_{f,2}) && \text{(2.7c)} \end{aligned}$$

Where $(h_{h,loc,1}, h_{h,loc,2})$ are the local convective transfer coefficients corresponding to the heat flow between the respective fluids and the separating wall through areas (dA_1, dA_2). The values of the thermal conductivity k_m and conductive transfer area dA_m are averaged over the conductive path length $\mathrm{d}x$. Replacing the wall temperatures in equations 2.7a and 2.7c with expressions from 2.7b yields:

$$d\dot{Q} = U_{loc} dA \cdot (T_{f,1} - T_{f,2}) \tag{2.8}$$

with

$$\frac{1}{U_{loc} dA} = \frac{1}{h_{h,loc,1} dA_1} + \frac{\mathrm{d}x}{k_m dA_m} + \frac{1}{h_{h,loc,2} dA_2} \tag{2.9}$$

Here, U_{loc} is the local overall heat transfer coefficient of the system and dA the corresponding reference area. The description of the heat transfer over the entire length of the system is possible using the mean convective transfer coefficients and the logarithmic mean of the fluid temperature differences at the system in- and outlet:

$$\dot{Q} = UA \cdot \Delta\overline{T}_{lm} = UA \cdot \frac{(T_{f,1} - T_{f,2})_{in} - (T_{f,1} - T_{f,2})_{out}}{\ln(T_{f,1} - T_{f,2})_{in} - \ln(T_{f,1} - T_{f,2})_{out}} \tag{2.10}$$

with

$$\frac{1}{UA} = \frac{1}{h_{h,1}A_1} + \frac{\mathrm{d}x}{k_m A_m} + \frac{1}{h_{h,2}A_2} \tag{2.11}$$

2.1.2 Mass transfer

Similar to the heat transfer by contact, two main mass transfer processes can be distinguished that have strong analogies to their heat transfer equivalents. The mixing of two species A and B due to random motion of molecules is called molecular diffusion and occurs in liquids, solids and gases. It is governed by Fick's law stating that the net transfer of species A is proportional to the concentration gradient:

$$j_A^* = -D_{AB}\nabla C_A \tag{2.12}$$

The validity of the equation above relies on a constant molar concentration $C = C_A + C_B$. A more general form can be obtained by expressing the concentration gradient as molar ($C_A^* = C_A/C$) or density ratios ($\rho_A^* = \rho_A/\rho$):

$$j_A^* = -\,C \cdot D_{AB}\nabla C_A^* \tag{2.13}$$

$$j_A = -\,\rho \cdot D_{AB}\nabla \rho_A^* \tag{2.14}$$

The mass transfer from a flowing fluid to the surface of another substance is termed convective mass transfer. In analogy to its heat transfer equivalent the molar and mass flows are related to the difference in surface and fluid concentrations:

$$J_A = \frac{h_m}{\rho_A} \cdot A \cdot \Delta C_A \tag{2.15}$$

$$\dot{m}_A = h_m \cdot A \cdot \Delta \rho_A^* \tag{2.16}$$

The calculation of the convective transfer coefficient is dependent on the physical model of the mass transfer process. The three main theories are the film, boundary layer theory, and penetration and surface renewal theories, that will not be discussed in detail here, but are explained in [Baehr and Stephan, 2011].

Similar to the heat transfer case, mean and overall mass transfer coefficients can be derived from equations 2.13, 2.14 and 2.15, 2.16, whose values are either determined experimentally or by means of literature correlations. For the latter, the dimensionless characteristics introduced in the following subsection play an important role.

2.1.3 Dimensionless characteristics

The values of the convective transfer coefficients are dependent on the problem specific flow conditions and material properties. They often have to be determined experimentally where the characteristics of the problem are summarised into dimensionless numbers, which help to make experimental conditions comparable and allow for the extraction of universal correlations that describe the heat and mass transfer behaviour of a system irrespective of its scale and individual material properties. The ones most important for the discussion of this work will be introduced in the following.

The Reynolds number describes the flow field characteristics. It is defined as the ratio of mass flux ($\rho \cdot u$) and dynamic viscosity μ multiplied by a characteristic length l_{ref}:

$$Re = \frac{\rho \cdot u}{\mu} \cdot l_{ref} \tag{2.17}$$

The Reynolds number relates the inertial forces in a flow field to the viscous forces, making it an important characteristic for the categorisation of the flow regime. At low Reynolds numbers the viscous forces are dominant, the flow is in the laminar regime, characterised by smooth continuous streamlines. A domination of inertial forces at high Reynolds numbers causes the flow to become turbulent, which signifies a disruption of the streamlines and produce instabilities in the flow such as eddies and vortices.

It is clear that the convective transfer of heat and mass is dependent on the flow field. For heat transfer, this connection is manifested in the Prandtl number Pr, which relates the momentum diffusivity to the thermal diffusivity [Incropera and DeWitt, 2002]. It is defined as the ratio of dynamic viscosity $\nu = (\mu/\rho)$ and thermal diffusivity $\alpha_h = k/(\rho \cdot c_p)$:

$$Pr = \frac{\nu}{\alpha_h} = \frac{\mu \cdot c_p}{k} \tag{2.18}$$

Its mass transfer equivalent is the Schmidt number Sc which is defined as the ratio of the momentum and mass diffusivities:

$$Sc = \frac{\nu}{D_{AB}} = \frac{\mu}{\rho \cdot D_{AB}} \tag{2.19}$$

Prandtl and Schmidt numbers are measures of the diffusive energy and mass transport relative to the diffusive momentum transport.

By dividing equations 2.19 by 2.18 the relation between temperature and concentration field can be expressed directly. The resulting dimensionless number

is called the Lewis number Le:

$$Le = \frac{Sc}{Pr} = \frac{\alpha_h}{D_{AB}} = \frac{k}{\rho c_p \cdot D_{AB}} \tag{2.20}$$

A dimensionless description of the convective heat transfer at a surface is given by the Nusselt Number Nu. It is defined as the ratio of convective transfer coefficient h and thermal conductivity k of the fluid multiplied by a characteristic length l_{ref}:

$$Nu = \frac{h_h}{k} \cdot l_{ref} \tag{2.21}$$

It can be shown that for a given geometry, the Nusselt number is a function of Reynolds number and Prandtl number

$$Nu = Nu(Re, Pr) \tag{2.22}$$

The mass transfer equivalent to the Nusselt number is the Sherwood number Sh given by:

$$Sh = Sh(Re, Sc) = \frac{h_m}{D_{AB}} \cdot l_{ref} \tag{2.23}$$

2.1.4 Boundary layer analogies

It can be shown from boundary layer approximations, that the thickness of the thermal (δ_t) and concentration boundary layers (δ_c) relative to the velocity boundary layer (δ) are approximately equal to an exponentiation of the Prandtl and Schmidt numbers [Incropera and DeWitt, 2002].

$$\left(\frac{\delta}{\delta_t}\right) \approx Pr^n, \qquad \left(\frac{\delta}{\delta_c}\right) \approx Sc^n \tag{2.24}$$

Because the temperature and concentration boundary layer equations can be shown to be of analogous form, the Nusselt and Sherwood numbers normalised by the respective relative coating layer thickness must be equal:

$$\frac{Nu}{Pr^n} = \frac{Sh}{Sc^n} \Leftrightarrow Sh = Nu \cdot Le^n \tag{2.25}$$

Relation 2.25 is called the heat and mass transfer analogy and is commonly used for the description of the convective transfer processes inside a desiccant wheel. As for most other applications, a value of the exponent is usually assumed to be $n = (1/3)$

[Goldsworthy and White, 2011],[Zhang and Niu, 2002],[Nia et al., 2006].

Chilton and Colburn [1934] proposed an even broader analogy, that is widely used today in the field of heat and mass transfer and links the transfer processes of momentum, heat, and mass by a common factor j_{hm}.

$$j_{hm} = \frac{f_F}{2} = \frac{Nu}{Re \cdot Pr^{1/3}} = \frac{Sh}{Re \cdot Sc^{1/3}} \tag{2.26}$$

where f_F is the Fanning friction factor defined as:

$$f_F = \frac{\tau_s}{\rho u^2/2} \tag{2.27}$$

The analogy was compared with experimental data for a variety of flow arrangements. For high Reynolds number flows, the analogy could be shown to be applicable for the heat transfer in conduits but not for other flow configurations such as the flow across tube banks where the friction factor is affected more strongly by the turbulence in flow. This discrepancy becomes less in the laminar flow regime, however, and the Chilton-Colburn-analogy was applied by Bejan [1990] to predict the low Reynolds number heat transfer across a bank of thin cylinders based on the friction factor.

2.2 Transport equations

The introduction of the transport equations relevant for this work is divided into two sections. First, fundamental equations for the three dimensional description of flow, heat and mass transfer will be derived. Subsequently, observational equations that describe the flow through porous media in a volume averaged sense will be introduced together with adapted formulations of the heat and mass transfer equations.

2.2.1 Detailed transport equations

The basic transport equations of momentum, heat and mass in a three-dimensional space can be derived by considering a control volume V located at an arbitrary fixed position in space, as schematised in figure 2.1. The dependent variables of interest in this context are functions of space and time. The total derivative of the dependent variables is given by:

$$\mathrm{d} = \frac{\partial}{\partial x}\mathrm{d}x + \frac{\partial}{\partial y}\mathrm{d}y + \frac{\partial}{\partial z}\mathrm{d}z + \frac{\partial}{\partial t}\mathrm{d}t \tag{2.28}$$

By dividing equation 2.28 by dt and noting that $\left(\frac{dx}{dt}, \frac{dy}{dt}, \frac{dz}{dt}\right)$ are the definitions of the local velocity components (u, v, w), this leads to the definition of the substantial derivative [Wendt et al., 2009]:

$$\frac{\mathrm{d}}{\mathrm{d}t} = \frac{\partial}{\partial t} + u\frac{\partial}{\partial x} + v\frac{\partial}{\partial y} + w\frac{\partial}{\partial z} \tag{2.29}$$

Equation 2.29 is commonly written in vector notation as:

$$\frac{\mathrm{d}}{\mathrm{d}t} = \frac{\partial}{\partial t} + (\overrightarrow{V} \cdot \nabla), \text{ with } \overrightarrow{V} = \begin{pmatrix} u \\ v \\ w \end{pmatrix} \tag{2.30}$$

where $(\partial/\partial t)$ is called the local and $(\overrightarrow{V} \cdot \nabla)$ the convective derivative.

The transport equations can be obtained from considering the basic physical principles of conservation of mass, momentum, and energy.

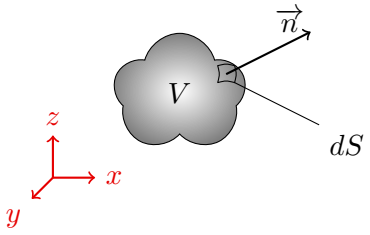

Figure 2.1: Stationary control volume for transport equations

Mass conservation

For the derivation of the mass conservation equation consider the control volume V depicted in figure 2.1 together with vector $\overrightarrow{n}$ standing normal to an infinitesimally small surface section dS. The principle of mass conservation demands that net mass flow out of the control volume through surface S is equal to the time rate of decrease of mass inside the control volume. By integrating the normal mass flows over the surface and the change in local densities over the control volume, this can be expressed in equational form by:

$$\oint_S \rho \overrightarrow{V} \cdot \overrightarrow{n} \cdot \mathrm{d}S + \oint_V \frac{\partial \rho}{\partial t} \mathrm{d}V = 0 \tag{2.31}$$

The surface integral term can be converted to a volume integral by utilising the divergence theorem from vector calculus, yielding [Wendt et al., 2009]:

$$\oint_V \frac{\partial \rho}{\partial t} \mathrm{d}V + \oint_V \nabla \cdot (\rho \overrightarrow{V}) \mathrm{d}V = \oint_V \left[\frac{\partial \rho}{\partial t} + \nabla \cdot (\rho \overrightarrow{V}) \right] \mathrm{d}V = 0 \tag{2.32}$$

Because the control volume is defined at an arbitrary position in space, equation 2.32 can be reduced to differential form by letting $\mathrm{d}V \to 0$, yielding the final expression for the mass conservation as:

$$\frac{\partial \rho}{\partial t} + \nabla \cdot (\rho \overrightarrow{V}) = 0 \tag{2.33}$$

Momentum transfer

The momentum equation can be derived from applying Newton's second law of motion to an infinitesimally small fluid element, stating that the net force acting on the control volume is equal to the acceleration of its mass.

$$\overrightarrow{F} = m \cdot \overrightarrow{a} \tag{2.34}$$

Similar to the velocity, the force and acceleration vectors $\overrightarrow{F}$ and $\overrightarrow{a}$ can be split into directional components (F_x, F_y, F_z) and (a_x, a_y, a_z) so that relation 2.34 represents a directional equation system. The forces acting on the control volume comprise two types:

- Body forces, such as gravity, acting directly on the volumetric mass of the control volume, and
- surface forces resulting from pressure distributions in the surrounding fluid and shear and normal stresses from the frictional contact between the control volume and surrounding fluid

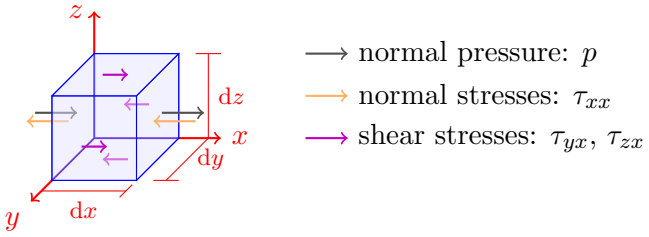

Figure 2.2: Schematic of forces acting on fluid element in x-direction

Figure 2.2 visualises the forces acting in the x-direction on a fluid element. As can be seen from the figure, the directional forces consist of four pairs acting on a corresponding face pair: The shear stress affecting the rear x-z-face at $y = 0$ in the schematic, for instance, has its counterpart at the frontal x-z-face at $y = \mathrm{d}y$, yielding the respective shear stress expressions:

$$F_{x,s}|_{y=0} = \tau_{zx} \cdot \mathrm{d}x\mathrm{d}z \tag{2.35}$$

$$F_{x,s}|_{y=\mathrm{d}y} = \left(\tau_{zx} + \frac{\partial \tau_{zx}}{\partial y}\mathrm{d}y\right) \cdot \mathrm{d}x\mathrm{d}z \tag{2.36}$$

An analogous notation can be applied to all forces acting on the remaining faces. By summing up the resulting force terms and denoting the body forces acting in x-direction as $(\rho \cdot f_x \cdot \mathrm{d}x\mathrm{d}y\mathrm{d}z)$, the net force in x-direction can be written as:

$$\begin{aligned} F_x = \quad & \left[p - \left(p + \frac{\partial p}{\partial x}\mathrm{d}x\right) + \left(\tau_{xx} + \frac{\partial \tau_{xx}}{\partial x}\mathrm{d}x\right) - \tau_{xx}\right] \cdot \mathrm{d}y\mathrm{d}z \\ & + \left[\left(\tau_{yx} + \frac{\partial \tau_{yx}}{\partial y}\mathrm{d}y\right) - \tau_{yx}\right] \cdot \mathrm{d}x\mathrm{d}z + \left[\left(\tau_{zx} + \frac{\partial \tau_{zx}}{\partial z}\mathrm{d}z\right) - \tau_{zx}\right] \cdot \mathrm{d}x\mathrm{d}y \\ & + \rho \cdot f_x \cdot \mathrm{d}x\mathrm{d}y\mathrm{d}z \\ = & \left(\frac{-\partial p}{\partial x} + \frac{\partial \tau_{xx}}{\partial x} + \frac{\partial \tau_{yx}}{\partial y} + \frac{\partial \tau_{zx}}{\partial z}\right) \cdot \mathrm{d}x\mathrm{d}y\mathrm{d}z + \rho \cdot f_x \cdot \mathrm{d}x\mathrm{d}y\mathrm{d}z \end{aligned} \tag{2.37}$$

The right hand side of equation 2.34 can be found for the x-direction by noting that the directional acceleration is defined by the total derivative of the directional velocity with respect to time:

$$a_x = \frac{\mathrm{d}u}{\mathrm{d}t} \tag{2.38}$$

The mass of the control volume is given by

$$m = \rho \cdot \mathrm{d}x\mathrm{d}y\mathrm{d}z \tag{2.39}$$

Combining equations 2.37-2.39 and dividing by the control volume $(\mathrm{d}x\mathrm{d}y\mathrm{d}z)$ yields momentum equation in x-direction is obtained as:

$$\rho\frac{\mathrm{d}u}{\mathrm{d}t} = \left(\frac{-\partial p}{\partial x} + \frac{\partial \tau_{xx}}{\partial x} + \frac{\partial \tau_{yx}}{\partial y} + \frac{\partial \tau_{zx}}{\partial z}\right) + \rho \cdot f_x \tag{2.40}$$

Through vector transformations it can be shown that the left hand side of the equation above is equal to [Wendt et al., 2009]:

$$\rho\frac{\mathrm{d}u}{\mathrm{d}t} = \frac{\partial\rho}{\partial t} + \nabla\cdot(\rho u\overrightarrow{V}) \tag{2.41}$$

Since air can be treated as a Newtonian fluid, the shear stresses are proportional to the velocity gradients, so that the directional stresses $(\tau_{xx}, \tau_{yx}, \tau_{zx})$ can be rewritten as:

$$\tau_{xx} = 2\mu\frac{\partial u}{\partial x} - \frac{2}{3}\mu\nabla\cdot\overrightarrow{V} \tag{2.42a}$$

$$\tau_{yx} = \mu\left(\frac{\partial v}{\partial x} + \frac{\partial u}{\partial y}\right) \tag{2.42b}$$

$$\tau_{zx} = \mu\left(\frac{\partial w}{\partial x} + \frac{\partial u}{\partial z}\right) \tag{2.42c}$$

Applying the identities above to equation 2.40 yields the momentum balance for the x-direction:

$$\begin{aligned}\frac{\partial\rho}{\partial t} + \nabla\cdot(\rho u\overrightarrow{V}) = -\frac{\partial p}{\partial x} &+ \frac{\partial}{\partial x}\left[2\mu\frac{\partial u}{\partial x} - \frac{2}{3}\mu\nabla\cdot\overrightarrow{V}\right] \\ &+ \frac{\partial}{\partial y}\left[\mu\left(\frac{\partial v}{\partial x} + \frac{\partial u}{\partial y}\right)\right] \\ &+ \frac{\partial}{\partial z}\left[\mu\left(\frac{\partial w}{\partial x} + \frac{\partial u}{\partial z}\right)\right] + \rho\cdot f_x\end{aligned} \tag{2.43}$$

The momentum equations for the y- and z-directions can be found in the same manner to be:

$$\begin{aligned}\frac{\partial\rho}{\partial t} + \nabla\cdot(\rho v\overrightarrow{V}) = -\frac{\partial p}{\partial y} &+ \frac{\partial}{\partial x}\left[\mu\left(\frac{\partial u}{\partial y} + \frac{\partial v}{\partial x}\right)\right] \\ &+ \frac{\partial}{\partial y}\left[2\mu\frac{\partial v}{\partial y} - \frac{2}{3}\mu\nabla\cdot\overrightarrow{V}\right] \\ &+ \frac{\partial}{\partial z}\left[\mu\left(\frac{\partial w}{\partial y} + \frac{\partial v}{\partial z}\right)\right] + \rho\cdot f_y\end{aligned} \tag{2.44}$$

$$\begin{aligned}\frac{\partial\rho}{\partial t} + \nabla\cdot(\rho w\overrightarrow{V}) = -\frac{\partial p}{\partial z} &+ \frac{\partial}{\partial x}\left[\mu\left(\frac{\partial u}{\partial z} + \frac{\partial w}{\partial x}\right)\right] \\ &+ \frac{\partial}{\partial y}\left[\mu\left(\frac{\partial v}{\partial z} + \frac{\partial w}{\partial y}\right)\right] \\ &+ \frac{\partial}{\partial z}\left[2\mu\frac{\partial w}{\partial z} - \frac{2}{3}\mu\nabla\cdot\overrightarrow{V}\right] + \rho\cdot f_z\end{aligned} \tag{2.45}$$

Equations 2.43-2.45 are called the Navier-Stokes equations that describe the isothermal single-phase flow of a Newtonian fluid through space.

Heat transfer

The heat equation can be derived from the first law of thermodynamics, according to which the rate of change in internal energy of a system is equal to the flux of heat entering the system in addition to the rate of mechanical work applied to it. Applying this to the control volume depicted in figure 2.1, this can be expressed as:

$$\oint_V \left(\rho \cdot \frac{\mathrm{d}e}{\mathrm{d}t}\right) \mathrm{d}V = -\oint_S \dot{q} \cdot \overrightarrow{n} \cdot \mathrm{d}S - \oint_S \dot{\omega} \cdot \overrightarrow{n} \cdot \mathrm{d}S \tag{2.46}$$

where the term on the left hand side describes the rate of change of the internal energy of the control volume and the right hand side terms represent the sum of heat heat fluxes $\dot{q}$ entering the system through its boundaries and the power densities $\dot{\omega}$ affecting them.

Applying the divergence theorem of vector calculus and letting $\mathrm{d}V \rightarrow 0$ yields:

$$\rho \cdot \frac{\mathrm{d}e}{\mathrm{d}t} = -\nabla \cdot \dot{q} - \nabla \cdot \dot{\omega} \tag{2.47}$$

The heat transfer between the control volume and the surrounding fluid is governed by Fourier's law (2.1). It can be shown [Baehr and Stephan, 2011] that the work experienced by the control volume consists of a pressure induced reversible part and dissipated mechanical energy resulting of the frictional contact with the surrounding fluid, also called viscous heating:

$$\nabla \cdot \dot{\omega} = p \cdot \nabla \overrightarrow{V} - \nabla \cdot \dot{\omega}_{diss} \tag{2.48}$$

The enthalpy of a system is defined as

$$H = m \cdot h = m \cdot \left(e + \frac{p}{\rho}\right) \Leftrightarrow h = e + \frac{p}{\rho} \tag{2.49}$$

Substituting equations 2.1,2.48-2.49 into 2.47, one can write:

$$\rho \cdot \left(\frac{\mathrm{d}h}{\mathrm{d}t} - \frac{\mathrm{d}(p/\rho)}{\mathrm{d}t}\right) = -\nabla \cdot (-k \cdot \nabla T) - p \cdot \nabla \overrightarrow{V} + \nabla \cdot \dot{\omega}_{diss} \tag{2.50}$$

Using the mass conservation formula 2.33, it can be shown that

$$\frac{\mathrm{d}p}{\mathrm{d}t} = \rho \cdot \frac{\mathrm{d}(p/\rho)}{\mathrm{d}t} - p \cdot \nabla \overrightarrow{V} \tag{2.51}$$

so that equation 2.50 can be rewritten to the general heat equation

$$\rho \cdot \frac{\mathrm{d}h}{\mathrm{d}t} = -\nabla \cdot (-k \cdot \nabla T) + \frac{\mathrm{d}p}{\mathrm{d}t} + \nabla \cdot \dot{\omega}_{diss} \tag{2.52}$$

If the fluid is incompressible $(\mathrm{d}p/\mathrm{d}t) = 0$ and $h = c_p \cdot (T - T_0)$. Using the definition of the total derivative and assuming negligible viscous heating, one arrives at:

$$\rho c_p \cdot \frac{\mathrm{d}T}{\mathrm{d}t} = \rho c_p \cdot \left(\frac{\partial T}{\partial t} + (\overrightarrow{V} \cdot \nabla) T \right) = -\nabla \cdot (-k \cdot \nabla T) \tag{2.53}$$

Although equation 2.53 is strictly speaking only valid for an incompressible fluid flow, it is regularly used to model the convective heat transfer of ideal gases, when the influence of the pressure gradients is negligible.

Mass transfer

As was mentioned in the context of the discussion of the basic heat and mass transfer principles, the two transfer processes are analogous. As a consequence, the mass transport equation has the same form as the ideal heat transfer equation and a detailed derivation is omitted here. Substituting the mass transfer equivalents for thermal conductivity and temperature into equation equation 2.53 yields the mass transport equation:

$$\frac{\partial C}{\partial t} + (\overrightarrow{V} \cdot \nabla) C = -\nabla \cdot (-D \cdot \nabla C) \tag{2.54}$$

2.2.2 Volume averaged porous medium transport equations

A porous medium in the context of this work consists of a solid structure with interconnected void spaces that is generally geometrically complicated. The porous medium is called fluid-saturated if all of its pores are filled with a fluid, in this case moist air. Due to the complexity of the solid structure it is usually impractical or impossible to calculate the detailed local flow, temperature and concentration fields using the equations introduced in section 2.2.1. The global performance of the flow system, however, follows simple rules that will be described in the following. The derivation is largely based on the introductions found in [Bejan et al., 2004] and [Nield and Bejan, 2006].

Central to the analysis of porous media is the definition of a representative elementary volume to which the balance equations of momentum, heat and mass are applied in a volume-averaged sense. The central characteristic is the fraction of solid material ρ_{rel} or fluid ϵ in the total volume:

$$\epsilon = \frac{V_f}{V_{tot}} \qquad (2.55) \qquad \rho_{rel} = \frac{V_s}{V_{tot}} \qquad (2.56) \qquad \epsilon + \rho_{rel} = 1 \qquad (2.57)$$

Closely related to the volume ratios is the specific surface area, defined as the ratio of solid surface area and total volume:

$$a_s = \frac{A_s}{V_{tot}} \qquad (2.58)$$

In the following the porous medium flow models relevant for the discussion of this work will be introduced together with adapted heat and mass transport equations.

Momentum transfer in porous media

The simplest porous medium flow model is the Darcy model which describes the seeping fluid flow through an unconfined porous medium. According to the Darcy flow model, the cross-sectional average seepage velocity is proportional to the driving pressure gradient. For a one dimensional flow it is:

$$\frac{\mathrm{d}p}{\mathrm{d}x} = -\frac{\mu}{K} \cdot u \qquad (2.59)$$

Here, K is a geometry dependent characteristic called permeability, that generally has to be determined experimentally.

The Darcy equation holds if the seepage velocity is sufficiently small. The linear relationship between pressure drop and velocity breaks down at intermediate velocities, when the form drag becomes comparable with the surface drag due to friction [Nield and Bejan, 2006]. An according modification to Darcy's model is given in equation 2.60, commonly referred to as the Forchheimer flow model:

$$\frac{\mathrm{d}p}{\mathrm{d}x} = -\frac{\mu}{K} \cdot u - C_F \cdot \rho \cdot u^2 = -\frac{\mu}{K} \cdot u - \frac{c_F}{\sqrt{K}} \cdot \rho \cdot u^2 \qquad (2.60)$$

The Forchheimer model introduces a second characteristic c_F, often referred to as the form drag coefficient. $(C_F = c_F \cdot K^{1/2})$ is called the form drag factor.

Both equations 2.59 and 2.60 are suitable for the determination of the porous medium characteristics by applying first- or second-order fitting functions to experimental data.

However, both models are incapable of accounting for effects of solid confining walls on the flow. In order to include this aspect, Brinkman proposed a modification

to Darcy's law in the form of:

$$\nabla p = -\frac{\mu}{K} \cdot \overrightarrow{V} + \mu^* \nabla^2 \overrightarrow{V} \tag{2.61}$$

Here, μ^* is a modification of the fluid viscosity. It was shown that the ratio of viscosities is equal to the product of porosity and tortuosity for isotropic porous media ($\mu/\mu^* = \epsilon \cdot \zeta_f$). In many cases it can be assumed to be equal to unity [Bejan et al., 2004], as it is here.

For cases of internal tube flows beyond the Darcy-regime, a Forchheimer-type extension to the Brinkman equation can be used to describe the flow in analogy to equation 2.60:

$$\nabla p = -\frac{\mu}{K} \cdot \overrightarrow{V} - C_F \cdot \rho \cdot \overrightarrow{V} \cdot |\overrightarrow{V}| + \mu^* \nabla^2 \overrightarrow{V} \tag{2.62}$$

Heat transfer in porous media

The heat transport inside a porous medium comprises the conductive heat transfer through the solid structure, the heat transport through the fluid by means of conduction and convection and the interaction between the two. This relation can be simplified in many cases, when a local thermal equilibrium between solid and fluid can be assumed and a single temperature field with effective transfer coefficients can be defined. In the case of highly porous structures and higher velocities, both temperature fields have to be determined. The respective transport equations are similar to the one derived in section 2.2 and only have to be adapted to reflect the fact that the corresponding control volume is now merely a fraction of the total volume and expanded by a term to describe the local heat transfer between fluid and solid structure. The transport equations for solid and fluid are given by:

$$\rho_{rel} \cdot \rho_s \cdot c_{p,s} \cdot \frac{\partial T_s}{\partial t} = \rho_{rel} \cdot \nabla \cdot (k_s \cdot \nabla T_s) + h_h \cdot a_s \cdot (T_f - T_s) \tag{2.63}$$

$$\epsilon \cdot \rho_f \cdot c_{p,f} \cdot \Big(\frac{\partial T_f}{\partial t} + (\overrightarrow{V} \cdot \nabla T_f)\Big) = \epsilon \cdot \nabla \cdot (k_f \cdot \nabla T_f) + h_h \cdot a_s \cdot (T_s - T_f) \tag{2.64}$$

Mass transfer in porous media

The mass transfer equation can be written in analogy to the heat transfer as:

$$\rho_{rel} \cdot \frac{\partial C_s}{\partial t} = \rho_{rel} \cdot \nabla \cdot (D_s \cdot \nabla C_s) + h_m \cdot a_s \cdot (C_f - C_s) \tag{2.65}$$

$$\epsilon \cdot \Big(\frac{\partial C_f}{\partial t} + (\overrightarrow{V} \cdot \nabla C_f)\Big) = \epsilon \cdot \nabla \cdot (D_f \cdot \nabla C_f) + h_m \cdot a_s \cdot (C_s - C_f) \tag{2.66}$$

2.3 Psychrometric relations

The mixture of dry air and water vapour can be seen as a special case of a gaseous two-component mixture, that has developed a specific nomenclature due to its significance for a variety of fields, such as air-conditioning and meteorology. For the majority of cases moist air can be treated as an ideal gas mixture, whose state is uniquely described by three independent variables, most commonly pressure, temperature, and mixture composition. The desiccant wheel process operates at atmospheric pressures and usually comparatively moderate temperature levels below 120°C, where errors due to the use of the ideal gas relations only lead to a slight loss of accuracy [ASHRAE, 1994]. The states of the individual components of an ideal gas mixture can be described by the ideal gas law linking the respective pressure and temperature state variables:

$$p_a = \frac{m_a}{V} \cdot \frac{\overline{R}}{M_a} \cdot T \tag{2.67}$$

$$p_v = \frac{m_w}{V} \cdot \frac{\overline{R}}{M_w} \cdot T \tag{2.68}$$

The partial air and vapour pressures are interlinked by Dalton's law, which states that the mixture of non-reacting gasses exerts a pressure equal to the sum of the partial pressures of the individual components it comprises.

$$p = \sum_i p_i \Rightarrow p = p_a + p_v \tag{2.69}$$

The composition of the moist air mixture is most commonly described in one of three ways, that will be described in the following.

The absolute humidity ratio is defined as the ratio of the mass of water vapour and that of dry air. Together with equations 2.67-2.68, one can write

$$Y_a = \frac{m_w}{m_a} = \frac{p_v \cdot M_w \cdot V \cdot (\overline{R} \cdot T)^{-1}}{p_a \cdot M_a \cdot V \cdot (\overline{R} \cdot T)^{-1}} = \frac{M_w}{M_a} \cdot \frac{p_v}{p_a} \tag{2.70}$$

The quantity of moisture that the dry air can hold, varies with temperature. A parameter to describe the level of saturation is the relative humidity. It is defined as the ratio of the actual partial water pressure and the water pressure that would be existent at saturation.

$$\phi = \frac{p_v}{p_{v,sat}} \tag{2.71}$$

An expression for the saturation vapour pressure function can be found in ASHRAE [1994]:

$$p_{v,sat} = \exp\left(c_0 + c_1 \cdot T + c_2 \cdot T^2 + c_3 \cdot T^3 + \frac{c_4}{T} + c_5 \cdot \log(T)\right) \tag{2.72}$$

with

$$\begin{aligned} c_0 &= 1.3914993 & c_1 &= -0.048640239 & c_2 &= 4.1764768 \cdot 10^{-5} \\ c_3 &= -1.4452093 \cdot 10^{-8} & c_4 &= -5800.2206 & c_5 &= 6.5459673 \end{aligned}$$

Together with Dalton's law equations 2.70 and 2.71 can be combined to:

$$Y_a = \frac{M_w}{M_a} \cdot \frac{p_v}{p_a} = \frac{M_w}{M_a} \cdot \frac{p_v}{p - p_v} = \frac{M_w}{M_a} \cdot \frac{\phi \cdot p_{v,sat}}{p - \phi \cdot p_{v,sat}} \tag{2.73a}$$

$$\Leftrightarrow \phi = \frac{Y_a}{(M_w/M_a) + Y_a} \cdot \frac{p}{p_{v,sat}} \tag{2.73b}$$

The temperature at which air at a given absolute humidity ratio reaches saturation is called the dew-point temperature, which constitutes the third measure of composition.

$$\phi(T = T_d) = 100\% \tag{2.74}$$

The amount of heat that is stored inside the mixture is described by the enthalpy and can be divided into a sensible and a latent heat part. Similar to the pressure, the overall enthalpy of the mixture is made up of the partial enthalpies of the individual components. It is convention to use the $T_0 = 0°\text{C}$ point as reference temperature in the enthalpy formulations. The partial enthalpy of dry air is given by:

$$H_a = m_a \cdot h_a = m_a \cdot c_{p,a} \cdot (T - T_0) \tag{2.75}$$

Since the term on the right hand side of equation 2.75 is only temperature dependent, it is referred to as stored sensible heat. Apart from the stored sensible heat, the water vapour comprises a second energy potential based on the heat of vaporisation that gets released during condensation:

$$H_v = m_w \cdot (c_{p,w} \cdot (T - T_0) + q_{vap}) \tag{2.76}$$

The summation of equations 2.75 and 2.76 yield together with relation 2.70:

$$H = H_a + H_v = m_a \cdot c_{p,a} \cdot (T - T_0) + m_w \cdot (c_{p,w} \cdot (T - T_0) + q_{vap}) \tag{2.77}$$

$$\begin{aligned} h = \frac{H}{m_a} &= c_{p,a} \cdot (T - T_0) + \frac{m_w}{m_a} \cdot (c_{p,w} \cdot (T - T_0) + q_{vap}) \\ &= (c_{p,a} + Y_a \cdot c_{p,w}) \cdot (T - T_0) + Y_a \cdot q_{vap} \end{aligned} \tag{2.78}$$

It can be shown from basic mixed phase thermodynamics [Mersmann et al., 2011], that the enthalpy of vaporisation is temperature dependent. It is well known for water and in this work calculated using the following equation:

$$q_{vap} = 2501.2 - 2.205 \cdot (T - 273.15) \tag{2.79}$$

2.4 Thermodynamics of adsorption

Adsorption describes the deposition of molecules on the surface of solid called the adsorbent. In the context of this work it refers to the bonding of molecules from a gaseous fluid onto the surface of a porous material forming a film called the adsorbate. The release of adsorbed molecules into the fluid is called desorption or regeneration.

In contrast to the process of condensation the change from the gaseous to the adsorbate phase occurs at a partial pressure below the saturation pressure. This is possible because of surface forces which reduce the potential energy of an adsorbed molecule below that of the ambient fluid phase. The bonding can be classified by the nature of these forces into chemisorption and physical adsorption. Relevant for this work is the latter, where van-der-Waals- and electrostatic forces are the most important forces governing the process.

The characterisation of the adsorption process can be divided into the description of the adsorption equilibrium characteristics and the kinetics of adsorption. The following discussion is mainly based on introductory texts by Mersmann et al. [2011] and Karge and Weitkamp [2008]. A review of desiccant wheel models conducted by other researchers revealed that the majority of publications concerning silica gel as a desiccant rely on adsorptive transport properties suggested by Pesaran and Mills [1987a,b], or use simplified generic expressions in case of parametric analyses.

2.4.1 Description of adsorption equilibria

When the partial pressure of the adsorbate is equal to the vapour pressure of the system, the same number of molecules are adsorbed as desorbed and the system is in equilibrium.

The adsorption system can be classified as a two component, two phase system. It follows from the Gibbs phase rule, that it can be fully described by two independent state variables [Bongs et al., 2013]. Adsorption equilibrium data are usually reported in from of isotherms, isobars, or isosteres. For desiccant cooling, the use of isotherms is most common, where the adsorbent loading is displayed as a function of relative humidity at a given temperature.

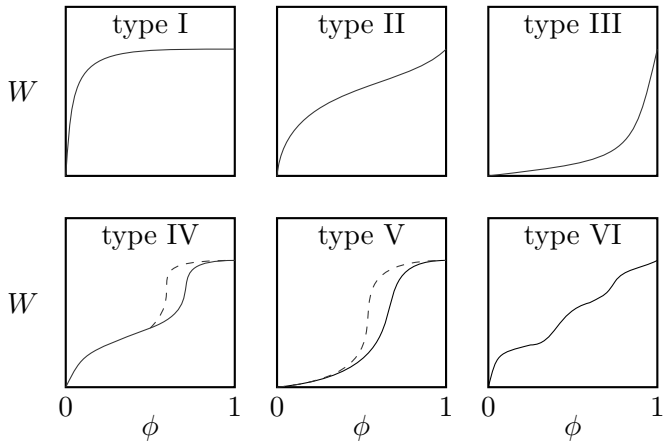

Figure 2.3: Brunauer classification of isotherms [Mersmann et al., 2011]

The shape of the material specific isotherm is either determined experimentally or calculated based on a physical model of the adsorption process. A summary of the most important models can be found in works from Karge and Weitkamp [2008] and Ruthven [1984]. The observed isotherm shapes of different materials can be categorised into five groups shown schematically in figure 2.3. Generally speaking, materials with concave isotherm shapes as the type I and type II are favourable for adsorption, because they signify a high uptake capability even at low vapour pressures [Mersmann et al., 2011]. In this respect, a type III isotherm is the most unfavourable one. It should however be noted, that an isotherm favourable for adsorption is naturally unfavourable for desorption. Nonetheless, materials used in solid desiccant systems commonly exhibit a behaviour of type type I, II, and IV.

Isotherms used in the desiccant dehumidification literature are generally reported as sole functions of relative humidity and any effects of system temperature and hysteresis between adsorption and desorption isotherms are commonly

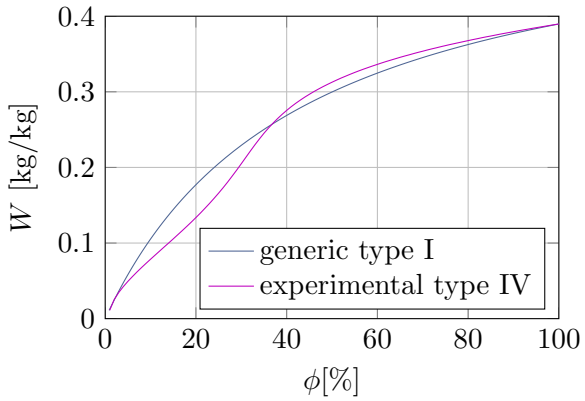

Figure 2.4: Common silica gel isotherm expressions

neglected. Figure 2.4 presents two isotherm formulations for silica gel, that have been routinely used in various recent models of desiccant wheels.

While the first curve represents a generic isotherm formulation, the second is based on a polynomial fit to experimental data. It is given by [Pesaran and Mills, 1987a,b]:

$$\phi = \Psi(W) = 0.0078 - 0.05759 \cdot W + 24.16554 \cdot W^2 - 124.478 \cdot W^3 + 204.226 \cdot W^4 \quad (2.80)$$

Previous models reported by Goldsworthy and White [2011] and White et al. [2011] showed that the relation above yielded results in good agreement with experimental data, that employed the same type of silica gel as used in the current work. Consequently, equation 2.80 is used as the isotherm formulation for the transient heat and mass transfer analysis discussed in section 10.

Similar to condensation, the process of adsorption is exothermic. The amount of heat released is equal to the heat of vaporisation augmented by the so-called bond enthalpy. The latter is often dependent on the loading of the adsorbent. In the case of polar adsorbents, such as silica gel, the heat of adsorption is significantly higher than the heat of vaporisation at low loadings, but the difference becomes negligible close to saturation. The equation 2.81 used here has been taken from Goldsworthy and White [2011], who modelled a desiccant wheel made up of the same silica gel material. The equation was established by Brandemuehl [1982] and was also used in works by Van Den Bulck et al. [1985] and others [Ge et al., 2008b].

$$q_{ads} = q_{vap} + q_{bond} = q_{vap} \cdot (1 + 0.2843 \cdot \exp(-10.28 \cdot W)) \quad (2.81)$$

2.4.2 Description of adsorption kinetics

The moisture transport in silica gel comprises several processes:

- The adsorption process itself, i.e. the transition from gaseous phase to adsorbate at the surface of the pore
- The diffusion of moist air into the pore
- The surface diffusion of adsorbate into the pore

The intrinsic rate of physical adsorption is very rapid, so that the overall sorption rate is generally controlled by the diffusional resistances associated with mass transfer to the adsorption site [Mersmann et al., 2011]. As a result, the kinetics of the phase change itself are commonly neglected in desiccant wheel models, i.e. adsorption equilibrium at the surface is assumed at all times.

The vapour transport through the pores takes place by ordinary molecular diffusion due to the random motion of molecules and Knudsen diffusion.

It was shown by Pesaran and Mills [1987a,b], that for regular density silica gel, which is employed in this work, the diffusion process is dominated by the surface diffusion of the adsorbate. As a consequence, the terms for ordinary and Knudsen diffusion are frequently neglected in desiccant wheel models, and are not accounted for in this work. Pesaran and Mills proposed the following relation for regular density silica gel based on an equation suggested by Sladek et al. [1974] that they fitted to their modelling data:

$$D_s = D_{o,eff} \cdot \exp\left[-0.947 \cdot 10^{-3} \cdot \left(\frac{q_{ads}}{T}\right)\right] \tag{2.82}$$

A value of $D_{o,eff} = 1.6 \cdot 10^{-6}\,\mathrm{m^2/s}$ was proposed for a silica gel water system [Pesaran and Mills, 1987b]. The loading dependency of D_s is accounted for in equation 2.82 by the q_{ads}-term.

Chapter 3

Review of pertinent literature

The focus of this chapter is the inference of the research incentive for this work from the review of current literature of desiccant cooling systems and the demarcation of its scope from examples of investigations on the heat and mass transfer performance of desiccant wheels and the thermo-hydraulic analysis of highly porous tube inserts.

The literature review is divided into three parts: First an overview of investigations of conventional desiccant wheels will be given, highlighting common approaches to their experimental and numerical analysis and the identified limitations of the process. Subsequently, recent related works focussing on the approach of isothermal dehumidification will be summarised. Thirdly, an overview of relevant publications focussing on the thermo-hydraulic analysis of porous tube inserts will be given.

3.1 Investigations of conventional desiccant wheels

Broadly speaking, research efforts in the field of desiccant cooling can be classified into numerical analyses and laboratory tests of individual components, simulations and experimental analysis of entire systems, and field tests of installed applications. An overview of recent research activities in the field is given in review works by La et al. [2010] and Deng et al. [2011].

The central component of the solid desiccant cooling system is the desiccant rotor, which is the focus of this work. Efforts to achieve an augmentation of the desiccant dehumidification has been the subject of numerous publications and can broadly be classified into the development of advanced desiccant materials for conventional desiccant rotors and advanced desiccant dehumidifiers.

A conventional desiccant wheel consists of a corrugated supporting structure,

on which a layer of solid desiccant particles is deposited, that has a typical thickness in the order of 10^{-1}mm [Zhang et al., 2014]. The wheel is continuously exposed to the process and regeneration air streams. The ideal conventional desiccant wheel process leads to an adiabatic conversion of latent to sensible heat in the process air stream and of sensible to latent heat in the regeneration air stream. As was already mentioned in section 2.4.1, the equilibrium moisture content of the desiccant material is usually uniquely related to the relative humidity of the system, which implies, that the theoretical limit to the sorption processes inside the desiccant wheel is given by the inlet relative humidity levels of the respective air streams. Therefore, Goldsworthy and White [2012] suggested a formulation of the dehumidification effectiveness of a desiccant wheel as the difference between process in- and outlet relative humidities divided by the difference between process and regeneration inlet relative humidity levels:

$$\varepsilon_\phi = \frac{\phi_{pi} - \phi_{po}}{\phi_{pi} - \phi_{ri}} \tag{3.1}$$

where the subscripts (pi, po, ri) stand for the process side in- and outlets and the regeneration side inlet, corresponding to indices $(1, 2, 8)$ in figure 1.1, respectively. Kodama et al. [2001] gave a graphical representation of the theoretical limits of a

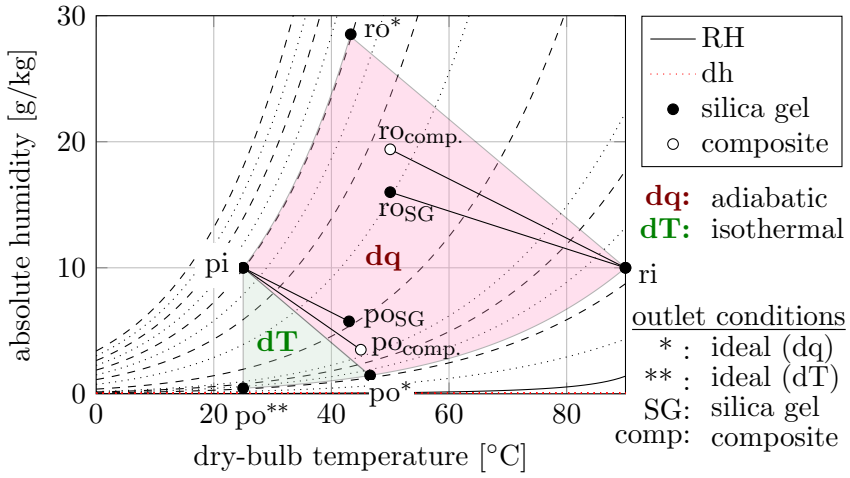

Figure 3.1: Theoretical limits to desiccant dehumidification

desiccant wheel process in a psychrometric chart, shown in figure 3.1, as the area between the isenthalps and lines of constant relative humidity going through the points representing the respective inlet air conditions.

Figure 3.1 also shows outlet conditions that were found experimentally by Jia et al. [2006] for a conventional silica gel coated desiccant wheel and an identical

wheel employing a silica gel-lithium chloride composite material. It can be seen that the composite material leads to a greater dehumidification and performance closer to the ideal limits of the adiabatic process. The discrepancy between ideal and real process outlet conditions is due to a combination of factors, including:

- Thermal mass effects, that lead to (a) thermal carry-over of regeneration heat into the adsorption process, reducing moisture uptake of the desiccant material and increasing the process outlet air temperature, and (b) a dampened temperature rise during the regeneration of the desiccant material, limiting the desorption rate;
- adsorptive heat release which has been shown in section 2.4.1 to be greater than the heat of vaporisation;
- diffusive and convective transport resistances to heat and mass, that limit the amount of moisture transfer during the respective adsorption and desorption half-cycles.

The severity of the influence of these factors on the system performance is, in turn, a function of a large set of material specific and operational parameters, including:

- desiccant material specific moisture uptake, heat of adsorption and adsorption kinetics,
- thermal diffusivity of active material and supporting matrix,
- inlet air conditions and flow rates, and
- lengths of adsorption and desorption half-cycles

Jia et al. [2006] reported test results for a number of air flow rates and inlet air conditions. They reported their results in terms of amount of moisture removed, i.e. $\Delta Y_p = Y_{pi} - Y_{po}$, and thermal coefficient of performance (COP_t). Their results show that the composite material leads to an augmentation in COP_t as well as dehumidification under all test conditions.

The COP_t is commonly defined as the ratio of latent heat removal rate and the energy consumed by the regeneration air heater:

$$COP_t = \frac{\dot{m}_p \cdot Q_{vap} \cdot \Delta Y_p}{\dot{Q}_{\mathrm{REG}}} = \frac{\dot{m}_p \cdot Q_{vap} \cdot (Y_1 - Y_2)}{\dot{m}_r \cdot (h_8 - h_7)} \tag{3.2}$$

where the indices correspond to the positions marked in schematic 1.1.

Similar comparative laboratory tests were performed by White et al. [2011], who compared the dehumidification performance of a silica gel based desiccant wheel to to that of wheels employing FAM-Z01 zeolite and a superadsorbent polymer for different inlet conditions at low regeneration temperatures. They found, that while the respective wheels reacted differently to the changes in inlet conditions and air flow rates, the discrepancies in achieved dehumidification did not reflect the significant differences in absolute moisture uptake capacity and isotherm shape. This indicates that the heat and mass transfer kinetics play an important role for the dehumidification performance.

Many researchers rely on numerical models to investigate the heat and mass transfer processes inside a desiccant wheel in detail. In their review work Ge et al. [2008b] classified models into gas-side, pseudo-gas-side, and gas-and-solid-side resistance models according to their complexity.

Models of the first category only consider the convective transfer resistance and consequently neglect any temperature and concentration gradients inside the solid material. Narayanan et al. [2011] utilised this kind of model for a comparison of different wheel designs. The advantage of the gas-side resistance models is that they are computationally inexpensive in comparison to the gas-and-solid-side resistance models. However, it was shown by Goldsworthy and White [2011] and Bongs [2013] in a Biot-number analysis, that the slow moisture diffusion rate through the desiccant coating layer results in a significant concentration gradient for conventional coating thicknesses, which compromises the applicability of this approach.

Pseudo-gas-side resistance models include a simplified expression for the solid side resistance in the problem formulation in the form of a linear driving force. The terms for the gas- and solid-side transfer resistances can be consolidated into a single lumped transfer coefficient, so that the resulting equation system has the same form as the gas-side resistance model. Due to the complexity of the adsorption equilibrium expression, values for the lumped transfer coefficients usually have to be obtained from correlations of experimental data [Ge et al., 2008b].

Gas-and-solid-side resistance models describe the heat and mass transfer processes inside a desiccant wheel most accurately, but are also more complex due to the inclusion of second order diffusive terms in the equation system. A complex model was proposed by Zhang and Niu [2002], where both gaseous and surface diffusion through the desiccant matrix were considered. Heat conduction and moisture diffusion were modelled in the transverse as well as in the axial direction, which was shown by Sphaier and Worek [2006] to have a noticeable impact on the calculated results for short residence times and low Biot numbers. The model was used to

compare the performance of desiccant wheels varying design parameters such as wall thickness and specific surface area at different rotation speeds for dehumidification and enthalpy recovery applications.

Goldsworthy and White [2012] conducted a similar model to investigate the relative importance of a number of dehumidification performance limiting factors. Since the surface diffusion of adsorbate has been shown to be the dominating transport mechanism [Pesaran and Mills, 1987a,b], the gaseous transport through the desiccant matrix was neglected and heat conduction and adsorbate diffusion were modelled in axial and transverse direction. The material properties of the desiccant matrix were allowed to vary according to the local conditions. In the simulation a number of material properties and transport parameters were varied individually and compared the results to the base case of a silica gel rotor model that was validated against experimental data. Their analysis included

- the separate variation of transverse and axial heat conduction,
- the separate variation of transverse and axial moisture diffusion,
- the variation of the heat of adsorption neglecting loading dependency,
- the variation of the convective transfer coefficients,
- the separate variation of the density and specific heat of the adsorbent, and
- the variation of the equilibrium moisture content.

They found that higher values of heat of adsorption, desiccant specific heat capacity, and density have a significant detrimental effect on the dehumidification of the wheel. While the heat of adsorption directly influences the temperature of the dehumidification process, the specific heat capacity and density both contribute to the thermal mass that is shifted between the process and regeneration air streams and their increase leads to more heat carryover. An increase in convective transfer coefficients led to a noticeable increase in dehumidification performance. The effects of heat carryover and sorptive heat generation on the system performance can be expected to be biggest at low air flow rates, where the process air is incapable of removing the heat from the system effectively, resulting in a higher temperature rise, and the regeneration air does not carry enough heat into the system to counteract the endothermic desorption process, resulting in a lower driving temperature gradient. Accordingly, it was found in a sensitivity analysis with varying channel velocity, that a reduction in specific heat of the desiccant material leads to a significant reduction in outlet humidity level at low air speeds. For the majority of

air flow rates a reduced heat of adsorption leads to a significant augmentation of dehumidification performance. They conclude that the combination of supply air heating through adsorption heat release and regeneration heat carryover are the major limiting factors influencing desiccant wheel performance.

3.2 Isothermal dehumidification

From the investigations of conventional desiccant wheels it can be deduced that the heat removal during the adsorption process has high potential for increasing the process performance. It is also worth pointing out, that a realisation of an isothermal adsorption process has the potential to achieve a deeper dehumidification beyond the theoretical limit of the adiabatic process. This is visualised in figure 3.1 by the green area extending the red area of the original adiabatic process by shifting the ideal process outlet condition from po^{*} to po^{**}. Recognising the potential of isothermal adsorption, several systems have been proposed by other researchers for the removal of heat during the dehumidification half-cycle, that will be introduced in the following. Proposed systems can broadly be classified into staged systems, that employ inter-cooling, and directly-cooled systems, that either operate continuously or in batch mode.

3.2.1 Staged systems

One example of a staged system is the double-rotor desiccant cooling system proposed by Ge et al. [2009] from the Shanghai Jiao Tong University. The system consisted of two desiccant wheels similar to the one tested by Jia et al. [2006, 2007] positioned in series. After each wheel the process air is cooled down in a dedicated cross-flow air-to-air heat exchanger, that uses a mixture of ambient and building return air as a cooling fluid, that has previously been cooled down in a direct evaporative cooler. After exiting the respective heat exchanger, the cooling-fluid streams are heated in dedicated electric heaters and used to regenerate the desiccant wheel. The system performance was measured at constant air flow rates and a ratio of process to regeneration air cross-sections of 3:1, varying the inlet conditions of the process and regeneration air streams. The thermal COP and moisture removal of the system were around 1.0 and 9g/kg, respectively, for the majority of data points and were most sensitive to process air inlet humidity level and regeneration temperature and humidity level. The two stage system was found to require a lower regeneration temperature than a one-stage system to achieve a similar thermal COP. In a follow-up study [Ge et al., 2010b], simulation results for a system employing solar thermal

heat sources for regeneration, optimal rotation speeds for the given configuration were identified and the system was found to yield a cooling capacity approximately 40% higher than a single-stage system at the same conditions. Li et al. [2012] reported on the performance measurements of an installed system with a nominal cooling power of 20kW, driven by evacuated glass tube solar air collectors, and capable of providing cooling in summer and space heating in winter for an electronics plant in China. The moisture removal of the system varied between 6.7-14.3g/kg with an average thermal COP of about unity.

The main disadvantage of stage systems like the one above are their size. Consequently, Ge et al. [2008a] also proposed a more compact realisation of principally the same cycle in the form of a single desiccant wheel divided into four rather than two sections. Process air is directed through the first section for dehumidification, a cross-flow heat exchanger for inter-cooling, the second section, and a final cross flow heat exchanger for further dehumidification and sensible heat removal. Similarly, the cooling air exhaust streams of the two heat exchangers are heated up in dedicated heaters and sent through the other two sections for regenerating the desiccant material. The size of the resulting system was about half of that of the original two-wheeled version. A comparison of system performances showed that the compact systems required higher regeneration temperatures to achieve the same dehumidification as the original system resulting in a lower thermal COP. A 5kW-version of the system was also installed utilising a solar thermal heat source for regeneration and tested under real operation conditions by Li et al. [2011]. They reported an achievable moisture removal of 8-9g/kg under Shanghai hot and humid climate conditions and a thermal and electrical COP of 0.95 and 5.83, respectively. The sectors of the desiccant wheel in the system above were arranged in a pattern alternating between supply and regeneration zones. Kodama et al. [2011] showed experimentally for a similar wheel, that an arrangement where process and regeneration sectors are grouped together can yield an increase in dehumidification effectiveness.

3.2.2 Directly cooled batch systems

Conventional heat exchangers, that have been coated with desiccant material and provide the possibility to remove latent and sensible heat simultaneously in a batch-type process, have been investigated by a number of researchers recently.

Researchers at the Shanghai Jiao Tong University proposed a fin-and-tube heat exchanger that was coated with desiccant material. Ge et al. [2010a] compared the performance of a silica gel coated example with a polymer coating. The

heat exchangers had the same dimensions of 50mm(H) × 160mm(W) × 200mm(D). They were prepared by dipping the cleaned heat exchangers into liquid glue and consequently depositing the solid desiccant material on the outer surfaces by pouring. The silica gel coated specimen was additionally dipped into a liquid desiccant solution repeatedly before curing so that both heat exchangers were coated with approximately 265g of desiccant material. In the experiments, supply air was directed to flow continuously through the heat exchanger while hot and cold water was sent alternately through the tubes in order to provide regeneration heat during the first and remove the heat of adsorption during the second half-cycle. Their performance was compared at different flow rates for several inlet conditions and regeneration temperatures. It was found, that the silica gel coated specimen has a superior moisture removal rate and longer effective dehumidification time than the polymer one and that the moisture removal increases significantly with regeneration temperature and inlet absolute humidity level. The optimal air flow rates were found to lie between 1.2m/s and 1.5m/s.

In a subsequent simulation work, that was shown to be in decent agreement with experimental data, Ge et al. [2011] predicted the performance for a bigger silica gel coated heat exchanger under ARI standard summer and humid conditions at different hot water temperatures. Their results showed that the system provides useful cooling from about 50s of operation after half-cycle-switching and the maximum cooling power between 2.3kW-2.7kW was reached after approximately 200s. In parametric analysis they also studied the effect of fin spacing and tube diameter on the outlet temperature and humidity levels, but did not quantify the effect this has on the pressure drop.

Similar to liquid desiccant systems, solid desiccant coated heat exchangers only allow for a batch-wise dehumidification of the building supply air. A continuously operating air-conditioning system must therefore consist of two such devices operating in opposite phases. Zhao et al. [2014] reported the experimental results of such a system, utilising a solar thermal heat source for regeneration water and a cooling tower to provide sub-ambient temperature cooling water for various cycle times at different ambient conditions and operation strategies. The thermal COP of the system was between 0.3-0.4 for the majority of the data points corresponding to a moisture removal between 3-5g/kg.

Löffler and Henning [2007] proposed a cross-flow heat exchanger, where the adsorption process could be cooled through evaporation of water. The heat exchanger consists of a sorption side, where the thermally conductive channel walls are coated with a desiccant material and a cooling side that is sprayed with liq-

uid water during the adsorption cycle forming a thin film, that covers the channel walls and evaporates into the cooling air stream. Bongs et al. [2013] investigated the dehumidification performance of a prototype by means of experimental analysis and simulation, consisting of a conventional air-to-air cross flow heat exchanger of dimensions 600(H) × 400(W) × 400(D) with a wall spacing of 5mm. Silica gel beads with an approximate diameter of 1mm were used as adsorbent material, that were adhered to the heat exchanger surfaces with an epoxy-coating. This resulted in a deposition of 7.4kg of active material. The investigated cycle times were much longer than typical for desiccant wheel processes, ranging from 40-120min. Experiments at different flow rates, regeneration temperatures, and cycle times showed a mean dehumidification between 3-4 g/kg for most data points and a thermal COP between 0.8-1.2. This represented an increase in dehumidification by a factor of approximately 1.5 and a factor of approximately 4 in thermal COP [Bongs, 2013] when compared to air-cooling alone.

A simpler construct was proposed by Finocchiaro and Beccali [2014] in the form of an ordinary fin-and-tube heat exchanger, where the spaces between the fins were filled with silica gel beads. A prototype solar thermally powered installation consisted of two such heat exchangers filled with approximately 15kg of silica gel beads located upstream of a wet heat exchanger and a cooling tower. The cooling tower provides sub-ambient temperature water for cooling the adsorption process and the wet heat exchanger is in place to further cool down the process air to the desired building supply inlet conditions. While such a setup maximises the packing density of active material in comparison to systems proposed by Ge et al. [2010a] and Löffler and Henning [2007], it can also be expected to impose a much higher pressure drop and poorer thermal contact between adsorbent material and cooling fin. The system was found to deliver a cooling power of about 1kW at a maximal parasitic energy consumption of 200W under outside summer air conditions.

3.2.3 Directly cooled continuous systems

A continuously running directly cooled system was presented by Kodama et al. [2005] if the form of a rotary zeolite coated honeycomb adsorber intersected by aluminium channels, dividing the desiccant wheel into a number of regular sectors, whose combined cross-sectional areas were 60% of that of the overall rotor. The thin aluminium passages were used to realise a low-temperature regeneration process directly with hot water and an air-cooled adsorption process. Experiments were conducted for face velocities between 1-3m/s and regeneration temperatures ranging from 45-60°C for three operation modes, namely regeneration by hot air and

air-cooled dehumidification, regeneration by hot water and air-cooled dehumidification, and regeneration by hot water and air and air-cooled dehumidification. The following observations can be made:

- The variation of the low-level regeneration temperatures only had a minor effect on the dehumidification performance.
- The convective cooling effect during the dehumidification half-cycle was dramatically increased when regenerating the desiccant wheel with hot water instead of hot air because of the evaporation of residual water droplets in the heating/cooling channels.
- The regeneration with hot water and hot air together resulted in a greater decrease in outlet humidity, however at the expense of a considerably higher outlet temperature. This effect could only be counteracted to a minor extent by increasing the cooling air flow rate. This can be seen as an indication, that the heat is not conducted efficiently from the core of the honeycomb block to the cooling air stream.
- Due to the increase in thermal mass of the wheel because of the aluminium channels, the optimal rotation speed was found to be three times slower than that of a conventional wheel.
- The system employing hot water and air regeneration and air-cooled dehumidification led to an increase in dehumidification performance by a factor of 1.3 in comparison to a conventional system at optimal rotation speed, despite its reduced active cross-sectional area due to the heating/cooling channels.

It can be concluded from the literature survey above, that near-isothermal dehumidification has been successfully shown to increase system performance significantly. While the majority of direct cooling systems are batch-systems, continuous systems have the potential of reducing the system's complexity and cost, because they do not rely on complex operation strategies and flow switch valves. The only system employing direct cooling discussed in the pertinent literature appears to be limited in its ability to achieve isothermal dehumidification, mainly because of the poor conduction of heat from the active heat and mass transfer regions to the cooling channels. The system proposed in this work where each channel is in direct contact with the cooling fluid has the potential of overcoming this limitation, if an effective way of conducting heat from the channel core to the channel wall is found.

3.3 Thermo-hydraulic analyses of porous tube inserts

The enhancement of the internal heat transfer of a channel can be classified into active techniques, which rely on an input of external power, and passive techniques [Reay, 1991]. Surface enhancing structures fall into the second category and a wealth of publications exist on the heat transfer enhancement of various kinds of structures, the most common ones being internally finned tubes and coiled-wire inserts. Bergles et al. [1979] summarised the following objectives for the use of passive heat transfer enhancement techniques: (1) To reduce prime surface area, (2) to increase heat-transfer capacity, (3) to reduce the approach temperature difference for the process streams, and (4) to reduce pumping power. In order to compare the thermo-hydraulic performance of different inserts, an overall enhancement ratio is defined that relates the heat transfer enhancement to the increase in pressure drop penalty [Dewan et al., 2004]:

$$\Pi = \frac{Nu/Nu_0}{(f/f_0)^{1/3}} \tag{3.3}$$

where Nu, f, Nu_0 and f_0 are the Nusselt numbers and friction factors for a duct configuration with and without inserts respectively. In general, the heat transfer enhancement from tube inserts is due to the extension of the active surface area available for heat transfer into the channel core and flow perturbation effects, that disrupt the viscous boundary layer near the tube wall. Highly conductive porous channel inserts, such as the metal foam and brush-type inserts under investigation here, therefore have high potential for heat transfer augmentation. The following summarises the most relevant works found in the literature for the experimental heat transfer performance investigation of these types of inserts.

While there are few investigations concerning flocked structures or brush-type tube inserts, metal foam structures have received quite a lot of attention in the pertinent literature and have been suggested for a variety of applications including heat sinks for electronics cooling [Boomsma et al., 2003b; Hsieh et al., 2004], tubular heat exchangers [Du et al., 2010; Odabaee and Hooman, 2012], compact reactors [Hutter and D. Büchi, 2011], and adsorption chillers [Bonaccorsi et al., 2006; Freni et al., 2009]. An overview of the various research efforts involving thermal transport in highly porous metal foams is given by Zhao [2012].

3.3.1 Experimental works

Mancin et al. [2010a,b, 2013] investigated the pressure drop and heat transfer behaviour of highly porous metal foam samples by means of wind tunnel tests applying

a constant heat flux at the foam base. The 100mm long and wide foam specimen were made of aluminium and copper at heights of 20 and 40mm, procured from ERG Aerospace Corporation with different pore sizes and porosities. It is customary to state the pore size in the inverted form, i.e. the number of pores per unit length. The ERG metal foam structures exhibit a high level of isotropy, so that the pore size is a measure of the average pore spacing in all three dimensions. Applying heat fluxes, that varied from $25 - 40\text{kW/m}^2$, they reported hydraulic and heat transfer performance as functions of air flow rate, inter alia in the form of length-normalised pressure drop, permeability based friction factor and effective convective heat transfer coefficient. Their results showed, that the pressure drop decreases with porosity at a given pore size of 10PPI (pores per inch) despite the attributed increase in solid volume. This behaviour is explained by the change in ligament cross-sectional profiles, which has been shown by [Bhattacharya et al., 2002] to change from approximately circular at porosities around 90% to approximately triangular at porosities above 94%. The resulting pressure drop data correlated well with the Brinkman flow equation and the thus determined values for permeability and drag factor were compared to other findings published by other researchers, revealing a noticeable scatter in reported literature values. The effective heat transfer coefficient increased with relative density and decreasing pore size and was found to vary between $400 - 1,200\text{W/m}^2\text{K}$ independently of heat flux for face velocities between $2 - 5\text{m/s}$ in case of the aluminium foams. The positive correlation between the effective heat transfer coefficient and the relative density can be explained by the change in ligament thickness dependent on the relative density, which in turn affects the amount of heat that is transferable through the ligaments.

Dukhan and Ali [2012] investigated the effect of the confining walls on the pressure drop of air flow through tubes of various diameters filled with aluminium foams with pore sizes of 10PPI and 20PPI and a porosity of 90%. Experiments were conducted on seven 10PPI- and 20PPI-foam filled tubes, respectively, that were 6 inches in length and had diameters ranging from 0.5 to 3.5 inches in 0.5 inch increments. The results show a clear departure from the Forchheimer-type flow behaviour when the tube diameter falls below a critical value of 63.5mm, equal to the sum of 15 10PPI-foam cell diameters and 30 20PPI-foam cell diameters.

The heat transfer through foam-filled pipes was studied by Hutter and D. Büchi [2011] for different types of structures including commercial 20PPI and 30PPI foams inserted into an empty tube and a porous tubular reactor made from a single solid block through selective laser sintering with a highly controllable foam filling. The test reactors were 200mm in length and were heated using electrical heating tape.

Water was used as a working fluid and temperature measurements were performed at several positions along the length of the pipe using thermocouples welded to the outer tube wall. They report tube diameter-based Nusselt numbers between 40 and 200 for water flow rates ranging from $0.1 - 1.4$m/s.

The enhancement of heat transfer and pressure drop with twisted wire brush inserts was tested by Naphon and Suchana [2011] for water flow in the turbulent flow regime. The test rig consisted of a 2 metre long double pipe heat exchanger utilising water as both working and cooling fluid. Brush inserts with packing densities of 100,200, and 300 wires per centimetre were compared. The reported tube diameter based Nusselt numbers and friction factors ranged from approximately $80 - 200$ and $1 - 8$, respectively.

3.3.2 Numerical works

The potential for heat transfer augmentation of thin highly conductive fibres, that have been deposited on a heat transfer surface through an electro-flocking process, has been suggested by Lund and Knowles. By utilising single cylinder correlations for friction factor and Nusselt number, they obtain analytical solutions for fully developed laminar [Lund and Knowles, 2001] and turbulent flow [Lund, 2001] through planar or circular ducts, that suggest a substantial potential for heat transfer improvement, that is dependent on the thermal conductivity of the fibres and comes at the expense of increased flow resistance.

For the case of the highly porous metal foam structures, numerical analyses of the flow and heat transfer performance of varying complexity have been proposed by a number of researchers.

Lu et al. [1998] and Ghosh [2009a,b] investigated the heat transfer behaviour by means of a simplified cubic unit cell model made up of twelve cylinders. They estimate the local convective transfer coefficients based on single-tube correlations and use the simplified cell model to derive volume averaged transfer coefficients for the entire structure.

In order to describe the convective heat transfer in foam filled pipes, Lu et al. [2006] proposed an analytical solution to the Brinkman flow model and the heat transfer without local thermal equilibrium. They also derived local convective transfer coefficients from correlations proposed for banks of cylinders. The modelling results were shown to be in acceptable agreement with experimental data.

More complex pore scale flow models involving the numerical solution of the three dimensional Navier-Stokes equations for flow through idealised foam cells were discussed by Boomsma et al. [2003b], Mills [2005], and Xu et al. [2008]. Xu

et al. [2008] employed a Kelvin foam model with cylindrical struts and used their results for different cell diameters and porosities to derive permeability, drag factor and relative surface area characteristics. Mills [2005] used the same cell model, however with quasi-triangular strut cross-sections, to model the air-flow permeability of polyurethane foams at various cell sizes and porosity related cell hole sizes. Boomsma et al. [2003b] utilised a more complex control volume for their calculations consisting of eight non-tetrakaidecahedron cells with equal volume. The agglomerate possesses a lower surface energy than the Kelvin foam model and is therefore believed to be a better representation of reality. A three dimensional conjugate heat transfer model over such a cell agglomerate was modelled by Kopanidis et al. [2010]. Using aluminium foam blocks supplied by ERG of pore sizes 10PPI and 40PPI as reference structures and air as a working fluid, they predicted velocity, pressure and temperature fields for varying boundary conditions, such as constant inlet velocity versus prescribed pressure drop, and constant ligament surface temperature versus conductive heat transport through the solid. Their calculated length normalised pressure drop results showed good agreement with experimental data from other literature sources. Taking the area of the heated outer wall area as a reference, they predicted a heat transfer coefficient for the conjugate case at prescribed pressure drop varying between approximately $400 - 600\mathrm{W}/(\mathrm{m}^2 \cdot \mathrm{K})$ for interstitial velocities from $2 - 9\mathrm{m/s}$, which showed decent agreement to a set of experimental data obtained by other researchers. They conclude that pressure drop and heat transfer performance are greatly affected by the pore scale structure.

Chapter 4

Preparation and geometrical characterisation of inserts

Three types of fibrous structures have been chosen for the heat and mass transfer analysis in the current work. Of all the structures under investigation the most promising ones based on their pressure drop and heat transfer performance were chosen to be coated with desiccant material and tested for their cyclic dehumidification performance. The inserts comprised:

1. three aluminium foams of same nominal porosity and different pore sizes, that were brazed into aluminium tubes,
2. five twisted-in wire brushes with a stainless-steel base wire and bristles made up of different materials and relative densities, namely
    - aluminium-alloy, twisted up to a low relative density
    - copper-nickel-alloy, twisted up to a low relative density
    - copper-nickel-alloy, twisted up to an intermediate relative density
    - carbon, twisted up to a low relative density
    - carbon, twisted up to an intermediate relative density
3. aluminium shim flocked with carbon fibres and rolled up to form
    - a circular tube
    - a flat oval tube.

Weight measurements were performed on all test objects that allowed for the determination of the relative densities based on material properties and structure geometries. In the following, the three-dimensional geometrical representations of

the three types of structures will be discussed and the measurements for the determination of their relative densities described.

4.1 Geometrical characterisation of metal foam inserts

The metal foam test objects consisted of three tubes made of 6061-T6 aluminium alloy, filled with Duocell® aluminium foam, that were supplied by ERG Aerospace Corporation and made of the same material. The tubes were $l_t = 200$mm long, had an inner and outer diameter of $d_{t,i} = 0.777$in.(19.7mm) and $d_{t,o} = 0.875$in.(22.2mm), respectively. The metal foam fillings had the same nominal relative density of $\rho_{rel}^{nom.} = 6 - 8\%$ and a nominal pore size of 5, 10, and 20 pores per inch (PPI), respectively. The foam inserts were made of the same aluminium-alloy as the tubes. A photograph of the three test objects is shown in figure 4.1.

Figure 4.1: Aluminium foam tubes (from left to right): 5, 10, 20 PPI

4.1.1 3D model of a metal foam cell

The Duocel® foam is manufactured by exposing the aluminium alloy in a superheated liquidus state to an environment of overpressures and high vacuum. This results in the formation of a uniform array of bubbles, which are interconnected by thin membranes that reduce in thickness during volumetric expansion. After the foam is solidified, the interfacial membranes are removed by a reticulation process, leaving only the thick outer perimeters of the frames that form the pores, thus creating the three-dimensionally continuous open cell structure. According to the manufacturer, the size of the resulting frames is between 50-70% of that of the associated bubble and is referred to as the pore size. Under ideal conditions the

resulting structure is three-dimensionally isotropic, i.e. formed of cells of a certain uniform shape and size that maximises the cell volume at the minimal surface energy and surface area. It was postulated by Thomson [1887] that the ideal shape to satisfy these criteria was a 14-faceted polyhedral, also called a tetrakaidecahedron. However, it was later found by Weaire and Phelan [1994] by means of numerical analysis that a unit of eight equal volume cells consisting of six 14-sided polyhedra and two pentagonal dodecahedra actually results in a further reduction in surface energy when compared to the packing with tetrakaidecahedronal cells commonly also referred to as Kelvin-foam cells. Nonetheless, the Kelvin foam model is a good representation of the cells making up the metal foam inserts according to the manufacturer. With the basic geometrical form set, the actual size and thickness of the interconnecting struts is now a sole function of the pore size and the relative density. Here, the pore size dictates the length of the interconnecting struts, while their thickness is also a function of the relative density. In the real foam the actual shape of the cross-section also varies with the relative density as shown in figure 4.2.

Figure 4.2: Strut cross-sectional areas at different relative densities

The three dimensional cell model employed in the current work is a simplified Kelvin foam model, where the cell is made up of straight struts with a perfectly circular cross-section. The model assumes that the vertical and horizontal spacings between adjacent cells are equal, which dictates that the length of the 36 individual struts making up the cell is the same. A comparison between an ideal Kelvin-foam cell taken from Boomsma et al. [2003a] and the simplified model employed here is shown in figure 4.3b and c, respectively.

The foam cells presented in figure 4.3 are referred to as dry foam cells with a porosity of $\epsilon = 100\%$, i.e. the bridging struts are mere lines with no volume. In order to create a model for a wet foam cell, the relationships between the nominal porous medium characteristics relative density ρ_{rel}, pore size s_p, the strut length l_{lig}, and radius r_{lig} have to be derived. In the following, relations linking the pore

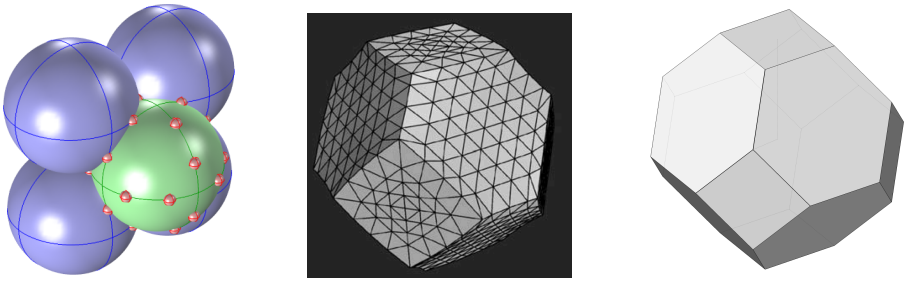

(a) uniform bubble distribution (b) ideal foam cell (c) simplified foam cell

Figure 4.3: Comparison of ideal [Boomsma et al., 2003a] and simplified Kelvin-foam cells

size to the strut lengths and overall cell size are discussed first. Subsequently, the thickness of the struts is derived as a function of pore size and relative density and approximate formulas for the volume and surface area of the resulting structure are obtained. The necessary geometrical relations are described in the following and visualised in figure 4.4.

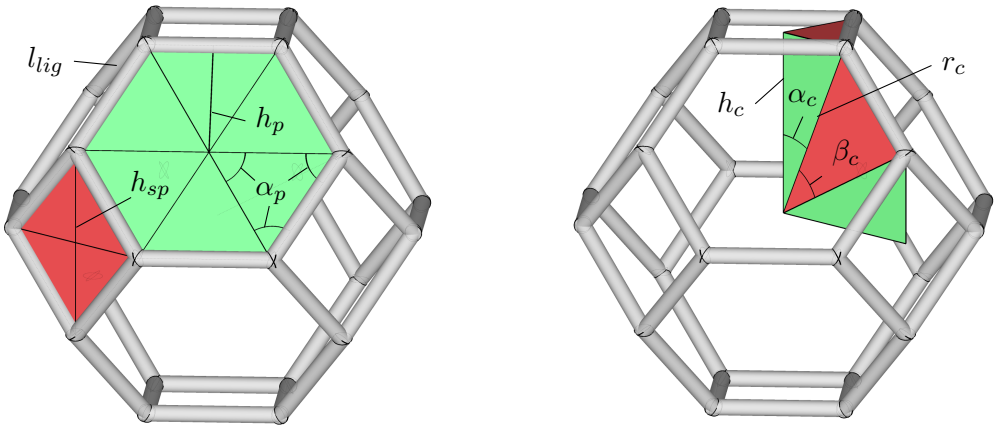

(a) pore related geometry (b) cell related geometry

Figure 4.4: Metal foam pore and cell geometry

The nominal pore size is assumed to correspond to the distance $s_p = 2 \cdot h_p$ between two parallel struts making up the big hexagonal pore marked in green in figure 4.4a. The pore is made up of six congruent triangles of height

$$h_p = \frac{s_p}{2} = \frac{1/2}{\mathrm{PPI}} \tag{4.1}$$

and internal angle

$$\alpha_p = \frac{\pi}{3} \tag{4.2}$$

From geometrical considerations, this yields the ligament (strut) length l_{lig} as:

$$l_{lig} = 2 \cdot \frac{h_p}{\tan(\alpha_p)} = \frac{2}{\sqrt{3}} \cdot h_p = \frac{s_p}{\sqrt{3}} \tag{4.3}$$

The smaller quadrilateral pore marked red in figure 4.4a is square as it is encompassed by four hexagonal pores. The auxiliary length h_{sp} equal to the distance between centre and vertex of the small pore can be found utilising the Pythagorean theorem

$$h_{sp}^2 = \left(\frac{l_{lig}}{2}\right)^2 + \left(\frac{l_{lig}}{2}\right)^2 \Leftrightarrow h_{sp} = \frac{l_{lig}}{\sqrt{2}} \tag{4.4}$$

Observing one of the green triangles in figure 4.4b, this path can also be interpreted as part of the triangle made up by the paths connecting vertex and midpoint of the quadrilateral pore to the cell origin. As is suggested by figure 4.3a, the length of the path connecting cell origin and pore vertex is equal to the radius r_c of the bubble forming the cell, while the path connecting cell origin and pore midpoint is the half-height h_c of the cell. The angle encompassed by the two lines is called α_c. Utilising the Pythagorean theorem and the definition of the cosine, one can derive:

$$h_{sp} = \sqrt{r_c^2 - h_c^2} \tag{4.5}$$

$$\alpha_c = \arccos\left(\frac{h_c}{r_c}\right) \tag{4.6}$$

Introducing the cell size $s_c = 2 \cdot h_c$, the volume of the unit cell is given by

$$V_c = s_c^3 = (2 \cdot h_c)^3 \tag{4.7}$$

Finally, the angle β_c of the red triangle in figure 4.4b that is formed by the two paths of length r_c to the vertices of the strut forming the hexagonal pore can be related to the angle α_c by

$$\beta_c = \frac{\pi}{2} - 2\alpha_c \tag{4.8}$$

Utilising the law of cosines one finds a second expression for l_{lig} that links the strut length to the cell radius

$$\begin{aligned} l_{lig} &= \sqrt{2 \cdot r_c^2 \cdot [1 - \cos(\beta_c)]} = \sqrt{2 \cdot r_c^2 \cdot \left[1 - \cos\left(\frac{\pi}{2} - 2 \cdot \alpha_c\right)\right]} \\ &= \sqrt{2 \cdot r_c^2 \cdot [1 - \sin(2 \cdot \alpha_c)]} \end{aligned} \tag{4.9}$$

Rearranging equation 4.4 and using eq 4.5 for h_{sp} one finds

$$l_{lig} = \sqrt{2 \cdot (r_c^2 - h_c^2)} \tag{4.10}$$

By setting eq. 4.9 equal to eq. 4.10 one is now able to find the characteristic aspect ratio (h_c/r_c) of the cell:

$$\begin{aligned}
&\sqrt{2 \cdot (r_c^2 - h_c^2)} = \sqrt{2 \cdot r_c^2 \cdot [1 - \sin(2 \cdot \alpha_c)]} \\
\Leftrightarrow &1 - \left(\frac{h_c}{r_c}\right)^2 = 1 - \sin(2 \cdot \alpha_c) = 1 - \sin\left(2 \cdot \arccos\left(\frac{h_c}{r_c}\right)\right) \\
\Leftrightarrow &\left(\frac{h_c}{r_c}\right)^2 = \sin(2 \cdot \alpha_c) = \sin\left(2 \cdot \arccos\left(\frac{h_c}{r_c}\right)\right) = 2 \cdot \left(\frac{h_c}{r_c}\right) \cdot \sqrt{1 - \left(\frac{r_c}{r_c}\right)^2} \\
\Leftrightarrow &\left(\frac{r_c}{r_c}\right) \cdot \left(\left(\frac{h_c}{r_c}\right) - 2 \cdot \sqrt{1 - \left(\frac{h_c}{r_c}\right)^2}\right) = 0 \\
\Rightarrow &\left(\frac{h_c}{r_c}\right) \cdot \left(\left(\frac{h_c}{r_c}\right) - \sqrt{4} \cdot \sqrt{1 - \left(\frac{h_c}{r_c}\right)^2}\right) = 0
\end{aligned} \tag{4.11}$$

Apart from $(h_c/r_c) = 0$, the only other solution of eq. 4.11 is $(h_c/r_c) = \sqrt{4/5}$. With the application of this ratio, equations 4.10 and 4.3 yield an expression for the cell size as a sole function of pore size:

$$\begin{aligned}
l_{lig} = &\frac{s_p}{\sqrt{3}} = \sqrt{2 \cdot (r_c^2 - h_c^2)} = \frac{h_c}{\sqrt{2}} = \frac{s_c}{2\sqrt{2}} \\
\Leftrightarrow s_c = &2\sqrt{2} \cdot l_{lig} = 2 \cdot \sqrt{\frac{2}{3}} \cdot s_p
\end{aligned} \tag{4.12}$$

For the idealised wet foam model, the lines forming the pore frames are replaced by cylinders of radius r_{lig}. The volume of the resulting solid matrix is only approximately equal to the sum of the individual strut volumes, because of discontinuities and partial overlapping the cylinders at the vertices, as can be seen in figure 4.5a. In order to smooth the profile at the vertices spheres of radius r_{lig} are added to the edges that help create a perfectly uniform structure. Figure 4.5b shows the final metal foam unit cell that is used in the 3D numerical analysis discussed in chapter 6, where volume of the surrounding air is distinguished in blue and the solid material in green. Note that only half of the cross-sections of the interfacial struts contribute to the solid volume fraction of the respective unit cell. One foam element is made of $6 \cdot 4 = 24$ interfacial struts forming the quadrilateral pores and twelve interconnecting struts, the volume of solid material V_s is approximately equal

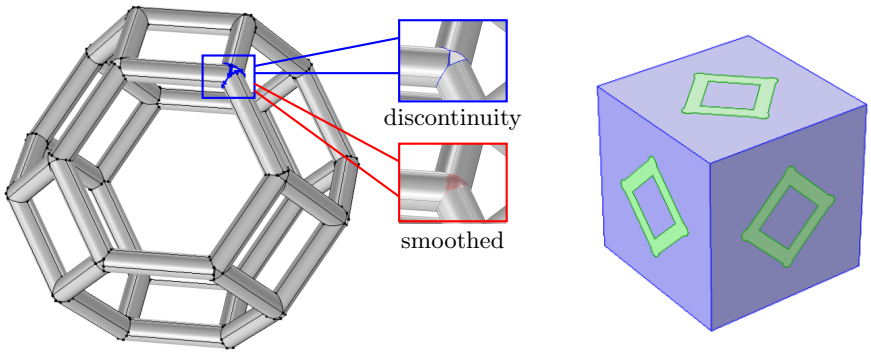

(a) smoothening of edge effects (b) control volume of a unit cell

Figure 4.5: Control volume of a metal foam unit cell

to V_s^*, defined as:

$$V_s^* = \left(\frac{24}{2} + 12\right) \cdot \pi \cdot r_{lig}^2 \cdot l_{lig} = 24 \cdot \pi \cdot r_{lig}^2 \cdot l_{lig} \tag{4.13}$$

By defining a nominal relative density $\rho_{rel}^* = (V_s^*/V_c)$, the radius of a single metal foam fibre is:

$$\begin{aligned} \rho_{rel}^* = & \frac{V_s^*}{V_c} = \frac{24 \cdot \pi \cdot r_{lig}^2 \cdot l_{lig}}{s_c^3} \\ \Leftrightarrow r_{lig} = & \sqrt{\frac{\rho_{rel}^* \cdot s_c^3}{24 \cdot \pi \cdot l_{lig}}} \end{aligned} \tag{4.14}$$

By utilising eq. 4.12, the fibre thickness is expressed as a direct function of nominal relative density and pore size:

$$r_{lig} = \sqrt{\frac{\rho_{rel}^* \cdot s_c^3 \cdot 2\sqrt{2}}{24 \cdot \pi \cdot s_c}} = \sqrt{\frac{\rho_{rel}^*}{\pi \cdot 6\sqrt{2}}} \cdot s_c = \sqrt{\frac{4 \cdot \rho_{rel}^*}{\pi \cdot 9\sqrt{2}}} \cdot s_p \tag{4.15}$$

The modelled unit cells used in the computational analysis in chapter 6 comprised ligaments, whose length and thickness were calculated based on the nominal pore size and relative density using equations 4.3 and 4.15. The exact values for the relative surface area and volume fraction of the created solid were then recalculated within the modelling software by means of volume and surface integrals.

For applications involving thermal conduction, the length ratio of the cell height and the shortest path created by the bridging ligaments is an important characteristic, because it approximates the elongation of the heat conduction path.

As can bee seen from equation 4.12, in the Kelvin foam model cell size and strut length are directly related so that their ratio is a geometrical characteristic independent of cell size and relative density. The effect of an elongated heat conduction path is commonly described by the thermal tortuosity ζ, defined as the ratio of effective thermal conductivity to that of the pure material:

$$\zeta = \frac{k_{eff}}{k_s} \tag{4.16}$$

It was shown by Yang et al. [2013] that the derivation of this characteristic from geometrical considerations of the Kelvin foam cell leads to an approximated value of $\zeta = 1/3$, which conforms with experimental values found by other researchers.

4.1.2 Experimental relative density determination

In order to determine the relative density of the actual test objects, weight measurements were performed on the three test metal foam tubes using a laboratory balance with an accuracy of $\Delta m = \pm 0.1\text{mg}$. Since the density of the matrix and tube material is known, the relative density of the aluminium foam inserts could be determined by comparing the mass of the test objects to the theoretical mass of a solid block of the same material of same volume. Together with their dimensions and the material data of 6061-T6 aluminium alloy, the relative density of the foam inserts could be determined by the following relation:

$$\begin{aligned}\rho_{rel} =& \frac{m_{foam}}{\rho_{Al} \cdot V_{ch}} = \frac{m_{tot} - m_{tube}}{\rho_{Al} \cdot V_{ch}} = \frac{1}{\rho_{Al} \cdot V_{ch}} \cdot [m_{tot} - \rho_{Al} \cdot V_{tube}] \\ =& \frac{1}{\pi \cdot (d_{t,i}^2/4) \cdot l_t} \cdot \left[\frac{m_{tot}}{\rho_{Al}} - \pi \cdot \frac{(d_{t,o}^2 - d_{t,i}^2)}{4} \cdot l_t \right]\end{aligned} \tag{4.17}$$

The results of measurements and the corresponding relative surface area that was obtained from the manufacturer's specification sheet are summarised in table 4.1. Since the amount of brazing material is not known and the exact dimensions of the tubes could not be determined with great accuracy, the uncertainty of the calculated individual masses is conservatively estimated to be $\Delta m^* = \pm 0.1\text{g}$.

Table 4.1: Relative densities of aluminium foam structures

Variable		5PPI	10PPI	20PPI
m_{tube}	[g]	45.0	45.0	45.0
m_{tot}	[g]	61.2	58.6	59.6
m_{foam}	[g]	16.2	13.6	14.6
ρ_{rel}	[%]	9.7	8.1	8.7

4.2 Geometrical characterisation of brush-type inserts

Twisted-in wire brushes consist of an array of densely packed ligaments that are placed between two stem wires, which are subsequently twisted up locking the filaments in place between them and forming the typical spiral geometry. Four of the five brush inserts were provided by Gordon Brush Mfg. Co., Inc. The base wire material was stainless steel and the bristle material and packing density varied from brush to brush. The brushes were delivered with an overall length of $l_{tot} = 11$in, with a brush part of $l_{br} = 8$in and a $l_{handle} = 3$in long handle. The twisted-up stem had a diameter of $d_{stem} = 0.075$in. During the production process the bristles were trimmed by the manufacturer to form a brush part of uniform diameter $d_{br} = l_{lig} = 4/5$in. The packing density of the brushes were classified by eye and the four tube inserts were labelled as:

- low-density (LD) aluminium brush
- low-density copper brush
- medium-density (MD) copper brush
- medium-density carbon brush
-
- low-density carbon brush.

The fifth brush using carbon fibres as ligaments was twisted up by hand to form a tube insert with a less dense packing. The stem wire was made of soft steel. While in an industrial production process the fibres are held in place mechanically by a designated tool, in the hand-made process a thin stripe of wood glue was used to attach the loose fibres to the base wire during the twisting process. The brush part of the hand-made insert was $l_{br} = 200$mm long and had a diameter of approx. $d_{br} \approx 21$mm. For the preparation of the brush-type test pieces, the handle was cut off leaving only the part with the bristles that was then fitted into a test tube of the same dimensions as the metal foam tubes discussed in the previous section. The tube was made of a copper-alloy commonly used as a material for heat exchanger

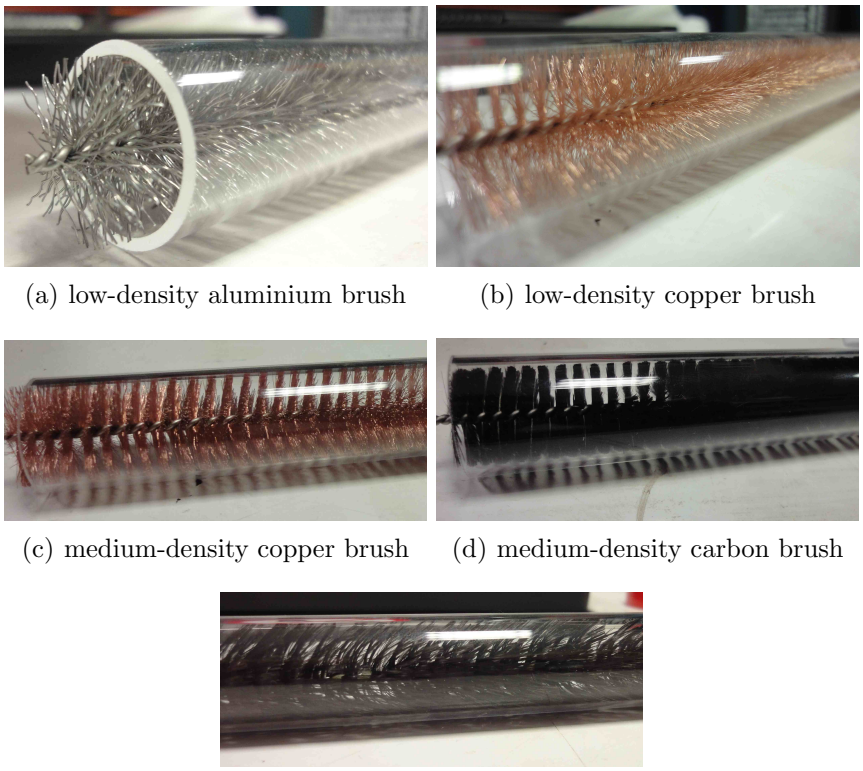

(a) low-density aluminium brush (b) low-density copper brush

(c) medium-density copper brush (d) medium-density carbon brush

(e) low-density carbon brush

Figure 4.6: Brush-type tube inserts

tubes. Figure 4.6 shows the five inserts that were placed inside transparent plexiglas tubes for the purpose of illustration.

4.2.1 Idealised 3D brush geometry

An idealised 3D-model of a brush-type insert is depicted in figure 4.7. In order to be able to create the 3D object, the number, position, and direction of the ligaments have to be derived from the global constraints, i.e. the geometries of the ligaments and core wire and overall relative density of the structure. The model discussed in the following is based upon two main underlying assumptions:

1. The packing at the stem surface is optimal, i.e. the individual fibres touch at $r = r_{stem}$ and the angle between each ligament is equal $\alpha_i = \alpha_{i+1} = \ldots$.

2. The fibres are perfectly straight and their orientation is orthogonal to the axial direction, i.e. the length of each ligament is exactly the tube diameter $l_{lig} = d_{tube}$.

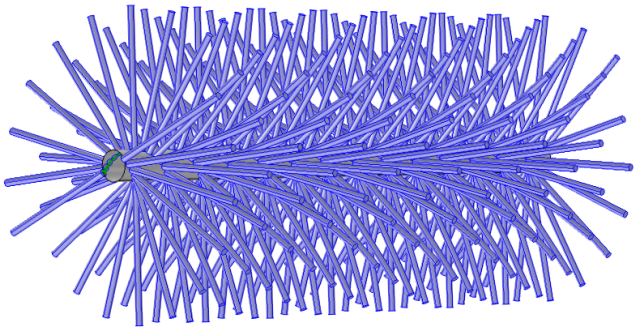

Figure 4.7: Idealised 3D brush geometry

As a result of these assumptions, the number and position of each ligament is the same for every turn and the whole brush can be seen as a repetition of one representative turn. This implies that the single turn has the same relative density and surface area as the brush as a whole, which puts a fixed constraint on the relation between number of ligaments per turn N^*_{lig} and the length of the turn l_{turn}

$$\rho_{rel} = \frac{V_s}{V_{tot}} = \frac{N^*_{lig} \cdot \pi \cdot r^2_{lig} \cdot l_{lig}}{\pi \cdot (l_{lig}/2)^2 \cdot l_{turn}} \Leftrightarrow \frac{N^*_{lig}}{l_{turn}} = \frac{\rho_{rel} \cdot l_{lig}}{4 \cdot r^2_{lig}} = \text{const.} \tag{4.18}$$

As shown in figure 4.8a, the position of the fibre bases that exit the twisted stem

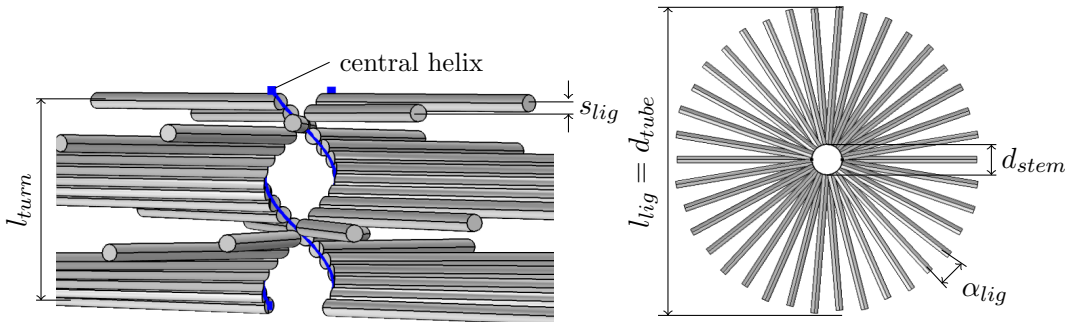

(a) side view (b) top view

Figure 4.8: Geometrical characteristics of a single turn

wire in one turn is described by a 3D-helix:

$$\sigma(t) = \{r \cdot \cos(t), r \cdot \sin(t), h \cdot t\} = \left\{ r_{stem} \cdot \cos(t), r_{stem} \cdot \sin(t), \frac{l_{turn}}{2\pi} \cdot t \right\} \tag{4.19}$$

Since the ligaments are assumed to touch when exiting the stem wire, the arc length of that helix must be equal to the product of the number of ligaments per turn and their diameter

$$s = \int_0^{2\pi} |\sigma'(t)|\, dt = 2r_{lig} \cdot N^*_{lig} \tag{4.20}$$

The helical path has a constant velocity of $\sigma'(t) = \sqrt{r^2 + h^2}$, so that

$$2 \cdot r_{lig} \cdot N^*_{lig} = 2\pi \cdot \sqrt{r^2_{stem} + \left(\frac{l_{turn}}{2\pi}\right)^2} = \sqrt{(2\pi \cdot r_{stem})^2 + l^2_{turn}} \tag{4.21}$$

Together with the fixed relation between N^*_{lig} and l_{turn} this becomes:

$$\begin{aligned} 2 \cdot r_{lig} \cdot N^*_{lig} =& \sqrt{(2\pi \cdot r_{stem})^2 + \left(\frac{N^*_{lig} \cdot 4 \cdot r^2_{lig}}{\rho_{rel} \cdot l_{lig}}\right)^2} \\ \Leftrightarrow N^*_{lig} =& \frac{\pi \cdot r_{stem}}{r_{lig}} \cdot \frac{\rho_{rel} \cdot l_{lig}}{\sqrt{(\rho_{rel} \cdot l_{lig})^2 - (2 \cdot r_{lig})^2}} \end{aligned} \tag{4.22}$$

This yields the turn length as:

$$\begin{aligned} 2 \cdot r_{lig} \cdot N^*_{lig} =& \sqrt{(2\pi \cdot r_{stem})^2 + l^2_{turn}} \\ \Leftrightarrow l_{turn} =& \sqrt{(2 \cdot r_{lig} \cdot N^*_{lig})^2 - (2\pi \cdot r_{stem})^2} \end{aligned} \tag{4.23}$$

The axial ligament spacing s_{lig} and angle between the ligaments α_{lig} is then simply:

$$s_{lig} = \frac{l_{turn}}{N^*_{lig}} \tag{4.24}$$

$$\alpha_{lig} = \frac{2\pi}{N^*_{lig}} \tag{4.25}$$

4.2.2 Experimental relative density determination

In order to determine the brush packing densities, the weight fractions of the brush stem wire and ligaments had to be estimated based on length and weight measurements of the cut off handles and the residual brush parts. Although not all of the materials are known exactly, the volumes occupied by the stem wires and brush ligaments could be calculated using estimated material densities, which allowed for the derivation of volume averaged characteristic values such as the relative density, relative surface area and the overall number of ligaments. The calculation procedure is summarised in the following.

The mass of the brush part is comprised of that of the ligaments and that of the stem wire

$$m_{tot} = m_{br} + m_{stem} \tag{4.26}$$

$$m_{br} = N_{lig} \cdot m_{lig} \tag{4.27}$$

By measuring the weight m_h of the cut off handle, its length l_{handle}, and the length of the residual brush part l_{br}, m_{stem} can be estimated and bristle mass m_{br} determined:

$$m_{tot} = m_{br} + m_{stem} = m_{br} + m_h \cdot \frac{l_{br}}{l_{handle}} \Leftrightarrow m_{br} = m_{tot} - m_h \cdot \frac{l_{br}}{l_{handle}} \tag{4.28}$$

The fibre dimensions are known from the manufacturer's specifications. Together with the estimated density of the bristle materials, the volume and mass of one individual ligament can be calculated as

$$V_{lig} = \pi \cdot r_{lig}^2 \cdot l_{lig} = \pi \cdot r_{lig}^2 \cdot 2r_{br} \tag{4.29}$$

$$m_{lig} = \rho_{lig} \cdot V_{lig} \tag{4.30}$$

It should be noted that the two equations above lead to a slight under-prediction in fibre volume and mass because it neglects the bending of the ligaments attributed to the twisting of the centre rod and also does not account for the crimp of the aluminium and copper wires.

With relation 4.30 the overall number of ligaments can be determined from eq. 4.27:

$$N_{lig} = \frac{m_{br}}{m_{lig}} \tag{4.31}$$

For the calculation of the relative density of the air permeable part of the structure, the volume V_s of the parts of the solid ligaments that emerge from the twisted up stem and interact with the fluid is divided by the overall channel volume, that is

Table 4.2: Brush insert properties

Variable		LD alum.	LD. copp.	MD copp.	LD carb.	MD carb.
material		Al	$CuNi_{10}$		PAN-based carbon	
m_h	[g]	1.2118	1.2243	1.0841	0.0334	1.1172
l_{handle}	[cm]	7.7	7.6	6.8	0.55	7.2
m_{tot}	[g]	8.227	10.407	20.5405	2.1804	6.0229
l_{br}	[cm]	20.2	20.3	21.1	20.8	20.9
m_{stem}	[g]	3.18	3.27	3.36	1.26	3.24
m_{br}	[g]	5.05	7.14	17.18	0.92	2.78
ρ_{lig}	[kg/m^3]	2.7	8.95	8.95	1.79	1.79
r_{lig}	[μm]	108	51	51	4	4
l_{lig}	[cm]	1.905	1.905	1.905	2.1	1.905
V_{lig}	[mm^3]	0.69741	0.15444	0.15444	0.00096	0.00087
N_{lig}	[-]	2,681	5,163	12,426	535,089	1,787,656
ρ_{rel}	[-]	0.030	0.013	0.031	0.008	0.025
a_s	[1/cm]	6.387	5.810	13.692	48.161	145.515

equal to the overall test tube volume V_{tot} without the volume of the stem wire V_{stem}:

$$V_{tot} = \pi \cdot r_{t,i}^2 \cdot l_t = \pi \cdot r_{t,i}^2 \cdot l_{br} \tag{4.32}$$

$$V_{stem} = \pi \cdot r_{stem}^2 \cdot l_{br} \tag{4.33}$$

$$V_s = N_{lig} \cdot \pi \cdot r_{lig}^2 \cdot (l_{lig} - 2 \cdot r_{stem}) \tag{4.34}$$

$$\begin{aligned} \Rightarrow \rho_{rel} &= \frac{V_s}{V_{tot} - V_{stem}} = \frac{N_{lig} \cdot r_{lig}^2 \cdot (l_{lig} - 2 r_{stem})}{(r_{t,i}^2 - r_{stem}^2) \cdot l_{br}} \\ &= N_{lig} \cdot \frac{r_{lig}^2}{l_{br}} \cdot \left(\frac{l_{lig} - 2 \cdot r_{stem}}{r_{t,i}^2 - r_{stem}^2} \right) \end{aligned} \tag{4.35}$$

The relative surface area of the brushes can be derived from basic geometrical considerations about a cylinder. The surface area of a cylinder is $A_s = 2\pi \cdot r \cdot l = V \cdot (2/r)$, yielding

$$A_s = V_s \cdot \frac{2}{r_{lig}} \tag{4.36}$$

$$A_{stem} = V_{stem} \cdot \frac{2}{r_{stem}} \tag{4.37}$$

For the investigated brushes, the surface area of the stem wire is at least 30 times smaller than that of the bristles and is neglected for the calculation of the relative

surface area a_s of the structure. This yields:

$$a_s = \frac{A_s}{V_{tot} - V_{stem}} = \frac{V_s}{V_{tot} - V_{stem}} \cdot \left(\frac{2}{r_{lig}}\right) = \rho_{rel} \cdot \frac{2}{r_{lig}} \tag{4.38}$$

The results of the measurements are summarised in table 4.2.

4.3 Preparation of fibre-flocked tubes

The fibre flocked aluminium sheets, that were bent into tubular shapes, were the third type of structure investigated. Electro-flocking is a process of depositing electro-statically charged fibres onto an adhesive covered electrically grounded surface. The highly charged fibres are mutually repulsive and are attracted by the substrate due to the high electric potential. This results in a uniform deposition of filaments on the substrate, that have a tendency to align perpendicular to the surface. The inserts were prepared using commercially available hand-held electro-flocking equipment, that was customised by researchers at CSIRO to achieve uniform and repeatable flocking results. The original apparatus and its modification is shown in figure 4.9. A typical flocking process begins with placing fibres, that

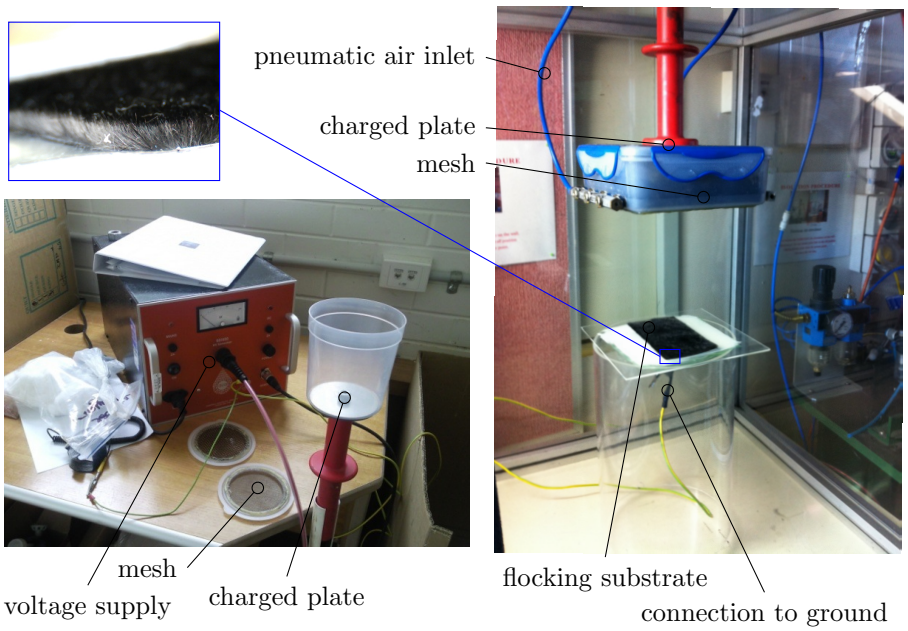

(a) hand-held flocking machine (b) customised flocking machine

Figure 4.9: Flocking machine

have been previously cut to the desired length, into the container of the applicator where they are in contact with the charged plate. The container is covered with a mesh, that helps to mechanically disperse the fibres during the application process. Subsequently a layer of adhesive is applied to the flocking substrate using a woollen roller. While the glue is still wet, the substrate is connected to the electrical ground. In the original apparatus depicted in figure 4.9a, the applicator is shaken by hand during the fibre deposition process in order to get them in contact with the plate, that is charged with a DC-voltage between 25-60kV. In the modified design this is achieved by agitating the fibres inside the applicator container with bursts of compressed air that allows for a exact stationary positioning of the rig elements to produce repeatable and uniform results. After the deposition of the fibres the substrates were put in an oven to cure for at least one hour at a temperature of approx. 80°C. After that the excess fibres were removed using a vacuum cleaner. Weight measurements were performed on the substrate before (s) and after (sa) the adhesive application, as well as on the uncured flocked sample (su) and the cured (sc) sample before (b) and after (a) the removal of the excess fibres. From these and the carbon fibre material data, the relative densities of the flocked samples could be estimated based on the following calculation procedure: The mass of dry glue (gc) is calculated by subtracting the the difference between sample weights before and after curing from the calculated mass of the wet adhesive (gu):

$$m^*_{sa} = m^*_s + m_{gu} \Leftrightarrow m_{gu} = m^*_{sa} - m^*_s \tag{4.39}$$

$$m_{gc} = m_{gu} - (m^*_{su,b} - m^*_{sc,b}) \tag{4.40}$$

The measured quantities are indicated by a star superscript. The mass of of the flocked fibres (lig) is calculated by subtracting the weight of the substrate and dry glue from the total mass of the cured sample after the removal of the excess fibres:

$$m_{lig} = m^*_{sc,a} - m^*_s - m^*_{gc} \tag{4.41}$$

The flocking density is defined as the ratio between fibre-covered and available surface area. This value is equivalent to the relative density when the fibre length is taken as the reference height of the structure.

$$\rho_{rel} = \frac{V_s}{V_{tot}} = \frac{l_{lig} \cdot A_{lig}}{l_{lig} \cdot A_{tot}} = \frac{(m_{lig}/\rho_C)}{l_{lig} \cdot A_{tot}} \tag{4.42}$$

For the preparation of the test objects two pieces of aluminium shim were electro-flocked with 3mm-long polyacrylonitrile(PAN)-based carbon fibres. In order

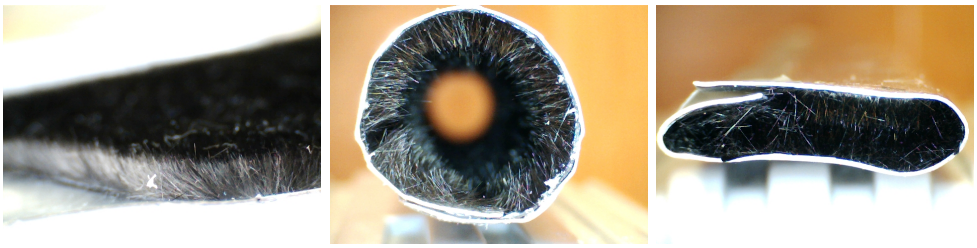

(a) planar flocked substrate (b) flocked circular tube (c) flocked flat tube

Figure 4.10: Flocked test objects

for the flocked test objects to have the same internal surface areas as the other inserts, the flocked areas were $l_t = 200\text{mm}$ long and $W = \pi \cdot d_t = \pi \cdot 19\text{mm}$ wide. As suggested from figure 4.10a, the resulting fibrous coating was fairly uniform. Due to the comparatively big fibre length, the majority of the fibres were aligned in an upright fashion, but not truly perpendicular to the surface. Using the calculation procedure described in equations 4.39-4.42 above, the relative density of both flocked structures were estimated as approx. $\rho_{rel} = 0.3\%$ with a corresponding relative surface area of $a_s = 12.0\text{m}^{-1}$. The width of the aluminium shim substrates was kept 5mm bigger than that of the flocked areas creating an overlap when bent into shape that facilitated the alignment during shaping and sealing of the formed tubular objects, depicted in figure 4.10b-c. Silicone sealant was used to make the objects water and air tight.

PAN-based carbon fibres were used for initial testing because they were readily available at the CSIRO laboratories and are much cheaper and easier to procure than their pitch-based counterparts. Due to the difficulties encountered with coating such fine structures, a replication of the structures with the thermally superior materials at a later stage was abandoned.

4.4 Application of desiccant coating

As a result of the experimentally determined pressure drop and heat transfer performance of the various test objects, that are discussed in chapters 5-8, the metal foam tubes and the aluminium brush insert were chosen to be coated with desiccant material for further transient heat and mass transfer testing. Silica gel was chosen as a desiccant material, since it is routinely used in conventional desiccant wheels and its sorption characteristics are well characterised. A suitable coating procedure had to be identified, that would yield a coating satisfying the following criteria:

- robust desiccant matrix with good adhesion to the substrate
- minimal impact on sorption behaviour of the desiccant material in terms of diffusion resistance and moisture uptake capacity
- high degree of uniformity in coating thickness and composition
- facilitation of coating thickness variation

Fischer and Mescher [1996] have patented a relatively straightforward approach, that satisfies all the above-mentioned criteria and was chosen as the coating procedure.

4.4.1 Preparation of coating mixture

The coating applied to the test objects was a uniform slurry of five components, namely

- ground silica gel as the desiccant material,
- polyurethane as the organic binder,
- N-methyl-2-pyrrolidone as the suspending/pore clearing agent,
- ammonium hydroxide as the pH-adjustment agent, and
- water as the solute.

According to the patent, the preferred size for the solid desiccant particles lies within the range of 3-10 microns. This was achieved by grinding RD silica gel beads, that were readily available at the CSIRO laboratories, in a ball mill. This resulted in particle size distributions, that were measured optically in a Malvern Mastersizer X machine. Over the course of the coating preparation process, the slurry was made three times for which silica gel beads were milled down to an average particle size of approx. 5-8 micron. Figure 4.11 shows a plot of the particle size distribution of one of the batches as an example.

For the slurry a basic recipe was followed. Due to minor variations in used quantities, the recipe in table 4.3 is presented as averaged values. As a first step in the preparation of the mixture, approx. 90% of the silica gel was added to a mixture of water and pH-adjustment agent under continuous stirring in a reaction vessel. The ammonium hydroxide is important to bring the acidic mixture down to a pH-level that is beneficial for the interaction between desiccant material, binding substance and substrate. For aluminium substrates, the preferred pH-level of the coating mixture lies between 7.5 and 9.5. The subsequent addition of N-methyl-2-pyrrolidone helps to keep the silica gel particles in suspension in the mixture. It also acts as a pore clearing agent, hindering the binder material from entering the

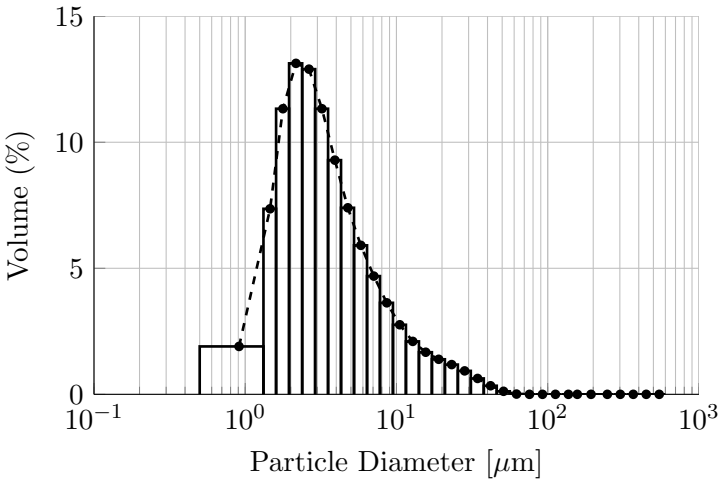

Figure 4.11: Particle size distribution of milled silica gel

Table 4.3: Recipe for desiccant coating

Component	Substance	weight (%)
desiccant	silica gel	39.2
binder	polyurethane	13.7
suspending agent	N-methyl-2-pyrrolidone	6.3
pH-adjustment agent	Ammonium hydroxide	4.0
solution	water	36.7
total		100.0

pores which would reduce the moisture uptake capacity. The remaining silica gel is mixed in afterwards. The addition of the solid particles is divided into two batches in order to prevent the build up of sediment which can be difficult to reverse. In between respective additions, the mixture was stirred for at least 20min. When the test objects were ready to be coated, the organic binder was added to the mixture and stirred in for 20min before the coating was applied.

After the coating process the samples were placed in an oven preheated to 180°C for at least 90min in order to drive off the volatile components and cure the organic binder. Based on the followed recipe, the fraction of active material f_a in the coating layer can be calculated by comparing the relative weights of desiccant (d) and binder (b):

$$f_a = \frac{m_d}{m_d + m_b} \tag{4.43}$$

It varied for the individual recipes between $f_a = 0.74$-0.75.

(a) 5PPI, coating 1

(b) 10PPI, coating 1

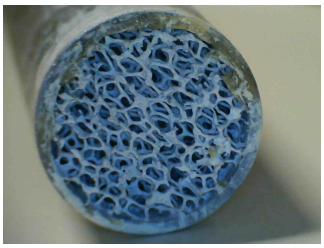

(c) 20PPI, coating 1

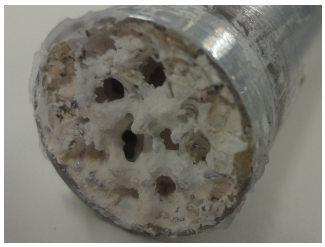

(d) 5PPI, coating 2

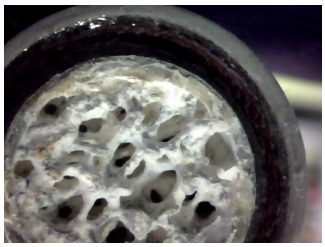

(e) 10PPI, coating 2

Figure 4.12: Desiccant coated aluminium foam tubes

4.4.2 Coating of aluminium foam tube inserts

The interior of the aluminium foam tubes were coated by filling them to the top with the prepared slurry with one tube end blocked off. The mixture was allowed some time to rest in order to let trapped air bubbles escape before the end was opened and the mixture drained from the tube. Excess inside the metal foam structure was blown off with compressed air to prevent the blockage of small pores by remaining droplets. The samples were placed in an oven heated to 50°C to set before the process was repeated a second time in order to achieve a thicker coating. Based on the properties of the plain metal foam tubes presented in table 4.4, the following properties for the coated foam could be determined:

Table 4.4: Coated aluminium foam properties

Variable			5PPI	10PPI	20PPI
m_{tot}	(uncoated)	[g]	61.2258	58.5875	59.605
m_{foam}		[g]	16.2	13.6	14.6
ρ_{rel}		[%]	9.7	8.1	8.7
m_{tot}	(coating 1)	[g]	65.2966	62.1951	64.9217
m_{coat}	(coating 1)	[g]	4.0732	3.6056	5.3105
ρ_{rel}	(coating 1)	[%]	17.9	15.3	19.4
m_{coat}	(coating 2)	[g]	8.1094	6.7902	–
ρ_{rel}	(coating 2)	[%]	23.4	21.4	–

The underlying calculation procedures were:

$$m_{coat} = m_{tot} - (m_{foam} + m_{tube}) \tag{4.44}$$

$$\rho_{rel} = \frac{(m_{foam}/\rho_{Al}) + (m_{coat}/\rho_{Si})}{V_{ch}} \tag{4.45}$$

Photographs of the coated foam inserts are shown in figure 4.12.

4.4.3 Coating of aluminium brush tube insert

A different approach was taken for the coating of the aluminium brush insert. Since it was not fixed inside the test tube, the application of desiccant material could be facilitated by simply submerging the brush into the coating slurry. After the dip coating the brush insert was spun at high speed using a Dremel rotary tool, creating high centrifugal forces to remove the excess liquid. Similar to the metal foam insert, this process was repeated several times with intermediate drying at 50°C until a satisfactory coating thickness was reached. For the coating process a brush with a smaller-diameter stem wire and the same nominal relative density was used.

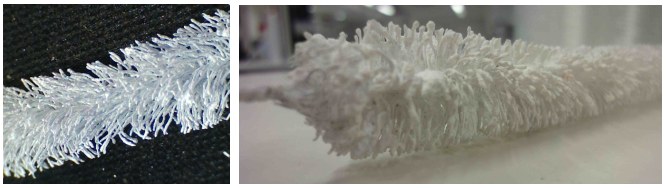

(a) coating 1 (b) coating 2

Figure 4.13: Desiccant coated aluminium brush insert

The aluminium brush is depicted with its two coatings in figure 4.13 and its properties are summarised in table 4.5.

Table 4.5: Coated aluminium brush properties

Variable	uncoated	coating 1	coating 2
m_{br} [g]	7.705	9.757	15.061
m_{coat}[g]	0	2.052	7.356
ρ_{rel} [%]	3.0	7.5	19.3

Chapter 5

Experimental investigation of flow and pressure drop over heat exchange structures

The pressure drop is an important design parameter for air conditioning systems and a central performance characteristic for the desiccant wheel tube inserts under investigation here. The pressure drop over the various test objects described in the previous section was determined experimentally. As will be discussed in the following, the experimental results allowed for a first preselection of inserts that imposed a flow resistance within the acceptable range.

5.1 Description of the experimental test rig

The experiments were performed using a TEXTEST FX 3030 Air Permeability Tester from the CSIRO laboratories, depicted in figure 5.1. The machine is designed for a pressure drop measurement up to $3,000$Pa over textiles and fibrous media. Laboratory air is drawn in through a circular orifice, over which the test object is positioned, by means of a two-speed suction fan at an adjustable flow rate up to $8,000$l/h. The pressure drop is measured with a class 1 electronic pressure sensor and is digitally displayed with a readability of 1Pa. After entering the machine, the test air is directed through one of four floating body flow meters, that cover different parts of the measurable flow regime. Their maximal measurement error is specified as 0.75% of the displayed value in addition to 0.25% of the respective maximum meter scale. For the current work, the test tubes with the various tube inserts were positioned inside the tubular fibre testing chamber of the permeability

machine using two O-rings. To prevent any air leakage past the test objects, the end of the test chamber was additionally sealed with adhesive tape. Pressure drop tests were performed on all tube inserts and the empty tube. The pressure drop data was corrected for the flow resistance imposed by the empty rig itself, which was also recorded.

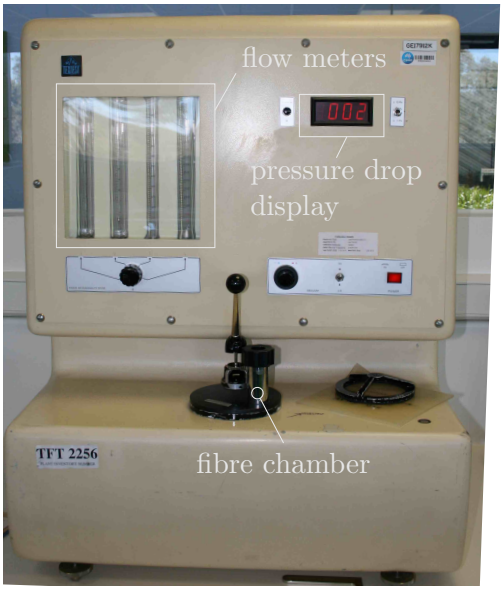

Figure 5.1: Pressure drop testing machine

5.2 Discussion of experimental results

Pressure drop tests were performed on the various uncoated inserts and repeated for the selected ones that were coated with desiccant material. These experiments are the foundation for the derivation of the porous medium flow characteristics, namely the permeability and drag factor. As has been discussed in section 3, in the majority of porous medium literature they are determined by means of a simple second order polynomial fit to the experimental data where the coefficients correspond to the parameters of the Darcy or Forchheimer flow models. However, Dukhan and Ali [2012] showed experimentally, that for tubular metal foam inserts of similar dimensions to the ones utilised here, the effect of the confining walls on the channel flow cannot be neglected. In this case the above-mentioned models are inapplicable and a direct derivation of the characteristic parameters from experimental data is not possible. They were instead derived from numerical flow modelling, which will be discussed

in the subsequent chapter 6. In the following the test results of the various uncoated inserts are discussed in detail, before the pressure drop data for the coated inserts are presented.

5.2.1 Pressure drop over uncoated inserts

The raw experimental results for the uncoated inserts are depicted in figure 5.2.

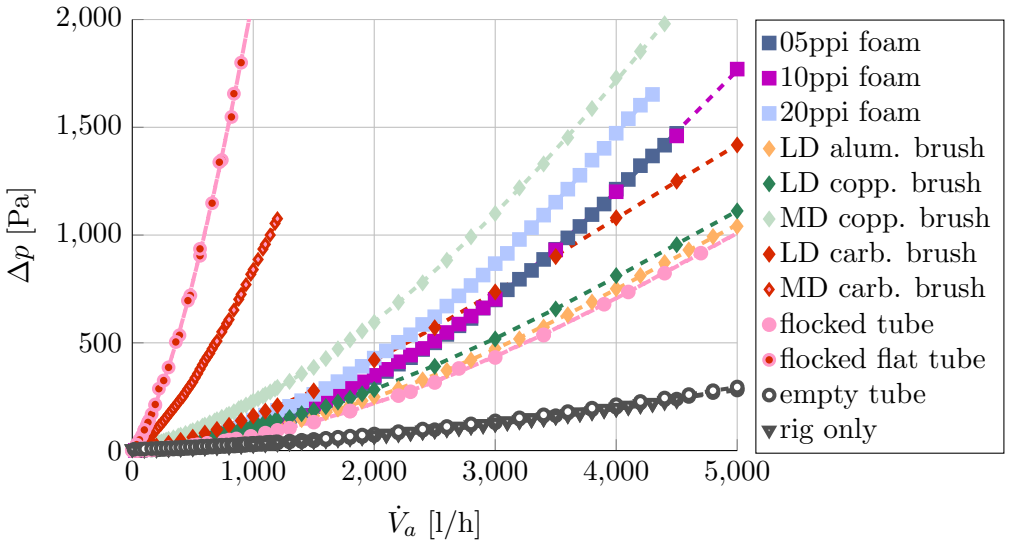

Figure 5.2: Raw experimental pressure drop data

The metal foam tubes are distinguished by solid square symbols in figure 5.2. It can be seen that the 20PPI-foam exhibits a bigger flow impedance than the other two inserts, which is most likely due to the attributed higher number of ligaments and surface area. It is interesting to note, that the pressure drop curves of the other two metal foam tubes only differ minimally and this surface area dependence of the pressure drop cannot be observed. This can be explained mainly by two effects: Firstly, the effect of the surface area on the pressure drop can be expected to lessen with increasing pore size as the turbulence promoting effect of the solid obstructions becomes less when their dispersion in space increases, i.e. the porosity increases. As a consequence, the difference between the 5PPI foam to the 10PPI foam slopes would be less than that between the 10PPI and 20PPI foam. Secondly, the comparison of the actual relative densities of the test objects in table 4.1 revealed, that the solid volume fraction of the 5PPI foam is higher than that of the other two inserts, which shifts its pressure drop curve further upwards on to the level of that of the 10PPI insert.

The brush-type inserts are marked by diamond-shaped symbols in figure 5.2. As could have been expected, the medium-density carbon brush resulted in the highest pressure drop over the test object by far for this group of inserts due to its superior number of ligaments and surface area. It was followed by the medium-density copper-brush, whose flow restriction still exceeded that of the 20PPI metal foam tube. The lower density aluminium and copper brushes cause a very similar flow impediment with the copper brush yielding a slightly higher pressure drop. The pressure drop profile of the low density carbon brush seems to differ from that of the other brush-type inserts, as it imposes a similar flow resistance as the metal foam structures for intermediate flow rates but then its slope becomes nearly linear for $\dot{V}_a > 2,500$l/h. Despite the higher relative surface area, the flow impediment is lower than that of the medium-density copper brush. Three contributing factors can be identified that help to explain these findings:

- during the production process of the carbon fibre tows they undergo a surface treatment that makes them stick together in order to make their handling easier. As a consequence, the bristles of the hand-made low-density carbon brush did not all separate during the twisting process but formed discrete bundles. This circumstance is visible to some extent from figure 4.6e. From this it can be inferred, that not all the surface area provided by the fibrous structure is effectively available for fluid interaction, thus obscuring the surface area related trend observed with the other inserts.

- Secondly, the fineness of the 8 micron thick carbon fibres making up the brush results in a very bendable structure. It is therefore conceivable, that high flow rates lead to a separation of fibres from the tube wall leading to a reduction in pressure drop.

- Thirdly, the ligament length hand-made low-density carbon brush was bigger than the tube diameter, which led to an obtuse contact angle between fluid and fibres, which has a diminishing effect on the pressure drop [Fowler and Bejan, 1994]. The difference in contact angles can be observed when examining figure 4.6.

The two flocked inserts had virtually the same flocking density and perimeter and only differed in their cross-sectional shapes. It can be seen, that when the fibres fill up the entire channel cross-section, as in the case of the flat tube, and the air is forced through the sparse forest of fibres, the pressure drop is dramatically higher than in the case of the circular tube where the air is not forced through

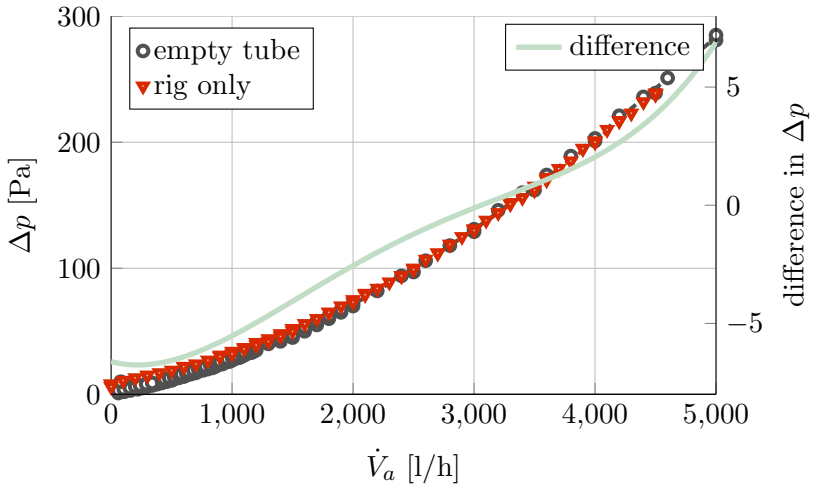

Figure 5.3: Comparison of empty tube data to intrinsic rig pressure drop

the flock. Since the pressure drop is a result of the interaction between fluid and solid flow obstructions, it can be concluded that for the case of the circular tube the majority of the air flows through the fibre free core of the channel without contacting the surfaces of the fibres. The circular tube still yields a significant pressure drop augmentation when compared to the empty tube reference case, indeed indicating an increased level of interaction between working fluid and surface-enhanced channel wall, as was suggested by Lund and Knowles [2001].

The pressure drop measurement of the empty tube alone was problematic, because of the minimal flow restriction it imposed, making its pressure drop curve almost indistinguishable from the empty rig reference measurement in figure 5.2. A magnification of these two curves is shown in figure 5.3 together with the difference between the two, which is plotted with reference to the second ordinate. It can be seen, that for flow rates up to about $3,500$l/min the recorded pressure drop data for the empty tube is actually below the reference measurement. While this makes the interpretation of the empty tube measurements corrected for the intrinsic rig pressure drop impossible, it indicates that the pressure drop over the empty tube is negligibly small in comparison to the other inserts.

In order to correct for the rig intrinsic flow restriction the experimental data were approximated by continuous fourth-order polynomial fitting functions that allowed the subtraction of the reference measurement from the test data. The resulting functions are presented in figure 5.4. The evaluation of the pressure drop data led to the exclusion of the medium density carbon brush insert and the flat

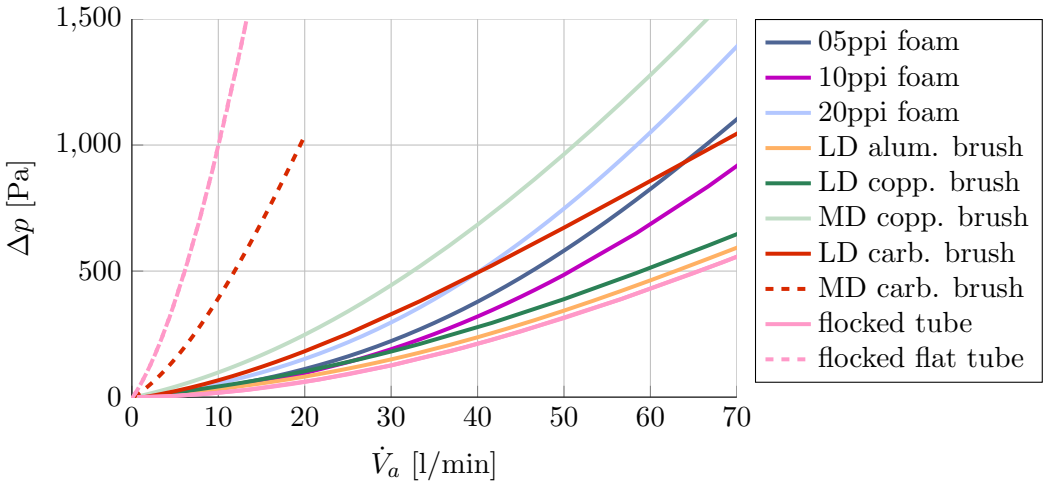

Figure 5.4: Polynomial fit functions to corrected pressure drop data

tube structure from subsequent heat and mass transfer tests. The attributed flow impedance, that was so great even at low flow rates, makes their suitability for an application in the water-cooled desiccant wheel very questionable.

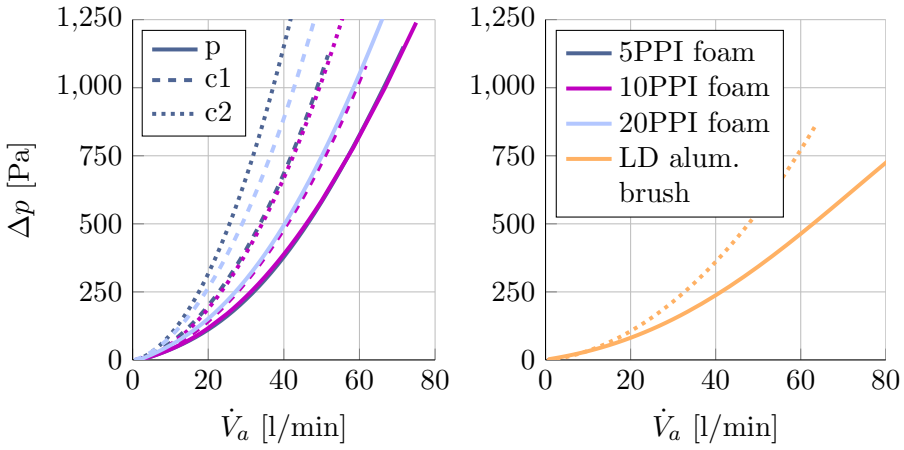

Figure 5.5: Effect of coating thickness on insert pressure drop

5.2.2 Pressure drop over coated inserts

The pressure drop tests were repeated for the coated metal foam and aluminium brush inserts and the results are depicted in figure 5.5. The tests were performed for both the thin first coating and the thick final coating in the case of the 5PPI and 10PPI foam structures, while for the aluminium brush insert only the flow resistance

of the final thickly coated brush was recorded. The colour coded solid lines refer to the respective plain inserts (p) and the dashed and dotted lines to the pressure drop with the first (c1) and, if applicable, second coating layer (c2). It can be seen that in all cases the desiccant coating causes a noticeable augmentation in pressure drop due to the attributed augmentation in ligament diameter and consequently relative density and surface area.

Chapter 6

Numerical investigation of flow and pressure drop over heat exchange structures

In addition to the experimental investigation of the insert specific flow impedance, the flow through the metal foam and the metal brush type inserts was also studied for various relative densities by means of computational fluid dynamics (CFD) models.

The difficulty with studying the flow through the test objects numerically is that their structural complexity makes it impractical to solve the problem as one comprehensive 3D-model. This internal complexity is an intrinsic property of porous media where the difference in characteristic lengths of micro- and macro-scale is commonly of several orders of magnitude. As such, one single cell of the metal foam inserts is roughly 40-160 times smaller than the test tube is long. Despite the complex underlying micro-scale structure, however, the macroscopic flow through a porous medium follows certain simple rules, that make it possible to calculate the main characteristics of the flow numerically at little computational cost. The modelling approach taken here is therefore tripartite:

1. First, the flow through a single array of representative unit cells is analysed by calculating the respective flow field in the laminar regime. This allows for the identification of a representative unit-cell pressure drop and average velocity at developed flow conditions for a range of inlet velocities and porosities.

2. As a next step, the unit-cell pressure drop-velocity function is correlated with the Forchheimer flow model to derive the characteristic porous medium flow parameters, i.e. permeability and form drag factor.

3. Using these two parameters, the flow through the entire test tube is then calculated as a 2D-axissymmetric problem using a Forchheimer-extended Brinkman flow model, which allows for a comparison of the modelling results to experimental data and captures the macroscopic flow behaviour at significantly less computational cost. This model also serves as the basis for the numerical heat and mass transfer analysis discussed in later chapters.

In the following, steps one and two will be discussed in section 6.1 for the metal foam inserts and in section 6.2 for the brush-type inserts. Subsequently, the setup of the Brinkman flow model will be described and the models calibrated to the experimental data.

6.1 Three dimensional model of flow through metal foam cells

The flow fields over an array of 25 unit-cells described in section 4.1.1 was calculated for the three tested pore sizes (5, 10, 20PPI) and various relative densities and using the in-built laminar flow module of the COMSOL Multiphysics® software. The geometry specific flow field was modelled for a range of inlet velocities. The respective porous medium characteristics, namely permeability and drag factor, could be derived by means of fitting a second-order polynomial function to the representative flow rate dependent pressure drop function over a unit cell.

6.1.1 Model setup

The three dimensional geometry was built within COMSOL's graphical user interface. Due to the regular shape of the metal foam matrix elements, the size of the computational domain could be reduced by only modelling one eighth of the respective unit cells. A similar modelling approach was taken by Xu et al. [2008] for their numerical analysis of a similar metal foam structure. An array of 10PPI-foam unit cells fractions is depicted in figure 6.1, that helps to visualise the set boundary conditions. For better visibility they are displayed on only the first two unit-cells, although the actual modelled structures consisted of 25 cells. A fixed uniform velocity field was set for the inlet boundary that was varied from $u_{in} = 0.1 - 3\text{m/s}$. As can be seen from figure 6.1, the inlet boundary was set one unit-cell length away from the first foam cell, in order to allow for a natural flow field formation around the first ligaments. The surface of the ligaments is distinguished in blue and modelled as a solid wall with no-slip flow conditions, i.e. the fluid velocity on those boundaries

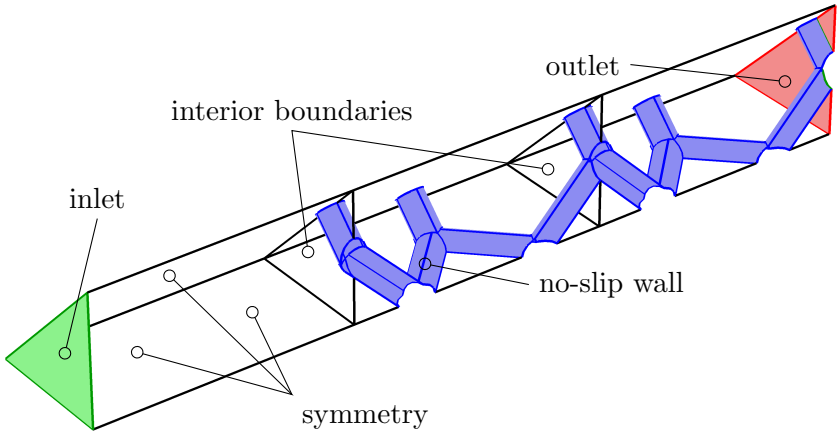

Figure 6.1: 3D modelling domain of metal foam section

is zero. At the outlet boundary, depicted in red in figure 6.1, the gauge pressure and viscous stress terms are set to zero. The three outer boundaries that make up the respective unit-cells are defined as symmetry boundaries, that prescribe no penetration of mass and vanishing shear stresses. This cell representation can be expected to yield less accurate results in the turbulent regime, where it would fail to represent possible vortex formations across the symmetry boundaries. However, it is deemed appropriate for the representation of the problem at hand, where the fluid flow is mainly in the laminar and transitional regime and only minor vortex formation can be expected. The triangular interior boundaries do not have any particular settings applied to them and merely serve as reference areas to facilitate the result post-processing. The fluid density and viscosity were set to those of dry air at 20°C. Since the changes in pressure dependent air properties could be expected to be minor, the model was simplified by treating the gas as an incompressible fluid.

The associated governing equation system 2.43-2.45 including the constraints at the boundary conditions is set-up automatically in COMSOL and is discretised using a stabilised finite element method.

The programme's internal physics-induced mesh-building algorithm was used to discretise the modelling domain. This resulted in an unstructured mesh of tetrahedral volume elements in the bulk of the fluid domain and with refined elements along the solid wall surfaces making up a two-layered boundary mesh. An example of a meshed unit cell is shown in figure 6.2. The complexity of the modelling mesh varied proportionally to the relative density and only to a minor extent with pore size between approximately 290,000-660,000 elements.

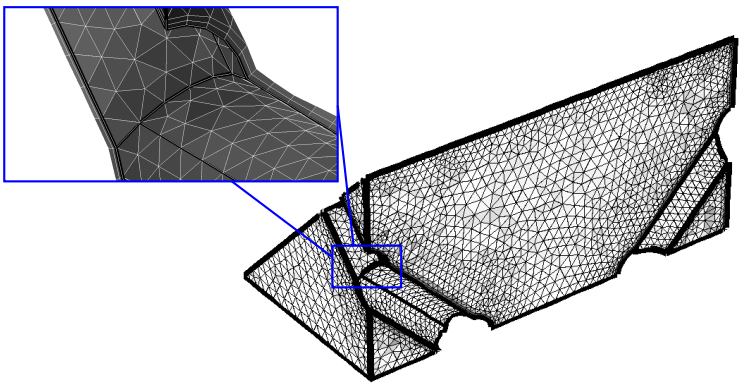

Figure 6.2: Meshed unit-cell and 2-layer boundary mesh

6.1.2 Modelling results

The resulting three-dimensional flow fields were analysed for the various relative densities and flow rates modelled by comparing cell individual volume averages of the velocity fields and cell-specific pressure drops. The cell in- and outlet pressures were determined by taking the surface average over the pressure field of the respective interior boundaries that encompass each cell as indicated in figure 6.1. The flow field was regarded as developed when the cell specific average velocity and pressure drop reached an approximately constant level ($\Delta_u < 0.05$m/s, $\Delta_{\Delta p} < 0.1$Pa). Figure 6.3 shows typical evolutions of those values for the example of the 10PPI foam at an intermediate relative density of $\rho_{rel} = 0.15$. Here it can be seen that the flow could be considered developed after about 7 cells. The deviation of the last data point representing cell 25 is a result of the defined outlet condition that sets the shear stresses to zero on that boundary which is in conflict with the calculated upstream

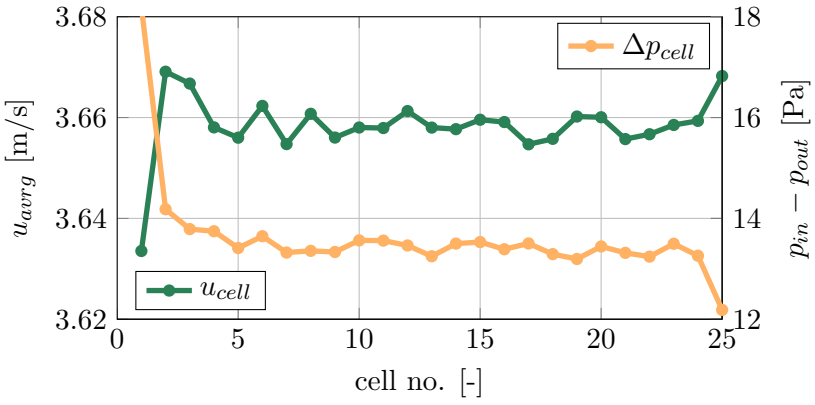

Figure 6.3: Typical average cell velocity and pressure drop distribution

flow field. The fluctuations in the developed flow region are due to the mesh size and could be reduced by a refinement of the grid, however at the cost of increased computational time.

Unit-cell flow

The flow field through cells 7 to 24 could therefore be seen as representative for the entire metal foam structure. Figure 6.4 and 6.5 show streamline plots of the flow through the twenty-third unit cell of the three foams at three different velocities for the cases of a low and high relative density. The flow direction through the cells is from right to left as indicated by grey arrows. [h]

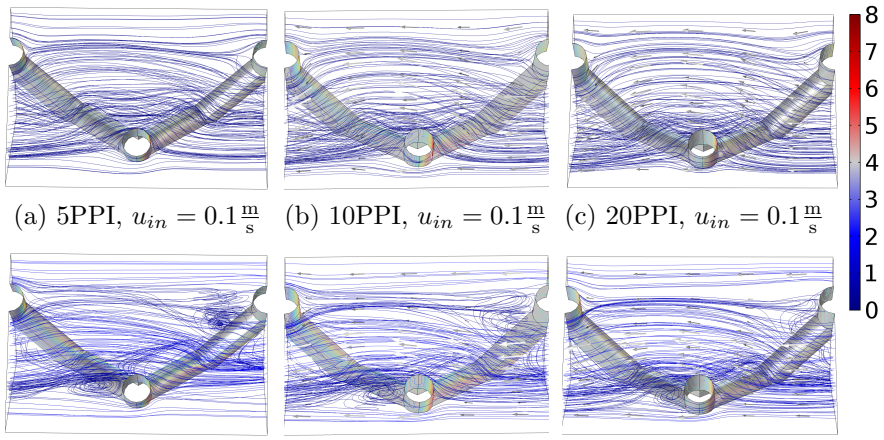

(a) 5PPI, $u_{in} = 0.1\frac{\mathrm{m}}{\mathrm{s}}$ (b) 10PPI, $u_{in} = 0.1\frac{\mathrm{m}}{\mathrm{s}}$ (c) 20PPI, $u_{in} = 0.1\frac{\mathrm{m}}{\mathrm{s}}$

(d) 5PPI, $u_{in} = 1\frac{\mathrm{m}}{\mathrm{s}}$ (e) 10PPI, $u_{in} = 1\frac{\mathrm{m}}{\mathrm{s}}$ (f) 20PPI, $u_{in} = 1\frac{\mathrm{m}}{\mathrm{s}}$

(g) 5PPI, $u_{in} = 3\frac{\mathrm{m}}{\mathrm{s}}$ (h) 10PPI, $u_{in} = 3\frac{\mathrm{m}}{\mathrm{s}}$ (i) 20PPI, $u_{in} = 3\frac{\mathrm{m}}{\mathrm{s}}$

Figure 6.4: Unit-cell velocity fields at $\rho_{rel} = 0.08$

When comparing plots (a)-(c) in the first row of the respective figures, it can be seen that the resulting flow fields look similar for the three pore sizes. The increased ligament thickness leads to a more pronounced wave in the streamlines, but in all six presented cases, the flow is completely laminar. The flow fields become more distinguishable at an intermediate inlet velocity of 1 m/s shown in plots (d)-(f), where the onset of turbulence in the flow can be observed by flow separation and swirl flow regions downstream of the ligaments perpendicular to the flow. The

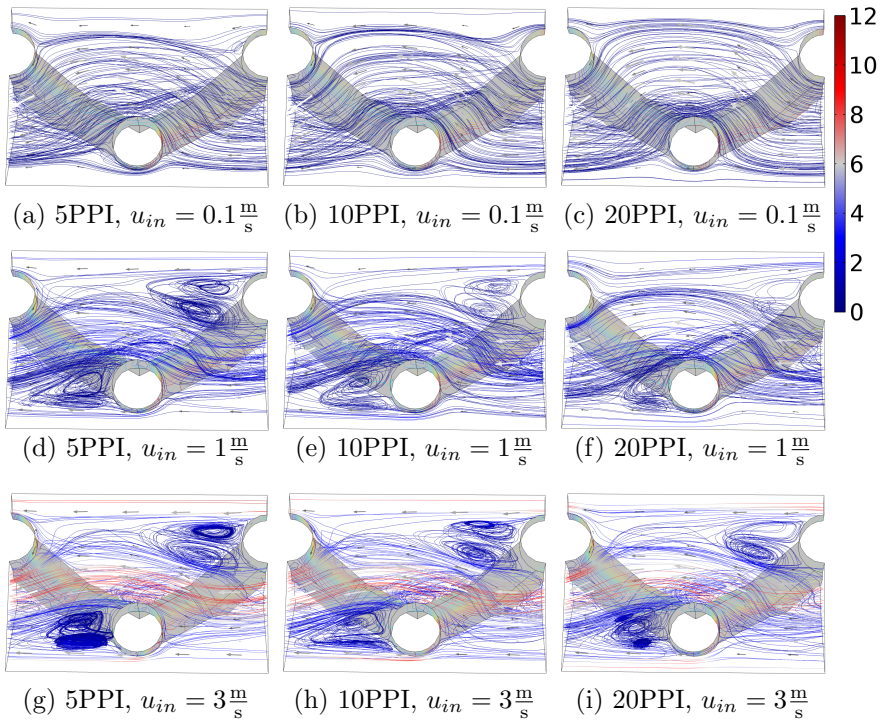

(a) 5PPI, $u_{in} = 0.1\frac{\mathrm{m}}{\mathrm{s}}$ (b) 10PPI, $u_{in} = 0.1\frac{\mathrm{m}}{\mathrm{s}}$ (c) 20PPI, $u_{in} = 0.1\frac{\mathrm{m}}{\mathrm{s}}$

(d) 5PPI, $u_{in} = 1\frac{\mathrm{m}}{\mathrm{s}}$ (e) 10PPI, $u_{in} = 1\frac{\mathrm{m}}{\mathrm{s}}$ (f) 20PPI, $u_{in} = 1\frac{\mathrm{m}}{\mathrm{s}}$

(g) 5PPI, $u_{in} = 3\frac{\mathrm{m}}{\mathrm{s}}$ (h) 10PPI, $u_{in} = 3\frac{\mathrm{m}}{\mathrm{s}}$ (i) 20PPI, $u_{in} = 3\frac{\mathrm{m}}{\mathrm{s}}$

Figure 6.5: Unit-cell velocity fields at $\rho_{rel} = 0.25$

intensity of the flow disturbance is dependent on the ligament size and spacing and is consequently lowest in the (20PPI, $\rho_{rel} = 0.08$)-case and highest in the (5PPI, $\rho_{rel} = 0.25$)-case. The degree of turbulence intensifies with higher flow rates, resulting in pronounced eddies at an inlet velocity of 3m/s shown in plots (g)-(i) in figures 6.4-6.5. From these plots it is also seen that a higher degree of turbulence also causes a wider spread in streamline velocities that range from approx. 0-8 m/s in the lowest (20PPI, $\rho_{rel} = 0.08$) to 0-11 m/s in the highest (5PPI, $\rho_{rel} = 0.25$) case. It is also apparent that an increasing ligament size due to a change in relative density leads to a more severe obstruction of the smaller interfacial quadrilateral pore. As a result, there are fewer streamlines visible in the upper part of the cell in figure 6.5 and the majority of flow is directed through the bigger pores.

Porous-medium model fit

In order to derive the porous medium characteristics, the relative density dependent unit-cell pressure drop data was plotted as a function of volume-averaged cell velocity for each of the three foam cell sizes. As has been mentioned before, the porous medium characteristics can be derived from simple second-order polynomial fitting

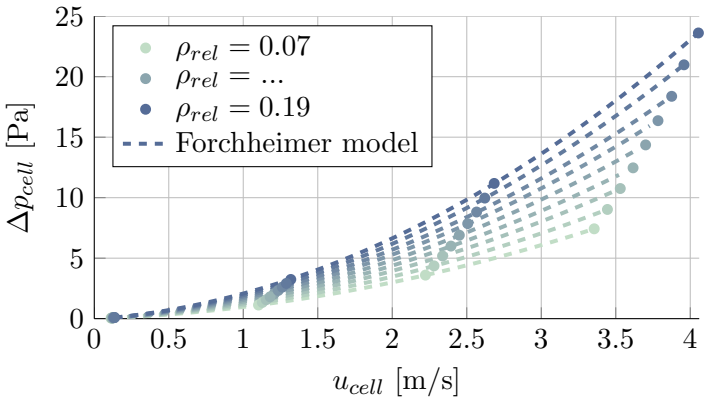

Figure 6.6: Forchheimer fit to CFD-modelling results

functions, if the flow behaves according to the Forchheimer model. This is confirmed by the quality of fit between CFD-modelling results and fitting functions that is shown as an example for the 10PPI foam in figure 6.6.

From the fitting parameters permeability and drag factor can be calculated by setting the fitting function equal to the Forchheimer flow model 2.60:

$$-\Delta p = c_2 \cdot u^2 + c_1 \cdot u = L \cdot \left(\frac{\mu}{K} \cdot u + \rho \cdot C_F \cdot u^2 \right)$$

$$\Rightarrow K = \frac{\mu}{c_1} \tag{6.1}$$

$$\Rightarrow C_F = \frac{c_2}{\rho} \tag{6.2}$$

The permeability and drag factor values calculated using the equations above are plotted for the three foams in figure 6.7.

The three pore sizes are distinguished by colours and the permeability values are represented by downward-pointing triangles. For the studied relative densities the values lie between $K = 0.05 - 0.6\text{mm}^2$. The permeability functions follow the expected trends decreasing with higher packing densities and smaller pore sizes. The drag factor values, marked by upward-pointing triangles are in the range of $C_F = 50 - 600\text{m}^{-1}$ and exhibit opposite trends to the permeability increasing with higher relative densities and lower pore sizes. It is apparent from figure 6.7 that the sensitivity of the permeability function to a change in relative density, i.e. a change in ligament diameter, is diminished when the pore/cell size decreases, while the drag factor function becomes more sensitive to a change in relative density at decreasing cell size.

The insert specific relative surface area functions are depicted in figure 6.8.

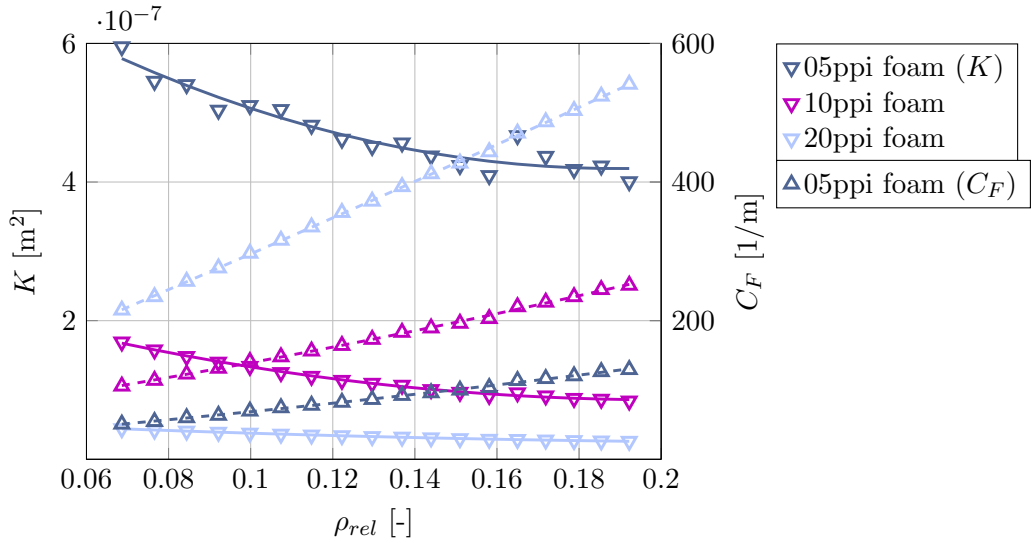

Figure 6.7: Porous medium characteristics of metal foam inserts

The relative surface areas of the unit-cells were determined numerically by integrating over the solid ligament surface boundaries and dividing the obtained values by one-eighth the cubed cell size. The functions exhibit a monotone increase with relative density with values ranging from $a_s \approx 300 - 520\text{m}^{-1}$ for the 5PPI-unit cell to $a_s \approx 1230 - 2100\text{m}^{-1}$ for the 20-PPI case. It can be seen that the relative surface area increases with decreasing pore size and that its absolute change with relative density becomes greater at smaller cell sizes.

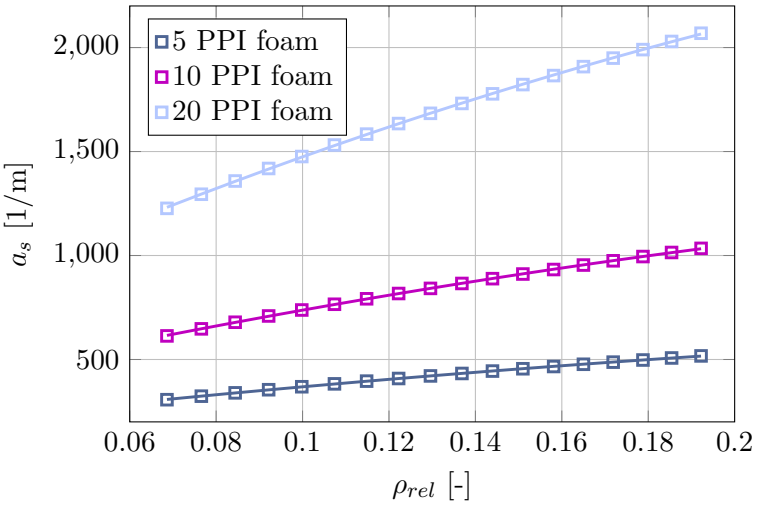

Figure 6.8: Numerical results for specific surface area of metal foam unit-cells

6.2 Two dimensional model of flow through banks of tubes

A different approach was taken to analyse the flow through the brush-type inserts: Their three dimensional structure can be seen as an agglomerate of linearly extruded circular faces, whose spacing is minimal at the centre of the brush and increases monotonely with distance to the central rod. Consequently it can be assumed that the flow around the brush ligaments at a given radius can be approximated by analysing the two-dimensional flow through an array of circular obstructions as shown schematically in figure 6.9.

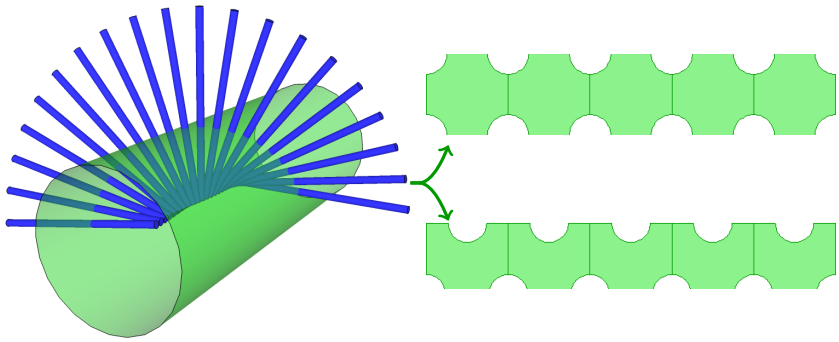

Figure 6.9: Simplified 2D model for brush flow analysis

6.2.1 Model setup

The flow past an array of uniformly spaced cylinders was modelled in COMSOL for a staggered and an inline arrangement. The respective modelling domains consisted of 25 unit-cells that are shown schematically in figure 6.10. The flow enters the cells

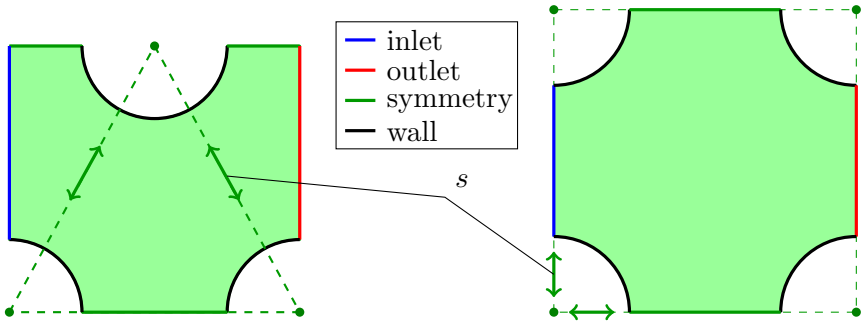

Figure 6.10: Brush modelling unit cell

shown in the figure through the left blue denoted inlet boundary and exits the cell

through the outlet boundary denoted in red. Similar to the metal foam model, a constant velocity was defined at the inlet and pressure and viscous stresses were set to zero at the outlet boundary of the cell agglomerate. No-slip wall conditions were applied at the cylinder surfaces while symmetry boundaries were defined for the residual confining boundaries, thus emulating an infinitely wide array of cylinders.

The diameter of the cylinders making up the cell was set to the manufacturer's specification of the respective brush insert. For a given radius the cylinder spacing s is directly related to the relative density. For the case of the inline (in) arrangement this is simply

$$\rho_{rel} = \frac{A_s}{A_{tot}} = \frac{\pi \cdot r_{lig}^2}{s_{in}^2} \Leftrightarrow s_{in} = \sqrt{\frac{\pi}{\rho_{rel}}} \cdot r_{lig} \tag{6.3}$$

In the case of a staggered alignment (st), the cell height is equal to the height of an equilateral triangle of side length s_{st}, which is equal to $s_{st} \cdot \sqrt{3/4}$. The relative density for the staggered alignment case is therefore:

$$\rho_{rel} = \frac{A_s}{A_{tot}} = \frac{\pi \cdot r_{lig}^2}{s_{st}^2 \cdot \sqrt{3/4}} \Leftrightarrow s_{st} = \sqrt{\frac{2\pi}{\sqrt{3} \cdot \rho_{rel}}} \cdot r_{lig} \tag{6.4}$$

Equations 6.3 and 6.4 also lead to a cell-specific maximal relative density that is reached when the cylinder spacing is equal to the cylinder diameter $s = d_{lig}$. At this point the solid objects touch and the flow channel is completely blocked. The corresponding values are

$$\min(s) = 2 \cdot r_{lig} \Rightarrow \max(\rho_{rel,in}) = \frac{\pi \cdot r_{lig}^2}{(2 \cdot r_{lig})^2} = \frac{\pi}{4} \approx 0.78 \tag{6.5}$$

$$\Rightarrow \max(\rho_{rel,st}) = \frac{\pi \cdot r_{lig}^2}{(2 \cdot r_{lig})^2 \cdot \sqrt{3/4}} = \frac{\pi}{2\sqrt{3}} \approx 0.91 \tag{6.6}$$

The two dimensional structure was created using COMSOL's internal geometry builder. The relative density was varied between 0.01-0.8 in the case of a staggered and 0.01-0.7 for the inline alignment case. The automated physics controlled meshing process resulted in an unstructured triangular grid of approximately 175,000-240,000 elements with a two-layered boundary mesh along the solid wall edges. Figure 6.11 depicts the mesh grid for the unit cells for the cases of minimal and maximal relative densities modelled.

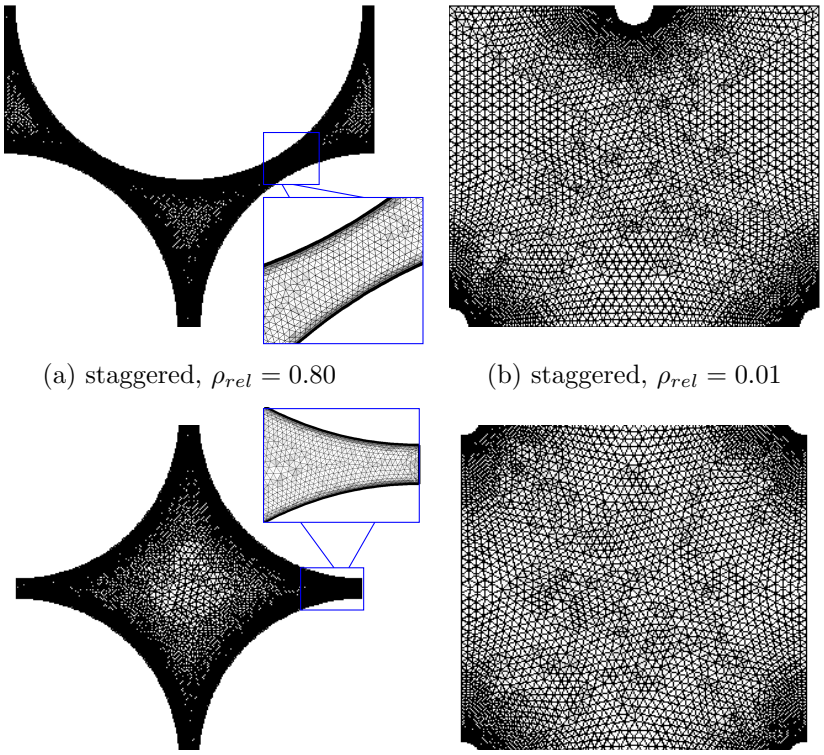

(a) staggered, $\rho_{rel} = 0.80$ (b) staggered, $\rho_{rel} = 0.01$

(c) inline, $\rho_{rel} = 0.70$ (d) inline, $\rho_{rel} = 0.01$

Figure 6.11: 2D brush unit-cell mesh grids

6.2.2 Modelling results

Similar to the analysis of the metal foam flow model, the point at which the flow could be considered developed was identified by comparing the surface averaged unit-cell velocities and the corresponding pressure drops. Figure 6.12 shows typical curve progressions for the example of a relative density of $\rho_{rel} = 0.15$ and the highest modelled nominal inlet velocity of $u_{in} = 4\text{m/s}$. Due to the reduced complexity of the two-dimensional mesh utilised here in comparison the metal foam modelling domain, it was possible to calculate the flow fields fro a broader range of boundary conditions. The curve progressions shown are typical for the majority of cases modelled where the flow could be considered developed after six cells. The entry region becomes longer only at cases of extremely high porosities.

Unit-cell flow

The representative flow fields of unit-cells at three different relative densities are shown in figures 6.13 and 6.14 for the two alignment cases at three different inlet

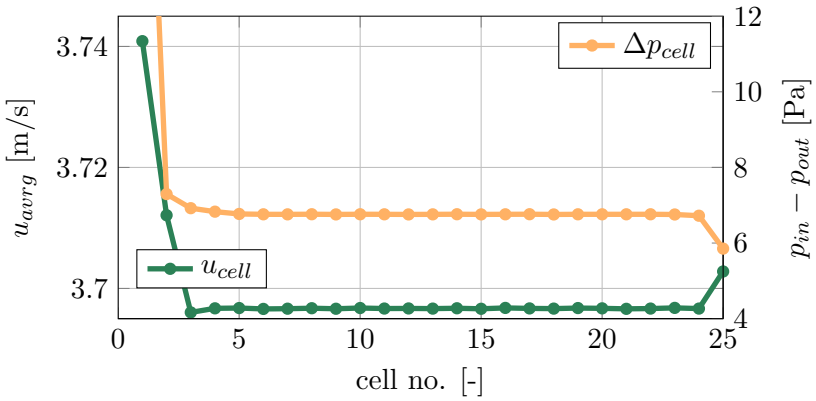

Figure 6.12: Typical average cell velocity and pressure drop distribution

velocities.

The flow field development at a staggered cylinder alignment can be understood best by examining the intermediate relative density case $\rho_{rel} = 0.15$ depicted in subfigures (d)-(f). Here, it can be seen that an inlet velocity of $u_{in} = 0.1$ m/s results in a creeping flow past the array of cylinders with no noticeable flow separations. The form drag that increases with flow rate eventually causes the flow to separate downstream of the cylinders resulting in a small swirl-flow region at $u_{in} = 1$ m/s visible in subfigure (e). The diameter of this vortex increases as the flow separation point moves further up the cylinder boundary with increasing air speed. Its growth in the traverse flow direction is inhibited by the core channel flow, whose velocity increases with the spread of the swirl flow region. As a result of this dampening, the vortex develops into an oval shape that grows in the longitudinal flow direction until it eventually reaches the next cylinder wall. This situation can be observed in subfigure (f), that depicts the flow field at an inlet velocity of $u_{in} = 4$ m/s. Vortex regions have developed on the top and bottom of the cells that take up most of the areas between two consecutive cylinders. This results in much flatter stream lines corresponding to a high velocity flow through the core of the cells.

The high and low relative density cases presented in subfigures (a)-(c) and (g)-(i) can be seen as extreme permutations of the discussed base case. As such, the cylinder spacing in the high relative density case is so small, that low-pressure vortices are present even in the low velocity case (a). Those grow in size with increasing flow rate and the air speed through the small gaps between the cylinders is augmented dramatically to up to 36 m/s at $u_{in} = 4$ m/s depicted in subfigure (c). A general increase in waviness of the flow path with relative density can be

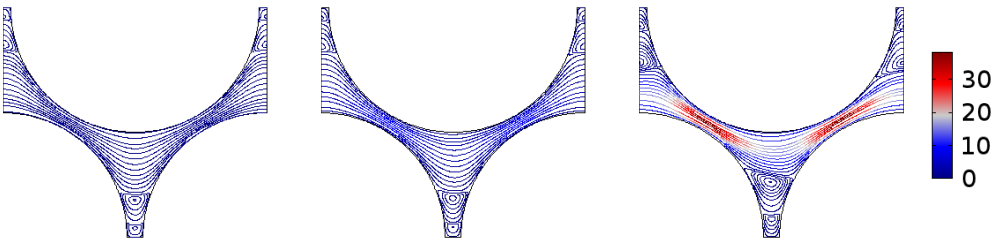

(a) $\rho_{rel} = 0.2$, $u_{in} = 0.1$ m/s (b) $\rho_{rel} = 0.2$, $u_{in} = 1$ m/s (c) $\rho_{rel} = 0.2$, $u_{in} = 4$ m/s

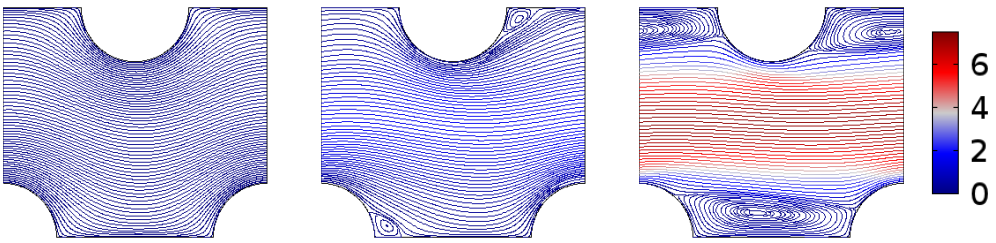

(d) $\rho_{rel} = 0.15$, $u_{in} = 0.1$ m/s (e) $\rho_{rel} = 0.15$, $u_{in} = 1$ m/s (f) $\rho_{rel} = 0.15$, $u_{in} = 4$ m/s

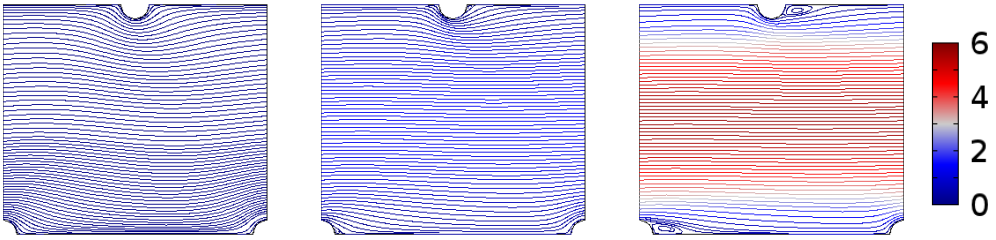

(g) $\rho_{rel} = 0.01$, $u_{in} = 0.1$ m/s (h) $\rho_{rel} = 0.01$, $u_{in} = 1$ m/s (i) $\rho_{rel} = 0.01$, $u_{in} = 4$ m/s

Figure 6.13: Staggered unit-cell flow fields

observed due to the staggered arrangement of the cylinders. In case of a highly porous structure, the cylinder spacing is so big that the vortex formed downstream of one cylinder does not impact the flow field around the consecutive one even at the high flow rate case (i). This shows that for this case, the flow field through the structure can indeed be described by single-cylinder correlations as was postulated by Lund and Knowles [2001] for the flow through a fibre flock.

Figure 6.14 depicts the flow through a cylinder array with an inline-arrangement. The flow fields exhibit the same characteristics as discussed for the case of a staggered alignment with swirl flow regions forming downstream of the cylinders that grow in size with increasing flow rate and take up the entire region between consecutive cylinders at higher flow rates for the majority of relative densities. The dead-flow zones at very high packing densities are also clearly visible in subfigures

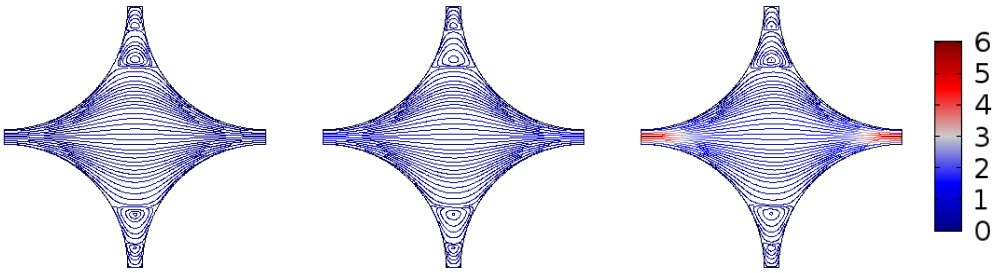

(a) $\rho_{rel} = 0.3$, $u_{in} = 0.1$ m/s (b) $\rho_{rel} = 0.3$, $u_{in} = 1$ m/s (c) $\rho_{rel} = 0.3$, $u_{in} = 4$ m/s

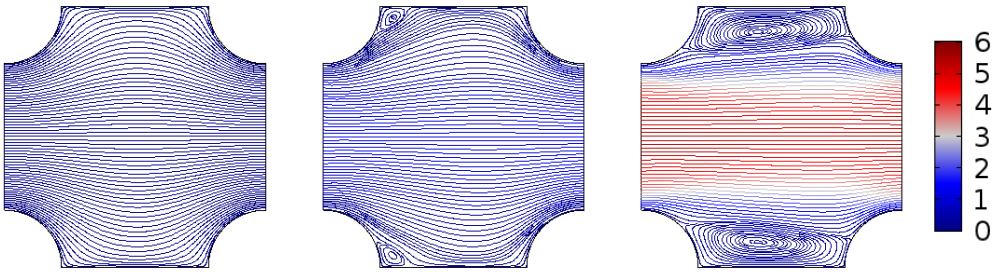

(d) $\rho_{rel} = 0.15$, $u_{in} = 0.1$ m/s (e) $\rho_{rel} = 0.15$, $u_{in} = 1$ m/s (f) $\rho_{rel} = 0.15$, $u_{in} = 4$ m/s

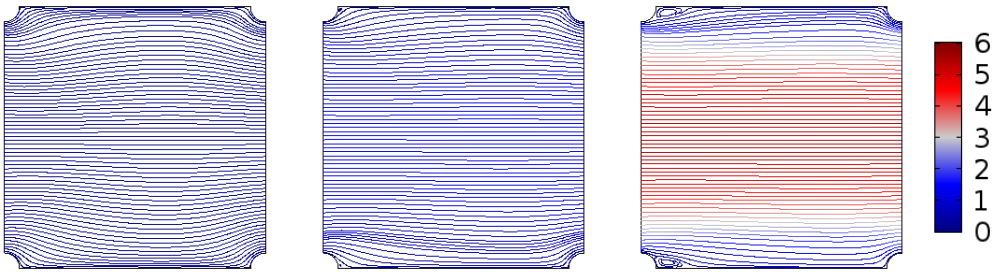

(g) $\rho_{rel} = 0.01$, $u_{in} = 0.1$ m/s (h) $\rho_{rel} = 0.01$, $u_{in} = 1$ m/s (i) $\rho_{rel} = 0.01$, $u_{in} = 4$ m/s

Figure 6.14: Inline unit-cell flow fields

(a)-(c) for the inline-arrangement. It is apparent that the effect of the cylinder alignment on the stream lines becomes stronger at higher packing densities. As a consequence the characteristic flow channel depicted in subfigures (a)-(c) in figure 6.14 is very different to that depicted for the staggered alignment case in figure 6.13.

Porous medium fit

The CFD modelling results were compared to a Forchheimer flow model in a similar manner as described in section 6.1.2. The porous medium flow characteristics were derived using equations 6.1 and 6.2 and are plotted in figure 6.15. It can be seen

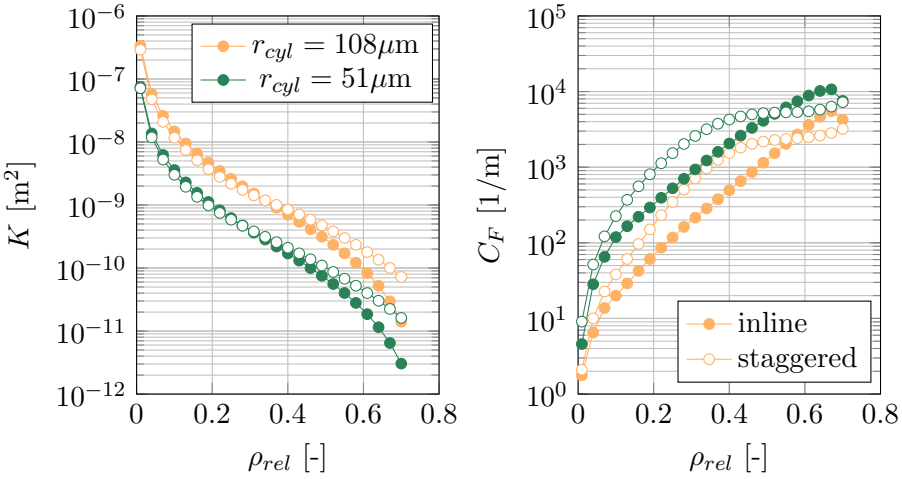

Figure 6.15: Porous medium characteristics for banks of cylinders

that for low relative density values below $\rho_{rel} < 0.3$, the specific alignment has little impact on the permeability function and only for values greater than that the curves start to differ, the staggered alignment leading to higher permeability values. The drag factor functions start off at the same level at $\rho_{rel} = 0.01$. The staggered alignment then leads to a steeper slope than the inline-arrangement but then reaches a plateau at $0.4 < \rho_{rel} < 0.6$, before starting to increase again for $\rho_{rel} > 0.6$. The curve corresponding to the in-line arrangement reaches the level of that corresponding to the staggered-alignment at a higher relative density of $\rho_{rel} = 0.6$. The fact that both functions are at the same level in the minimal relative density range is a result of the large corresponding cylinder spacing. As was discussed in context with figures 6.13 and 6.14 this yields the flow around one cylinder independent of the disturbance of the neighbouring ones so that permeability and drag factor function become independent of the shape of the alignment. A similar observation can be made for the case of an extremely high packing density at $\rho_{rel} > 0.6$, where the form drag factor C_F appears to be influenced little by the alignment as well. This leads to the conclusion that the high relative surface areas and consecutive restrictions of the flow channels corresponding to the small cylinder spacings in this range of relative densities have a bigger impact on the pressure drop behaviour than the actual shape of the flow channel.

6.3 Modelling of flow through porous-medium-filled tubes

The CFD models yielded relative density dependent functions of the permeability and drag factor for the unconfined investigated idealised structures. In order to model the flow through the actual test tubes, the CFD derived flow characteristics were utilised in a Forchheimer-extended Brinkman model that is capable of capturing the effect of the solid tube wall. In the following the flow models for a metal foam filled tube and a tube with a brush-type insert are presented. A comparison to the experimental pressure drop data presented in chapter 5 allows for a calibration of the porous medium characteristics to yield best fitting numerical models of the test object specific flow fields that also served as a basis for the numerical heat and mass transfer analysis discussed in chapters 8 and 10.

6.3.1 Metal foam tube flow model

Due to the isotropic nature of the metal foam inserts, the geometrical and flow characteristics of the unit-cells, i.e. relative density and surface area, permeability and drag factor, are spatially independent and representative for the entire structure. The flow through the metal foam tubes could therefore be described by a two-dimensional axis-symmetric model of a fluid saturated porous medium utilising the Forchheimer-extended Brinkman-flow equation 2.62, while the flow in the foam-free domains is governed by the Navier-Stokes equations 2.43-2.45. Apart from the tube dimensions, the only global modelling parameters are the relative density of the porous structure and underlying pore size, which allowed for the determination of the permeability and drag factor according to figure 6.7.

Model setup

The two dimensional axis-symmetric modelling domain was setup using COMSOL's internal geometry builder and is depicted in figure 6.16. The program automatically

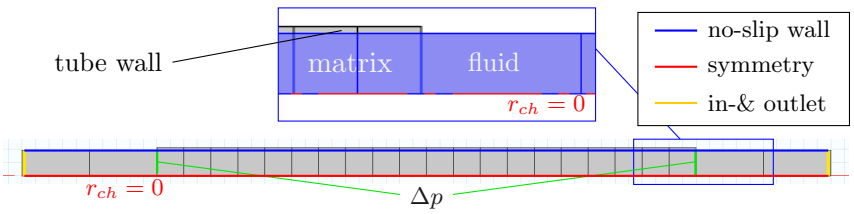

Figure 6.16: Aluminium foam porous medium flow modelling domain

assigns the symmetry boundaries depicted in red in the figure on edges located

at $r_{ch} = 0$. The model uses air as an incompressible working fluid that enters the modelling domain through the inlet boundary on the right hand side of the schematic. From there it travels through 50mm long in- and outlet channels before entering and after exiting the test tube. A range of constant velocities were set as boundary conditions at the channel inlet, while the pressure viscous stresses were set to zero at the channel outlet. The in- and outlet boundaries are depicted in yellow in the picture. The test tube section is visualised in figure 6.16 with the onset of the confining tube walls that is magnified for better visibility. It is common practice to position the in- and outlet boundaries some distance away from the porous matrix in order to omit a falsification of numerical results due to conflicting boundary conditions. No-slip wall conditions are applied for the blue coloured edges located at $r = r_{ch}$. Numerous internal boundaries were defined, that facilitated the extraction of cross-sectional average values for the result post-processing. This way, the in- and outlet channels were respectively divided into two and the test section into 20 sections. The interior boundaries, that were used to calculate the pressure drop over the test section, are highlighted in green in the schematic. It should be noted, that the model setup was chosen in order to resemble the geometry of the heat and mass transfer test rigs, that will be presented in later chapters. For the flow model itself an explicit definition of the confining channel wall domains is unnecessary, because the flow equations are only defined on the fluid domains that are partly visualised in blue in the magnified picture in figure 6.16. The flow in- and outlet channels are further additions to the flow problem that were not part of the experimental pressure drop rig. They were, however, found to have a negligible impact on the calculated pressure drop over the test section.

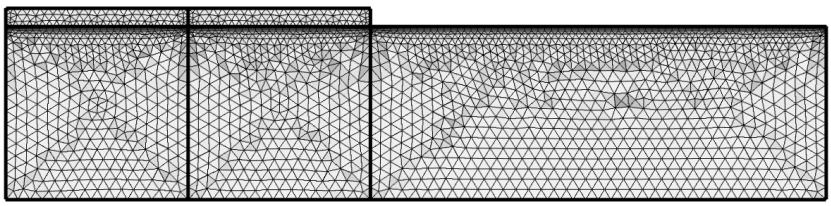

Figure 6.17: Mesh section of aluminium foam porous medium flow model

COMSOL's automatic meshing algorithm was used to create a physics-induced unstructured triangular mesh discretising the fluid and solid domains that was linked to a triple-layered quadrilateral boundary mesh at the edges corresponding to the inner surface of the confining tube. The overall mesh consisted of 25,004 elements. A section including the second half of the inlet channel and the first two sections of

the test section is visualised in figure 6.17.

Modelling results

The typical cross-sectional flow profile corresponding to the metal foam is depicted in figure 6.18 in a nominalised manner and compared to that of an empty channel at the same flow rate. From the profiles, it can be seen that the flow obstruction of the isotropic metal foam matrix causes a dampening of the unrestrained flow at the channel core. The resulting velocity profile is uniform for the majority of the channel cross-section and exhibits a strong gradient in the near wall boundary layer that is significantly thinner than in the case of the empty tube.

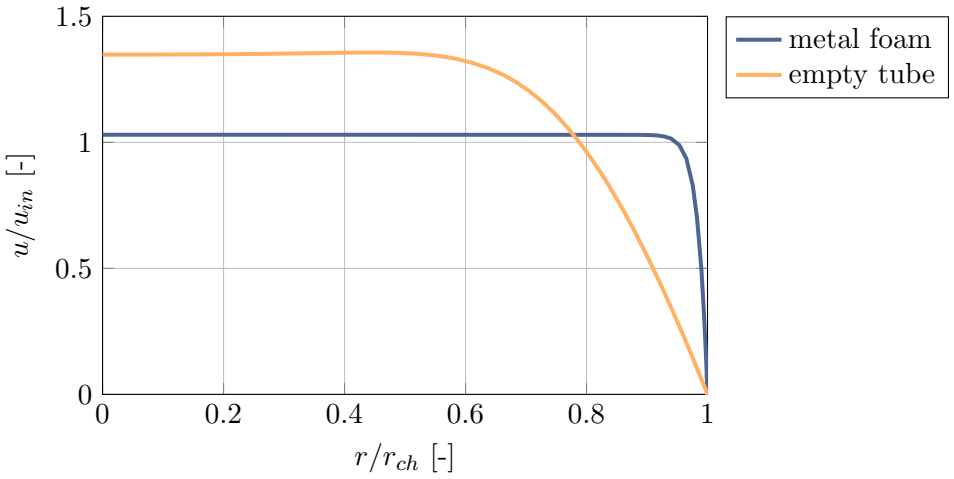

Figure 6.18: Comparison of foam related cross-sectional velocity profiles

The flow model could be calibrated to give the best fit to experimental data by varying the relative density of the structure. Figure 6.19 shows the resulting pressure drop curves for the three inserts in comparison to the experimental data from chapter 5 as functions of flow rate and the required calibration offsets. As can be seen from the first three subplots, the porous medium flow model yields a decent agreement with experimental data when calibrated. The difference between the relative density of the idealised 3D structure best fitting the experimental trends and the experimentally determined relative density $\Delta\rho_{rel} = (\rho_{rel,\mathrm{CFD}} - \rho_{rel,\mathrm{exp}})$ is shown in the fourth subplot at the lower right of figure 6.19. It is apparent that these calibration offsets differ noticeably between inserts. The best agreement with the experimentally determined relative density values was achieved by the 10PPI flow model, denoted in purple in the plot. In order to yield the best fit to experimental pressure drop data, the relative density used in the flow model had to

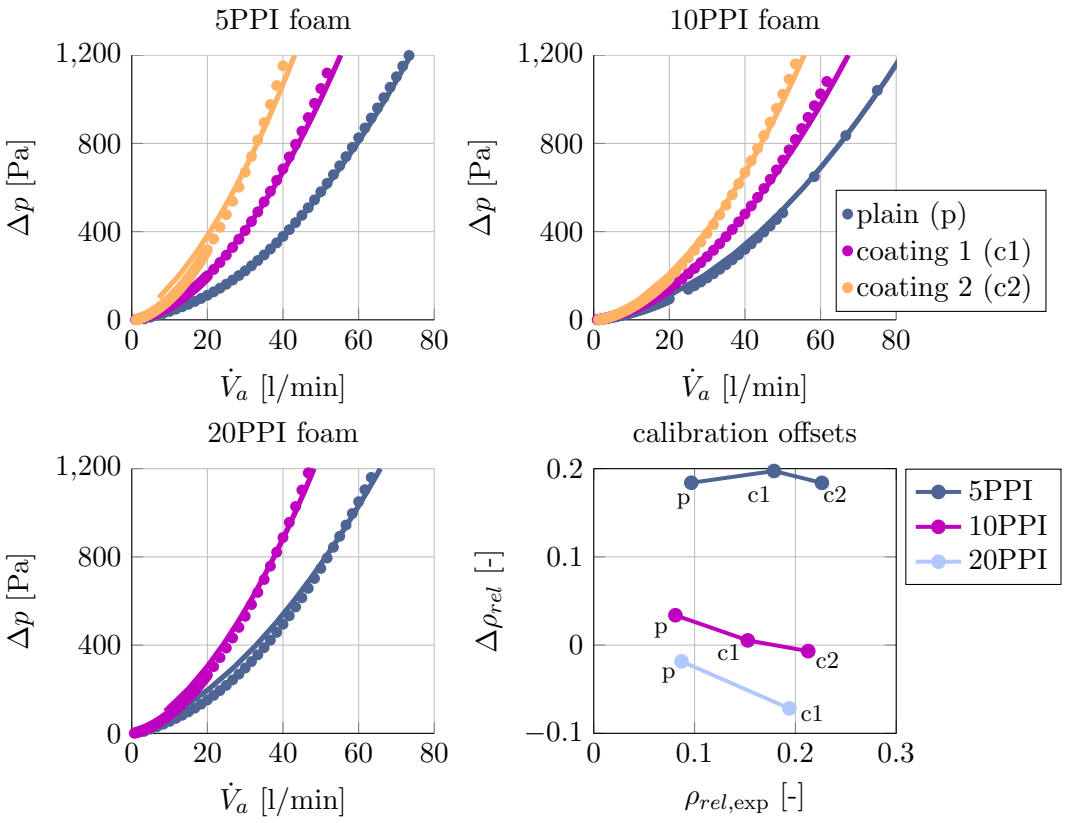

Figure 6.19: Comparison of calibrated foam tube flow model with experimental data

be set $\Delta\rho_{rel} \approx 0.03$ higher than the experimentally determined value for the plain (p) case and less for the coated cases (c1& c2). This can be taken as an indication that the idealised three dimensional model proposed in section 4.1.1 is an adequate representation of the real foam cells. A positive offset indicates that the pressure drop over the idealised three dimensional structure is lower than the real structure at a given relative density.

In contrast to the case of the 10PPI foam, the flow model of the 20PPI foam overestimates the pressure drop over the structure, requiring a negative offset of $\Delta\rho_{rel} \approx -0.02$ for the plain and $\Delta\rho_{rel} \approx -0.07$ for the coated case. The cell size of the idealised structure is solely a function of the pore size. As a consequence, an increase in relative density at a given pore size corresponds to a uniform increase in strut diameter, so that the inconstancy of the insert specific calibration offsets can be explained with possible inhomogeneities in the real coating layers. As such, agglomerates of desiccant material in low flow zones would lead to smaller increase in pressure drop than a perfectly uniform increase in coating thickness, which is

reflected in a decreasing calibration offset that can be observed for the majority of data points in figure 6.19.

The biggest deviation from experimentally determined relative density values is observed for case of the 5PPI-foam tube. All three data points require offsets of around $\Delta\rho_{rel} > 0.18$ to yield a decent agreement with experimental data. Given that such great offsets are needed, the adequateness of the Kelvin-foam model must be put in question for this foam insert despite the manufacturer's claims of its suitability. Noting that Weaire and Phelan [1994] have proposed a packing structure that leads to a lower surface energy than the Kelvin foam, it is likely that this more complex model is a better representation of the real foam matrix at least for the 5PPI foam.

While a more detailed analysis of the benefit of using more complex cell structures is beyond the scope of the current work, it can nonetheless be concluded that the metal foam flow models allowed for the determination of flow characteristics, which have been directly derived from idealised representations of the respective structures, and yield a decent agreement with experimental data when the correct calibration offsets are applied. According to the best fit-parameters, the porous medium characteristics of the respective inserts are summarised in table 6.1.

Table 6.1: Aluminium foam tube porous medium characteristics

Quantity			5PPI	10PPI	20PPI
plain	$K \cdot 10^8$	$[\mathrm{m}^2]$	33.08	1.20	4.61
	C_F	$[\mathrm{m}^{-1}]$	138.68	156.16	195.86
coating 1	$K \cdot 10^8$	$[\mathrm{m}^2]$	11.47	9.22	3.41
	C_F	$[\mathrm{m}^{-1}]$	167.38	203.00	356.09
coating 2	$K \cdot 10^8$	$[\mathrm{m}^2]$	3.75	7.90	–
	C_F	$[\mathrm{m}^{-1}]$	177.64	263.52	–

6.3.2 Brush-inserted tube flow model

Similar to the metal foam inserts, the regular structure of the brush-type inserts allows for an axis-symmetric formulation of the Brinkman model describing the flow through the brush-inserted test tubes. The brush insert is thus modelled as a fluid saturated porous medium with radially varying porosity, which accounts for the increase in ligament spacings with distance away from the central stem wire. Subtracting the volume of the solid stem wire from the inner tube volume, the flow through the test tubes can be represented by a spherical shell containing the porous medium as illustrated in figure 6.20.

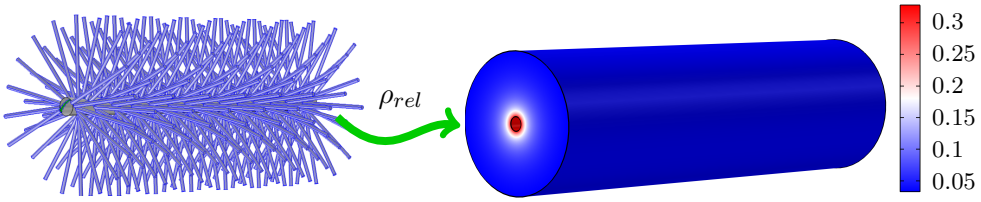

Figure 6.20: Representation of brush as continuous fluid saturated porous medium with radially varying relative density

The relative density values reported in table 4.2 correspond to the volume averaged ratio of solid ligament volume to channel volume. The volume of the solid ligaments V_s in the air channel was derived in equation 4.34. For the idealised brush, length of the ligaments is equal to the channel diameter and the relation can be rewritten as:

$$V_s = N_{lig} \cdot \pi \cdot r_{lig}^2 \cdot (l_{lig} - 2 \cdot r_{stem}) = N_{lig} \cdot \pi \cdot r_{lig}^2 \cdot 2 \cdot (r_{ch} - r_{stem}) \tag{6.7}$$

The volume of the cylindrical channel is given by:

$$V_{ch} = \int_0^{2\pi} \int_{r_{stem}}^{r_{ch}} \int_0^{l_{ch}} r \; d\phi dr dz \tag{6.8}$$

The expression for the local $\rho_{rel} = f(r_{ch})$ and overall relative density $\overline{\rho}_{rel}$ can be derived from relating equations 6.7 and 6.8 according to the relative density definition (eq. 2.56):

$$\begin{aligned} V_s =& V_{ch} \cdot \rho_{rel} \\ \Leftrightarrow N_{lig} \cdot \pi \cdot r_{lig}^2 \cdot 2 \cdot (r_{ch} - r_{stem}) =& \int_0^{2\pi} \int_{r_{stem}}^{r_{ch}} \int_0^{l_{ch}} r \cdot \rho_{rel} \; d\phi dr dz \end{aligned} \tag{6.9}$$

In case of the overall space-independent relative density, the expression on the right-hand side of 6.9 can be rewritten as:

$$\begin{aligned} V_s =& \overline{\rho}_{rel} \cdot \int_0^{2\pi} \int_{r_{stem}}^{r_{ch}} \int_0^{l_{ch}} r \; d\phi dr dz = \overline{\rho}_{rel} \cdot \pi \cdot (r_{ch}^2 - r_{stem}^2) \cdot l_{ch} \\ \Rightarrow \overline{\rho}_{rel} =& \frac{N_{lig} \cdot \pi \cdot r_{lig}^2 \cdot 2 \cdot (r_{ch} - r_{stem})}{\pi \cdot (r_{ch}^2 - r_{stem}^2) \cdot l_{ch}} = \frac{2 \cdot N_{lig} \cdot r_{lig}^2}{l_{ch}} \cdot \frac{(r_{ch} - r_{stem})}{(r_{ch}^2 - r_{stem}^2)} \end{aligned} \tag{6.10}$$

It is worth mentioning that equation 6.10 is a relation of the same quantities used in equation 4.35 for the real brush insert. The two expressions become identical for a brush with an idealised geometry where $l_{br} = l_{ch}$ and $l_{lig} = d_{ch}$.

The local relative density expression is dependent on the radial position in the channel and can therefore not be factored out of the volume interval.

$$\begin{aligned} N_{lig} \cdot \pi \cdot r_{lig}^2 \cdot 2 \cdot (r_{ch} - r_{stem}) =& 2\pi \cdot l_{ch} \cdot \int_{r_{stem}}^{r_{ch}} r \cdot \rho_{rel}\, dr \\ \Leftrightarrow \frac{2\pi \cdot N_{lig} \cdot r_{lig}^2 \cdot (r_{ch} - r_{stem})}{2\pi \cdot l_{ch}} =& \int_{r_{stem}}^{r_{ch}} r \cdot \rho_{rel}\, dr \end{aligned} \tag{6.11}$$

Solving for $\rho_{rel}(r)$ yields:

$$\Rightarrow \rho_{rel}(r) = \frac{2\pi \cdot N_{lig} \cdot r_{lig}^2}{2\pi \cdot l_{ch} \cdot r} = \frac{N_{lig}}{l_{ch}} \cdot \frac{r_{lig}^2}{r} = \overline{\rho}_{rel} \cdot \frac{(r_{ch}^2 - r_{stem}^2)}{(r_{ch} - r_{stem}) \cdot 2r} \tag{6.12}$$

Figure 6.21 depicts the overall and local relative density for the aluminium brush insert as functions of the normalised radial channel position. It can be seen that

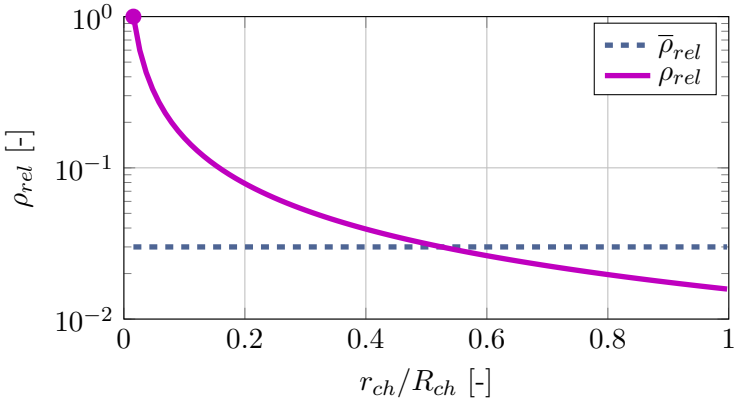

Figure 6.21: Local porosity distribution of the aluminium brush insert

the relative density is equal to unity near the channel core and then continuously decreases in value until

$$\lim_{r_{ch} \to \infty} (\rho_{rel}) = 0$$

Model setup

The relative density function 6.12 was inserted into the Forchheimer-extended Brinkman flow equation 2.62 and the overall relative density was set to the experimentally determined values. Figure 6.22 shows the modelling domain that was created using COMSOL's geometry composition tool.

The modelling domain is very similar to that of the metal foam model, with the exception that the volume of the stem wire is subtracted from the fluid domain

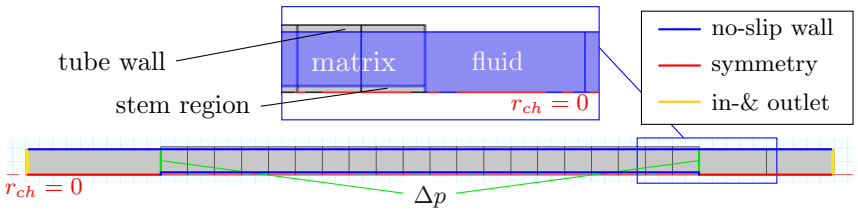

Figure 6.22: Brush porous medium flow modelling domain

and its solid surface is treated as a no-slip wall. All other boundary conditions resemble those of the metal foam model discussed in the previous section and are therefore not mentioned explicitly here anymore.

Similar to the metal foam model, COMSOL's automatic meshing algorithm was used to construct a triangular mesh linked to a triple-layered quadrilateral boundary layer mesh at the edges corresponding to the inner tube wall and stem surfaces. Because of the additional edges that required the boundary layer refinement, the resulting mesh, shown in figure 6.23, was more complex than that of the metal foam model and consisted of 30,351 elements.

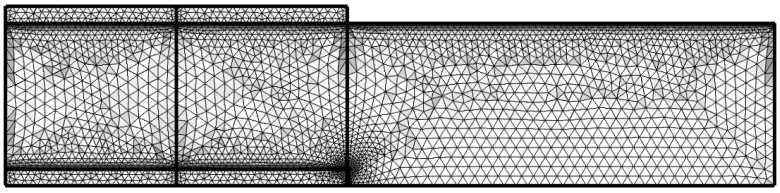

Figure 6.23: Aluminium foam porous medium flow modelling mesh

Modelling results

The radially varying characteristics of the porous medium representing the brush type inserts create a distinct flow field that is depicted in figure 6.24 and compared to the velocity profile of a flow through an empty cylindrical shell and one with an isotropic porous medium insert. It can be seen that an empty channel ($\epsilon = 1$) results in a bell shaped curve as denoted by the yellow curve in the figure. The air velocity is zero at the points of contact with the solid surfaces, i.e. $r_{ch} = r_{stem}$ and $r_{ch} = r_{ch}$. If the channel is filled with an isotropic ($\epsilon = 1 - \overline{\rho}_{rel}$) porous medium as represented by the blue line, a similar dampening of the velocity profile can be observed as already discussed for the metal foam case in figure 6.18. The radial porosity variation according to equation 6.12 causes an augmentation of the velocity dampening effect at the regions of higher relative density that causes the bulk of the

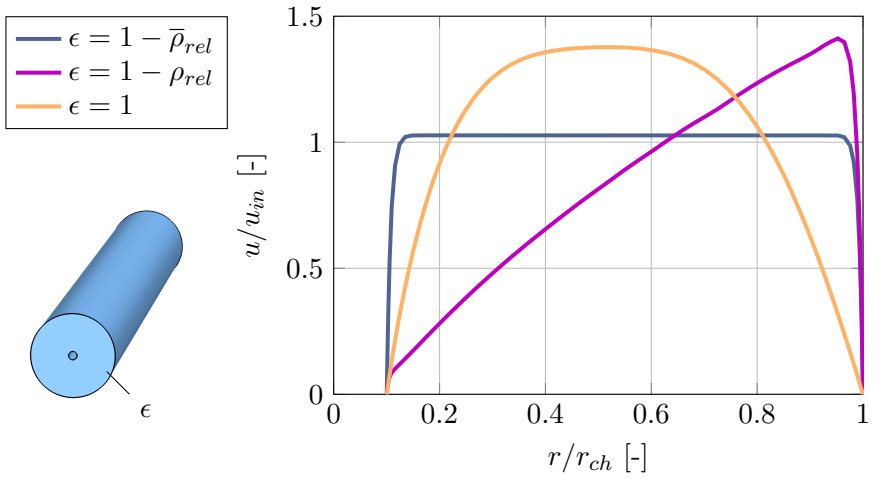

Figure 6.24: Comparison of brush related cross-sectional velocity profiles

gas to flow through the channel section where the packing is sparsest. The resulting velocity profile reaches its maximum in close proximity to the the channel walls.

The flow models were performed for the two copper and the aluminium brush tube inserts. Figure 6.25 shows the comparison of the copper brush modelling results to the experimental results in the left graph. The dark green coloured curves correspond to the low-density (LD) copper brush insert, while the medium density (MD) brush is depicted in light green. By comparing the experimental data, shown as discrete points in the graph, to the dashed lines, it can be seen that the uncorrected model leads to a dramatic under-prediction of flow impedance. If the underlying overall relative density in the respective models is doubled, the modelling results, shown by the dashed lines, are closer to experimental data. While the agreement of the medium density brush pressure drop curves is in this case better than the low density brush, both lines fail to reproduce the characteristic shapes of the experimental pressure drop curves in an acceptable manner. It was therefore considered more appropriate to apply fitting factors to the permeability (f_K) and form drag coefficient (f_{cF}) functions and leave the underlying relative density at its experimentally determined level. The fitting factors were varied manually to yield the best agreement with experimental data. The resulting curves are shown as solid lines in figure 6.25. It can be seen that the porous medium flow modelling results are in decent agreement with experimental data for both the low and medium relative density cases when calibration factors of $f_K = 0.7$ and $f_{cF} = 5.5$ are applied to the local permeability and drag coefficient functions. The resulting best fitting curves of the local porous medium characteristics are plotted as solid lines in the

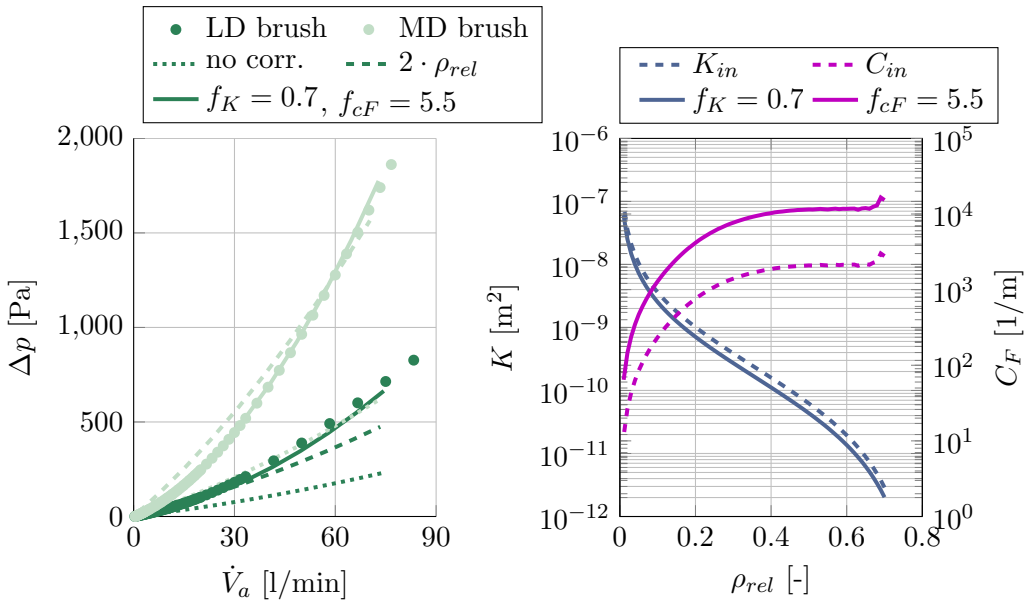

Figure 6.25: Comparison of copper brush flow model with experimental data

second graph of the figure, where they are compared to the respective uncorrected functions, that are shown as dashed lines.

The curves presented in the figure above correspond to the underlying unit-cell model with an inline cylinder arrangement discussed in section 6.2. While the comparison to experimental data was performed for both the staggered and inline arrangement cases, it was found that the inline cylinder arrangement led to smaller values in fitting factors, indicating that this was the more appropriate model.

The comparison of the calibrated porous medium flow model to the experimental pressure drop data of the uncoated and coated low-density aluminium brush insert is depicted in figure 6.26. From the first graph on the left it can be seen that the porous medium model exhibits a decent agreement with experimental pressure drop data, if the fitting factors $f_K = 0.7$ and $f_{cF} = 8.0$ are applied to the local porous medium characteristics, that are shown as functions of local relative density in the second graph on the right. It is likely that the application of a thick desiccant coating layer does not lead to a linear extrapolation of flow characteristics, e.g. due to non-uniform layer thickness, bridging between ligaments in the core region, and/or changes in ligament cross-sectional shapes. As a consequence the quality of fit is reduced in the case of the coated brush, if the calibration factors are not adapted accordingly.

It can be deduced from the discussion above about the comparison of numerical and experimental data, that the underlying unit-cell model presented in section

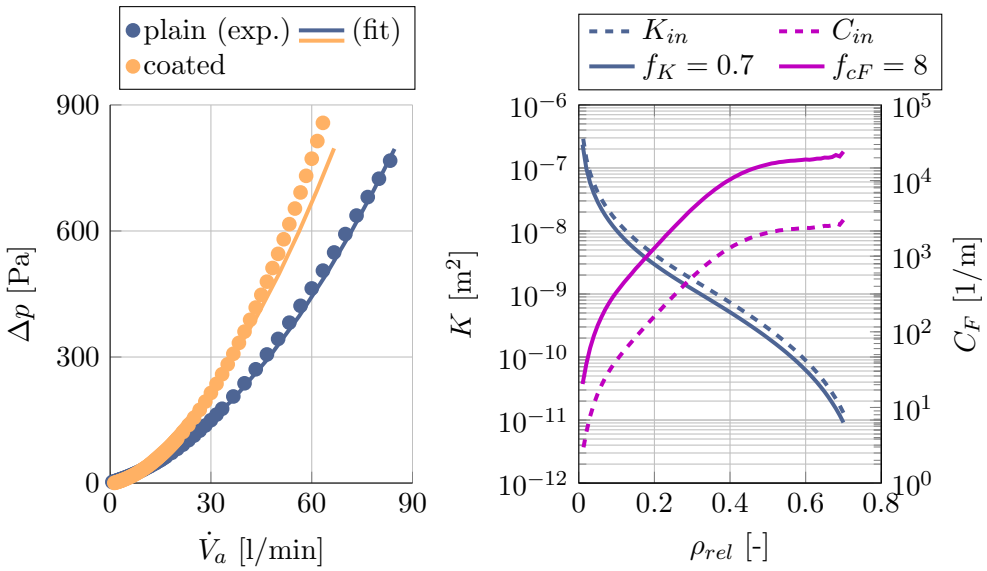

Figure 6.26: Comparison of aluminium brush flow model with experimental data

6.2 leads to flow characteristics that are related but not truly representative of the overall structure. This is highlighted by the fact that a mere adjustment of the overall relative density is not enough to achieve an acceptable fit to experimental data, but an adjustment of the relative density dependent porous medium characteristics themselves is necessary. A number of aspects can be identified that are likely to be part of the cause for the discrepancies:

- The two-dimensional model is incapable of capturing any flow effects that occur in the radial direction of the actual channel. This can be expected to be significant especially at high flow rates, where small ligament spacings are likely to create three-dimensional swirl flow regions.
- The fibres in the 2D models are spaced uniformly in the longitudinal and traverse direction. In an actual brush the longitudinal spacing is equal to the twisting pitch of the brush and is much larger than the traverse spacing of two touching fibres.
- The fibres of the actual brush are crimped which is likely to have an augmenting effect on the form-drag.

In conclusion, the porous medium flow model is capable of describing the pressure drop over a given tube insert accurately when calibrated against experimental data. The fact that the same calibration factors yielded decent agreement with experimental data for both the low and medium density copper brush inserts

may be taken as an indication that an extrapolation to other relative densities is possible. However, an adapted model of the underlying unit-cell flow that links the porous medium characteristics more closely to the that of the real three dimensional structure would be a useful refinement of the numerical analysis of the problem.

Chapter 7

Experimental investigation of steady-state heat transfer performance of test objects

The heat transfer performance of the inserts is of fundamental importance for their applicability to achieving isothermal dehumidification as their ability to remove heat from the channel and tendency to store heat are mainly dependent on their respective effective thermal diffusivities. Furthermore, knowledge of the convective transfer characteristics such as the convective transfer coefficient give useful implications concerning the inserts' mass transfer characteristics, as has already been illustrated in chapter 2.1.4.

The current chapter focuses on the design and conduct of experiments to compare the steady-state heat transfer performance of the several inserts that have been chosen for closer examination. The determination of overall convective heat transfer coefficient has a central role in this context as it not only serves as a meaningful basis for comparison of the individual inserts, but also serves as a further benchmark for the friction factors derived experimentally and by means of numerical calculations described in the previous chapters 5 and 6.

7.1 Design of the experimental test rig

An experimental test rig was commissioned to investigate the heat transfer performance of potential inserts for the application at hand. It was realised in the form of a double-pipe counter-flow heat exchanger, where hot air was sent through the test pieces which were externally cooled with water at ambient temperature. As men-

tioned earlier, the length of the test tubes of the prototype is $l_t = 200$mm. While this corresponds to the typical thickness of a desiccant wheel of intermediate size, it is a rather short length for a heat exchanger when air is used as a working fluid, especially considering the comparatively large channel diameter. Heat transfer tests on such small length scales are challenging for several reasons:

1. The comparatively low thermal mass of air leads to small overall heat transfer rates in the regime of flow rates under investigation. As a result even small absolute errors might constitute large relative errors compromising the significance of the measurements.

2. The poor thermal conductivity of air leads to the formation of a pronounced temperature distribution at the tube outlet when the mixing inside the tube is poor. This can make temperature measurements difficult, that are representative for the average air outlet temperature.

3. The small total heat transfer rates furthermore result in a very small temperature difference between water in- and outlet, because of the comparatively high thermal mass of water. Consequently, accuracy and resolution of temperature sensors are critical parameters for achieving consistent heat flow measurements.

4. For the forced convection inside an empty tube, the aspect ratio d_t/l_t that relates the internal diameter of the tube to its length is an important parameter. The tubes under investigation here are short with $d_t/l_t = 0.095 \approx 0.1$. This can be problematic because for $d_t/l_t > 0.1$ the thermal and hydrodynamic entrance may not be neglected anymore and commonly used Nusselt number correlations cannot be applied [sec. G, VDI, 2010].

In order to address the above-mentioned challenges, a careful selection of sensing equipment was necessary and the amount of insulation material was increased dramatically in comparison to initial experimental designs in order to minimise ambient effects on the measurements. The following provides a detailed description of the individual components of the test rig, whose schematic is depicted in figure 7.1. The test rig consists of several elements, namely the test section itself, the system for hot air supply, the insulation of the test assembly from the environment, the system for cooling water supply, the sensing equipment and the data acquisition and monitoring system. The individual elements are described in the following and figure 7.2 shows a photograph of one test assembly inside the insulation box with focus shots of details of the some of the elements.

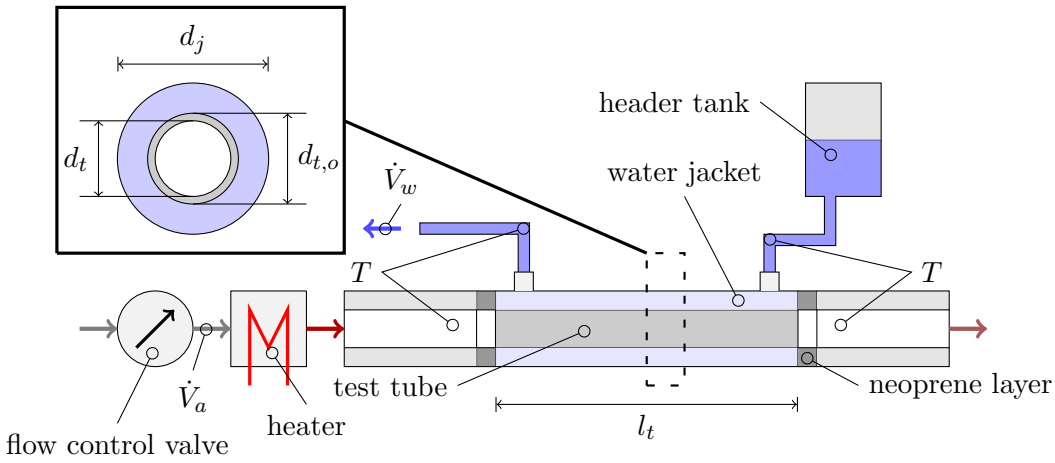

Figure 7.1: Schematic of the heat transfer test rig

7.1.1 Test section

The heat exchanger was constructed by fitting an outer PVC-tube with an inner diameter of $d_j = 28$mm around the test objects. This created a water jacket with an annulus of thickness $(d_j - d_{t,o})/2 \approx 3$mm. The test pieces were positioned concentrically inside the water jacket with the help of two O-rings and sealed water tight using high temperature tolerant silicone sealant. Three test pieces were fabricated in this manner for the respective metal foam tubes. A fourth test piece was made up with an empty heat exchanger tube made of a copper alloy that served as a reference measurement and was used to slide in the four brush type inserts. The thermal material properties of the test objects are summarised in section B together with other quantities used for the heat and mass transfer analysis following in the next chapters.

7.1.2 Hot air supply

The water jacket was joined to two polystyrene tubes that served as air in- and outlet channels. In order to have smooth transitions, the inner diameter was set to match that of the test tubes while the outer diameter was equal to that of the water jacket. The channels were hot-wire cut from a solid piece polystyrene, resulting in an approximately 3mm wide axial gap where the cutting tool entered the material. Temperature sensors were pushed through a hole in the channel walls approximately 3cm from the respective test piece in- and outlet. Silicone sealing of the holes for temperature sensors and the axial gap were used together with adhesive tape to

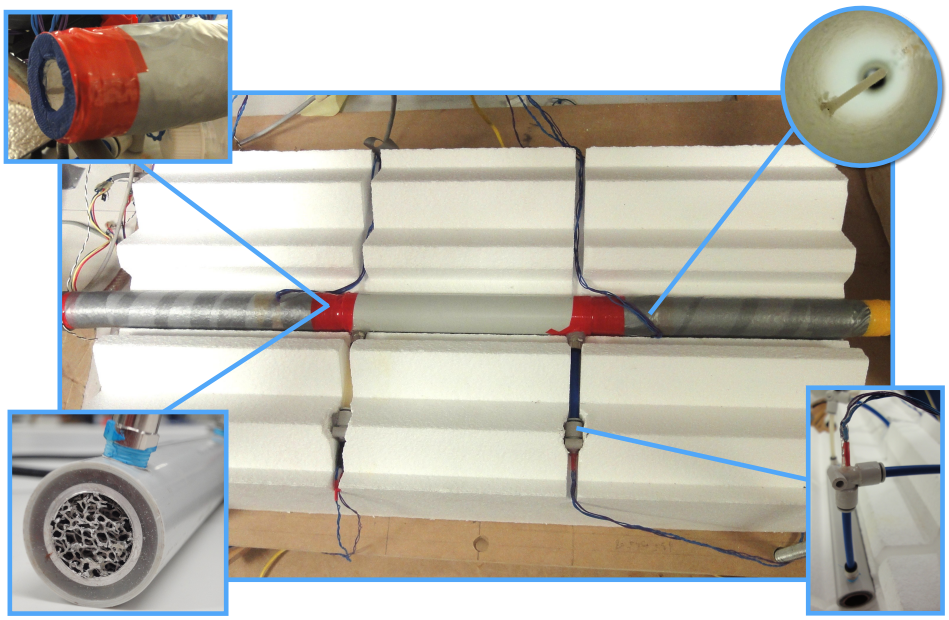

Figure 7.2: Photograph of the heat transfer test rig with foci on (clockwise) the connecting neoprene layer, the positioning of the temperature sensor inside the channel, the positioning of the water temperature sensors and the silicone sealed test section

restrain the temperature sensors from moving and ensure the air-tightness of the channels. In order to ensure a good contact between the channels and the test object, a gasket made of elastic neoprene was attached to the ends of the in- and outlet channels. The pieces were joined by compressing the neoprene material, ensuring a good fit and using adhesive tape to tighten and seal the connection. Compressed air was used as the process-side working fluid, that was supplied to the laboratory from an external compressor. The flow rate was adjusted manually with a flow control valve. The air was heated up to the desired temperature level by a heating element that was connected to the end of the inlet channel. The heating element was taken from a hand-held hot-air gun and driven by mains power. The voltage applied to the coil could be varied via a potentiometer, which allowed for the manual variation of the heat emission by the coil.

7.1.3 Insulation box

The resulting assembly was placed in an extruded rigid polystyrene box for the purpose of insulating it against the environment and connected up to the hot air supply. Polystyrene was chosen as a material, because it is routinely custom cut into various shapes for packaging and has good insulation properties, that are summarised in table B.2. The box was hot-wire cut into two pieces in order to facilitate an easy access to the test section and equipped with groves that provided snug-fitting guides for air and water channels. Figure 7.2 shows a photograph of the lower half of the insulation box with the assembly in place and focus shots of individual rig elements. During the tests, the two halves were put together and compressed between two wooden boards creating a snug fit around the assembly minimising the number of potential air gaps.

7.1.4 Water supply

In order to realise a continuous water stream at a low flow rate and line pressure, tap water was used to continuously replenish a header tank to a constant water level. This way, any effects of variations in mains water pressure on the test conditions could be avoided and the water flow was kept at a constant rate for each experiment. In order to increase the anticipated cooling water temperature difference, the header tank outlet flow rate was restricted by a partly closed ball valve. The water from the header tank was directed into the water jacket of the test section through 8mm OD flexible PVC hosing that was attached to the quick-fit connectors of the water jacket. The water from the header-tank entered the water-jacket at the air outlet end, creating a counter-current flow arrangement. The continuous water outflow was directed to the drain via flexible hosing.

7.1.5 Air and water temperature and flow rate measurements

Air flow rate measurements were performed upstream of the heater using a TSI 40246 hot-film-type mass flow meter. The measurements taken by the device are converted into a mass flow rate internally and are transmitted to the data acquisition system via RS-232 protocol in terms of a standard volume flow rate at reference conditions $T_{ref} = 21.1°\text{C}$ and $p_{ref} = 101.3\text{kPa}$. The measurement accuracy is specified as $\Delta\dot{V}_a = \max\{0.05\text{l/min}, 2\% \cdot \dot{V}_a\}$ plus additional $0.075\% \cdot \dot{V}_a$ per 1°C-temperature difference from reference conditions. By measuring the inlet air flow rate upstream of the heater the operating conditions of the mass flow meter were always known to be close to its reference conditions.

Air temperature measurements were performed in close proximity to the ends of the test tube. In general, the selection of temperature sensors is dependent on the requirements of the measurement task in terms of temperature range, accuracy, repeatability, sensitivity, response time, mechanical stability and cost effectiveness. Since the sensing equipment is not operating in a harsh environment and the roughly estimated temperature range between 20-90°C is narrow in comparison to the operating ranges of most temperature sensors, the main selection criterion was a high degree of accuracy over the measurement range. Bearing in mind that it would be beneficial to use the same sensors for the transient heat and mass transfer tests discussed below in section 9, the sensor response time and compactness was a secondary criterion and while the cost and availability made up the third aspect. The temperature sensors chosen for the measurements were plain wire-wound Pt-100Ω-elements that were 15mm long and 1.6mm in diameter. For their positioning, a small hole was drilled into the polystyrene in- and outlet channels where the elements were fed through and positioned, so that they were approximately perpendicular to the flow and the entire sensing section was exposed to the air stream. The same temperature sensors were used to measure the water in- and outlet temperatures. They could be positioned conveniently inside two L-shaped quick-fit connectors, that were used to connect the vertical water in- and outlet hoses to the horizontally placed water-jacket connectors. The positioning of the temperature sensors is depicted in figure 7.2.

The average water flow rates were measured for each experimental data point by recording the time required to fill a beaker to the 1l-mark. The tolerances of the beaker meter is specified as $\Delta V_w = 0.015$l and the uncertainty of the time recording is estimated to be $\Delta t = 0.5$s.

7.1.6 Data acquisition system and control program

The sensor signals were measured by a National Instruments CDAQ-9174 system. The DAQ system was equipped with a NI-9217 4-Channel Pt100-module that internally converted the RTD-voltage measurements into the respective temperature signals. The flow meter measurements were acquired digitally via RS-232 protocol. That way an additional error for the conversion of the measured air temperature and flow rate into a continuous voltage signal could be omitted. Data monitoring and recording was controlled using the National Instruments LabView software package. The sampling rate of 1Hz was chosen, as it allowed the RTD module to operate in high-resolution mode improving the accuracy of measurement and transient temperature effects are of minor concern in this measurement task. The time

series containing the measurement data were saved as text-files, that were imported into MATLAB for post-processing.

7.2 Test program

The main objective of the stationary heat transfer experiments was the determination of the overall heat transfer coefficient, that relates the amount of heat that is transferred by the test object to the driving temperature difference between the two fluids. The variation of this performance parameter was tested for each insert over a range of air flow rates, while the cooling water flow rate was kept at approximately the same level for all tests with the exception of one insert. The inlet air flow rate was kept constant for each experiment at a level varying between $\dot{V}_a \approx 15-50\text{l/min}$.

An intermediate temperature level was chosen for the inlet air temperature. Efforts were undertaken to keep the change in the inlet conditions during the test period minimal. However, some experiments were subject to a slow drift in inlet temperature due to a change in ambient conditions, since no temperature control loop feedback mechanism was in place for adjusting the heater power output and the temperature of the cooling water inlet was not directly controlled at all. Similarly, the manual heater setting resulted in different inlet air temperatures for different experiments. The inlet temperature level was allowed to vary between $T_{a,in} \approx 40-60°\text{C}$. The cooling water temperature was also subject to variations due to different ambient conditions for different experiments.

The majority of the data points was collected at a water flow rate of $\dot{V}_w \approx 0.36\text{l/min}$. Some changes in the setup during the course of the experiments affected the positioning of the header tank and the length of the hosing, which led to a reduced water flow for some data points of $\dot{V}_w \approx 0.31\text{l/min}$. Exceptions to this were the low density aluminium brush tests, where the majority of the data points was unintentionally collected at a water flow rate of $\dot{V}_w \approx 0.1\text{l/min}$.[1]

After the setup-up of the inlet conditions for the respective test points, the system was given time to reach steady-state operating conditions where the measured quantities did not change appreciably with time anymore. The data points were then derived by taking the time-average of the measured values. Measurements were taken over time intervals of at least 10min at a sampling rate of 1Hz to give a sufficiently large number of data points to reduce the effects of natural fluctuations

[1] This setting was a remnant of preliminary heat transfer tests where the water flow rate was kept at a lower level to increase the water-side temperature spread. When this discrepancy was found during the data post-processing, the brush insert had already been used for coating trials so that the tests could not be redone at the correct flow rate level.

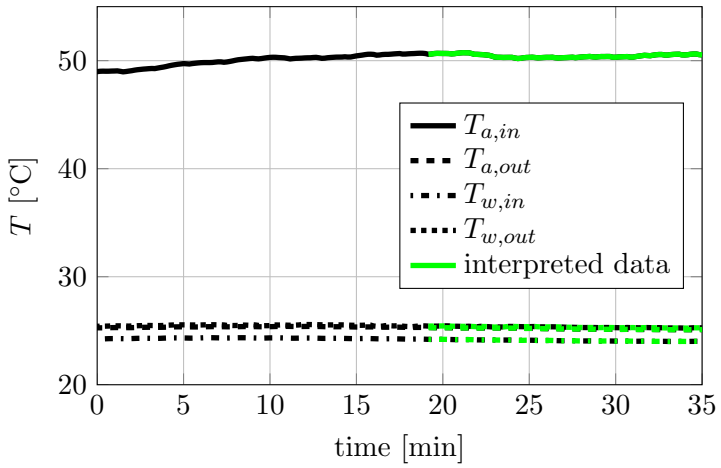

Figure 7.3: Exemplary plot of air and water temperature signals (black) and test interval chosen for interpretation (green)

in the measurements and noise in the sensor signals on the formed averages. Figure 7.3 shows a typical sample plot of the in- and outlet temperature levels during a test of the 5PPI-Metal foam insert at an air flow rate of $\dot{V}_a \approx 63$l/min. The inserts under investigation comprised:

- The three metal foam inserts of nominal pore sizes 5, 10, 20PPI,
- the twisted-in aluminium-wire brush,
- the two twisted-in copper-nickel-wire brushes with different pitches,
- the twisted-in low-density carbon wire brush,
- the carbon fibre flocked circular tube, and
- the empty tube as a reference case.

7.3 Discussion of experimental results

A total number of 107 data points were collected. Due to the number of data points a detailed listing of the individual measured quantities is omitted here but presented in the form of tables in Appendix A.

7.3.1 Comparison of air- and water-side heat flow rates

The validity of the test results is confirmed by the consistency of air- and water-side calculated heat flow rates that are compared in figure 7.4, where the various inserts are differentiable by their specific colors. For the majority of the data, the discrep-

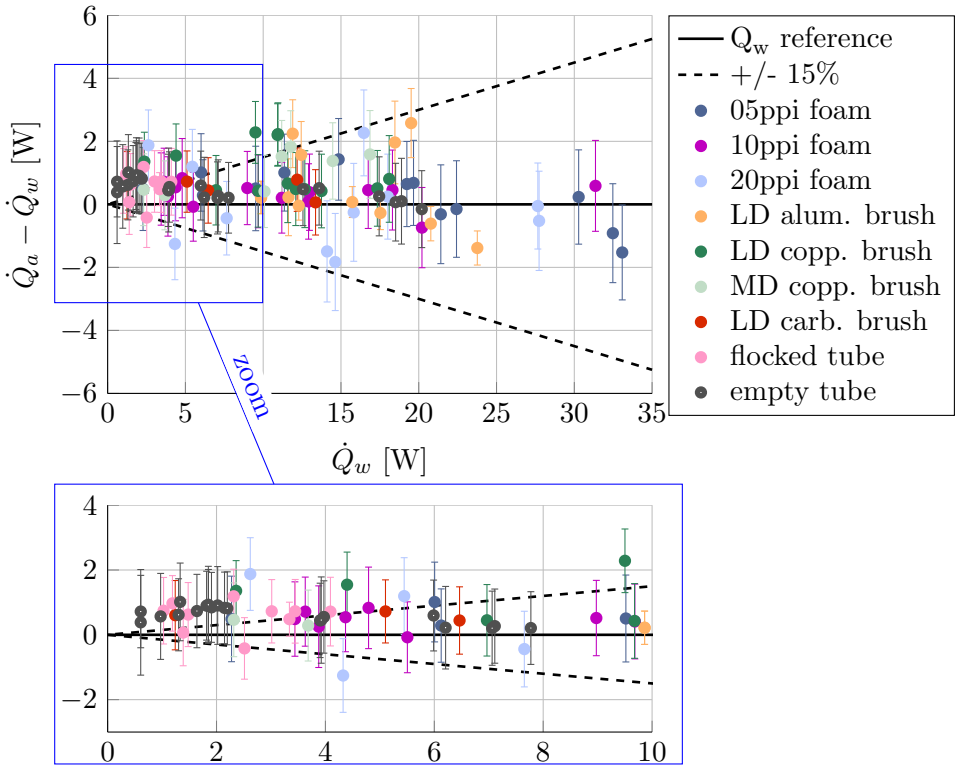

Figure 7.4: Heat balance

ancy between the readings can be explained by the inaccuracies of the measurements. A bigger discrepancy between heat flow rates was noted during the testing of the brush-type inserts, which is most likely due to a different cross-sectional temperature profile attributed to this type of insert. Since the RTD-temperature sensor reading is interpreted as the average temperature along the radius of the channel, a pronounced cross-sectional temperature profile can result in a temperature reading that differs from the actual cross-sectional average temperature. The maximal absolute difference in heat flow rates is $\Delta\dot{Q}_{max} \approx 2.2$W, which signifies a relative error within $\pm 15\%$ for the majority of data points excluding those at low heat flow rates below 5W. It can furthermore be seen from figure 7.4, that the uncertainties varied between experiments as a result of the more or less stable inlet temperature levels.

7.3.2 Difference of working fluid temperatures at channel outlet

A good first indication of the heat transfer performance of the test objects can be obtained by observing the difference between the working fluid temperatures at the channel air outlet. Figure 7.5 depicts this quantity for each of the 107 obtained data points. It is apparent, that for the majority of the data corresponding to the metal

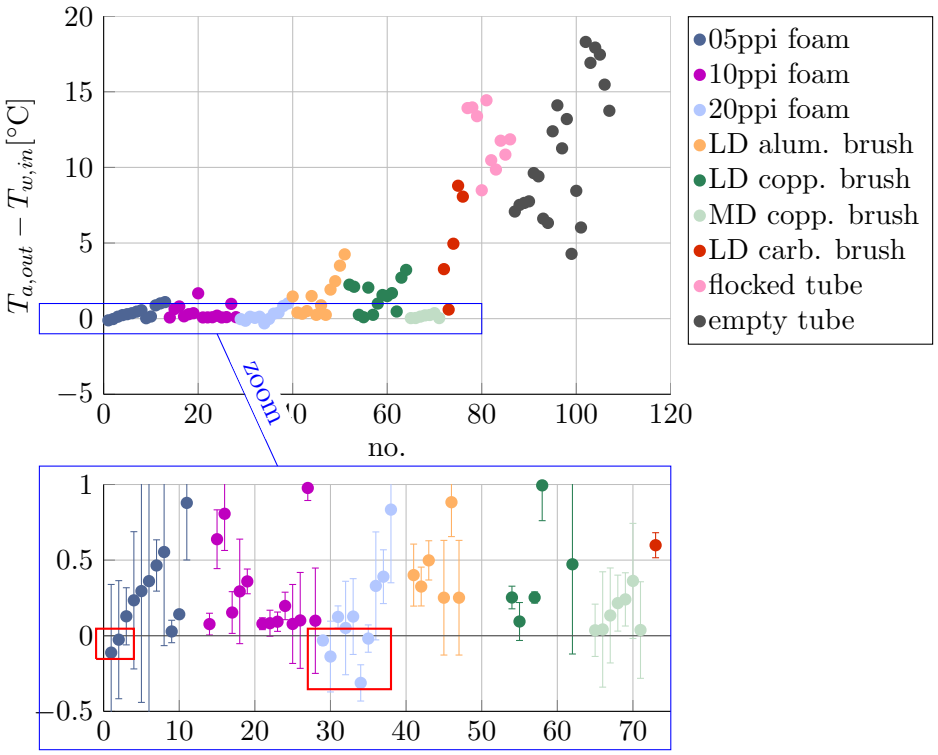

Figure 7.5: Difference between working fluid temperatures at channel outlet

inserts, the working fluid temperature difference is below 1°C, indicating a very effective heat transfer where the working fluid has nearly reached the maximum temperature difference possible. Furthermore, it is clearly seen that the carbon based structures did not yield a comparable augmentation in heat transfer and resulted in working fluid temperature differences closer to those of the empty tube reference case. It must be noted that for 6 data points, emphasised in figure 7.5 by the surrounding red boxes, the measured air outlet temperature was lower than the recorded water inlet temperature. It is obvious that the working fluid in a counter-current heat exchanger can never be cooled down to a temperature level below that of the coolant inlet temperature, which means that the measurements are clearly erroneous. It is, however, apparent that for five of the six cases this error can be

fully explained by the prevailing uncertainty of measurement.

7.3.3 Thermohydraulic performance characteristics

Figure 7.6 presents the experimental results in terms of the characteristic UA-value as a function of air flow rate. As was discussed earlier in section 2, this characteristic value can be obtained from relating the total heat flow to the logarithmic mean temperature difference of the working fluids:

$$\dot{Q} = \dot{Q}_a = \dot{V}_a \cdot \rho_a \cdot C_{p,a} \cdot \Delta T_a \tag{7.1a}$$

$$\dot{Q} = \dot{Q}_w = \dot{V}_w \cdot \rho_w \cdot C_{p,w} \cdot \Delta T_w \tag{7.1b}$$

$$\dot{Q} = (UA) \cdot \Delta \overline{T}_{lm} = (UA) \cdot \frac{(T_a - T_w)_{in} - (T_a - T_w)_{out}}{\ln(T_a - T_w)_{in} - \ln(T_a - T_w)_{out}} \tag{7.1c}$$

While the overall agreement between measured air- and water-side heat flow rates

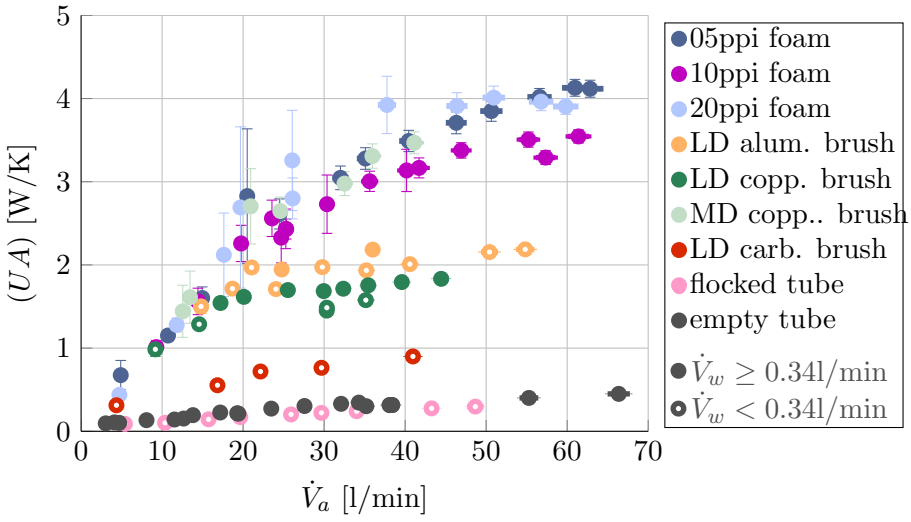

Figure 7.6: Heat transfer performance of tube inserts as a function of air flow rate

was quite good, the use of the air-side heat flow rate resulted in clearer, less scattered trends for the characteristic curve families. This is likely due to the much lower air-side heat capacity flows resulting in a higher temperature difference attributed to the heat flow, which makes the calculation of the latter less prone to be affected by sensor inaccuracies in both temperature and flow measurements. Furthermore, the discontinuous nature of the water flow rate measurements will have an amplifying effect on the error in the calculated heat flow rates as minuscule variations in water flow rates that result in outlet water temperature variations cannot be captured due

to the large time interval during and between measurements. As a consequence, the UA-values corresponding to figure 7.6 and the following were calculated as:

$$(UA) = \frac{\dot{Q}_a}{\Delta T_{lm}} \tag{7.2}$$

The data points corresponding to experiments with a lower water flow rate than $\dot{V}_w = 0.34\text{l/min}$ are visualised in figure 7.6 with empty symbols. When comparing these symbols to those representing the higher water flow rates for the low density aluminium and copper brushes, it can be seen that the higher water flow rate only results in a minor increase in UA-value. This is particularly remarkable for the case of the low density aluminium brush insert, where the ratio in corresponding water flow rates is approximately three. This is a clear indication that the water-side heat transfer resistance is of minor importance for the heat exchanger under investigation. The best heat transfer performance is achieved by the three metal foam tubes and the medium density copper brush insert, which all exhibit very similar slopes yielding a UA-value of approx. $(UA) \approx 4\text{W/K}$ at $\dot{V}_a \approx 60\text{l/min}$. The fact that all three metal foam tubes show a similar performance leads to the conclusion, that the pore size only plays a minor role for the heat transfer performance under the given conditions. Only towards higher flow rates some dependence to the relative density becomes noticeable, where the 10PPI foam, that has the highest porosity of the three specimen, does not reach the same level as the other two foam inserts. It is curious to note that the dependency to the relative density cannot be observed in the case of the brush-type inserts: The medium density copper alloy brush shows a significantly better performance than the low density aluminium brush, although their calculated relative densities of $\rho_{rel}^{MD,CuNi} = 0.030$ and $\rho_{rel}^{LD,Al} = 0.031$ are very similar and the thermal conductivity of the aluminium alloy is far superior to that of Cupronickel. A likely explanation for this circumstance can be found in the different radial porosity distributions: while the metal foams are three-dimensionally isotropic, the spacing between the individual ligaments of a brush increases radially. The bulk of the air tends to flow through the section with the sparsest packing with little interaction with the bristles located in the channel core. Consequently, an insert with a higher number of thinner ligaments can be expected to perform better than an insert with fewer thicker ligaments of the same porosity, because the active surface area that interacts with the fluid is higher due to the higher number of ligaments in the sparsely packed region. This notion is supported when comparing the relative surface areas of the three brush inserts: the relative surface area of the medium density copper brush is approximately twice as high as that of the alu-

minium brush, which is in turn slightly higher than that of the low density copper brush. The additional benefit of the higher thermal conductivity of the aluminium alloy is counteracted by the contact resistance between ligaments and tube wall. The carbon brush performs significantly worse than its metal counterparts. This can be explained mainly by the poor thermal conductivity of PAN-based carbon fibres, that were utilised here and its much lower relative density. The conception of a decent interaction between fibre surface area and fluid as a necessity for heat transfer augmentation is also highlighted by the comparison of the carbon fibre flocked tube with the carbon fibre brush: since the pressure drop over the forest of flocked carbon fibre is great, the bulk of the air flows through the fibre free core with little to no interaction with the additional surface area provided by the carbon fibres, yielding a heat transfer performance approximately similar to that of the empty tube reference case. Only when the fibres reach in to the channel core and the air is forced to flow past the bristles of the carbon fibre brush, the augmenting effect of the additional surface area available for heat transfer is noticeable.

In order to derive the heat transfer augmentation factor, a second order polynomial function was fitted to empty tube measurement data. This allowed for building the ratio of the insert-specific UA-value and the empty tube reference case at the air flow rate of the respective insert measurement.

$$f_{UA} = \frac{(UA)}{(UA)_0} = \frac{Nu}{Nu_0} = f_{Nu} \tag{7.3}$$

Figures 7.7 shows a plot of the fitting function and the corresponding raw test data with shadings proportional to the underlying water flow rate.

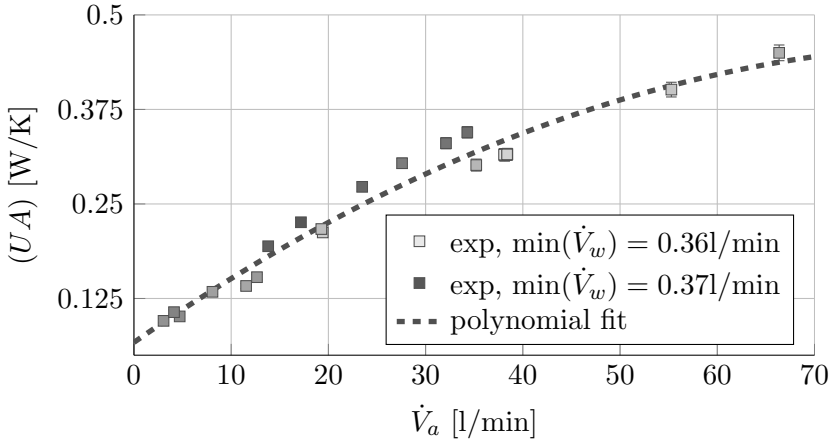

Figure 7.7: Poloynomial fitting function to empty tube reference case

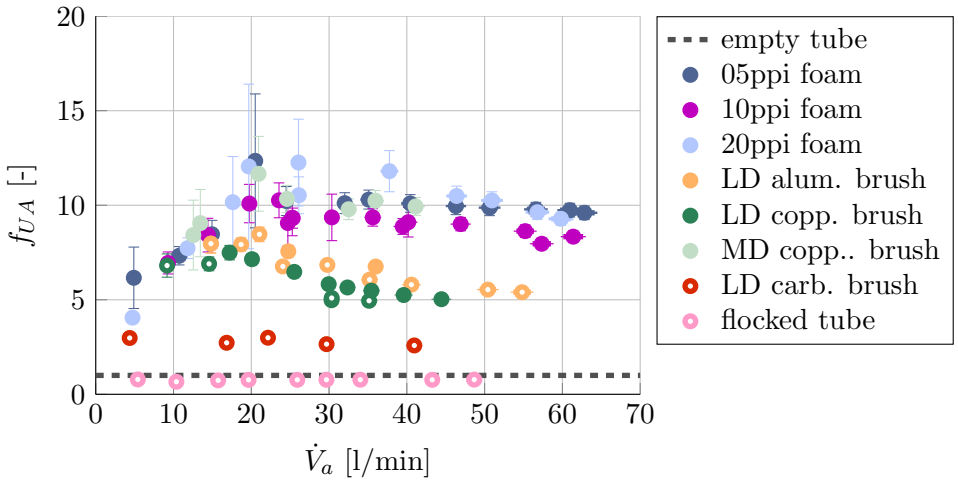

Figure 7.8: Overall heat transfer augmentation factors

The resulting graph of the heat transfer augmentation factors are given in figure 7.8. It can be seen, that the heat transfer augmentation of all the metal inserts relative to the base case is maximal at a flow rate around $\dot{V}_a \approx (20 \pm 5)$l/min. This can be explained by the turbulence promoting effect of the tube inserts, that cause the flow to enter the transitional regime at lower velocities than in the empty tube base case. In this regime both the heat transfer and the pressure drop increase faster with flow rate than in the laminar flow regime. The carbon fibre brush exhibits a much flatter profile with all values around $f_{UA} \approx 3$ that decrease marginally as $\dot{V}_a > 20$l/min. The augmentation can be interpreted mainly as the result of the effective turbulence promotion of the brush type insert. The poor thermal conductivity of the insert prevents an effective conductive heat transfer removal from the channel core to the tube wall, so that the local temperature difference between ligament surface and surrounding air is not high enough to make use of the intensified interaction between fluid and solid. As could already be seen from figure 7.6, the flocked tube does not lead to any heat transfer augmentation, but on the contrary the flocked forest appears to act as an insulation layer that reduces the interaction between fluid and solid tube wall, resulting in f_{UA}-values less than unity.

It is useful to evaluate the heat transfer augmentation provided by the inserts taking into consideration the attributed increase in flow impedance. This can be

achieved by observing the ratio of the (UA)-value to the ideal pumping power:

$$\frac{(UA)}{P} = \frac{(UA)}{\Delta p \cdot \dot{V}_a} \tag{7.4}$$

This figure of merit is closely related to the overall thermo-hydraulic performance factor introduced in eq. 3.3, but is deemed more appropriate in the context of this work, since the channel geometry is fixed and provides a more immediate representation of the absolute quantities. It is plotted in figure 7.9 as functions of air flow rate.

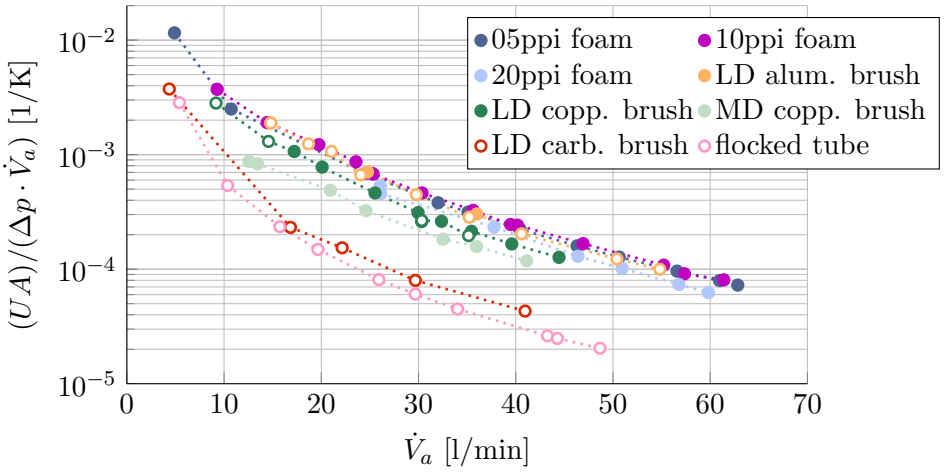

Figure 7.9: Thermo-hydraulic performance comparison of channel inserts

It can be seen that the high pressure drop attributed to the medium density copper brush reduces the depicted performance characteristic to a level below other inserts, despite achieving one of the highest augmentations in heat transfer. A similar circumstance can be observed for the 20PPI foam, whose function is reduced to a level slightly below those of the other foam inserts. Accordingly, the low pressure drop of the low density brush type inserts results in a better thermo-hydraulic performance to the extent that the low density aluminium brush reaches the same level as the 5 and 10PPI foam structures.

Based on the findings above, it was decided to focus on the three foam structures and the low density aluminium brush insert for coating trials and the further analysis of their cyclic heat and mass transfer performance.

Chapter 8

Numerical investigation of steady-state heat transfer performance of selected test objects

The steady-state heat transfer experiments are complemented by a stationary (time-independent) numerical study of the temperature fields of the metal foam and metal brush inserts. For this, first the flow field through the test object was calculated using the two-dimensional axis-symmetric porous medium flow models described in section 6.3 for the tested cases. The calculated pressure and velocities were subsequently used as independent field variables in a heat transfer model, that accounted for the convective heat transfer between porous matrix and fluid and the conductive heat transfer between tube wall and porous matrix. The heat transfer between fluid and porous matrix is governed by the convective heat transfer coefficient h_h that was derived from the flow modelling results by utilising the Colburn j-factor analogy. The imperfect contact between the insert and tube wall was accounted for by means of a thin thermally resistive layer defined between the porous matrix and the tube wall, that was adjusted to yield the best agreement with experimental data.

The main objective of this model was the implementation of a heat transfer model, which could serve as the basis for the transient heat and mass transfer model, that will be described in section 10. The comparison to the experimental steady-state data is helpful to ensure that the modelling assumptions are sound for the conditions under investigation.

In the following, the setup of the heat transfer model together with the deriva-

tion of the convective heat transfer coefficient will be detailed before the comparison between modelling results and experimental results will be presented.

8.1 Model setup

The heat transfer model is implemented as a mere extension to the flow model discussed in section 6.3 by adding the fluid and solid side heat transfer equations to the governing equation system. This implies that the modelling domains for the metal foam and brush inserts are the same as already reported there. The following description of the equation system will refer to the brush type insert depicted schematically in figure 8.1, but can be directly applied to the metal foam model when removing the central stem wire region (IV).

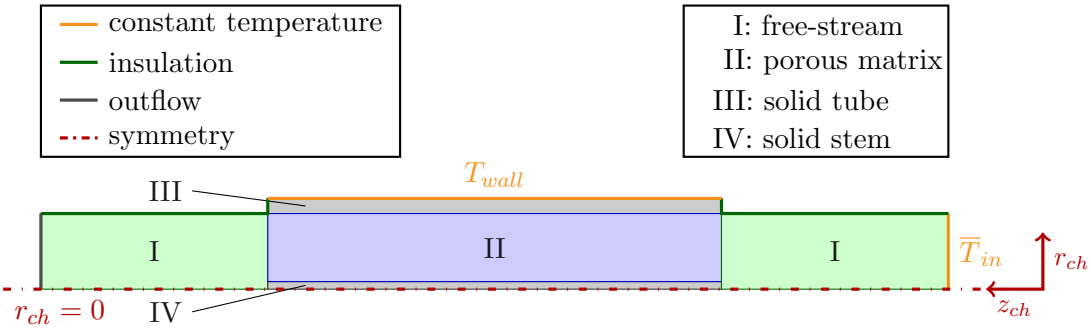

Figure 8.1: Schematic of porous medium brush modelling domain

8.1.1 Field equations

The governing equation system for the heat transfer is made up of the air and solid side porous medium heat balance equations, that are adapted to describe the physics in domains (I-IV) in the schematic. In the free-stream sections (I), air flows through the insulated empty in- and outlet channels, yielding the steady-state transport equation:

$$\rho_a \cdot c_{p,a} \cdot u \cdot \nabla T_a = \nabla \cdot (k_a \cdot \nabla T_a) \tag{8.1}$$

Inside the test section (II), the temperature fields of the fluid and the porous matrix are calculated with separate equations. The convective heat transfer between air

and ligaments is expressed as a heat source acting on the modelling domain:

$$\epsilon \cdot \rho_a \cdot c_{p,a} \cdot u \cdot \nabla T_a = \nabla \cdot (\epsilon \cdot k_a \cdot \nabla T_a) + a_s \cdot h_h \cdot (T_s - T_a) \tag{8.2}$$

$$0 = \nabla \cdot (\rho_{rel} \cdot k_{mat} \cdot \nabla T_s) + a_s \cdot h_h \cdot (T_a - T_s) \tag{8.3}$$

Here, a_s is the relative surface area of the porous matrix that is a function of the local relative density. In the case of the brush, this parameter could be calculated based on geometrical considerations using equation 4.38, while for the metal foam model the values were numerically found as shown in figure 6.8.

The thermal conductivity term of the porous matrix k_{mat} in equation 8.3 represents a diagonal matrix that contains the matrix specific values for its thermal conductivity in radial and axial direction:

$$k_{mat} = \begin{pmatrix} k_{rr} & 0 \\ 0 & k_{zz} \end{pmatrix} \tag{8.4}$$

While for the metal foam inserts the thermal conductivity could be considered undirectional, i.e. $k_{rr} = k_{zz} = k_{Al}$, the bristles of the brush type inserts only conduct heat in the radial and in axial direction. The effective thermal conductivity of the foam matrix is less than that of the material due to the prolonged conduction path, captured in the thermal tortuosity factor ζ, so that:

$$k_{foam} = \begin{pmatrix} \zeta \cdot k_{\mathrm{Al}} & 0 \\ 0 & \zeta \cdot k_{\mathrm{Al}} \end{pmatrix} \tag{8.5}$$

$$k_{Br} = \begin{pmatrix} k_{\mathrm{Al/Cu}} & 0 \\ 0 & 0 \end{pmatrix} \tag{8.6}$$

Since no exact correlations exist for the determination of the convective heat transfer coefficient h_h for the structures under investigation, it was derived from the modelled pressure drop data by utilising the Colburn j-factor analogy. A similar approach was taken by Bejan [1990] who used it to investigated the heat transfer from a surface covered with hair, based on the investigation of the Darcy flow through the hair strands. While this approach cannot be expected to yield precise predictions, it yields sensible approximations due to the similarities between the basic momentum and heat transfer mechanisms. The analogy 2.26 can be rewritten as:

$$j_H = \frac{f_f}{2} = \frac{f_D}{8} = \frac{Nu}{Re \cdot Pr^{1/3}} = \frac{h_h}{c_{p,a} \cdot \rho_a \cdot u_z} \cdot Pr^{2/3} \tag{8.7}$$

The Darcy friction factor is defined by the Darcy-Weisbach-equation as:

$$f_D = \frac{\Delta p}{L_t} \cdot \frac{2}{\rho_a \cdot u^2} \cdot d_h \tag{8.8}$$

In order to use equation 8.8 above, the hydraulic diameter of the porous structure has to be approximated. A simple approximation expressing the hydraulic diameter as a function of porosity and ligament diameter is utilised here, that is based on the air space of a matrix formed by parallel cylinders [VDI, 2010]:

$$d_h = 4 \cdot \frac{A}{P} = \frac{\epsilon}{\rho_{rel}} \cdot D_{lig} \tag{8.9}$$

Together with equation 8.8, this yields:

$$f_f = \frac{f_D}{4} = \frac{\Delta p}{L_t} \cdot \frac{d_h}{2 \cdot \rho_a \cdot u^2} = \frac{\Delta p}{L_t} \cdot \frac{r_{lig}}{\rho_a \cdot u_z^2} \cdot \frac{\epsilon}{\rho_{rel}} \tag{8.10}$$

By inserting relation 8.10 into equation 8.7 and noting that for air $Pr_a^{2/3} \approx 1$, the convective heat transfer coefficient can be approximated as:

$$h_h = \frac{f_f}{2} \cdot c_{p,a} \cdot \rho_a \cdot u_z = \frac{\Delta p}{l_t} \cdot \frac{r_{lig} \cdot c_{p,a}}{2 \cdot u_z} \cdot \frac{\epsilon}{\rho_{rel}} \tag{8.11}$$

The conductive heat transfer through the solid domains (III and IV) is governed by:

$$0 = \nabla \cdot (\rho_{rel} \cdot k_{tube} \cdot \nabla T_s) \tag{8.12}$$

$$0 = \nabla \cdot (\rho_{rel} \cdot k_{stem} \cdot \nabla T_s) \tag{8.13}$$

In the case of the metal foam heat transfer model, equation 8.13 becomes redundant and domain of the fluid saturated porous medium (II) is extended to cover the area of the stem-wire domain (IV).

8.1.2 Boundary conditions

Absolute temperatures were specified at the air inlet and outer tube wall boundaries to emulate the water-cooling of the hot air flowing through the channel in the experiments. A constant temperature $\overline{T}_{in}$ corresponding to the respective experimental inlet conditions was set as the boundary condition for the air inlet shown on the right of schematic 8.1. The boundary condition for the channel outlet was specified to represent a convective outflow, setting the diffusive heat flux over that boundary to zero while allowing a convective transfer of heat out of the modelling domain.

In order to approximate the experimental conditions, the wall temperature was set to vary linearly in axial direction between the experimentally determined

water in- and outlet temperatures:

$$T_{wall} = T_{w,out} + \frac{T_{w,in} - T_{w,out}}{l_t} \cdot z_{ch} \tag{8.14}$$

For all remaining outer boundaries depicted in green in figure 8.1 and the symmetry boundary at $r_{ch} = 0$ the normal heat fluxes were set to zero, thus creating adiabatic insulation boundaries.

In the case of the brush type inserts the thermal contact between the ligaments and solid tube wall is bound to be suboptimal as the inserts were simply slid into the tube without any form of binding substance. In the case of the metal foam tubes this was attempted to be overcome by brazing the metal foam inserts to the wall, although some thermal resistance is still conceivable due to possible structural irregularities at the interfacial surface created during the machining of the foam blocks into their tubular shape. In order to model the contact resistance between the inserts and the inner tube wall, a thin thermally resistive layer was added to the model at the interfacial boundary between the porous matrix (II) and tube (III) domains. The heat flux across that boundary is defined by

$$\begin{aligned} -\overrightarrow{n}_{III} \cdot (-k_{tube} \cdot \nabla T_s) &= -\, k_{res} \cdot \frac{T_{s,II} - T_{s,III}}{d_{res}} \\ -\overrightarrow{n}_{II} \cdot (-k_{mat} \cdot \nabla T_s) &= -\, k_{res} \cdot \frac{T_{s,III} - T_{s,II}}{d_{res}} \end{aligned} \tag{8.15}$$

which effectively introduces a temperature discontinuity of $(T_{s,II} - T_{s,III})$ at the boundary that varies in size depending on the specified thermal conductivity of the resistive layer k_{res} and its thickness d_{res}. The thermal conductivity of the resistive layer was set to that of dry air and the thickness of the layer was varied until the modelled outlet air temperature yielded the best agreement with experimental data.

8.1.3 Model execution

The model was run for the aluminium foam and metal brush inserts using the experimentally determined inlet air temperatures and flow rates as boundary conditions for the flow and heat transfer models. The experimentally determined water temperatures were used to calculate the outer tube wall temperature according to equation 8.14. For each data point, the modelling procedure had two steps.

First, the pressure drop and flow fields were calculated using the applicable porous-medium flow model presented in section 6.3. The pressure drop over the porous matrix was calculated by subtracting the cross-sectional average pressures

at the test tube in- and outlet, cp. figures 6.1 and 6.10. From this the fanning friction factor and convective heat transfer coefficient could be determined for the modelled case using relations 8.10 and 8.11.

As a consequent step the temperature fields of air and solid material were calculated utilising the modelling results of the previous step as input variables. By solving the flow and temperature field equations separately the complexity of the model is greatly reduced. The drawback of this approach is, that it precludes accounting for any interdependencies between the momentum and heat transfer processes through variable material properties. However, pressure drop and temperature dependencies of the material properties can be considered negligible, because of the small driving temperature difference of the problem at hand and the minor pressure elevation in comparison to atmospheric pressure due to the flow restriction of the test objects at the flow rates investigated. Consequently the above-mentioned simplification does not impair the predictive capabilities of the model significantly, while reducing calculation times noticeably.

8.2 Model validation

The model was run once without accounting for the contact resistance between porous matrix and tube wall before relation 8.15 was added to the analysis and d_{res} was varied to yield the best fit between modelled air outlet temperatures and experimental results. The resulting modelled air outlet temperatures are compared to the experimental findings in figure 8.2. The data in the plot is colour coded to correspond to the various inserts under investigation, while the filled and empty symbols correspond to the modelling cases with and without accounting for the contact resistance. The best fit parameters for the thickness of the thermally resistive layer of thermal conductivity $k_{res} = k_a$ are also noted in the figure legend.

It is apparent from the figure, that the model can be calibrated to yield a decent fit to experimental data when accounting for the thermal contact resistance with the majority of the data points lying within ± 0.3°C of the experimental findings. The small subfigure on the right shows the difference $\Delta T = T_{\text{mod.}} - T_{\text{exp.}}$ between modelled and experimental air outlet temperatures as a function of air flow rate. It can be seen, that the empty symbols start to deviate from the ($\Delta T = 0$)-base line at different flow $\dot{V}_a > 18$l/min depending on the insert and the discrepancy increases with flow rate, while the solid symbols scatter around the base line independent of air speed. The fact that the deviation of the metal foam insert related symbols takes place at higher flow rates is a result of their superior heat transfer

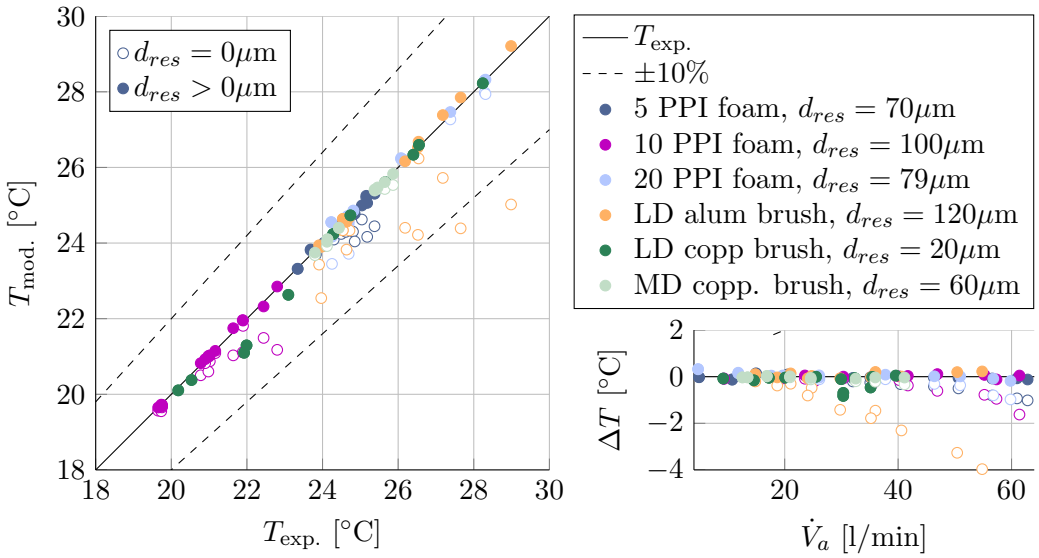

Figure 8.2: Comparison of modelled outlet temperatures to experimental results

performance in comparison to the brush inserts. The region of the curves where the solid and empty symbols overlap correspond to conditions where the heat transfer in the channel is close to maximal despite the imperfect contact between insert and tube wall. In general, the two plots in figure 8.2 show, that an adaptation of the contact resistance is enough to yield a good agreement with experimental data. The corresponding layer thicknesses of the brush inserts between $20\mu\text{m} \leq \text{d}_{\text{res}} \leq 120\mu\text{m}$ can be considered to lie within realistic ranges. The fact that the metal foam models require a thermal resistance of similar magnitudes to yield a fit to experimental data, however, may be taken as an indication that the underlying j-factor analogy leads to an over-prediction in convective heat transfer coefficient, which is not unlikely given the approximative nature of the approach in this context. However, for the purposes of this work a more detailed analysis of the individual heat transfer resistances could be omitted, because the insert specific pressure drop penalties attributed to the flow around the tube inserts make the regime with lower air flow rates favourable, where the sensitivity of the outlet temperatures to the heat transfer resistances is limited. The heat and mass transfer tests, that are discussed in the following chapter, were accordingly performed at air flow rates up to $\dot{V}_a \leq 20\text{l/min}$, where the effect of an added thermal resistance has been shown to be of minor importance for the inserts under investigation.

Chapter 9

Experimental investigation of transient heat and mass transfer performance of selected test objects

The cyclic heat and mass transfer performance of the coated inserts was assessed in a purpose-built experimental test rig that simulated the ad- and desorption cycles in the water-cooled desiccant wheel prototype. The dehumidification performance of the silica-gel coated inserts was compared to that of a polymer-coated honeycomb structure taken from a commercial desiccant wheel.

The experiments were run for three different flow rates. The effect of coating thickness could be analysed by repeating the tests after the application of additional coating layers to the inserts. The performance of the recoated inserts was compared to that at an alternative inlet condition for selected inserts.

While the experimental results allow for a qualitative performance comparison, the extraction of robust values for the absolute moisture uptake was impaired above all by the response time and measurement accuracy of the relative humidity sensors.

9.1 Design of the experimental test rig

A new test rig was designed to investigate the heat and mass transfer performance of a single channel of the water-cooled wheel prototype. The advantage of the single-tube test rig design is that it facilitates a comparison of various channel con-

figurations without having to build an entire desiccant wheel, making the process of preselecting candidate structures much more cost and time efficient. The test rig simulates the desiccant wheel process by instantaneously exposing the test section alternately to process and regeneration air streams, that are arranged counter-current to one another. The channel in- and outlet air conditions are measured at several locations using thermocouples and relative humidity sensors. Although principally the same quantities are measured as in the conventional desiccant wheel tests, the single-channel tests entail additional challenges because of two main reasons:

1. The conventional measurements performed on a desiccant wheel are typically in steady-state, i.e. temperature and humidity sensors are positioned in the process and regeneration air ducts up- and downstream of the rotating wheel, so that they measure constant conditions once the wheel has reached steady-state operating conditions. The conditions on the ends of a single channel, however, constantly change with time and undergo rapid changes during the switch between half-cycles. This has important implications for the choice of sensing equipment for temperature and humidity measurements towards sensors with fast response times.

2. Furthermore, the smaller cross-sectional area of the single-tube in comparison to the flow channel of a desiccant wheel leads to a much lower flow rate at the same face velocity. As was already mentioned in section 7.1 in the context of the heat transfer test rig design, this leads to very low values of absolute heat and mass flow rates, which results in high relative measurement uncertainties. This is especially problematic, since the choice of sensors with adequate accuracies is limited due to the additional requirement of a fast response time.

The instantaneous switching between process air steam and the counter-current regeneration air stream is critical for accurately simulating the desiccant wheel process and was the most challenging part of the test rig design. The aim to expose the test objects to steady inlet conditions in the respective half-cycles demanded the realisation of two continuous air streams alternately flowing through the test channel in opposite directions.

The original design envisaged the positioning of the test object between two dummy channels inside an insulated foam box that was pneumatically shifted to connect the middle channel with one of the continuous inlet streams, while the other was diverted through one of the dummy channels. This design, where the test piece itself was moved from one continuous stream to the other, would have had the advantage of being a very close representation of a single channel in an

actual desiccant wheel process. However, the drawbacks included the necessity of implementing some form of variable flow restrictions in the dummy channels, that would match the pressure drop over the various test objects in order to minimise temperature fluctuations due to variations in pressure drop dependent flow rates, and the difficulty of achieving an air tight seal at the interfacial faces. When the problem of insufficient sealing against air leaks could not be overcome after several alterations in design, the concept of pneumatically moving the test object from one stream to the next was abandoned.

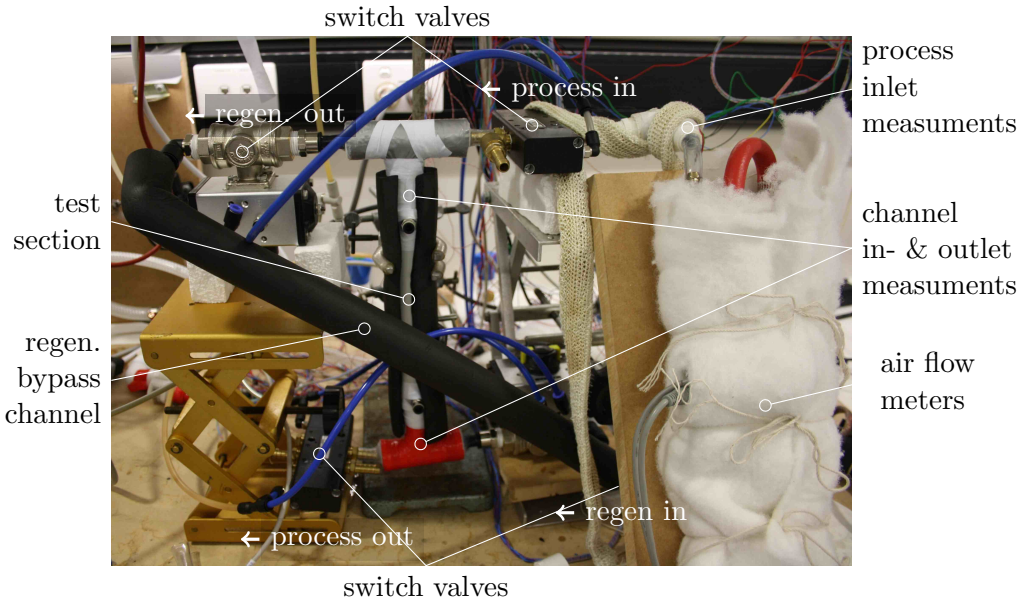

Figure 9.1: Photograph of heat and mass transfer test rig

It was substituted by the configuration depicted in figure 9.1, where the paths of the air streams were redirected using a system of switch valves. In order to realise a counter-current flow arrangement, a system of four 3-way switch valves had to be used, that were controlled pneumatically to simultaneously redirect the air streams either through the test section or a respective bypass channel. A schematic of the final configuration is shown in figure 9.2.

The test air stream was produced by combining dry compressed air with moist air, that had been passed through a water tank. The absolute humidity level could then be adjusted by altering the ratio of dry air and moist air using two manually operated flow control valves. The test air was split into two streams, one for regeneration air marked by solid red lines in the schematic and one being the process air to be dehumidified, distinguished in blue. The flow rates of the two

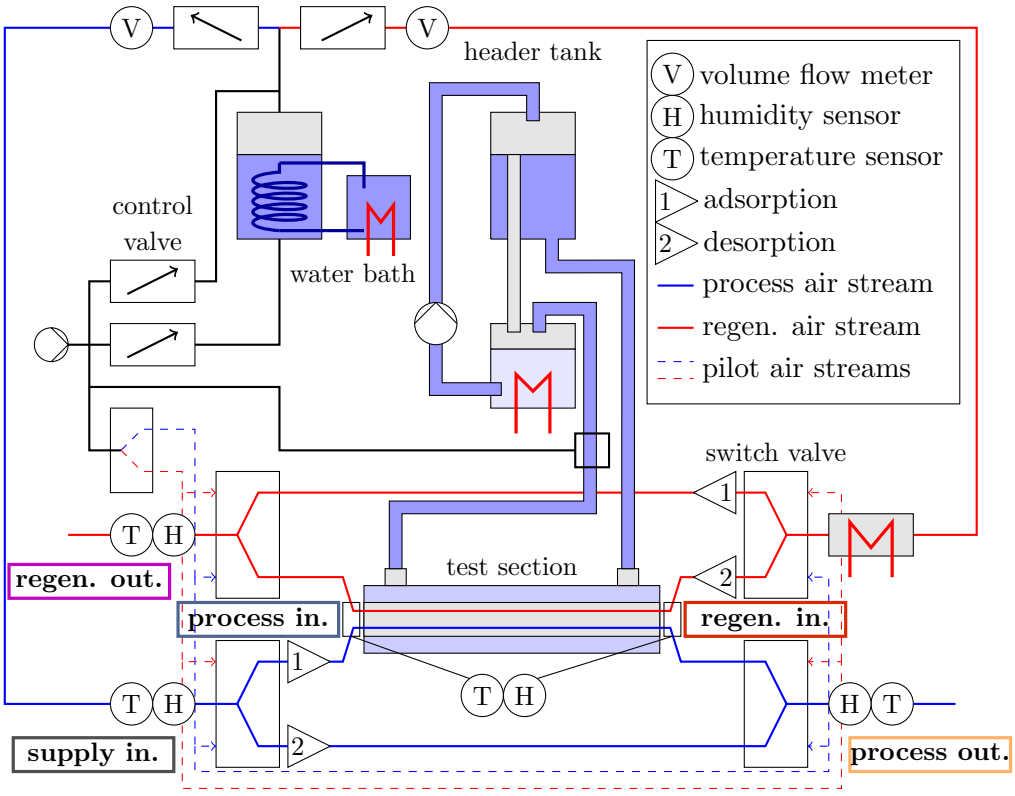

Figure 9.2: Schematic of heat and mass transfer test rig

streams were set to the desired levels using two additional flow control valves similar to the ones used for the air preconditioning. The two air streams were then directed past flow meters to the respective inlet switch valves using flexible hosing. The four switch valves send process and regeneration air streams alternately through the test section and the respective bypass-channels. The respective flow paths are illustrated in the schematic by the numbers 1 (adsorption half-cycle) and 2 (regeneration half-cycle). The valves were controlled by pneumatic pilot air streams shown as dashed lines in the schematic. Electrical heating tape was wrapped around all connecting hoses except for the insulated regeneration bypass channel, in order to prevent condensation and to heat up the air to the desired process air inlet temperature level. The regeneration air stream was heated up further to the regeneration temperature level by a heating coil placed directly before the regeneration inlet switch valve. For the cooling water supply the same header tank as already described in section 7.1.4 in the context of the heat transfer experiments was used. In order to interrupt the cooling water flow, a further dedicated switch valve activated an air stream during the regeneration half-cycle counter-current to the water flow. The gauge pressure

was set high enough to overcome the head of the water tank, so that the cooling water was forced out of the water jacket back into the header tank. A superior design where the air stream is only active during the switching to purge the cooling water out of the header tank could not be realised in the current setup due to the lack of an additional valve that would have allowed for a redirection of the cooling water flow to bypass the test section during the regeneration half-cycle.

In the following, a description of the experimental setup up will be given, detailing the preparation of the test section, the arrangement of process- and regeneration air streams, the conditioning of the process inlet air, the realisation of the cooling water supply, selection and positioning of sensing equipment, and the system implemented for the control of the test rig and the data acquisition.

9.1.1 Test section

The coated test objects were fitted into the same water jacket as in the heat transfer experiments made of a PVC-pipe with an inner diameter of $d_j = 28$mm. In order to reduce their thermal mass for the cyclic process, the test tubes had previously been turned down to a reduced wall thickness of 1mm. During preliminary testing it was found, that the thermal mass of the insulation has a noticeable impact on the thermal swing of the system. This is unwanted, because it leads to an obscuration of the half-cyclic step changes in temperature. The amount of insulation was therefore greatly reduced in comparison to the steady-state heat transfer test rig and the water jacket was insulted from the ambient by an approx. 2cm thick tube of flexible closed cell foam.

9.1.2 Process and regeneration air supply

The test sections were connected to T-pieces made of the same polystyrene tubes that were used in the heat transfer test rig. They served as in- and outlet flow channels for the process and regeneration air streams connecting the test tube to the switch valves and bore the sensing equipment for the local air temperatures and moisture loading. The length of the channels was greatly reduced in comparison to the stationary heat transfer test rig setup in order to minimise the system's thermal inertia.

As can be seen from schematic 9.2, one end of the test tubes was connected to the process air inlet/ regeneration air outlet valve pair, while the other was connected to the regeneration air inlet/ process air outlet valve pair. On the process side, two pneumatically piloted 5/3-way directional control valves were used. Three way ball

valves, that were also operated pneumatically, had to be used on the regeneration side due to the elevated temperature levels. Due to the low line pressures of the application at hand, double-activated valves had to be used, that required pneumatic impulses for the shift in both directions. The pressurised valve pilot air streams themselves are controlled by a 5/3-way solenoid valve, that pressurises the relevant lines based on signals emitted from the rig control system.

Flexible PVC hosing was used for all other connections where the temperature levels were low, i.e. the process-air preconditioning section and the connections to the process air switch valves. Temperature resistant rigid teflon tubing was used for the regeneration bypass channel while the connections up- and downstream of the regeneration air heater utilised flexible teflon hosing capable of with standing temperatures up to 120°C.

All connecting hoses except for the regeneration bypass line were wrapped in electrical heating tape, whose output could be controlled manually using a potentiometer. This was important for the prevention of condensation due to ambient cooling and was also used to elevate the temperature of the process inlet air to the desired temperature level. Due to the high temperatures of the regeneration air it was deemed unnecessary to externally heat channel walls of the regeneration bypass channel.

9.1.3 Inlet air conditioning

The test air was preloaded with moisture to the desired level by passing a variable fraction of it through a water bath, that is depicted in figure 9.3. The water bath was equipped with two copper coils of different sizes. The outer bigger one was used to circulate temperature controlled heating water that made it possible to increase the water bath temperature, if a high moisture loading of the test air was desired. During the experiments the circulating heating water was usually kept at a temperature around 30°C. The dry air fraction was passed through the smaller coil in the middle of the tank, in order to obtain approximately equal temperature levels of the two air streams.

The two air streams are merged again after the water bath. The resulting mixed air stream serves as source for both process and regeneration air stream, so that the absolute moisture content of both flows is the same. While an equal absolute moisture content in both air streams can be considered as the sensible base case for the purpose of desiccant wheel performance assessment, it is dependent on the underlying thermodynamic cycle concept whether this is representative of the ultimate application.

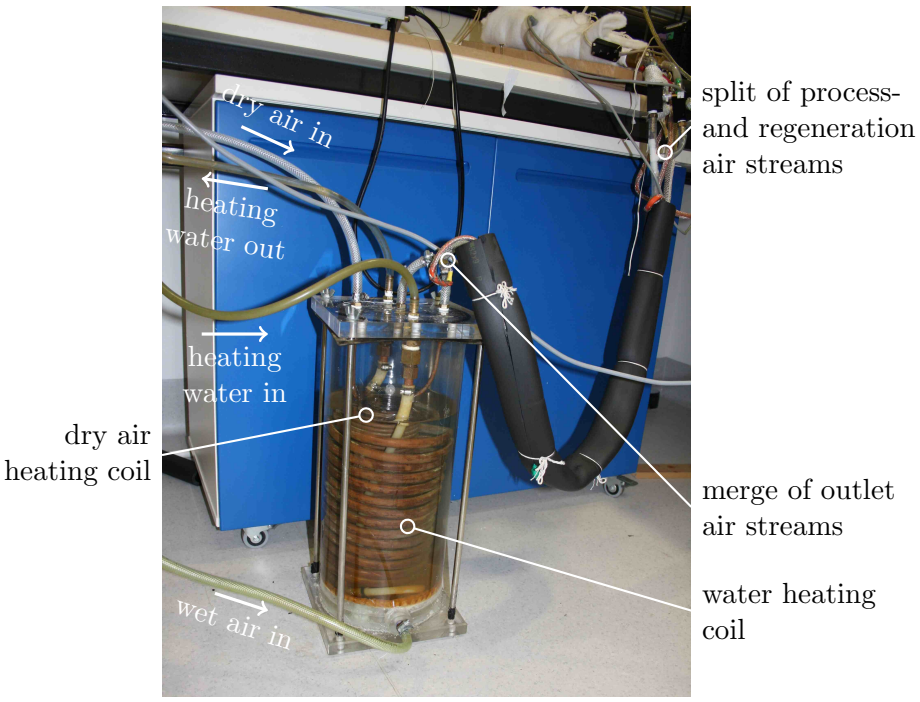

Figure 9.3: Water bath for test air humidification

After the air is divided into the two distinct streams, it is directed past the air flow meters, that have previously been used for the heat transfer experiments, to the respective inlet valves. Heating tape wrapped around the channel walls prevents any mass losses due to condensation and its output is set, so that the temperature at the process air inlet position is at the desired level.

The regeneration air has to be heated up further using a similar heating element as the one described in the context of the steady-state heat transfer experiments before. It is positioned upstream of the regeneration switch valve. In order to minimise temperature fluctuations, the heat output is varied by controlling its feed voltage using a variable autotransformer connected to mains power.

9.1.4 Cooling water supply

The same header tank, that was used in the heat transfer experiments, provided a constant water supply during the water-cooled adsorption half-cycles. Since the test conditions were above ambient lab air, the water temperature was elevated by continuously replenishing the tank with water from a recirculator bath, that was kept at process inlet air temperature level. The header tank outlet was connected to the water jacket inlet. In contrast to the heat transfer tests, the header tank outlet

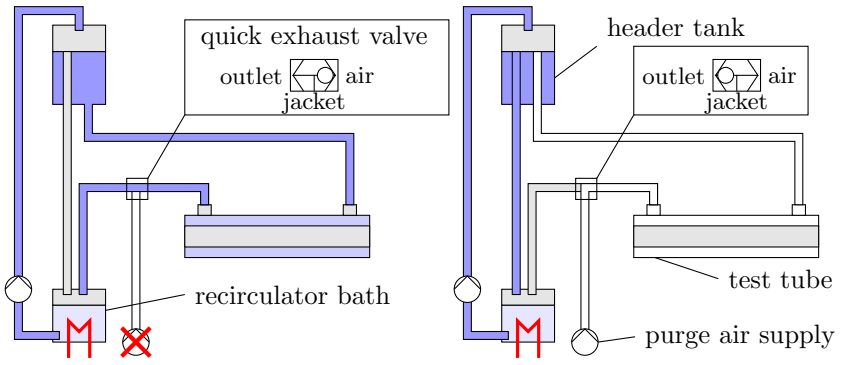

(a) adsorption cycle (b) desorption cycle

Figure 9.4: Schematic of cooling water circuit

flow was not restricted by a ball valve, in order to achieve the highest flow rate. The flow exiting the water jacket was redirected to the recirculator bath, from where it was pumped back into the header tank. The purge air stream was connected to the system via a quick-exhaust ball-valve located downstream of the water-jacket outlet before the exhaust to the recirculator bath. The valve is actually designed for pneumatic applications, but could be used to close off the water exhaust that was open to atmosphere when the purge flow was active. This way the air pressure in the line could build up to force the water out of the water jacket back into the header tank. The cooling water circuit is depicted schematically in figure 9.4. Although the test section is depicted as a horizontal tube in the schematics, it was mounted vertically in the actual experimental with the air stream entering from the bottom that ensured a complete removal of all the cooling water out of the water jacket.

9.1.5 Measurements of air conditions

The air flow rates of the process and regeneration air streams were measured upstream of the process inlet valve and regeneration air heater using the same TSI 40246 flow meters as in the heat transfer experiments. The measurement data was transmitted to the test program digitally using RS-232 protocol. Air temperature and relative humidity levels were measured at several locations in the test rig. At each location the relative humidity was measured using a capacitive polymer film sensor positioned in the centre of the flow channel cross-section. The temperature measurements were performed in very close proximity using J-type thermocouples. Based on the measurements of these sensors, the absolute humidity level could be

determined from combining relations 2.70 and 2.71:

$$Y = \frac{M_v}{M_a} \cdot \frac{p_v}{p - p_v} = \frac{M_v}{M_a} \cdot \frac{\phi \cdot p_{v,sat}(T)}{p - \phi \cdot p_{v,sat}(T)} \tag{9.1}$$

where $p_{v,sat}$ was calculated from equation 2.72. In the following the sensor positioning is explained first, before the choice of temperature and humidity sensors is shortly discussed.

Sensor positioning

Five sets of sensors were installed at different locations in the test rig, that are labelled in schematic 9.2 inside colour coded boxes. This position-based colour coding will be maintained throughout the following discussion. Two were installed in the polystyrene T-pieces at the end of the test section, providing the immediate channel in- and outlet measurements. Depending on the half-cycle, the sensors at one test tube end measured either the process inlet and regeneration outlet air conditions, while the sensors on the other end were alternately exposed to the regeneration inlet and process outlet air stream. Because the meaning of the sensor readings is different with each half-cycle, the sensors are given names referring to their position in the test rig, that are also noted in the schematic in figure 9.2. The sensors at the test tube in- and outlets are called "channel process inlet" ("ch,pi") and "channel regeneration inlet"-sensors ("ch,ri").

Another set of sensors was installed upstream of the process air inlet valve. It provides a steady-state measurement of the test air humidity level close to process air inlet conditions. The absolute humidity level calculated from these sensor readings is also representative of that of the regeneration inlet air, because both the process and regeneration air stream have the same source. This location in the test rig is therefore labelled as the "valve supply inlet" ("v,si"). These were the only sensors exposed to constant air conditions throughout the experiments and were therefore used as reference for setting up the desired inlet conditions.

The final two sets of sensors were installed downstream of the process- and regeneration air outlet valves. Their main purpose was to give a duplicate absolute humidity reading of the respective channel outlet air streams and are consequently labelled "valve process outlet" ("v,po")and "valve regeneration outlet"-sensors ("v,ro"). An anticipated benefit of measuring the humidity levels downstream of the switch valves was the introduction of some thermal mass, that may contribute to a reduction of the amplitude of system inherent thermal fluctuations the hygrometers are exposed to. This may in-turn influence the quality of the sensor

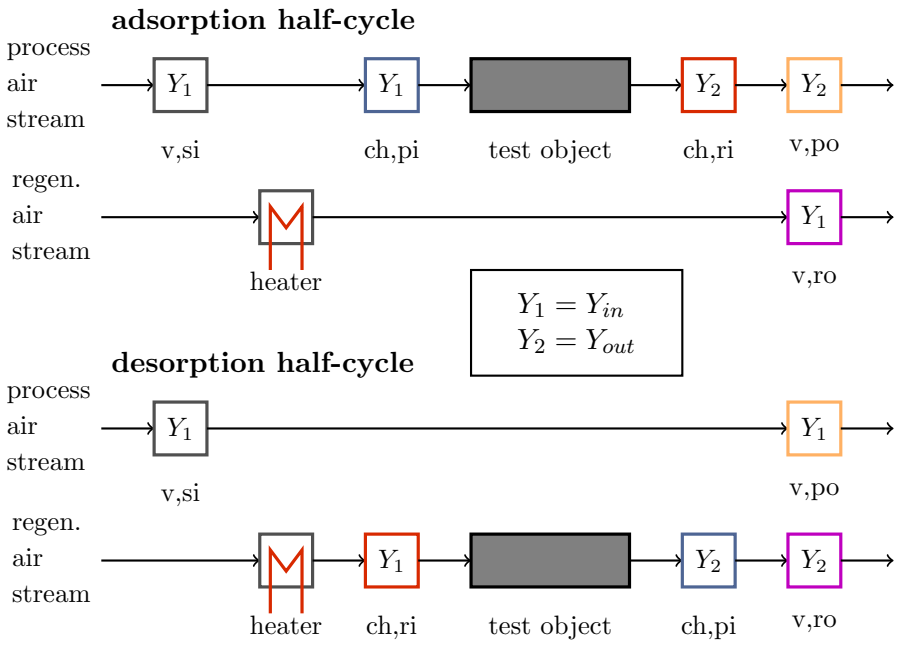

Figure 9.5: Schematic of flow through measurement locations

readings.

Depending on the half-cycle, the sensors downstream of a particular switch valve were either exposed to the air leaving the test section, thus measuring the same absolute humidity as the the corresponding channel outlet sensor, or they were measuring the conditions at the outlet of the bypass channel, which should be at the same absolute humidity level as the supply inlet air. In order to help visualise the flow paths, figure 9.5 schematises the flow through the respective measurement locations and the corresponding absolute humidity levels measured at the respective for each half-cycle. The measurement locations are represented as color coded boxes containing information on whether the absolute humidity level calculated from the measurements at that point represents the inlet or the outlet condition. It can be seen, that for each half-cycle three sensors measure the channel inlet condition and two sensors measure the outlet condition.

In addition to the above-mentioned measurements, thermocouples were installed in some other locations to provide auxiliary temperature readings, for instance for the purpose of a safety measurement right after the air heater that triggered a routine to protect from overheating or a measurement of ambient laboratory temperature.

Choice of temperature sensors

The choice of temperature sensors was governed by finding a suitable compromise between measurement response time and accuracy.

In preliminary tests the response of the RTD-elements, that had previously been used in the heat transfer tests, was compared to that of J-type thermocouple sensors. It was found, that the reaction time of the RTD elements to the cyclic temperature jumps was much longer than that of the thermocouple sensors, so that it was decided to rely on the thermocouple readings for the heat and mass transfer analysis.

Thermocouples are a popular choice for transient measurements because of their fast response time, simplicity and low procurement cost. The drawback is their limited accuracy and inferior sensitivity in comparison to other sensors, such as RTD's and thermistors. They are classified by the conductor pair they are made of, which influences the temperature range, accuracy and sensitivity. J-type thermocouples were chosen for the application at hand because of their comparatively high sensitivity. They were procured in form of one continuous cable made up of twisted 0.2mm-diameter conductors, that could be cut to desired lengths and joined together by hand using a thermocouple welder available in the CSIRO laboratories. The output voltage of a thermocouple sensor is proportional to the temperature difference between the measurement junction and the cold junction created at the terminals to the data acquisition board. Therefore, the thermocouple signal only reflects an absolute temperature when the cold junction is equal to 0°C. A separate measurement of the cold junction temperature is therefore necessary, in order to compensate for the discrepancy from the 0°C-reference temperature. The data acquisition module used to measure the thermocouple signals was equipped with an internal sensor for the cold junction temperature measurement and automatically performed the cold junction temperature compensation. The thermocouples were calibrated against one of the RTD elements to improve the accuracy of the temperature readings for the experimental temperature range. The calibration data is summarised in appendix C.

Choice of relative humidity sensors

The choice of suitable humidity sensors was considerably limited by the demand for a fast response time at an acceptable level of accuracy and small size. Polymer film electronic hygrometers are widely used hygrometers, that satisfy these demands comparatively well [ASHRAE, 2005]. They consist of a hygroscopic polymer, that

is deposited as a thin film on a water permeable substrate. The change in polymer capacitance is a function of its water content, that depends on the relative humidity of the test air. It is converted into a voltage signal through sensor integrated circuitry. Often the sorption characteristics of the polymer material are temperature dependent making temperature corrections necessary.

A capacitive humidity sensor with a specified response time and accuracy far superior to similar sensors was procured, but could not be used for the experiments at hand because of delays in their shipment. Instead, Honeywell HIH-4000-003 sensors, that were readily available from local suppliers, were chosen for the utilisation in the test rig. Due to their compactness, nearly linear dependence of the output voltage signal to a change in relative humidity and still comparatively fast response time, they were a reasonable second choice. The sensors' specified time constant of $\tau_{resp} = 5$s is lower than most other candidate sensors although still leading to undesirably long reaction times for the application at hand. The factory calibrated sensors had a specified accuracy of $\Delta\phi = 0.035$, which is typical for these kind of hygrometers.

9.1.6 Measurements of water conditions

Preliminary tests showed that the difference in water temperatures at the test conditions was minuscule due the high prevailing water flow rates. It was deduced, that the experimental setup succeeded in creating a isothermal boundary condition during the adsorption half-cycle.

The water inlet temperature was measured using the RTD-element from the previous heat transfer experiments, while the measurement of the water outlet temperature and flow rate was omitted after the preliminary tests.

9.1.7 System for rig control and data acquisition

A control program for the test rig was written using the LabVIEW 2010 Professional Development System. Apart from the real-time visualisation and recording of direct measurements and calculated values, it comprised routines for the controlled cyclic operations of the solenoid valves and a temperature and flow rate dependent disruption of the current supply to the transformer powering the regeneration air heater to prevent an overheating.

The same NI CDAQ-9174 data acquisition system was used as in the stationary heat transfer experiments. Apart from the NI-9217 4-Channel Pt100-module, it was furthermore equipped with a NI-9205 module for the measurement of the

relative humidity sensor voltage signals, a NI-9213 module for the acquisition of the thermocouple signals, and a NI-9402 module for the output of digital signals for the control of the valves and safety power disruption.

The digital outlet signals from the rig control program were used to control the AC-current supply to the solenoid valves, that supplied the pilot air for the switch valves and the purge air for the water jacket, and the automated transformer powering the regeneration air heater through a set of solid-state relays. A time delay of 5 seconds between purge air (de-)activation and test air switch was implemented, in order to allow for enough time for a complete filling/drainage of the water jacket before the change in flow direction.

The sampling rate of 2Hz was chosen in order to capture the fast changes in the thermocouple signals. The time series containing the measurement data were saved as text-files, that were imported into MATLAB for post-processing.

9.2 Test program

For the assessment of the water-cooled dehumidification performance of the candidate structures a total of 49 experiments were performed. The majority of data points was collected at the following air conditions: $T_{ch,pi} \approx 35$ °C, $Y_{v,pi} \approx 19$ g/kg. The regeneration temperature was kept constant at $T_{ch,ri} \approx 80$ °C for all experiments. Due to limitations in the manual adjustment precision and the cyclic variations of the channel inlet measurements, the inlet conditions averaged over the respective half-cycle time of the experiments varied around these nominal values within $\Delta T_{ch,pi} \approx \pm 2$ °C, $\Delta T_{ch,ri} \approx \pm 6$ °C, and $\Delta Y_{ch,pi} \approx \pm 2$ g/kg. With only a few exceptions, the dehumidification performance of each insert was tested at three different cycle times $t_{cyc} = \{5, 10, 20\}$ min for a range of flow rates $\dot{V}_p = \dot{V}_r = \{5, 10, 15\}$ l/min, that were equal for both air streams. The inserts investigated comprised the three metal foam inserts and the aluminium brush insert. Their cyclic behaviour was compared to that of a section of a commercial polymer coated desiccant wheel, that had been rolled up into a scroll and used as a test tube insert. Variations of these baseline tests were performed on selected inserts. These included :

- the tests were repeated for the 5- and 10PPI foam tubes and the aluminium brush insert with a thicker desiccant coating layer,
- the dehumidification performance of the polymer scroll and the 10- and 20PPI foam tubes were compared to cases without water-cooling, and

- the performance of the recoated 10PPI foam tube was additionally tested at an alternate inlet condition of $T_{p,in} = 27 \pm 3$ °C, $Y_{p,in} = 14 \pm 2$ g/kg.

An overview of the tests performed on each insert is given in table 9.1.

Table 9.1: Inlet conditions of heat and mass transfer tests

Insert	$T_{p,in}$ °C	$Y_{p,in}$ g/kg	Cycle time min	BC*	Air flow rate l/min
Al. brush coating I	35	19	5, 10	dT	20, 15, 10
Polymer scroll	35	19	5, 10, 20	dT,dq	20, 15, 10
05PPI foam coating I	35	19	5, 10, 20	dT	15, 10
10PPI foam coating I	35	19	5, 10, 20	dT,dq	20, 15, 10
20PPI foam coating I	35	19	5, 10, 20	dT,dq	20, 15, 10
Alum. Brush coating II	35	19	5, 10, 20	dT	20, 10
05PPI foam coating II	35	19	5, 10, 20	dT	20
10PPI foam coating II	35	19	5, 10, 20	dT	20, 15, 10
(10PPI foam coating II)	27	14	5, 10	dT	20, 10

*Boundary conditions: dT - water cooling, dq - adiabatic

9.3 Description of typical experimental profiles

In order to illustrate the transient system behaviour and describe the signal processing routines employed for the data analysis, typical profiles of direct measurements and derived quantities will be presented in the following for selected cases.

9.3.1 Profiles of directly measured quantities

The adiabatic test of the heat and mass transfer performance of the polymer scroll tube insert at a nominal flow rate of 10 l/min and a cycle time of 20 min is taken as a base case for the following presentation of the cyclic test data, where the characteristic trends are clearly visible. It should be noted, however, that not all the measurements produced results as consistent as the base case presented here. Especially at cases with a high flow rate of 20 l/min and active water-cooling the experimentally determined data is compromised by a number of factors, as will be discussed later.

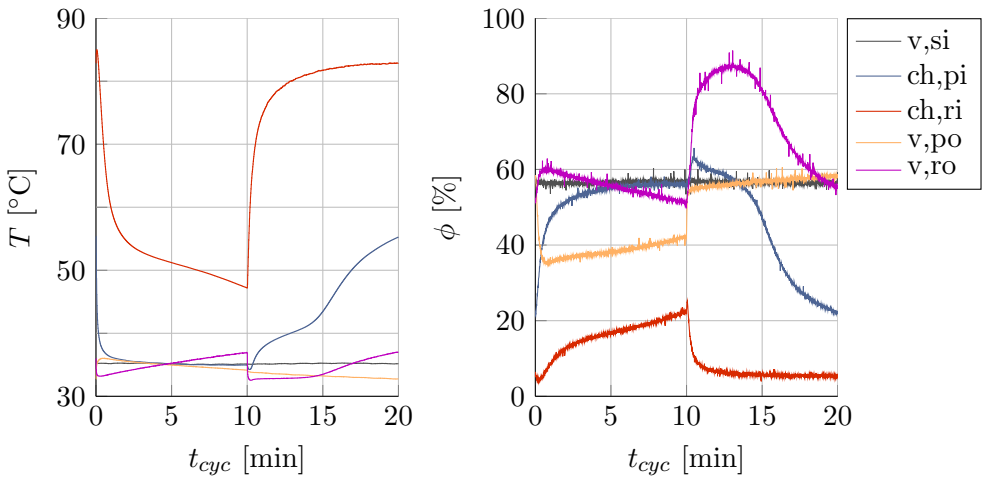

Figure 9.6: Sensor profiles of adiabatic polymer test

The profiles of thermocouple and relative humidity sensor readings for the base case are plotted in figure 9.6. The first 10 min in the plot refer to the adsorption, while the latter correspond to the desorption half-cycle. This half-cycle order will be maintained for all the time-dependent plots in the following. The curve colours correspond to the colour coded measurement locations in schematics 9.2 and 9.5.

From the plot on the left hand side of figure 9.6 it can be seen, that the grey denoted supply inlet temperature measured upstream of the process inlet valve stays at a constant level for both half-cycles.

During the adsorption half-cycle, the blue curve corresponds to the process inlet air. After having been exposed to the regeneration outlet air in the previous half-cycle, the temperature sensor reading decreases from the regeneration outlet temperature level to the constant level of the supply inlet air feeding the process. The amount of time it takes for the inlet air to reach a constant level is a measure of the thermal mass of the inlet channel. It can be seen, that despite the efforts made to minimise the thermal mass of the system by reducing path lengths and insulation volume, the thermal inertia is still noticeable and it takes about 2.5min for the inlet air to equilibriate.

The temperature of the air leaving the test object during the adsorption half-cycle is shown in red in the plot. It can be seen, that without water-cooling, the generated heat of adsorption and the thermal mass of the insert lead to a gradual decrease in temperature that reaches a level approximately 12°C above the inlet temperature level at the end of the 10min half-cycle. During the second half-cycle the roles of the channel sensors are reversed, i.e. the red curve now corresponds to

the inlet air stream, while the blue slope represents the regeneration outlet air. A thermal mass effect similar to the one observed for the adsorption inlet air can be noted during the regeneration half-cycle, where the red line gradually approaches a steady regeneration inlet temperature level at approximately 85°C.

It is apparent, that the amplitude of temperature fluctuations the sensor at the channel regeneration inlet position is exposed to is significantly larger than at the channel process inlet position. At the same time, the sorptive heat dissipated to and from the fluid affects the shape of the outlet temperature read by the blue sensor during the second half-cycle more profoundly than during the first half-cycle, where the outlet air is measured by the red sensor.

The yellow and purple curves correspond to the valve process and regeneration outlet measurements. A comparison of yellow to the red coloured curve during the adsorption half-cycle and the the purple to the blue line during the desorption phase shows, that the switch valves do indeed act as effective thermal buffers greatly reducing the temperature fluctuations of the respective outlet sensors.

The plot on the right hand side of figure 9.6 shows that the relative humidity readings are noisier than the thermocouple readings, but exhibit clear trends. Due to the different temperature levels corresponding to the relative humidity levels, little information about the dehumidification performance of the system can be derived from those measurements directly. It is, however, worth noting the different regimes the sensors operate in, although at times corresponding to the same absolute humidity level. The channel regeneration inlet sensor operates in the lowest relative humidity regime between 5 and 20% RH, while the channel process inlet sensor, valve supply inlet sensor, and valve process outlet sensor operate at an intermediate relative humidity level between 20 and 60% RH. The valve outlet sensor operates at the highest relative humidity level during the measuring the second half-cycle, where it is exposed to the same air stream as the sensor denoted in blue in the plot, but at a significantly lower temperature level. The variation in the channel process inlet sensor signal of $\Delta RH \approx 40\%$ is approximately twice as high as that of the other sensors.

Similar to the temperature sensors, the purple and curves correspond to the measurements of the bypass outlet air during adsorption and desorption half-cycle, respectively.

9.3.2 Profiles of calculated quantities

The relative humidity measurements can be converted into absolute humidity values with help of the the temperature measurements using equation 9.1. However, the

use of the raw measurement data for the calculation was problematic because of three reasons:

- The capacitance of the polymer used for the relative humidity sensors is not only a function of relative humidity, but also of the temperature itself. As a result the discrepancy between measured and actual relative humidity levels changes with temperature.
- The impact of small fluctuations in temperature and relative humidity values on the calculated absolute humidity level increases with the temperature level because of the exponential rise in saturation pressure. This amplified the noise in the calculated absolute humidity functions especially during the regeneration half-cycle.
- The reaction time of the thermocouples to a change in conditions is much faster than that of the relative humidity sensors. Since the flow switching involved a step change in both temperature and humidity level for the respective inlet sensor, the absolute humidity levels calculated during these sharp changes were either over- or undervalued.

In order to address these issues, routines for signal processing have been developed in MATLAB that were applied to the relative humidity signals and will be discussed in the following.

Temperature drift compensation

The drift of the humidity sensor with temperature is accounted for by an approximative formula provided by the sensor manufacturer:

$$\phi_{\text{corr}} = \frac{\phi_{\text{raw}}}{1.054 - 0.00216 \cdot T} \tag{9.2}$$

where T is the sensor temperature in degrees Celsius.

Running average filtering

Figure 9.7 shows the temperature corrected relative humidity signals on the left hand side and calculated absolute humidity signals for the two channel sensors and the valve supply inlet sensor on the right hand side as light grey, blue, and red coloured lines. It can be seen from comparing the two plots, that the limited amount of noise in the relative humidity signal is amplified when converted to an absolute humidity signal at high temperature levels. In order to reduce the amplitude of the variations,

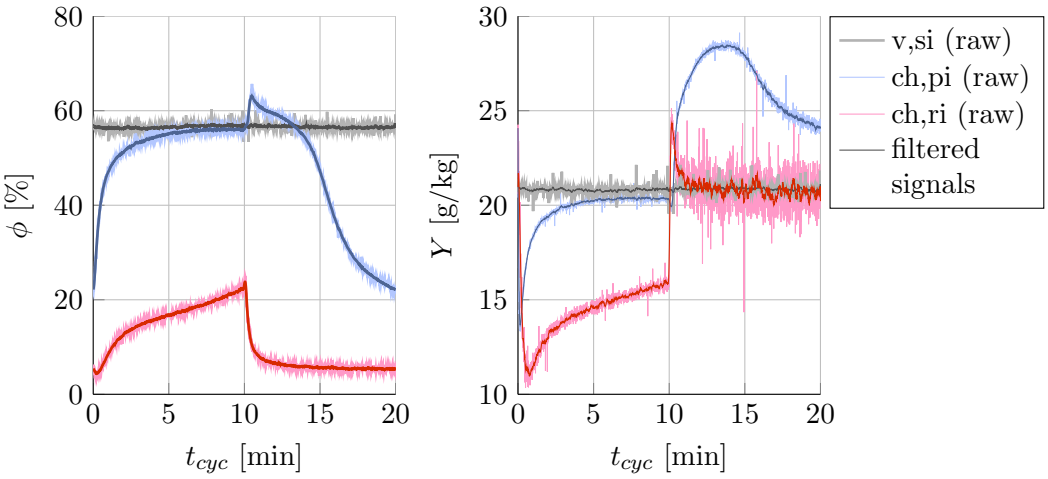

Figure 9.7: Running average filter application to experimental data

a running average filter with a constant window size of 15 samples was applied to the data.

$$\phi_i^* = \frac{1}{15} \cdot \sum_{k=i-7}^{i+7} \phi_k \tag{9.3}$$

The time equivalent of the window size is 7.5 seconds and was found to limit the signal scattering to an acceptable level, while not obscuring the fast transients in the signal significantly. The filtered ϕ^*-signals are plotted in figure 9.7 as darker shaded solid lines.

Response time correction

During the adsorption half-cycle the sensor at the blue coloured channel process inlet location measures the constant channel inlet condition and the sensor corresponding to the red coloured line is measuring the air at the outlet of the test section. From the absolute humidity slopes depicted in the right hand plot in figure 9.7 the moisture removal from the process air during the adsorption process is clearly visible from the discrepancy between the two curves. While this overall trend conforms with the expected behaviour, the apparent sharp decrease in moisture content at the channel inlet immediately after the switch at $t_{cyc} = 0$min is a curiosity, since a genuine step change to the constant inlet absolute humidity level was to be expected here. A similar situation can be observed after the switch to the regeneration half-cycle at $t_{cyc} = 10$min: While the blue line, now representing the channel outlet air, shows the expected shape, the red line should exhibit a step change from the previous adsorption cycle outlet absolute humidity level to the constant regeneration inlet level.

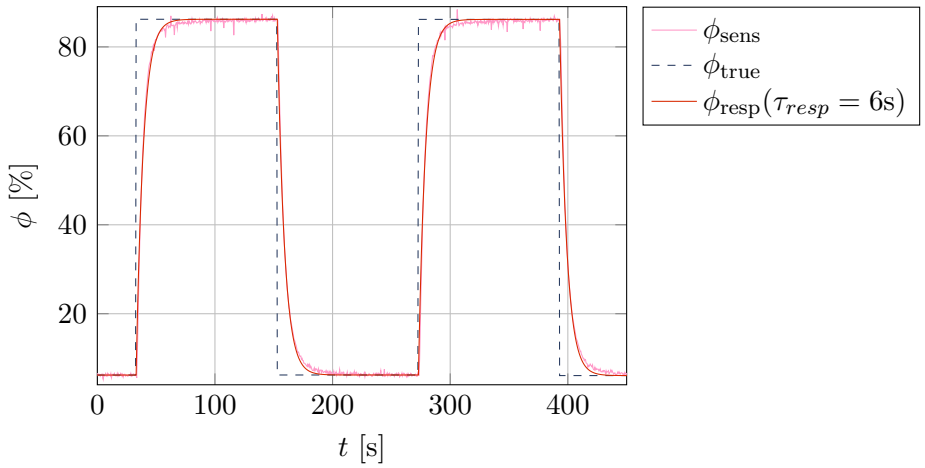

Figure 9.8: response time tests for relative humidity sensors

These positive and negative overshoots during the sudden changes in conditions are due to the slower response of the relative humidity sensors in comparison to the thermocouples.

In order to quantify the transient behaviour of the relative humidity sensors, they were alternately exposed to a hot and a dry air stream in a preliminary test depicted in figure 9.8. It was found that the sensor behaviour could be approximated by a first order response function:

$$f(t) = \Delta f_0 \cdot \left(1 - e^{-t/\tau_{resp}}\right) = (f(1) - f(0)) \cdot \left(1 - e^{-t/\tau_{resp}}\right) \tag{9.4}$$

A decent fit to the sensor function for flow rates ranging from 5-45 l/min was obtained with a time constant of $\tau_{resp} = 6\text{s}$, which is one second higher than the typical value quoted by the manufacturer. In order to be able to approximate the original signal from the sensor signals, the true signal is interpreted as a series of consecutive step changes occurring every Δt seconds. The sensor response signal to this function is then a superposition of the response functions of the individual step changes, given as:

$$\overrightarrow{\phi}_{\text{resp}}(t) = \phi_a(0) + \begin{pmatrix} 1 - e^{-0\cdot\Delta t/\tau_{resp}} & 0 & 0 \\ 1 - e^{-1\cdot\Delta t/\tau_{resp}} & 1 - e^{-0\cdot\Delta t/\tau_{resp}} & 0 \\ 1 - e^{-2\cdot\Delta t/\tau_{resp}} & 1 - e^{-1\cdot\Delta t/\tau_{resp}} & \ddots \\ \vdots & \ddots & \ddots \end{pmatrix} \cdot \begin{pmatrix} \phi_a(1) - \phi_a(0) \\ \phi_a(2) - \phi_a(1) \\ \phi_a(3) - \phi_a(2) \\ \vdots \end{pmatrix} \tag{9.5}$$

With the response signal $\phi_{\text{resp}} = \phi_{\text{sens}}$ and the time constant $\tau_{resp} = 6\text{s}$ known, the

original signal can be found by solving equation system 9.5. A comparison of the response time corrected signals and the filtered sensor signals is given in figure 9.9 for the two channel sensors.

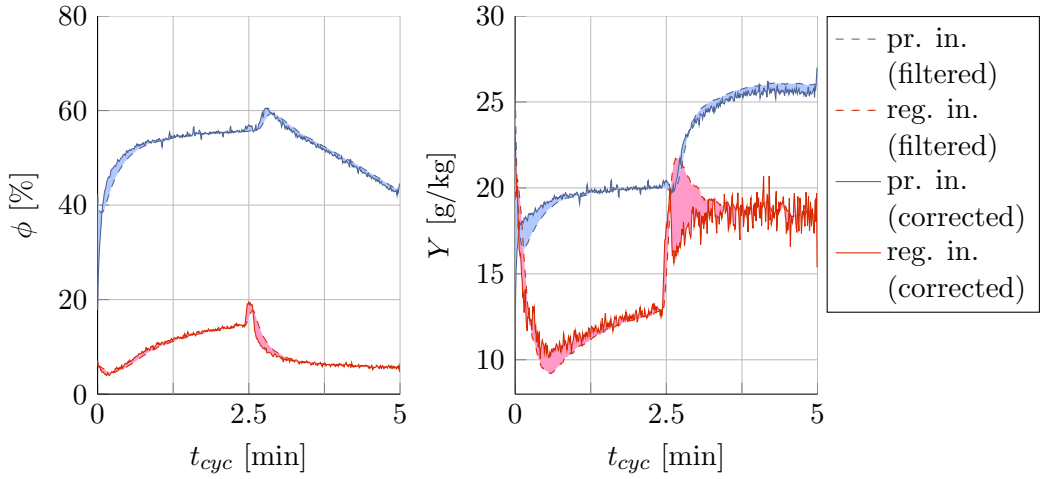

Figure 9.9: Effects of response time correction

In order to make the effects more clearly visible, the tests with a cycle length of 5min were utilised as the basis for this plot. As can be seen from the shaded areas between the plots, the response time correction has a noticeable impact on the shape of the calculated absolute humidity curves and helps to reduce the amplitude of the artificial peaks significantly.

The drawback of the utilisation of the above-mentioned response time routine is that the noise in the original signal is amplified dramatically. Considering that the amount of scatter could be reduced effectively by the running average filtering and the general increase in physical soundness of the calculated absolute humidity values, it was considered appropriate to utilise the response time correction routine for the further analysis of the data.

A comparison of the filtered response time corrected absolute humidity profiles used as the basis for the following analysis is depicted in figure 9.10. It can be seen, that during the first half-cycle the blue coloured channel process inlet and purple coloured valve regeneration outlet sensor readings approach the constant grey valve supply inlet level. It can be taken as a sign of consistency of measurement that the absolute humidity levels calculated at the two measurement locations upstream of the test section agree with the readings at the regeneration bypass channel outlet. The agreement between the blue and purple line remains satisfactory during the second half-cycle as well, where both measure the regeneration outlet air. Similar to

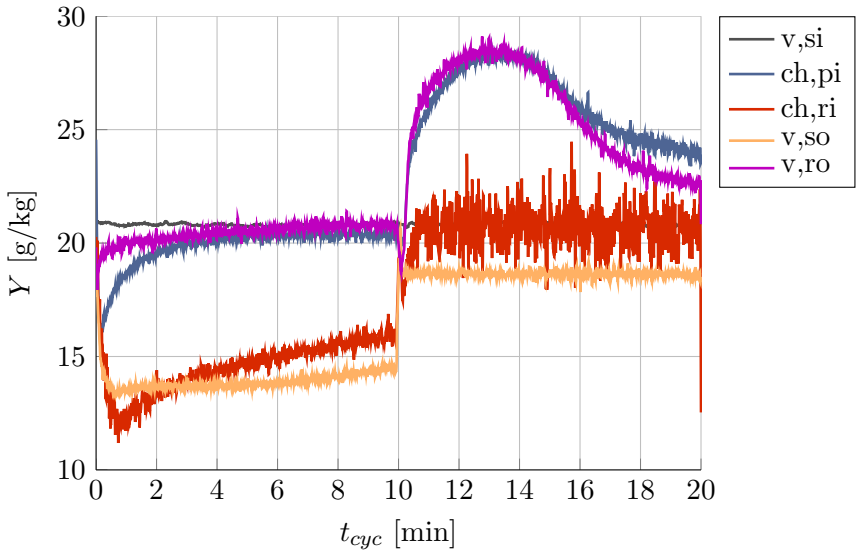

Figure 9.10: Comparison of calculated absolute humidity levels at different channel positions

those of the process side sensors, the calculated absolute humidity levels based on the measurements at the red channel regeneration inlet and yellow valve process outlet positions should coincide with the constant valve supply inlet level. It can be seen, that the channel measurement is in better agreement with the valve supply inlet levels than the valve process outlet measurements despite the dramatically different temperature levels and the fact the yellow and grey sensors are directly connected by the process air bypass channel. This discrepancy is most likely a result of the inaccuracy of the relative humidity sensors and is entirely explainable by the sensor error. The possibility that the discrepancy is due to condensation could be ruled out, because the heated process air bypass channel was made of transparent PVC hosing and the formation of condensate would have likely been visible.

During the adsorption half-cycle, where the red and yellow sensors measure the process outlet air conditions their levels are in approximate agreement while the red sensor measurements show a stronger variation with time.

Furthermore, it is interesting to note that the response time correction helped to almost completely remove the positive overshoot during the switch to the desorption half-cycle, while the negative peak in the adsorption inlet air measurement is still noticeable. This is likely due to the bigger difference between the initial and steady state relative humidity level at this measurement location increasing the impact of the discrepancy between first order response model and the true sensor signal.

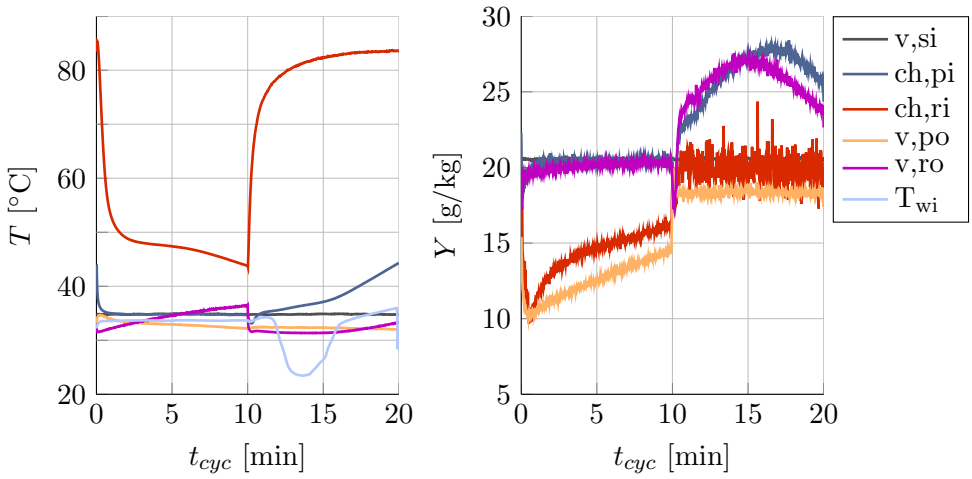

Figure 9.11: Polymer scroll measurement profiles with water-cooling

9.3.3 Effect of water-cooling on experimental profiles

The temperature and absolute humidity profiles of the same test with activated water-cooling are presented in figure 9.11. In contrast to the temperature plot of the adiabatic test, the cooling water inlet temperature is plotted here as well as a light blue line. It can be seen, that the temperature of the channel outlet air decreases more rapidly during the adsorption process due to the water-cooling. The difference between channel outlet air and cooling water inlet air is approximately 10 °C after 10min and is testimony to the poor thermal conductivity of the polymer scroll insert that fails to transport heat effectively from the channel core to the water-cooled wall. The benefit of water-cooling during the adsorption process, however, is still noticeable in the lower absolute humidity level at the channel outlet.

During regeneration the cooling-water is purged out of the water jacket using by a stream of compressed air. In this half-cycle the water inlet temperature sensor is exposed to the compressed air exiting the water jacket. It can be seen that the temperature fluctuates heavily, reaching its minimum after approximately 3-4 minutes at a level below that of the inlet cooling water. This is most likely due to residual water droplets cooling down the system while evaporating into the dry purge air stream. The necessity of using a continuous stream of dry air to keep the cooling water from entering the water jacket is a weakness of the experimental design, that could not be overcome due to the lack of an additional flow valve. The convective and evaporative cooling of the channel walls during the desorption-half cycle in the test rig has a detrimental effect on the system performance that is likely to be less severe in the actual desiccant wheel prototype, where no air flow is present and the

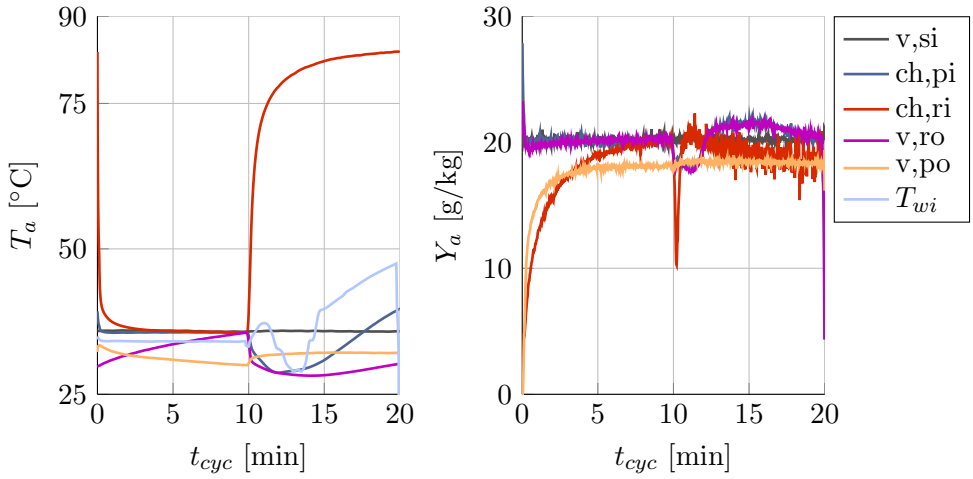

Figure 9.12: 10PPI foam measurement profiles with water-cooling

outer channel walls can be treated to minimise the retainment of water droplets on the tube surface after exiting the bath. The poor thermal conductivity of the polymer insert can be seen as a benefit in this case, because it reduces the amount of regeneration heat that is lost to the environment. It can be seen from figure 9.11, that the switch to regeneration flow still leads to an instantaneous, however dampened increase in channel regeneration outlet temperature denoted in blue in the plot.

The channel wall temperature has a much stronger effect on the system performance, when a highly conductive insert is used. This can be seen from comparing the results of the water-cooled polymer tests to those of the thickly coated 10PPI foam depicted in figure 9.12. Here it can be seen, that the channel outlet temperature is almost instantaneously cooled down to the cooling water temperature in the dehumidification stage, which by itself should lead to a significant improvement in dehumidification. When observing the outlet air temperature profiles in the regeneration stage, however, it can be seen that this benefit is derogated significantly by the unwanted heat removal during the regeneration process in the experiments that causes the temperature level to drop below that of the cooling water and process inlet air during the first half-cycle.

Observing the absolute humidity profiles, it seems that due to the amplitude of the sharp rises and drops in temperature at the channel regeneration inlet location, the overshoot in calculated absolute humidity level is dampened, but not completely removed by the response time correction. At the same time, the negative overshoot observed in the adiabatic polymer tests at the beginning of the adsorption half-

cycle at the channel process inlet location is not visible anymore, now that the temperature spread has decreased.

The calculated absolute humidity levels at the locations measuring the outlet air in the regeneration half-cycle drop by approximately 2 g/kg during the first 3 minutes of the regeneration cycle before starting to rise in the expected way. This indicates, that the desiccant material is removing moisture from the regeneration air stream during the first part of the half-cycle due to the reduced system temperature levels, which signifies a drastic performance impairment. As a consequence, the time of active adsorption during the dehumidification phase exhibited by the yellow line is significantly shortened, if one ignores the constant level offset due to sensor the inaccuracy. While the outlet humidity measurements at the channel and valve positions are in good agreement during the regeneration half-cycle, the red line corresponding to the channel outlet condition during the adsorption phase is not congruent with the measurement downstream of the switch valve denoted in yellow. It is likely that this is again explainable by the sub-optimal synchronisation of temperature and relative humidity measurement despite the response time correction, whose effect is amplified at this measurement location by the big amplitude of the corresponding temperature transient. The dehumidification profile exhibited by the yellow curve is more physically consistent, because the shorter active adsorption phase can be expected to yield a better mass balance.

The comparison of the experimental profiles showed, that while the response time correction routine improves the physical soundness of the derived absolute humidity profiles significantly, the first-order response model is not sophisticated enough to remove all artefacts completely, that stem from the asynchronous temperature and relative humidity measurements. The analysis is furthermore limited by the uncertainty of the relative humidity measurements.

9.4 Analysis of experimental results

As a result of the above-mentioned limitations, the uncertainties in the following analysis are quite significant and mass balance between air moisture pickup and release could often not be obtained.

Since the moisture content of the process air was measured at five locations, its cyclic moisture gain/ release air can be calculated in five different ways:

1. Taking the channel sensors as a reference, the difference in moisture content can be determined by subtracting the absolute humidity level measured at the

respective outlet of the test channel from the level at the respective inlet:

$$\Delta Y_{ads} = Y_{\mathrm{ch,pi}} - Y_{\mathrm{ch,ri}},\ \Delta Y_{des} = Y_{\mathrm{ch,ri}} - Y_{\mathrm{ch,pi}} \tag{9.6}$$

2. One alternative is to take the constant valve supply inlet absolute humidity level as a reference for the inlet air stream. This has the advantage that response time related artefacts are reduced.

$$\Delta Y_{ads} = Y_{\mathrm{v,si}} - Y_{\mathrm{ch,ri}},\ \Delta Y_{des} = Y_{\mathrm{v,si}} - Y_{\mathrm{ch,pi}} \tag{9.7}$$

3. Another alternative is the utilisation of the humidity measurements up- and downstream of the switch valves. This has the advantage, that the sensors were less subject to thermal gradients.

$$\Delta Y_{ads} = Y_{\mathrm{v,si}} - Y_{\mathrm{v,po}},\ \Delta Y_{des} = Y_{\mathrm{v,si}} - Y_{\mathrm{v,ro}} \tag{9.8}$$

4. The drawback of the approaches above is that the calculation of the half-cycle specific differences in moisture content is based on two sensors. Any accuracy induced offsets are then carried into the calculated humidity difference. A good example of this problematic can be seen in figures 9.10-9.12 when comparing the yellow sensor line to the gray line. During the regeneration half-cycle both sensor signals should be on top of one another and their discrepancy can be explained purely by the sensor inaccuracies. Since each sensor except for that at the valve supply inlet location is alternately exposed to the outlet air stream of one half-cycle and the inlet air stream of the other, an equivalent to shifting the curves vertically to the same level is to reference each sensor reading to its own measurement of the inlet air condition of the previous cycle. For the channel sensors this yields:

$$\Delta Y_{ads} = Y_{\mathrm{ch,pi}}(\mathrm{ads}) - \mathrm{Y_{ch,pi}(des)},\ \mathrm{\Delta Y_{des} = Y_{ch,ri}(des) - Y_{ch,ri}(ads)} \tag{9.9}$$

5. The same train of thought can be applied to the sensors located downstream of the outlet switch valves. The signals are always referenced to the inlet air condition reading at the end of the previous half-cycle, where the humidity levels have stabilised.

$$\Delta Y_{ads} = Y_{\mathrm{v,po}}(\mathrm{des}) - \mathrm{Y_{v,po}(ads)},\ \mathrm{\Delta Y_{des} = Y_{v,ro}(ads) - Y_{v,ro}(des)} \tag{9.10}$$

It was found that equation 9.10 resulted in the clearest trends and lead to the smallest deviations in the mass balance. From the difference in moisture content the total amount of moisture transferred per half-cycle could be determined by integrating the time-dependent moisture uptake and removal rates:

$$\Delta m_{ads} = \int_0^{t_{ads}} \rho_a \cdot \dot{V}_p \cdot \Delta Y_{ads}\, dt \tag{9.11}$$

$$\Delta m_{des} = \int_{t_{ads}}^{t_{des}} \rho_a \cdot \dot{V}_r \cdot \Delta Y_{des}\, dt \tag{9.12}$$

In steady-state operation the cyclic moisture uptake and release should sum up to zero $\Delta m_{ads} + \Delta m_{des} = 0$. The experimental results are presented in terms of flow rate dependent moisture uptake and release functions in figure 9.13 together with the sum of the two terms. Here, the double-coated inserts are demarked by a "2" in the name and the tests at the alternate inlet condition are distinguished by empty symbols.

As a general trend, the experimental results show that the amount of moisture transferred per half-cycle increases with flow rate and cycle length. A general increase in moisture pickup and release when the water-cooling is active can also be noted, although the sensitivity of the objects to the change in boundary condition becomes greater with increasing flow rate and cycle time.

The polymer insert gives the best performance by far in both the adiabatic and water-cooled tests. The main reason for the poor performance of the conductive inserts during the water-cooled tests is their high sensitivity to the unwanted heat loss during the regeneration stage. This reduces the ability of the system to regenerate the desiccant material effectively and consequently limits the amount of moisture that can be adsorbed in the following half-cycle. While the highly conductive inserts are strongly affected by this, the poor thermal conductivity of the

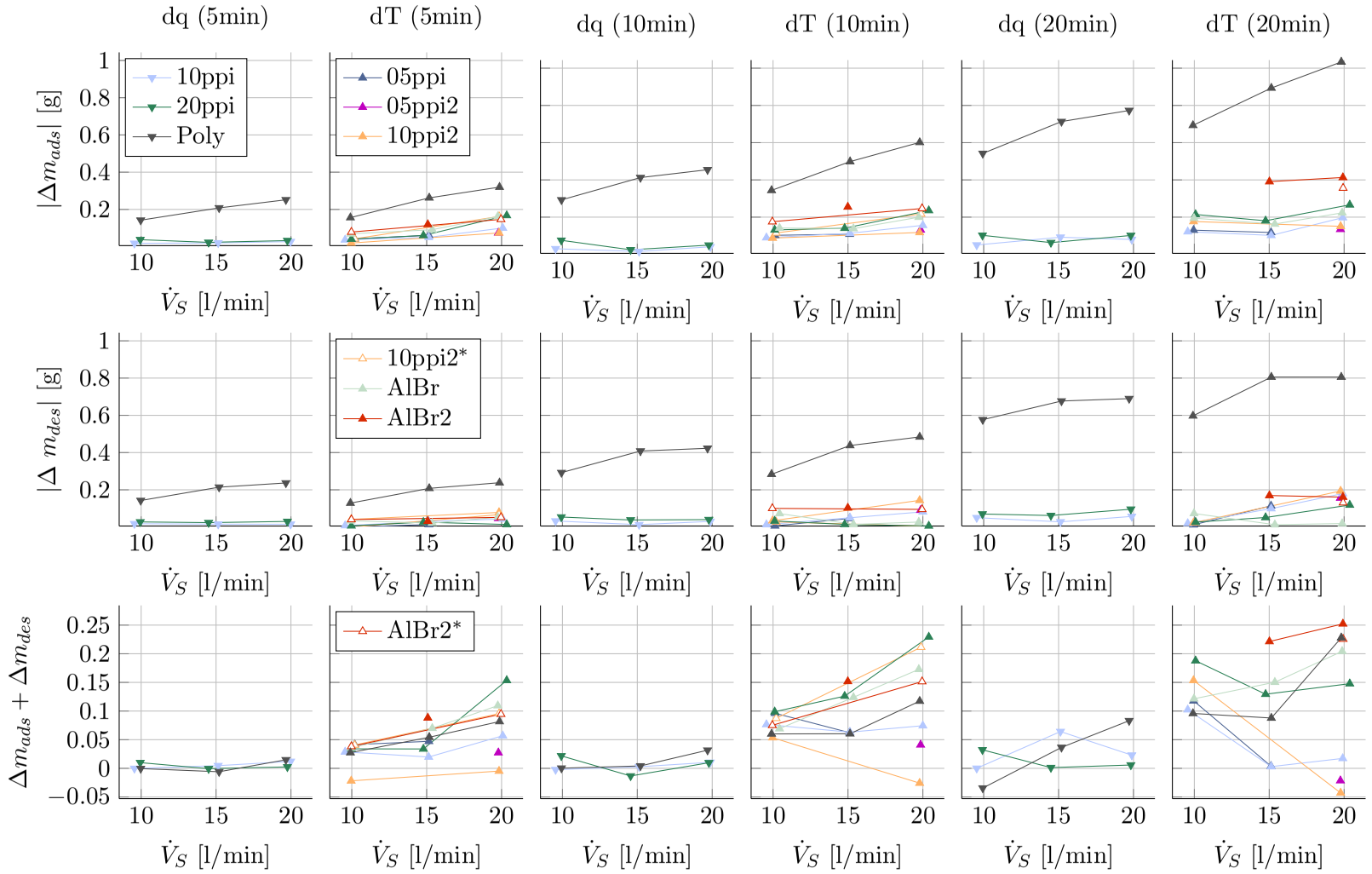

Figure 9.13: Comparison of insert moisture uptake and release values

polymer scroll makes it less sensitive to the channel boundary condition. The metal foam tubes and wire-brush inserts could be expected to perform worse than the polymer scroll without water-cooling because the increased heat carry over between the cycles due to their higher thermal mass is detrimental to the system's efficiency while their high thermal conductivity is no benefit in the adiabatic case.

The experimental results also suggest that the performance of the inserts with only one coating was also limited by the amount of desiccant material in the channel. By comparing the light green to the dark red data points, it can be seen that the moisture pickup of the aluminium brush is greatly increased by a thicker coating layer. This effect most likely obscured in the case of the 10PPI foam, because it is affected by the unwanted heat loss during the regeneration half-cycle more strongly that the brush insert. This can be explained by its superior thermal transport performance that was observed during the heat transfer experiments.

As can be seen from the lower row of plots, the uncertainties of measurements are quite substantial with a maximal discrepancy between calculated moisture pickup and release values of 0.25g. While this puts the meaningfulness of the experimentally determined values into question in a quantitative sense, the deduced trends retain their validity when observing the regeneration half-cycle shown in the second row of plots in the figure and the performance can at least be assessed in a qualitative sense.

A more detailed insight into the driving performance parameters is obtained from the numerical study of the heat and mass transfer processes inside the channel which will be the focus of the following chapter.

Chapter 10

Numerical investigation of transient heat and mass transfer performance of selected test objects

In order to model the heat and mass transfer processes inside the test tubes, the porous medium model utilised in sections 6 and 8 was adapted to incorporate transient formulations of the governing equations for heat and mass transfer. The transport of adsorbate into the thickness of the coating layer was described using an equation system consisting of five distinct dependent variables, that correspond to different positions within the coating layer. This way, the diffusive transport resistance could be accounted for while maintaining the 2D axis-symmetric formulation of the problem.

In the following the model setup will be described before the modelling results will be discussed.

10.1 Model Setup

In the experimental rig, the test piece is alternately subjected to one of two continuous air streams. This is reflected in the model by a stationary, i.e. time-independent formulation of the flow field equations that are solved in a preliminary study step for the two air streams. The resulting velocity vectors could then be applied as field variables to the transient heat and mass transfer equations. In comparison to a fully coupled time-dependent problem formulation, this approach resulted in a significant

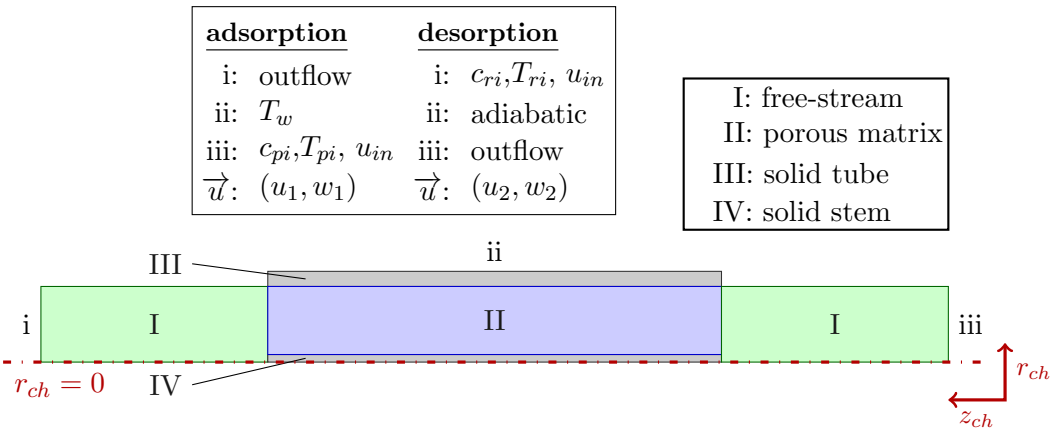

Figure 10.1: Schematic of the modelling domains for the transient heat and mass transfer analysis

reduction in complexity and computational time. The effect of this simplification on the modelling results can be expected to be minor because the interdependencies between the flow field and temperature and concentration fields could be expected to be negligible due to the comparatively narrow ranges of pressure and temperature fluctuations that only have a minor effect on the density and viscosity of the working fluid.

Similar to the stationary heat transfer model, the current model builds upon the two-dimensional axis-symmetric porous medium flow model described in chapter 6, whose modelling domains are depicted in figures 6.16 and 6.22 for the respective inserts. A schematic of the model and its boundary conditions is depicted in figure 10.1.

10.1.1 Mathematical problem formulation

It was pointed out by Goldsworthy and White [2012] that solid side resistance to the mass transfer into the thickness of a desiccant layer of similar properties as the one under investigation here is several orders of magnitude higher than that to the heat transfer. A Biot number comparison reveals that for desiccant layer of conventional thicknesses a discrete modelling approach can be expected to yield more precise results than a lumped capacitance approach [Goldsworthy and White, 2011; Bongs et al., 2013]. Consequently the numerous recent sophisticated desiccant wheel models comprise domains for the spacial discretisation of the coating layer. The resulting equation system is made up of equation sets describing the fluid and solid side heat and mass transport, that will be described in the following. Material

properties were assumed to be constant and are summarised in section B.

Momentum transfer

The flow fields of process (1) and regeneration (2) air are governed by the same set of equations, consisting of equations 2.43-2.45 and 2.62 familiar from chapter 6 and differ only in the location of the in- and outlet flow boundary, as can be seen from schematic 10.1.

Air-side heat transfer

As was already discussed for the stationary case in chapter 8, the model for the air-side heat transfer consists of three domains, one each for the in- and outlet channels, respectively, and one for the test section were the porous matrix is present. The governing equation for the transient heat transfer in the empty channels can be written as:

$$\rho_a \cdot c_{p,a} \cdot \left(\frac{\partial T_a}{\partial t} + u \cdot \nabla T_a \right) = \nabla \cdot (k_a \cdot \nabla T_a) \tag{10.1}$$

The air-side heat transfer inside the test tube can be described as:

$$\epsilon \cdot \rho_a \cdot c_{p,a} \cdot \left(\frac{\partial T_a}{\partial t} + u \cdot \nabla T_a \right) = \nabla \cdot (\epsilon \cdot k_a \cdot \nabla T_a) + \dot{q}_s^* \tag{10.2}$$

where $\dot{q}_s^*$ is the volume specific heat the air picks up from the solid material inside the channel:

$$\dot{q}_s^* = a_s \cdot h_h \cdot (T_s - T_a) \tag{10.3}$$

Air-side mass transfer

The equation governing the air-side mass transfer process is the exact mass transfer equivalent to the air-side heat transfer equation 10.1. In order to conform with COMSOL's standard notation, the mass transfer equations are implemented as units of molar concentrations. The molar concentration is related to the absolute humidity by

$$Y_a = \rho_a \cdot \frac{C_a}{M_a} \tag{10.4}$$

Since ρ_a and M_a are treated as constants in the analysis, this yields the governing equation for mass transfer:

$$\frac{\partial Y_a}{\partial t} + u \cdot \nabla Y_a = \nabla \cdot (D_v \cdot \nabla Y_a) \tag{10.5}$$

$$\Leftrightarrow \frac{\partial C}{\partial t} + u \cdot \nabla C = \nabla \cdot (D_v \cdot \nabla C) \tag{10.6}$$

Similar to the heat transfer case, equations 10.6-10.5 have to be corrected for the volume occupied by the solid matrix inside the test tube domain, so that

$$\epsilon \cdot \frac{\partial Y_a}{\partial t} + u \cdot \nabla Y_a = \nabla \cdot (\epsilon \cdot D_v \cdot \nabla Y_a) + a_s \cdot \frac{h_m}{\rho_a} \cdot (Y_s - Y_a) \tag{10.7}$$

$$\Leftrightarrow \epsilon \cdot \frac{\partial C}{\partial t} + u \cdot \nabla C = \nabla \cdot (\epsilon \cdot D_v \cdot \nabla C) + a_s \cdot \frac{h_m}{M_w} \cdot (C_s - C_a) \tag{10.8}$$

Here Y_s denotes the moisture content of the air at the interface between fluid and solid where it is in thermodynamic equilibrium with the desiccant material.

Solid-side heat transfer

The solid-side model consists of a domain for the diffusive heat transfer through the solid tube wall (III), a domain for the heat transfer through the solid matrix (II) inside the test tube that interacts with the air, and if applicable a domain for the heat transfer through the solid stem wire (IV). A thin thermally resistive layer is added to the interfacial boundary of the porous matrix with the confining tube wall in order to capture the effect of an imperfect thermal contact between insert and tube wall in a volume-averaged sense.

The governing equation for the diffusive heat transfer through the solid tube wall and stem wire can be written as

$$\rho_s \cdot c_{p,s} \cdot \frac{\partial T_s}{\partial t} = \nabla \cdot (k_s \cdot \nabla T_s) \tag{10.9}$$

with ρ_s, $C_{p,s}$, and k_s taking on values of the respective materials.

The governing equation for the porous matrix is similar, but with added terms for the packing density, convective transfer with the working fluid and generated heat of adsorption:

$$\rho_{rel} \cdot (\rho_{lig} \cdot c_{p,lig} + \rho_{\mathrm{Si}} \cdot c_{p,tot}) \cdot \frac{\partial T_s}{\partial t} = \nabla \cdot (\rho_{rel} \cdot k_{mat} \cdot \nabla T_s) + \dot{q}_a^* + \dot{q}_{ads}^* \tag{10.10}$$

Here $c_{p,tot}$ represents the specific heat capacity of the loaded desiccant coating. It

is given by [Zhang and Niu, 2002]:

$$c_{p,tot} = c_{p,\mathrm{Si}} + W \cdot c_{p,w} \tag{10.11}$$

The thermal conductivity of the porous matrix is defined analogously to equations in the heat transfer case, where the directional thermal conductivity terms are equal to the weighted averages of ligament and coating values:

$$k_{foam} = \begin{pmatrix} \zeta \cdot k_1 & 0 \\ 0 & \zeta \cdot k_1 \end{pmatrix} \tag{10.12}$$

$$k_{Br} = \begin{pmatrix} k_{1,2} & 0 \\ 0 & 0 \end{pmatrix} \tag{10.13}$$

with

$$k_1 = (f_c \cdot k_{\mathrm{Si}} + (1 - f_c) \cdot k_{\mathrm{Al}}) \tag{10.14}$$

$$k_2 = (f_c \cdot k_{\mathrm{Si}} + (1 - f_c) \cdot k_{\mathrm{Cu}}) \tag{10.15}$$

Here, f_c is the ratio of the cross-sectional area of the coating layer and the total cross-sectional area of the ligament

$$f_c = \frac{A_c}{A} = \frac{A_c}{A_c + A_{lig}} \tag{10.16}$$

The volume specific convective heat flow $\dot{Q}_a$ from the interaction with the working fluid is given by:

$$\dot{q}_a^* = -\dot{q}_s^* = a_s \cdot h_h \cdot (T_a - T_s) \tag{10.17}$$

Similarly, the generated heat of adsorption is dependent on the amount of moisture transferred:

$$\dot{q}_{ads}^* = a_s \cdot h_m \cdot q_{ads} \cdot (Y_a - Y_s) \tag{10.18}$$

Solid-side mass transfer

In order to realise a spacial discretisation of the desiccant coating in the model at hand without leaving the two-dimensional formulation of the problem, the moisture transport through the desiccant material is expressed by a set of four dedicated equations, that comprise terms to describe the storage and diffusive transport of moisture inside a section of the coating and terms for the transfer of moisture between two adjacent sections.

In order to derive the formulation of the equation system in porous medium terms, first consider schematic 10.2 that depicts the approximately cylindrical cross

section of the solid ligaments with a desiccant coating layer divided into four sections of equal thickness Δr^*. In order to distinguish between the radial dimensions referring to the ligament from those referring to the channel, the former are denoted with a star.

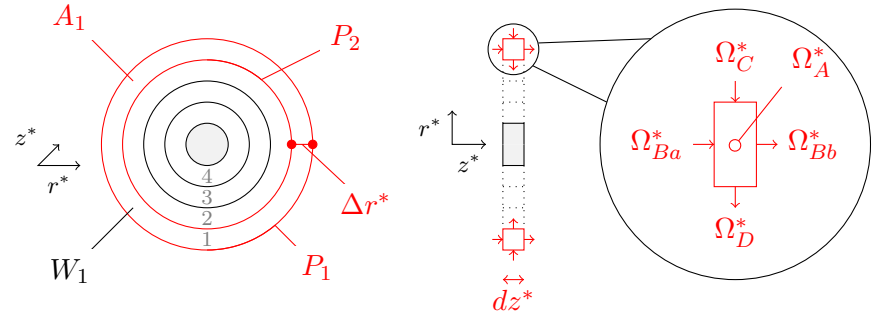

Figure 10.2: Discretisation of desiccant coating layer

The cross-sectional areas and perimeters of the respective sections are labelled A_i and P_i. The moisture content of each section is denoted by W_i.

Considering a piece of the outer layer of infinitesimally small depth dz^*, it can be seen from the side view on the right hand side of the schematic, that moisture is transferred in and out of the control volume by an axial (Ω^*_{Ba} and Ω^*_{Bb}) and a radial flux pair (Ω^*_C and Ω^*_D). The mass balance can be written as:

$$\begin{aligned}(A_1 \cdot \partial z^*) \cdot f_a \cdot \rho_{Si} \cdot \frac{\partial W_1}{\partial t} = {} & A_1 \cdot \rho_{Si} \cdot D_S \cdot \frac{\Delta W_{1,I}}{\partial z^*} - A_1 \cdot \rho_{Si} \cdot D_S \cdot \frac{\Delta W_{1,II}}{\partial z^*} \\ & + P_1 \cdot \partial z^* \cdot h_m \cdot (Y_a - Y_s) \\ & - P_2 \cdot \partial z^* \cdot \frac{\rho_{Si} D_S}{\Delta r^*} \cdot (W_1 - W_2) \end{aligned} \tag{10.19}$$

The term on the left hand side of the equation describes the change in moisture content of the control volume, i.e. what part of the incoming flows are stored in the cell. The first two terms on the right hand side describe the diffusive transfer of adsorbate in the axial direction, i.e. the flows normal to the cross-sectional area A_1. The third term accounts for the convective mass transfer between the working fluid and the outer surface ($P_1 \cdot dz^*$) of the control volume. Similarly, the fourth term describes the radial diffusive mass transfer between the outer layer and the

one beneath it. Introducing the relative variables

$$f_i = \frac{A_i}{A_c} = \frac{\pi \cdot ((r_{lig} + d_{coat} - (i-1) \cdot \Delta r^*)^2 - (r_{lig} + d_{coat} - i \cdot \Delta r^*)^2)}{\pi \cdot (r_{lig} + d_{coat})^2} \tag{10.20}$$

$$g_i = \frac{P_i}{P} = \frac{2 \cdot \pi \cdot (r_{lig} + d_{coat} - (i-1) \cdot \Delta r^*)}{2 \cdot \pi \cdot (r_{lig} + d_{coat})} \tag{10.21}$$

the above equation can be rewritten in compact form as:

$$f_1 \cdot \Omega_A^*(1) = f_1 \cdot (\Omega_{Ba}^*(1) - \Omega_{Bb}^*(1)) + g_1 \cdot \Omega_C^*(1) - g_2 \cdot \Omega_D^*(1) \tag{10.22}$$

with

$$\Omega_A^*(i) = A_c \cdot \partial z^* \cdot f_a \cdot \rho_{Si} \cdot \frac{\partial W_i}{\partial t} \tag{10.23}$$

$$\Omega_{Ba}^*(i) = A_c \cdot \rho_{Si} \cdot D_S \cdot \frac{\Delta W_{I,i}}{\partial z^*} \tag{10.24}$$

$$\Omega_{Bb}^*(i) = A_c \cdot \rho_{Si} \cdot D_S \cdot \frac{\Delta W_{II,i}}{\partial z^*} \tag{10.25}$$

$$\Omega_C^*(1) = P \cdot \partial z^* \cdot h_m \cdot (Y_a - Y_s) \tag{10.26}$$

$$\Omega_D^*(i) = P \cdot \partial z^* \cdot \rho_{Si} D_S \cdot \frac{(W_i - W_{i+1})}{\Delta r^*} \tag{10.27}$$

Equation 10.22 can be easily adapted to describe the mass transfer in the second coating layer section by replacing the convective term Ω_C^* at the outer surface with a diffusive term Ω_D^* which yields:

$$f_2 \cdot \Omega_A^*(2) = f_2 \cdot (\Omega_{Ba}^*(2) - \Omega_{Bb}^*(2)) + g_2 \cdot \Omega_D^*(2) - g_3 \cdot \Omega_D^*(3) \tag{10.28}$$

The equations above merely refer to a single ligament and utilise a coordinate system relative to the ligament dimensions. Since the ligaments conduct heat from the channel wall along their axes to the channel core, the axial dimension z^* respective to the ligament is related to the radial channel dimension r. This is especially obvious in the case of the brush insert where the ligaments are approximately normal to the channel walls and thus $\partial r = \partial z^*$.

For the conversion of equation 10.22 into a porous medium notation respective to the channel dimensions, the solid control volume ($A_c \cdot \partial z^*$) is replaced by the product of the channel control volume and relative density ($2\pi r \cdot \partial z \partial r \cdot \rho_{rel}$). Carrying out the conversion and dividing each term by $2\pi r \cdot \partial r$, equation 10.22

becomes:

$$f_1 \cdot \Omega_A(1) = f_1 \cdot \left(\frac{\Omega_{Ba}(1) - \Omega_{Bb}(1)}{\partial r} \right) + g_1 \cdot \Omega_C(1) - g_2 \cdot \Omega_D(1) \tag{10.29}$$

where

$$\Omega_A(i) = f_a \cdot \rho_{rel} \cdot \rho_{Si} \cdot \frac{\partial W_i}{\partial t} \tag{10.30}$$

$$\Omega^*_{Ba}(i) = \rho_{rel} \cdot \rho_{Si} \cdot D_S \cdot \frac{\Delta W_{I,i}}{\partial z^*} = \rho_{rel} \cdot \rho_{Si} \cdot D_S \cdot \frac{\Delta W_{I,i}}{\partial r} \tag{10.31}$$

$$\Omega^*_{Bb}(i) = \rho_{rel} \cdot \rho_{Si} \cdot D_S \cdot \frac{\Delta W_{II,i}}{\partial z^*} = \rho_{rel} \cdot \rho_{Si} \cdot D_S \cdot \frac{\Delta W_{II,i}}{\partial r} \tag{10.32}$$

$$\Omega_C(1) = \rho_{rel} \cdot \frac{P}{A_c} \cdot h_m \cdot (Y_a - Y_s) \tag{10.33}$$

$$\Omega_D(i) = \rho_{rel} \cdot \frac{P}{A_c} \cdot \rho_{Si} \cdot \frac{D_s}{\Delta d_c} \cdot (W_i - W_{i+1}) \tag{10.34}$$

With $\partial r \to 0$, terms Ω_{Ba} and Ω_{Bb} can be consolidated into:

$$\Omega_B(i) = \frac{\Omega_{Ba}(i) - \Omega_{Bb}(i)}{\partial r} = \frac{\partial}{\partial r} \cdot \left(\rho_{rel} \cdot D_s \cdot \rho_{Si} \cdot \frac{\partial W_i}{\partial r} \right) \tag{10.35}$$

The resulting equation for the outer layer can be easily adapted to describe the moisture transfer through any other layer by replacing the convective transfer term Ω_C with a diffusive transfer term Ω_D.

In case of the metal foam insert, the ligaments cannot be idealised as straight cylinders as was the case for the aluminium brush insert. The additional length of the conduction path due their complex cell structure can be accounted for by means of tortuosity factor ζ. The axial dimension relative to the ligament is then related to the channel dimensions by $\partial z = \partial r = \partial z^*/\zeta$. As a further contrast to the brush insert, the geometry of the aluminium foam cells also allow for a diffusive transfer along the length of the channel. As a result, the term for the diffusive transfer along the axis of the metal foam insert $\Omega_E(i)$ differs from that corresponding to the brush insert $\Omega_B(i)$:

$$\Omega_E(i) = \frac{\partial}{\partial r} \cdot \left(\rho_{rel} \cdot D_s \cdot \rho_{Si} \cdot \zeta \cdot \frac{\partial W_i}{\partial r} \right) + \frac{\partial}{\partial z} \cdot \left(\rho_{rel} \cdot D_s \cdot \rho_{Si} \cdot \zeta \cdot \frac{\partial W_i}{\partial z} \right) \tag{10.36}$$

The final equation system is presented in compact form in equations 10.37-10.40.

$$f_1 \cdot \Omega_A(1) = f_1 \cdot \Omega_{B/E}(1) + g_1 \cdot \Omega_C(1) - g_2 \cdot \Omega_D(1) \tag{10.37}$$

$$f_2 \cdot \Omega_A(2) = f_2 \cdot \Omega_{B/E}(2) + g_2 \cdot \Omega_D(1) - g_3 \cdot \Omega_D(2) \tag{10.38}$$

$$f_3 \cdot \Omega_A(3) = f_3 \cdot \Omega_{B/E}(3) + g_3 \cdot \Omega_D(2) - g_4 \cdot \Omega_D(3) \tag{10.39}$$

$$f_4 \cdot \Omega_A(4) = f_4 \cdot \Omega_{B/E}(4) + g_4 \cdot \Omega_D(3) \tag{10.40}$$

Note that third term on the right hand side of equation 10.40 is omitted, because there is no mass transfer with the solid base material.

Boundary conditions

The positions of the inlet and outlet boundaries applied to the equation system varies depending on the underlying half-cycle. They are visualised in schematic 10.1 by means of lower capital roman letters (i-iii).

For the flow field calculations, a constant velocity is specified at the inlet boundaries (i and iii) and the outlet boundary at the respective opposite ends of the channel is set to zero pressure with no viscous stress. Since process and regeneration air speeds were always kept the same, this resulted in two identical counter-current flow fields, specified by field variables (u_1, w_1) and (u_2, w_2) that were passed on to the transient heat and mass transfer analysis.

Similarly to the flow fields, constant temperature and concentration values were specified as the inlet conditions while the outlet boundary fluxes were set to be convection dominated, i.e. diffusive fluxes were forced zero. Additionally the nature of the wall surface boundary condition (ii) varied between Dirichlet-type during the adsorption half-cycle with $T_s = T_w$ and adiabatic during the regeneration half-cycle.

10.1.2 Model implementation

The model was implemented by controlling the setup and solution sequence of the COMSOL model externally using MATLAB. This was necessary because it enabled an automated cyclic assignment of inlet conditions that gave the flexibility to setup up models with high cycle numbers and various sweep parameters. It also helped to limit the size of the stored solution data files by only extracting the complete time series of certain variables of interest and storing the complete solution merely for the last two cycles.

A schematic of the execution routine is given in figure 10.3. As a first study step, the stationary flow fields are calculated in ways described in section 6. The

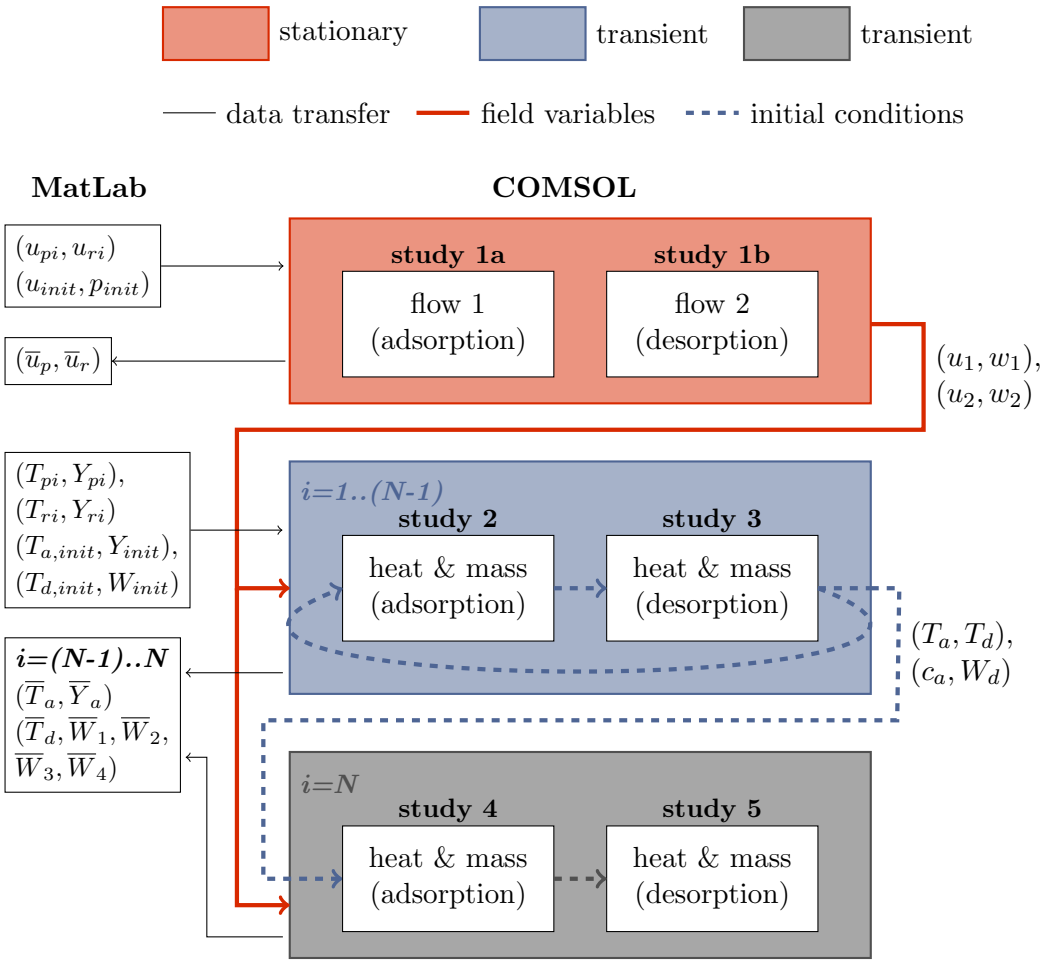

Figure 10.3: Schematic of numerical model

desired inlet velocities are specified as boundary conditions for the two equation systems. The resulting stationary, i.e. time independent velocity vectors (u_1, w_1) and (u_2, w_2) are used as field variables in the air-side transport equations 10.1-10.7. The term "study" in this context is borrowed from the terminology used in the COMSOL environment, where a "study" represents a self-contained equation system with specified boundary and initial conditions that is solved and stored.

For the second step, the equations for the adsorption and desorption half-cycles are setup as a consecutive study pair with the respective boundary conditions. For the first half-cycle, the initial conditions for the field variables were set to represent a thermal and sorption equilibrium at the mean temperature between the two

half-cycles, i.e.:

$$T_{a,init} = T_{s,init} = \frac{T_{pi} + T_{ri}}{2} \tag{10.41}$$

$$Y_{a,init} = Y_{s,init} = \frac{Y_{pi} + Y_{ri}}{2} \tag{10.42}$$

$$W_{1,init} = W_{2,init} = W_{3,init} = W_{4,init} = \Psi^{-1}(\phi_{a,init}) \tag{10.43}$$

where $\phi_{a,init}$ calculated from $T_{a,init}$ and $Y_{a,init}$ using relation 9.1 and $\Psi^{-1}(\phi)$ is the inverse of the material isotherm function 2.80. After the calculation of the first half-cycle, the final values of the field equations of the dependent variables are taken as initial conditions of the second half-cycle. The resulting final values of the second half-cycle are then used as inlet conditions for the first half-cycle that is then rerun with updated initial conditions. Thus a continuous loop is established that is executed a set amount of $(N-1)$ times.

The final N-th iteration of the loop is performed with two dedicated studies, so that the detailed results of the final two cycles stored in studies 2-5 are accessible for post-processing and detailed analysis.

The information of the previous iterations is extracted for selected variables in form of cross-sectional average values obtained at the internal boundaries depicted in figure 6.16 and exported into MATLAB.

10.2 Modelling results

The mathematical model was utilised to predict effect of coating thickness and cycle time on the dehumidification performance of the three inserts under investigation. In the following, typical profiles of air temperature and absolute humidity will be presented and a comparison made between numerical and experimental findings. Consequently the modelling results of the parametric variation of cycle time and coating thickness will be discussed.

10.2.1 Ideal profiles

The channel air temperature profile corresponding to the adiabatic dehumidification process with a cycle time of 600s is depicted for the 10PPI foam insert with an intermediate coating thickness of 150μm in figure 10.4. The process and regeneration inlet air temperature were set to $T_{pi} = 35°C$ and $T_{ri} = 80°C$, respectively and the inlet absolute humidity level of both streams was set to $Y_{in} = 17g/kg$. Both air streams had a flow rate of $\dot{V}_a = 15l/min$.

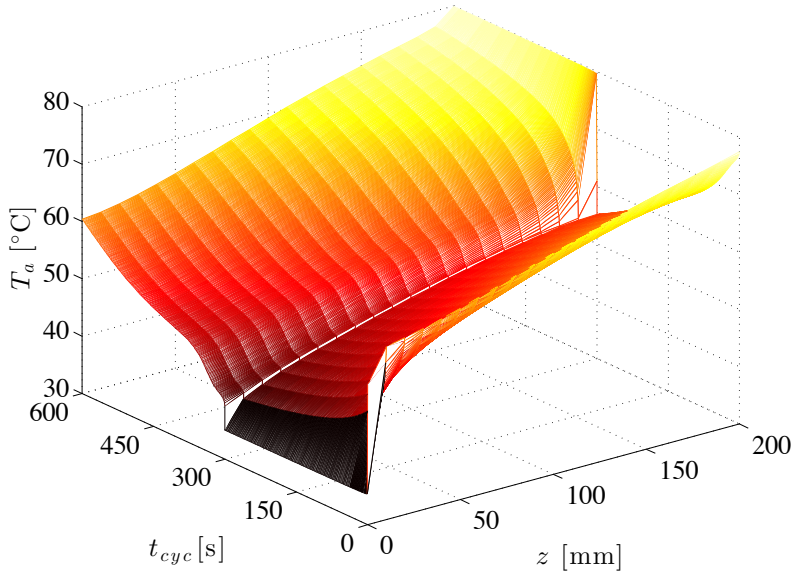

Figure 10.4: Typical temperature profile of adiabatic process (10PPI foam)

Prominent axial temperature gradients are visible throughout the entire lengths of the respective adsorption and desorption half-cycles. At $t_{cyc} = 0$s, the channel temperature is at the temperature level of the previous regeneration phase and is exposed to the cool process air stream that enters the channel at $z = 0$mm with a constant temperature of $T_{pi} = 35°$C. The process air flowing through the channel is heated up by the stored regeneration heat in the solid material and the heat of adsorption generated during mass transfer. The local temperature levels decrease as time progresses as the solid material cools down and the difference in partial pressure driving the exothermic adsorption process becomes less as the moisture loading of the desiccant material increases. At the end of the adsorption cycle at $t = 300$s, the channel outlet air has reached a level of $T_{po} = 55°$C. With the switch to regeneration stream, hot air enters the channel at $z = 200$mm with a constant temperature of $T_{pi} = 80°$C, that is then cooled down quickly due to the low temperature of the solid material and the energy intensive desorption process. As time progresses the local temperature levels rise again to the conditions encountered at the beginning of the adsorption cycle at $t_{cyc} = 0s$.

The corresponding dehumidification profile is shown in figure 10.5, where the local difference in moisture content is defined as $\Delta Y_a = Y_a - Y_{in}$. Here it can be seen, that although the inlet absolute humidity level Y_{in} is the same for process and regeneration air streams, the air is quickly dehumidified as it travels through channel due to the partial pressure difference between adsorbate and gaseous phase at the

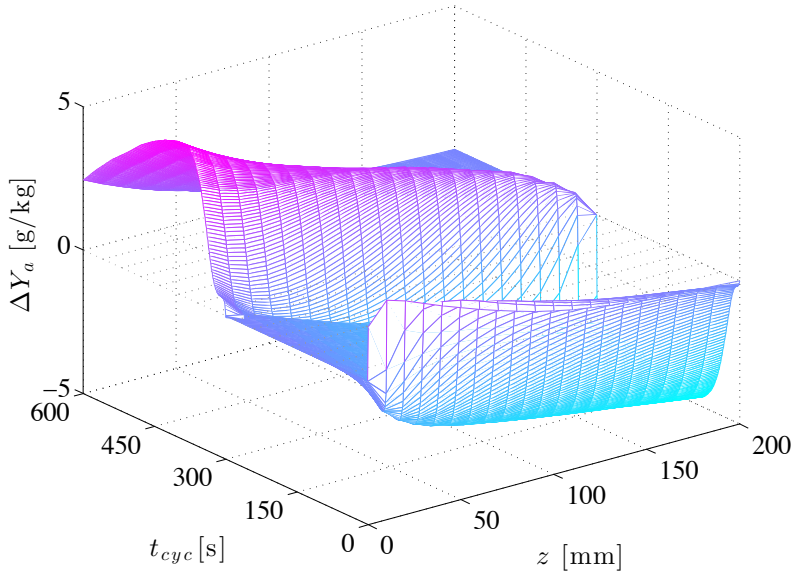

Figure 10.5: Typical dehumidification profile adiabatic process (10PPI foam)

interfacial surfaces. During the adsorption phase, two opposing effects take place: While the continuous reduction of adsorbent temperature due to the exposure to cool process air has an augmenting effect on the partial pressure difference driving the mass transfer, the resulting increase in adsorbate loading has a detrimental effect. As a consequence, the resulting local dehumidification curves exhibit bell-shaped profiles, where the local absolute humidity reaches a minimum at a certain point in time. The time required to reach the local minimum increases with distance from the channel inlet. Similar observations can be made for the regeneration half-cycle, where the mass transfer process first benefits from the rise in temperature level, which causes the adsorbent to release the moisture to the fluid, until it is inhibited by the limited amount of adsorbate held by the desiccant.

The solid-side counterpart to the dehumidification profile is the adsorbent's moisture uptake profile depicted in figure 10.6. Note that for better visibility of the low moisture content at the process air outlet/ regeneration air inlet end of the channel, the plot is rotated, so that the origin ($t_{cyc} = 0, z = 0$) is now located at the back of the plot.

In contrast to the air-side dehumidification profile, the moisture content profile is not constant at the respective channel inlet ends, but approaches the equilibrium loading corresponding to the respective channel air inlet relative humidity progressively with time. Similar to the temperature, a strong axial gradient in moisture content can be observed throughout the entire process. It can furthermore be

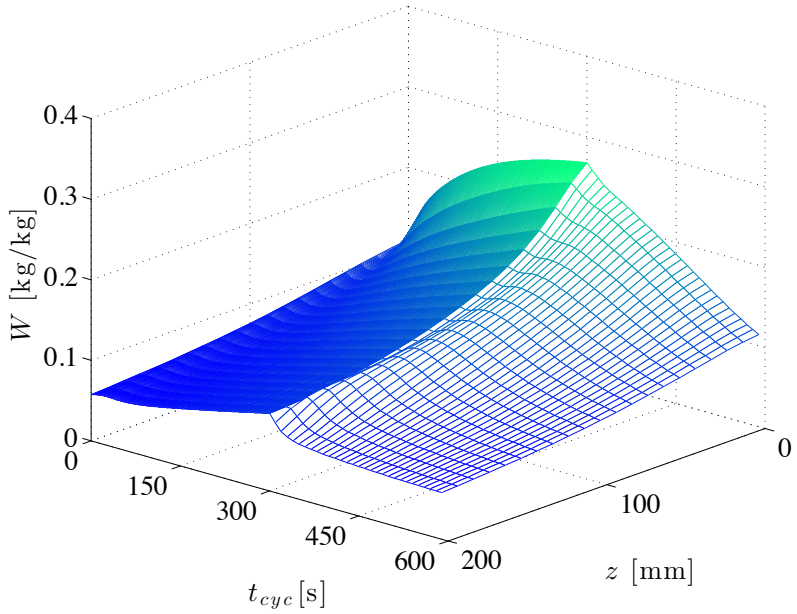

Figure 10.6: Typical moisture content profile adiabatic process (10PPI foam)

noticed, that the cyclic fluctuations in local moisture content are much more pronounced at the cold/wet end of the channel ($z = 0$mm) than at the hot/dry end ($z = 200$mm), indicating that this part of the channel is not participating actively in the mass transfer process. The axial gradient can be explained by the continuous decrease in adsorption potential with distance from the channel inlet due to the increase in air temperature and decrease in absolute humidity. The overall low level of moisture content shows that the system is limited by the adsorption process, i.e. the desiccant material does not have enough time under the given conditions to pick up acceptable amount of moisture.

For the purpose of comparison, the temperature, dehumidification, and moisture content profiles of the process with water-cooling are shown in figures 10.7 to 10.9.

The impact of the water-cooling on the temperature profile is clearly visible from figure 10.7, where the local channel temperatures almost instantaneously drop to the constant level of the cooling water which is set equal to that of the process inlet air. However, as a result of the reduced temperature levels of the solid material at the end of the adsorption phase, the temperature gradients observed in during the regeneration half-cycle are also intensified to the extend that the outlet temperature level at $t_{cyc} = 600$s is reduced from $T_{ro} = 60°$C (adiabatic) to 40°C (water-cooled). This can be expected to have a detrimental effect on the overall system performance

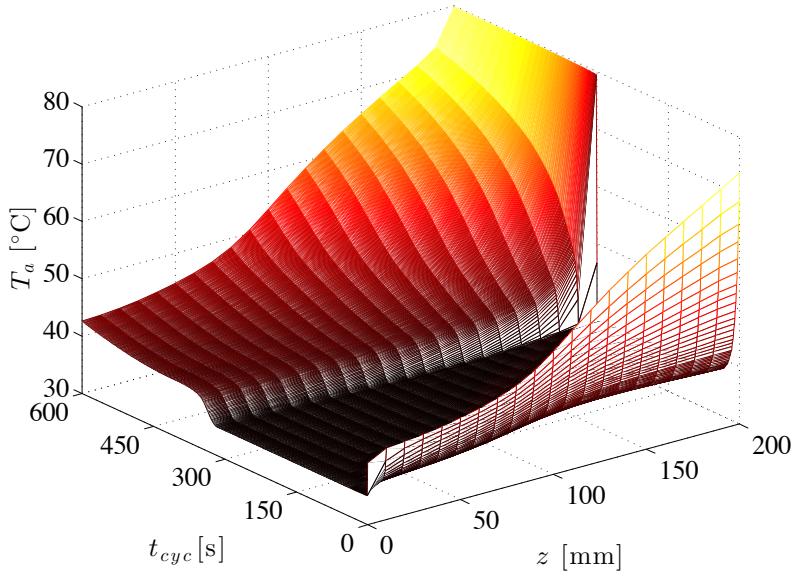

Figure 10.7: Typical temperature profile water-cooled process (10PPI foam)

as it limits the regeneration effectiveness.

Nonetheless, a clear increase in moisture removal is observable from the dehumidification profile depicted in figure 10.8. The effective and almost instantaneous removal of the sensible heat stored from the regeneration phase, the system is capable of utilising the high dehumidification potential stemming from the low adsorbent moisture loading at the beginning of the adsorption half-cycle much more effectively. As a result, the local minima in local absolute humidity curves are shifted to lower cycle times and the minimum level of the channel outlet absolute humidity difference is reduced from $\Delta Y_{po} = -4.5$g/kg (adiabatic) to -12g/kg (water-cooled). During the regeneration phase a similar high peak cannot be observed because of the thermal dampening of the desorption process, that is caused by the low temperature level of the solid materials in the channel. As a result, the local absolute humidity curves exhibit a flatter profile that in the adiabatic case indicating that the desorption process is effective for longer.

The moisture content profile for the water-cooled process is shown in figure 10.9. It is apparent that the sensible heat removal during the dehumidification phase helps to engage a bigger portion of the channel actively in the adsorption process, resulting in an overall higher moisture content in the adsorbent. Due to the temperature related limitations to the desorption process, however, the higher moisture content cannot be transferred fully to the regeneration air stream in the second half-cycle. As a result, the area of small cyclic moisture content changes

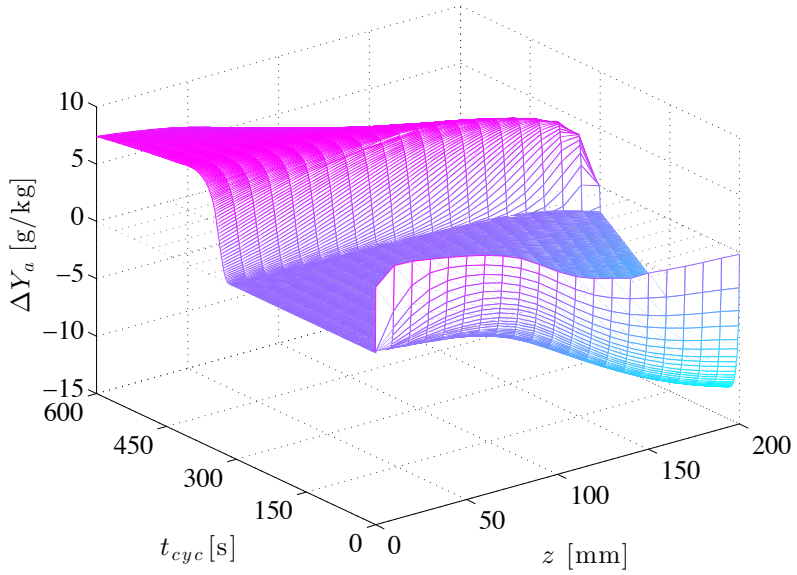

Figure 10.8: Typical dehumidification profile water-cooled process (10PPI foam)

is shifted towards the process air inlet/ regeneration air outlet end ($z \to 0$) of the channel, indicating together with the overall higher moisture content that the system is now limited by the regeneration process.

10.2.2 Comparison to experimental findings

The comparison of the modelling results to the experimental findings will be described in the following taking the 10PPI foam as an example. As has been mentioned during the description of the experimental profiles in section 9.3.1, the inlet conditions of the test rig did not instantaneously change with the flow-switching, but gradually approached the steady-state conditions over a course of ca. 2.5min due to the thermal mass of the inlet channels. In order to account for this in the model, the experimentally measured inlet temperature signals were used as boundary conditions for the respective half-cycles, while the absolute humidity levels were kept at a constant level equal to the average of the measured channel inlet levels. A comparison between experimental and modelling results is shown for the adiabatic test of the thinly coated 10PPI aluminium foam tube using an air flow rate of 15l/min is shown in figure 10.10, where experimental profiles are represented by lighter shaded curves. It can be seen from the upper plot, that the experimental outlet temperatures deviate noticeably from the numerically determined ones: During the first 300s of the adsorption cycle, the experimentally measured process outlet temperature, distinguished in light red, decreases faster than the dark red line

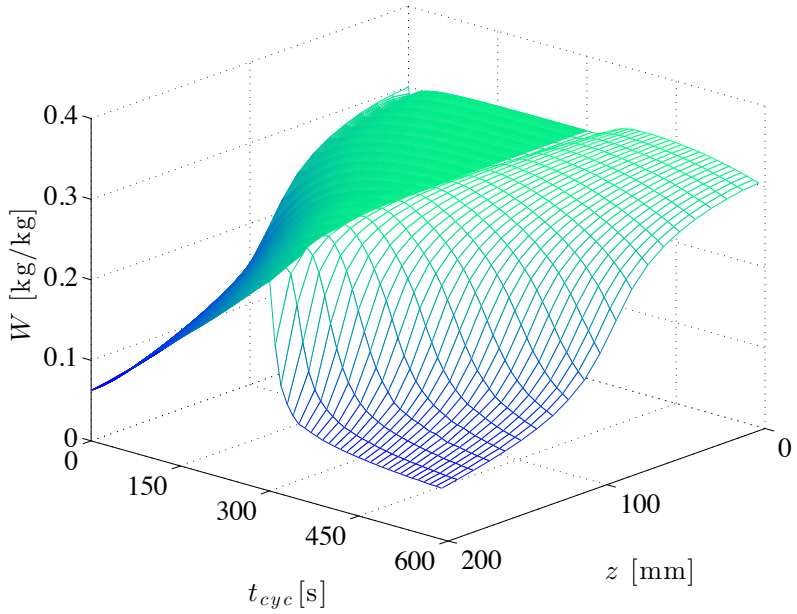

Figure 10.9: Typical moisture content profile water-cooled process (10PPI foam)

representing the modelling results. During the second half-cycle, however, it can be seen that the numerically determined curve exhibits a more dynamical profile and undergoes a greater change in temperature than the experimentally determined one.

These differences in behaviour also have an impact on the related absolute humidity levels shown in the lower plot in the figure. Comparing the solid lines during the two half-cycles, it can be seen, that the process air outlet humidity level appears in reasonable agreement with the experimental findings, although exhibiting a slower decay at the beginning of the adsorption half cycle at $t_{cyc} = 0$. During the desorption phase, however, the profile of the solid dark blue curve differs from the light blue line representing the experimental case.

The dashed lines represent absolute humidity levels, that are recalculated from the modelled outlet temperature levels and the first-order response function of the local relative humidity level. This emulates the effect of the slow response time of the relative humidity sensors on the calculated absolute humidity level when assuming an instantaneous thermocouple response. The model confirms, that the artificial peaks in the experimentally determined absolute humidity levels are indeed entirely explainable from the slow relative humidity sensor response.

An additional complication in comparing the numerical results with experimental findings arises in the water-cooled case from the evaporative cooling of the channel wall during the purging of the water-jacket in the regeneration process. This

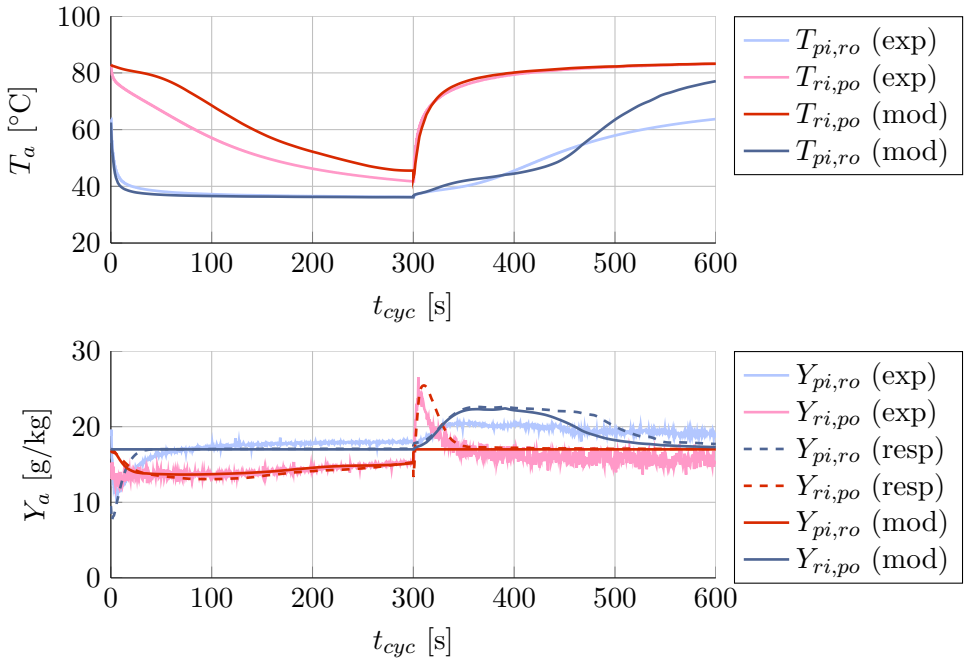

Figure 10.10: Comparison to 10PPI foam adiabatic experimental data with adapted boundary conditions

situation is depicted in figure 10.11. It can be seen, that the evaporative cooling of the channel wall has a significant impact on the experimental regeneration outlet air temperature, which is not captured in the ideal modelling case. As a result, the modelled dehumidification exceeds the experimentally determined one significantly. Since the amount of heat removed through evaporative cooling cannot be obtained from the experimental data, it was not possible to account for this situation adequately in the model. Attempts to fix the outer wall temperature to the measured purge air outlet temperature lead to an overestimation of the cooling effect and did not yield a better agreement with experimental findings.

A number of factors can be identified that contribute to the model's limited representation of the experimental results:

- Solid-side mass transfer resistance: While the coating technique was chosen, because of it's supposed limited pore-obstruction, it is conceivable that the diffusion through the adsorbent matrix consisting of ground silica gel beads and organic binder differs from the commonly assumed behaviour used in the numerical calculations, which is based on experimental findings of other researchers. An over-prediction in diffusion coefficient would lead to a higher mass transfer and heat release/dissipation during adsorption/ desorption. This

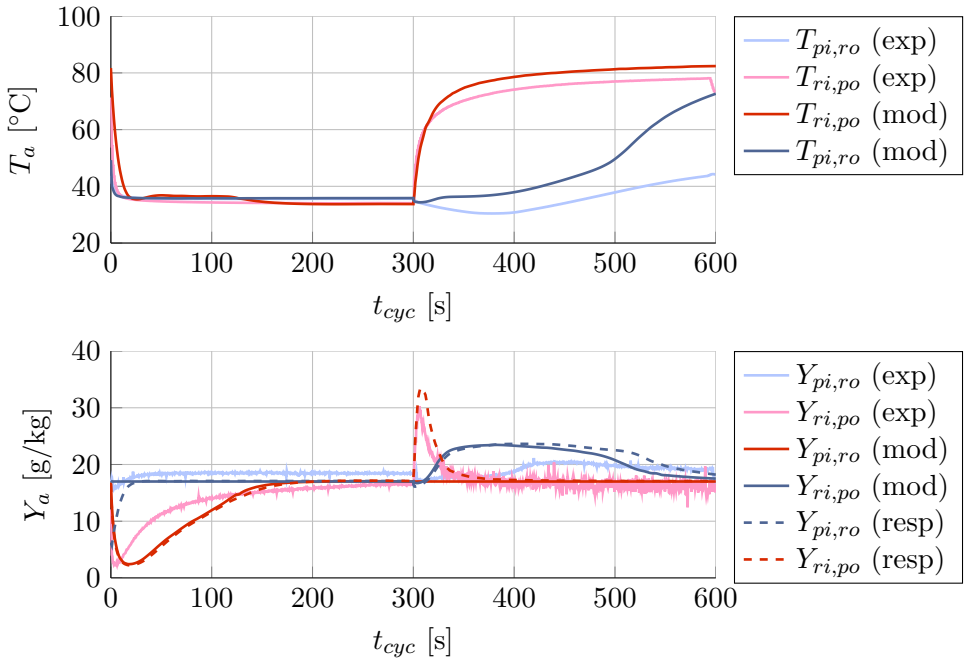

Figure 10.11: Comparison to 10PPI foam water-cooled experimental data with adapted boundary conditions

can help explain the observation, that the numerically predicted change in process outlet air temperature is less than that of the measurement during the dehumidification half-cycle and more during the regeneration phase. The more prominent depression in the modelled regeneration air channel outlet temperature profile during the phase of highest desorption can be taken as another indication, that the intensity of the sorption processes are overestimated in the model.

- Air-side transfer resistance: Although the heat transfer modelling results yielded a decent agreement with experimental data, the derivation of the the convective transfer coefficients from the Colburn j-factor analogy cannot be expected to yield precise predictions. A decrease in convective transfer coefficients signifies a reduction of interaction between fluid and solid, resulting in a smaller heat transfer behind fluid and solid on the one hand side and a reduction in mass transfer related sorptive heat generation and dissipation on the other.

- Coating layer thickness: The model assumes a uniform coating thickness based on the difference in relative densities before and after the coating. An uneven

distribution could diminish the dehumidification performance when areas of thin coating reach their maximum equilibrium uptake before the end of the half-cycle and/or sections of thin coating are not used efficiently due to the slow moisture diffusion process. The associated reduction in adsorption heat generation entails, that the process air outlet temperature would tend to be lower during the adsorption process and the regeneration outlet air temperature would tend to be higher. This concurs with the observation of the discrepancies between numerical and experimental curves in the figures.

- Heat loss to environment: The discrepancy between inlet and outlet channel temperatures at the end of the experimental adsorption cycle is approximately 20°C. It is possible, that heat loss to the environment through the empty water jacket occurred despite the insulation around the outer walls of the water jacket. The resulting lower temperature level during regeneration would have a detrimental effect on the dehumidification performance. For the water-cooled case, the evaporative cooling of the channel wall during regeneration has a similar effect.

The model was used to investigate the effect of augmented solid- and air-side transfer resistances and pseudo-convective heat loss to the environment in a parametric study. While all parameters affected the modelling results in expected ways, it was not possible to identify a single dominating influencing factor to explain the discrepancy to the experimental findings, which is likely due to a combination of all of the above factors. Given the decent agreement between model and experiments in the heat transfer case, it is likely, that the reasons for the discrepancy are due to deviations of the solid side mass transfer from the expected behaviour and external influences on the experiments.

Due to the number of influencing factors it was decided, that a variation of all factors to calibrate the model to experimental data would be of limited value without a further experimental investigation of the solid-side transport properties, which was beyond the scope of the current work.

Nonetheless it can be concluded, that the model gives physically consistent results and resembles the basic experimental trends. It can be usefully employed to investigate the heat and mass transfer performance different system configurations using the idealised structures assuming a solid-side mass transfer behaviour similar to that of conventional silica-gel coatings.

10.2.3 Model utilisation

The mathematical model was used to investigate the effect of an increase in coating thickness on the dehumidification performance of the structures under investigation for different cycle times under ideal conditions. For this, the relative density value resulting in the best pressure drop model fit was used to determine the radius of the bare ligament, to which a coating layer of varying thickness was applied. The overall relative density used in the model was then recalculated using the radius of the coated ligament as reference length. Process and regeneration air inlet temperatures were set to $T_{pi} = 35°\text{C}$ and $T_{ri} = 80°\text{C}$, respectively. The inlet humidity level of both air streams was set to $Y_{pi} = Y_{ri} = 17\text{g/kg}$.

An understanding of the system behaviour can be obtained by comparing the outlet profiles of the dependent variables for the different modelling cases, which will be discussed in the following exemplarily for the case of the 10PPI foam structure, before the effect on dehumidification performance characteristics will be summarised and compared to the other structures for the water-cooled case.

Detailed comparison of system profiles

Figure 10.12 shows the profiles of air temperature, relative and absolute humidity, and desiccant moisture content at the two channel ends for four different cases. The blue lines in the plots correspond to the process air inlet/ regeneration air outlet end of the channel, while the red lines correspond to the opposite end. The four different cases are distinguished by colour depth and line style: The lightly shaded blue and red lines correspond to an adiabatic process while their darkly shaded counterparts represent the water-cooled case. The solid and dashed lines indicate two different coating thicknesses, namely $d_c = \{150,\ 300\}\mu\text{m}$, respectively.

A comparison of the red and blue lines in the plot on the upper left of the figure shows, that the discrepancy between the solid and dashed lines is only minor, indicating that an increase in coating thickness by a factor of two somewhat dampens the temperature profiles. The rapid fall exhibited by the dark red lines from regeneration inlet temperature level to the process air inlet level during the first 75s in contrast to the gradual decrease of the light red lines highlight the effectiveness of cooling the outer tube walls for sensible heat removal during the adsorption half cycle, that has already been mentioned during the discussions of figure 10.7. The negative impact on the regeneration process is also apparent from the lower temperature level of the dark blue lines in comparison to the light blue lines for $t_{cyc} > 300\text{s}$. This shows, that the lower temperature of the solid material

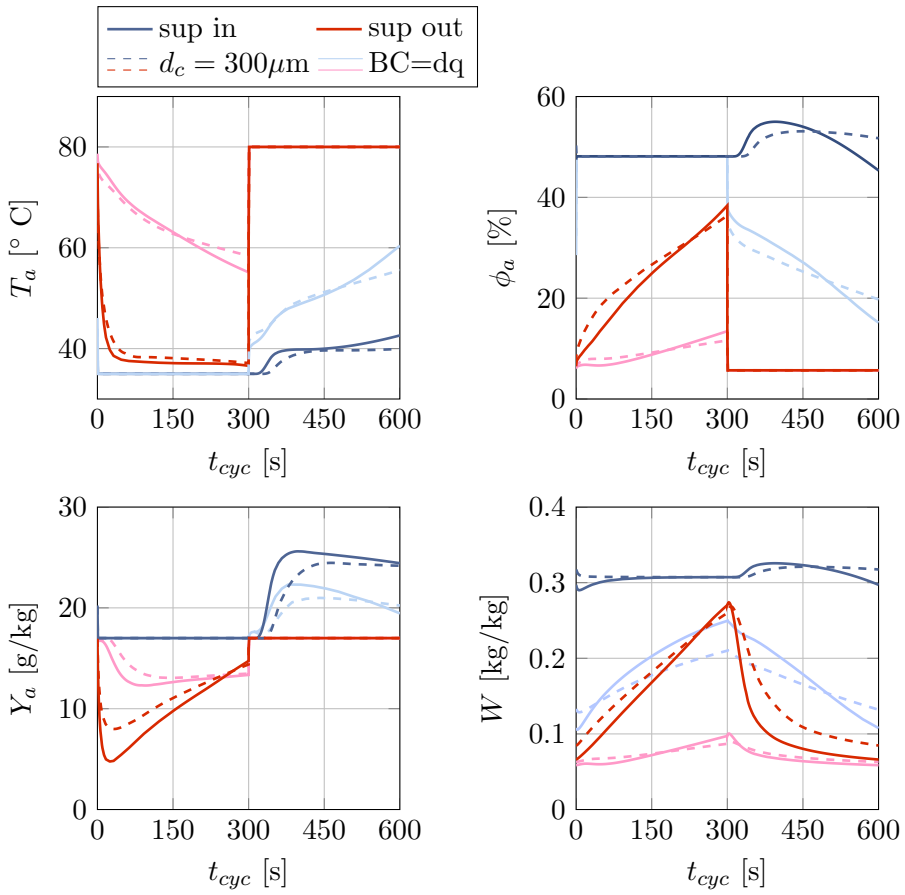

Figure 10.12: Comparison of 10PPI-foam process outlet conditions during 600s-cycle

hinders the realisation of high regeneration temperatures beneficial for desorption.

The channel in- and outlet absolute humidity levels are depicted in the bottom left plot in figure 10.12. The comparison of the dark lines to their lightly shaded counterparts shows the augmenting effect of the water-cooling during the adsorption step, manifested in steeper outlet humidity profiles during the dehumidification ($t_{cyc} < 300$s, red lines) and regeneration half-cycles ($t_{cyc} > 300$s, blue lines). While this was to be expected based on the previous discussion of figure 10.8, it can furthermore be noted, that the dashed lines corresponding to a thicker coating are closer to the the inlet conditions than their solid counterparts in both the adiabatic and water-cooled case, indicating that the dehumidification lessens with increasing coating thickness under the given cycle conditions. Although a decrease in dehumidification due to an increase of active material in the channel is somewhat counterintuitive, this effect can be explained with the attributed increase in thermal mass, whose detrimental effect on the dehumidification performance can outweigh

the potential of a higher moisture uptake capacity, if the material is not efficiently used: If the mass transfer is limited by the solid-side diffusion, an increase in coating thickness will not lead to a deeper dehumidification when the half-cycle length is too short for the moisture to reach the deeper coating layers, while the thermal mass still increases the system's thermal inertia. Finally, it can be noted that a discrepancy remains between the respective channel inlet and outlet conditions at the end of both half-cycles, indicating that the respective sorption process is still ongoing at the time of the switch of air streams and that the material never reaches the adsorption equilibrium point during the length of either half-cycle.

The relative humidity increases with the absolute humidity of the air and decreases with increasing temperature dependent saturation pressure. Consequently, the relative humidity curves given in the top right plot of the figure can be explained by the absolute humidity profiles together with the temperature data. In the water-cooled case, both outlet temperature and absolute humidity levels undergo a rapid decrease at the beginning of the adsorption cycle, leading to a gradual rise in relative humidity. The spread is bigger for the water cooled case, because the drop in absolute humidity is higher and a change in absolute humidity corresponds to a bigger change in relative humidity at lower temperature levels. Analogously, the drop in relative humidity of the regeneration outlet air is deeper in the adiabatic case because of the the bigger elevation in temperature. Because of the small rise in temperature in the water-cooled case, the relative humidity function actually increases before following its typical decremental path.

The final plot in the bottom right plot of figure 10.12 shows the local adsorbent moisture content. The comparison of the light and dark lines confirms the observation made in context of figures 10.6 and 10.9, that the process shifts from being limited from the dehumidification side in the adiabatic case to being limited by the regeneration side in the water-cooled case. A comparison of the discrepancies between inlet and outlet desiccant moisture content curves also confirms, that the moisture uptake is greater with the thinner coating.

Further insight into the moisture transfer behaviour of the system can be obtained by comparing the curves of the desiccant moisture content averaged over the entire channel volume, depicted in figure 10.13. As can been seen from comparing the dashed lines to the solid lines, a higher coating thickness leads to a higher adsorbent moisture content level, but only affects the amount of moisture transferred in a minor way. From this it becomes obvious that the cycle time is too short to utilise the potential of the additional active material available for adsorption and the process is limited by the solid side diffusion into the adsorbent layer. The resulting

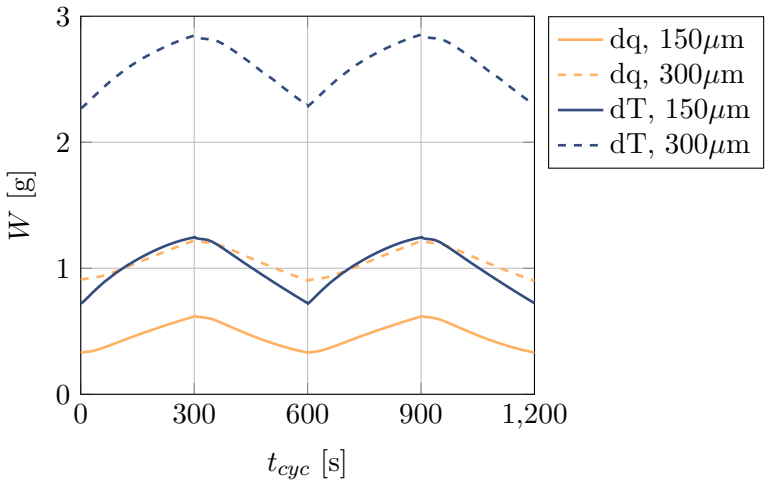

Figure 10.13: Comparison of 10PPI-foam moisture uptake during 600s-cycle

higher overall moisture content is an additional disadvantage, because the thermal mass of the adsorbed water increases the thermal mass of the system.

The steady-state dehumidification achievable by a desiccant rotor employing the channels under investigation and the corresponding temperature lift is given by the time averaged differences between in- and outlet absolute humidity and temperature levels. Figure 10.14 summarises the process employing the different configurations in a psychrometric chart. From this visualisation, the inefficiency of

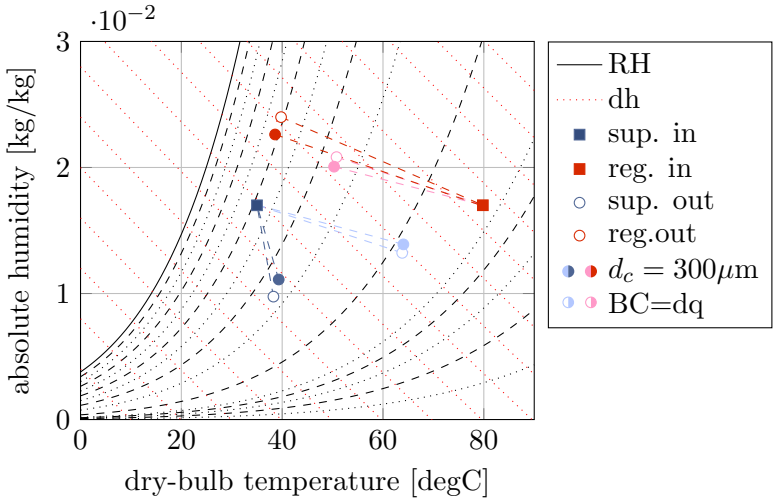

Figure 10.14: Comparison of 10PPI-foam average dehumidification profiles during 600s-cycle

the adiabatic operation become apparent from the deviation of the process specific

lines from the isenthalps representing the ideal process. It can furthermore be seen, how the water-cooling allows the realisation of outlet conditions beyond the theoretical limits of the adiabatic process. The white dots representing the thinner coating are in all cases closer to the ideal process limits, also implying a thermal mass related performance detriment at higher coating thicknesses.

The effect of a prolongation of the cycle time on the system performance can be studied from figures 10.15 to 10.17 for the water-cooled case.

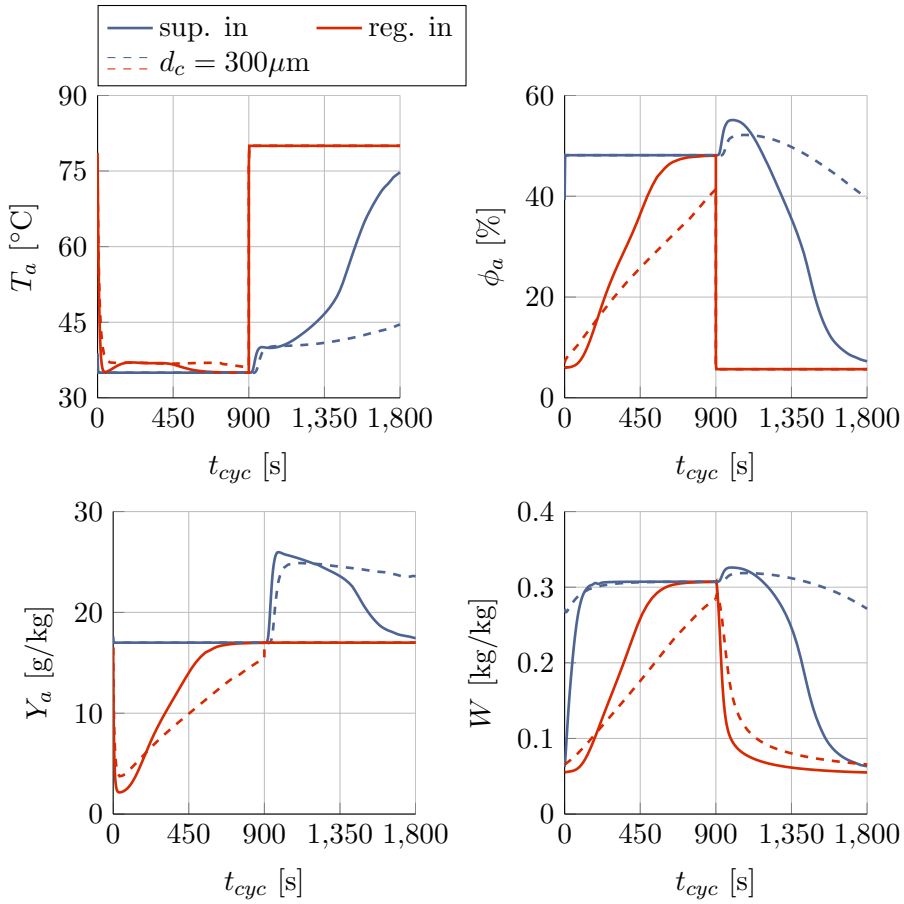

Figure 10.15: Comparison of 10PPI-foam process outlet conditions during 1,800s-cycle

It can be seen from the plots of absolute humidity and moisture content in figure 10.15, that in contrast to the previous case, the thinner desiccant coating (solid line) saturates before the end of the longer adsorption half-cycle. As a result, the corresponding temperature curve drops to the level of the inlet air/ outer wall temperature after approx. 600s. This allows the conclusion, that the previous nearly constant discrepancy was solely due to the heat of adsorption released during mass

transfer. It is furthermore noticeable, that the adsorption equilibrium is reached much later during the regeneration half-cycle, highlighting the beneficial effect of simultaneous sensible heat handling on the mass transfer kinetics. The dashed lines show, that the thicker coating results in flatter profiles of the dependent variables with an extended phase of active mass transfer. It can therefore be anticipated, that the thicker coating results in an dehumidification augmentation at a cycle time of 30min.

The corresponding curves of absolute moisture uptake are shown in figure 10.16. The full saturation of the thinner desiccant coating is clearly visible in form

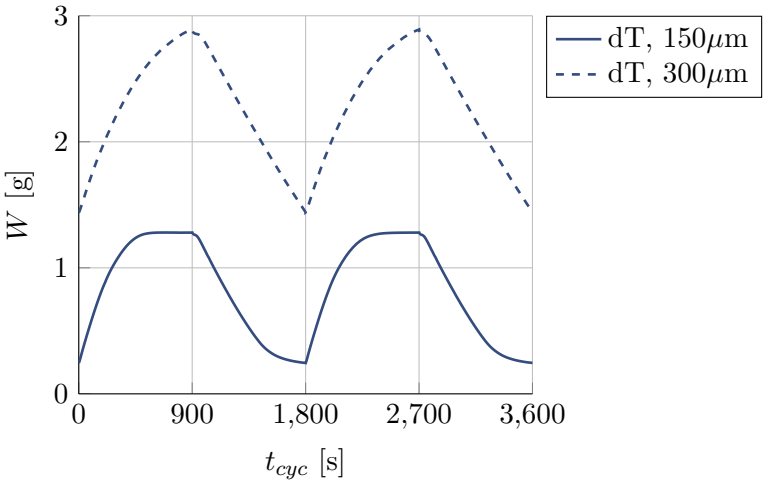

Figure 10.16: Comparison of 10PPI-foam moisture uptake during 1,800s-cycle

of the plateau reached by the solid line. Since the curve approaches zero towards the end of the regeneration half-cycle, it can be concluded that the moisture uptake capacity of the adsorbent is almost completely exhausted in the 30min cycle. Since the material saturates within about the first two thirds of the adsorption half-cycle time, a further dehumidification improvement can be expected for the same overall cycle time from a reduction in adsorption half-cycle length for the benefit of a longer regeneration process. With desiccant rotors such system improvements are routinely implemented by varying the cross-sectional area ratios process and regeneration sectors, although the flexibility of such adjustments is somewhat reduced in the case of the water-cooled wheel due to the necessity to change the cooling-water level accordingly.

In contrast to the above mentioned thin coating, the higher baseline of the moisture uptake curve for the thicker coating suggests, that the moisture uptake capacity is not exhausted during the adsorption half-cycle and that the system is

limited by the amount that can be desorbed during regeneration.

Nonetheless, the increase in coating thickness leads to an overall augmentation in dehumidification performance, as can be seen from the psychrometric chart view of the process in figure 10.17, where it is manifested in the shift from the white markers (thin coating) to their coloured counterparts (thick coating).

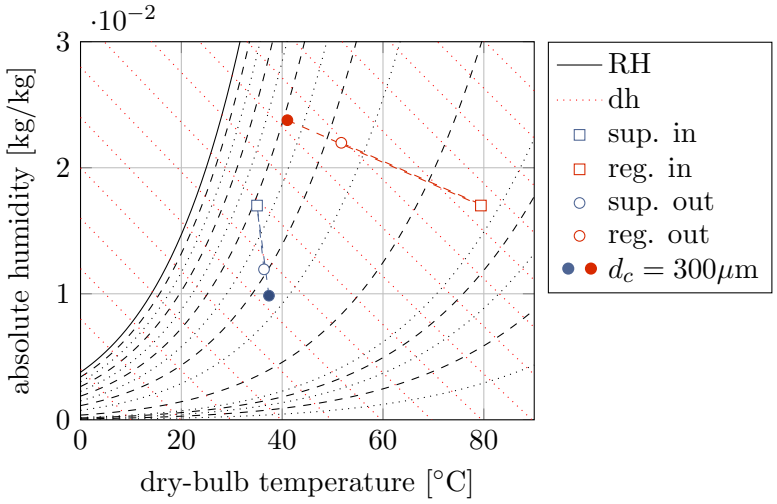

Figure 10.17: Comparison of 10PPI-foam average dehumidification profiles during 1,800s-cycle

Comparison of heat and mass transfer performance characteristics

In the desiccant cooling literature, the performance of a desiccant rotor is usually summarised by three parameters, averaged over the dehumidification half cycle time: the process air outlet temperature level T_{po}, the dehumidification $\Delta Y_{po} = Y_{pi} - Y_{po}$, and the thermal coefficient of performance according to equation 3.2. The modelling results of the 10PPI-foam tube are presented in figure 10.18 in form of these three variables as functions of the cycle length. The model was executed for the adiabatic (lighter shade in the plots) and isothermal (darker shade) process at three different inlet flow rates (distinguished by colour) with three different coating thicknesses (distinguished by symbol).

It is apparent from the temperature plots in the first row of the figure, that the water-cooling has a significant effect on the outlet temperature level, which decreases with increasing cycle time and lessening coating thickness. The dependency on these two factors is a result of the thermal inertia of the system on the one hand, whose thermal mass increases with coating thickness, and the generated heat of adsorption on the other, that lessens over time. Due to the lack of additional cool-

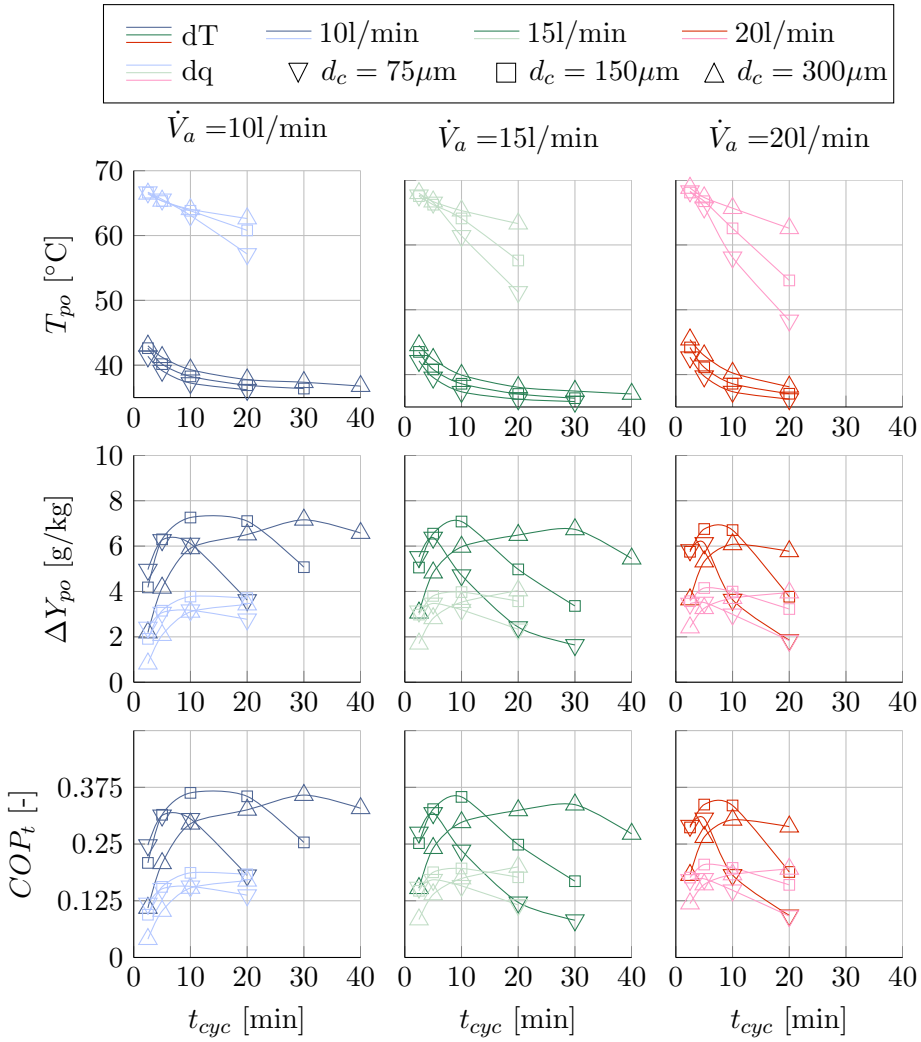

Figure 10.18: Dehumidification performance of 10PPI foam tube

ing energy, the curves corresponding to adiabatic dehumidification exhibit a stronger sensitivity to both factors, resulting in an increasing discrepancy between the lightly shaded curves with cycle length. A minor increase in outlet temperature level with augmenting flow rate can also be observed, mainly due to the higher corresponding solid matrix temperature at the end of the regeneration phase.

The average dehumidification is shown in the second row of plots in figure 10.18. It can be seen, that the water-cooled process generally results in a significantly higher moisture removal than its adiabatic counterpart. The slow solid-side moisture diffusion prevents an efficient utilisation of the system's moisture uptake capacity at low cycle lengths, as was already discussed in the context of figure 10.13.

As the cycle length increases, more moisture can be adsorbed by the desiccant, resulting in an initial rise in the dehumidification curves. The high temperatures corresponding to the adiabatic process further reduce the system's performance, since they result in a reduction in mass transfer driving partial pressure difference, so that the dehumidification is significantly less than in the water-cooled case. As the moisture content of the desiccant increases with cycle time, the mass transfer potential reduces continuously until it eventually reaches zero and the adsorbent is in equilibrium with the process air. Consequently, the average dehumidification curves reach a maximum value at a certain critical cycle length. As can be seen from the plots, the optimal cycle length increases with coating thickness, i.e. moisture uptake capacity. An augmentation of the cycle length beyond the optimal value results in a reduction in average dehumidification. If the cycle length is long enough for the desiccant material to fully saturate in both the water-cooled and the adiabatic case, the moisture removal of both cases is the same. This can be seen from the curves corresponding to the thin coating for $t_{cyc} \geq 20$min and $\dot{V}_a \geq 15$l/min. An increase in air flow rate reduces the convective transfer resistances, resulting in a narrower family of bell shaped curves, indicating faster material saturation, and a tendency to shift the optimal dehumidification point to lower cycle lengths. Comparing the optimal dehumidification values at a flow rate of 15l/min, it appears that the intermediate coating thickness results in a highest dehumidification. From this it can be deduced, that aside from the moisture uptake capacity, the thermal mass of the system also influences the dehumidification performance. Depending on the coating thickness, the maximal dehumidification lies between 6 and 8g/kg for the 10PPI foam for the modelled conditions, corresponding to optimal cycle lengths between 5 and 10min for thin and intermediate coating thicknesses and between 10 and 30min for the thick coating.

The thermal coefficient of performance is depicted in the last row of plots in figure 10.18. Since all flow-rate specific curves correspond to the same regeneration heat input, they exhibit the same trends and are influenced by the same parameters as the dehumidification plots discussed above. The maximal thermal coefficient of performance lies between 0.3 and 0.36 for the water-cooled case and between 0.17 and 0.205 for the adiabatic process.

The modelling results for the dehumidification performance of the residual inserts is compared to that of the 10PPI foam for the water-cooled case at an intermediate flow rate of $\dot{V}_a = 15$l/min in figure 10.19.

From comparing the temperature curves of the three metal foam tubes in the three plots in the first row of the figure, it can be seen that the mean outlet temper-

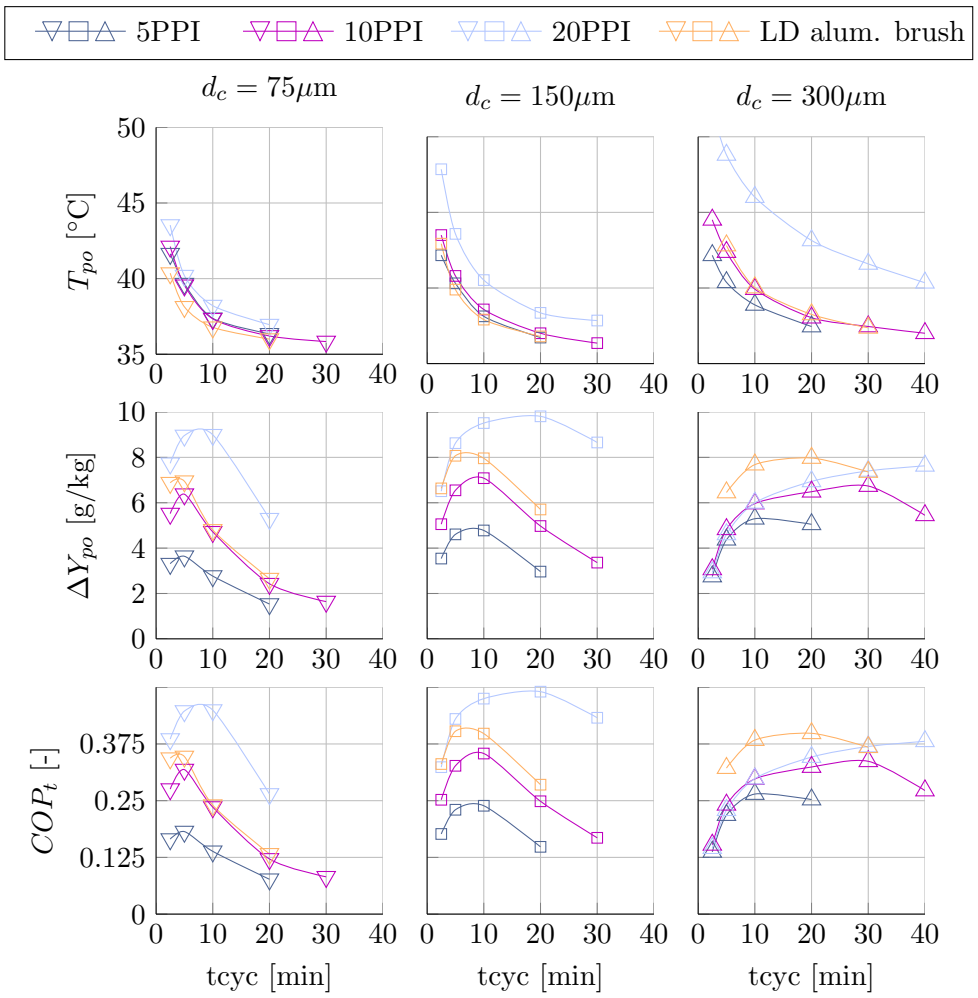

Figure 10.19: Comparison of inserts' dehumidification performance with water-cooling at $\dot{V}_a = 15$l/min

ature increases with decreasing pore size and increasing coating thickness, i.e. the outlet temperature is highest for the thickly coated 20PPI foam and lowest for the 05PPI foam with the a coating layer of 75μm. This can be explained by the difference in thermal mass of the respective structures: Due to the higher specific surface area, a coating layer of a certain thickness results in a higher volume of desiccant material in the channel for smaller pore sizes and consequently a higher increase in thermal mass. The observation of the trends corresponding to the aluminium brush also reveals an interdependence of outlet temperature and dehumidification: Due to its low thermal mass, the brush insert specific outlet temperatures are below those of the other inserts at a low coating thickness, where its dehumidification performance is similar to that of the 10PPI foam. With increasing coating thickness, the

comparative dehumidification performance of the insert improves, which is reflected in the outlet temperature level, which increases until it is slightly above that of the 10PPI foam structure.

Similar to the temperature case, the dehumidification curves of the foam inserts in the second row of the figure show that the dehumidification generally increases with decreasing pore size. Because the solid side resistance is the same due to the fixed coating thickness if one neglects temperature and loading effects, the increase can be expected to be mainly due to the greater active surface area corresponding to the smaller pores and the higher moisture uptake capacity. However, as the point of optimal insert specific dehumidification is shifted towards longer cycle times with increasing coating thickness, the discrepancies between the inserts' performance, becomes less in the range of cycle times investigated. This situation is illustrated well in the third plot corresponding to a coating thickness of 300μm, where the three metal foams exhibit similar dehumidification levels until the respective maximal level is reached. It is remarkable that the dehumidification achieved by the aluminium brush insert is comparable to that of the metal foam inserts despite its significantly lower active surface area. This finding highlights the importance of the thermal mass related performance hindrance typical for this application.

The thermal coefficient of performance is depicted in the final row of plots in figure 10.19. The curves exhibit the same bell shaped profiles as the dehumidification lines. The values corresponding to the optimal dehumidification conditions are summarised in table 10.1.

Table 10.1: Points of best performance using water-cooling at an air flow rate of 15l/min

Insert	d_c [μm]	t^*_{cyc} [min]	T^*_{po} [°C]	ΔY^*_{po} [g/kg]	COP^*_t [-]
05 PPI foam	75	5	39.7	3.6	0.18
	150	10	38.1	4.8	0.24
	300	10	38.9	5.3	0.26
10 PPI foam	75	5	39.6	6.4	0.32
	150	10	38.6	7.1	0.35
	300	30	37.5	6.7	0.34
20 PPI foam	75	10	38.2	9.0	0.45
	150	20	38.4	9.8	0.49
	300	≥ 40	≤ 40.4	≥ 7.6	≥ 0.38
Alum. brush	75	5	38.1	6.9	0.35
	150	5	42.9	8.1	0.40
	300	20	38.3	8.0	0.40

Chapter 11

Summary and Conclusions

The aim of this work was the preparation, characterisation and performance analysis of desiccant coated structures that serve as surface enhancing tube inserts for a novel water-cooled desiccant wheel prototype developed at the CSIRO laboratories.

11.1 Summary

The usefulness of sensible heat removal during the adsorption process was demonstrated in the survey of the pertinent literature, highlighting the limitations of the conventional adiabatic solid desiccant rotor systems and summarising approaches taken by other researchers to approach an isothermal dehumidification process.

The novelty of the device under investigation lies in its ability to realise a continuous dehumidification process, where all channels are in direct contact with the cooling medium. This way, shortcomings of other isothermal dehumidification systems can be avoided. Furthermore, the utilisation of coated highly porous metal structures as channel inserts for an open-cycle desiccant dehumidification system has not been investigated before in the pertinent literature.

The potential inserts comprised aluminium foam structures, twisted-in wire brushes, and carbon fibre flocked channels, from which the aluminium foams and aluminium brush were chosen for further desiccant coating and heat and mass transfer analysis. For the application of the desiccant coating, a patented procedure was followed, that involved preparation of a uniform coating mixture combining among other components an organic binder and ground up silica gel beads. Consecutive applications of the mixture were needed to achieve acceptable coating thicknesses. A visual inspection of the aluminium brush insert showed a fairly uniform coating thickness with limited amount of bridging between ligaments. A visual inspection

of the metal foam tubes, for which the coating process was somewhat different was not possible without destroying the specimen. The achieved mass ratio of desiccant coating and substrate weight varied between 25% and 36% for the thin coatings and between 50% and 95% for the thicker coatings.

The characterisation and performance assessment conducted in this work was divided into four aspects that will be summarised briefly in the following.

Geometrical characterisation

Firstly, the geometrical characteristics of the structures under investigation were determined. This involved the calculation of the relative densities of the structures from weight measurements based on their dimensions. In case of the metal foam and brush type inserts, that were to be analysed further by means of mathematical modelling, detailed three-dimensional geometrical models were developed. This allowed for the unique description of the complex structures by a pair of characteristics, namely the relative density and pore size in the case of the metal foam and the relative density and ligament dimensions in the case of the brush.

Flow characterisation

Secondly, the impedance of the channel flow due to the tube inserts was investigated experimentally and numerically. The experimental results showed a positive dependency between relative insert surface area and pressure drop that appears to lessen with pore size in case of the metal foam inserts. The high flow impedance of the flat flocked tube in comparison to the other inserts led to its exclusion from further analysis. Since wall effects could be expected to have an influence on the pressure drop, the porous medium flow characteristics could not be obtained from experimental data directly, but relied on a numerical flow investigation.

For this, the flow field through an array of characteristic unit cells was calculated explicitly by solving the Navier-Stokes equation system. In case of the metal foam structures, the detailed three-dimensional geometrical model was utilised for the analysis, while a simplified two-dimensional representation in form of arrays of uniformly spaced cylinders was adopted for the brush-type structures. By fitting a Forchheimer flow model to the modelling results of the pore scale flow, porous medium flow characteristics, namely permeability and drag coefficient, could be obtained as functions of the geometrical characteristics.

The numerical findings could be compared to the experimental results by utilising the determined characteristics in a Forchheimer-extended Brinkman flow

model. In general, it was found that the experimental profiles could be duplicated satisfactorily with the chosen flow model. However, the flow characteristics yielding the best fit to the pressure drop measurements differed from the ones expected based on the measured relative density data. In case of the metal foam inserts, the 10 and 20PPI inserts generally required smaller offsets in relative density to agree with the experimental data than the 5PPI foam. The fact that an adjustment of the single geometric characteristic suffices for the calibration of the macro-scale flow model can be taken as an indication that the dependencies of the hydraulic and geometrical characteristics derived at the pore-scale are indeed representative for the macro-scale structure, possibly with the exception of the 5PPI foam structure, where the magnitude of the required offsets suggest that an adaptation of the cell model might be necessary. In contrast to the metal foam case, adjustments of the hydraulic characteristics themselves were necessary for the brush type inserts, indicating that the simplified pore-scale model is not fully representative of the macro-scale structure. Nonetheless, once the appropriate fitting factors were chosen, the flow models fitted the experimental trends well and adequately predicted the effects of a change in ligament number and thickness.

Thermal characterisation

Similar to the hydraulic performance, the heat transfer behaviour of the test tubes was studied both experimentally and numerically. The experimental investigation was carried out with a purpose built test rig consisting of a double-pipe counter flow heat exchanger using water as a cooling fluid. The experiments revealed a similar heat transfer performance of the three metal foam inserts, that was matched by the medium density copper brush insert. The overall heat transfer coefficients of the lower density metal brushes were found to be similar at flow rates below 15l/min, but only reached levels approximately half as high as the metal foam inserts at higher flow rates. When normalising the overall heat transfer coefficient by the pumping power it was found that the three metal foams and the aluminium brush insert gave the best thermo-hydraulic performance.

The heat transfer model yielded a decent agreement with experimental data when a thermally resistive layer with a thickness varying from case to case between $20 - 120\mu$m was applied to the inner channel boundary, representing the contact resistance between tube insert and tube wall. The heat transfer coefficient between fluid and matrix was derived from friction factor analogy.

Cyclic heat and mass transfer performance investigation

The cyclic heat and mass transfer performance was evaluated experimentally in a purpose built experimental test rig, that emulated a desiccant wheel system by alternately exposing the test tubes, situated inside a water-jacket for simultaneous sensible heat removal, to one of two continuously flowing air streams at the respective process and regeneration air inlet temperature levels. The performance of the inserts was compared to that of a scroll of a polymer coated sheet of corrugated fabric taken from a commercial desiccant wheel. The analysis of the experimental results was complicated by the necessity to compensate for the slow response of the relative humidity sensors and their limited accuracy. Furthermore, an unwanted heat loss due the evaporation of residual water droplets on the outer tube walls during the regeneration phase obscured the expected benefits of the highly thermally conductive inserts. Measurements performed at several air flow rates and cycle times showed a far superior performance of the polymer scroll insert in comparison to the test objects, likely attributed to its lesser sensitivity to the tube wall temperatures. The moisture uptake of the inserts was found to increase with cycle time, flow rate, and coating thickness.

A more detailed view of the heat and mass transfer driving factors could be obtained from a numerical model of the transient process. Modelling results showed the thermal mass of the test channels is a critical performance limiting factor, causing the process to shift from a limitation on the adsorption side in adiabatic operation to a limitation on the desorption side when employing water-cooling during the dehumidification phase. The water-cooled dehumidification was shown to yield a significant performance augmentation in comparison to the adiabatic process. The optimal cycle time was found to be positively correlated with thermal mass and moisture uptake capacity and was found to decrease with air flow rate. An optimisation of individual part-cycle times towards a longer regeneration phase can be expected to improve the system's performance. The generally highest dehumidification was achieved by the 20PPI foam and the average moisture removal decreased with increasing pore size. The aluminium brush was found to achieve high dehumidification levels at lower cycle times due its lower thermal mass and can be considered a promising alternative also because of the lower attributed flow impedance and costs of procurement.

11.2 Conclusions

Based on the investigation summarised above, it can be concluded that there are four structure specific characteristics, that influence the heat and mass transfer performance, namely

- the ligament spacing, manifested in the pore size in the case of the metal foam inserts and the number of ligaments in the case of the brush type inserts,
- the ligament thickness, which is a function of the relative density at a given ligament spacing,
- the thickness of the desiccant coating layer, which is reflected in an augmentation of the relative density of the structure, and
- the effective thermal conductivity of the structure, which is dependent on the ligament orientation, material, and imperfect contact to the channel wall.

Generally speaking, a reduction in ligament spacing and an increase in ligament thickness increase the conductive transfer of heat through the solid structure, however at the expense of an increased thermal mass and decrease in volume available for fluid flow. The fact that all three foam specimen showed a very effective heat transfer in steady-state operation indicates that the solid side heat transfer is not the limiting factor in this configuration. As a consequence, the effect of the pore size on the heat transfer performance was not noticeable in the analysis. A reduction in relative density, i.e. ligament diameter, would therefore be likely to reduce the thermal dampening observed in the cyclic heat and mass transfer analysis while still achieving an effective conductive heat removal during dehumidification. From the manufacturer's side a reduction of relative density down to $\rho_{rel} = 0.03$ is achievable, making this a viable option for further research.

Nonetheless, the disadvantage of the foam structures is their reduced effective thermal conductivity due to the tortuous conduction path. A more effective heat transfer can be expected from a structure with more ligaments in transverse alignment. As such, the metal brush inserts are a promising alternative. The aluminium brush specimen was shown in the numerical analysis to be able to give a comparable dehumidification performance despite a significantly lower relative density of the insert's supporting structure. The issue of insufficient thermal contact between insert and channel wall is likely to be easily overcome by means of brazing or similar processes.

While the ligament alignment of the brush type inserts is ideal in the sense that it minimises the conductive path length, it has the disadvantage that the distance between the bristles continuously decreases as they approach the channel core. This is reflected in a relative density function that rapidly approaches unity. Since the channel core is blocked off, it leads to a poor interaction between fluid and solid and consequently insufficient utilisation of the moisture uptake capacity of the desiccant material in this region. This can be envisioned to become problematic when such an insert is to be utilised in smaller diameter pipes, where the proportion of air permeable to blocked cross-section is reduced.

The cyclic heat and mass transfer analysis revealed a high sensitivity of the conductive inserts to the outer channel wall temperatures. This is testimony for the effective removal of the sensible heat during adsorption. However, the experiments highlighted that it is of fundamental importance for overall efficiency of the system to ensure an effective reduction of any evaporative cooling effects during the regeneration half cycle.

While the limitations in the experimental heat and mass transfer analysis precluded the identification of an optimal system configuration, the following recommendations can be summarised, that will likely lead to an improvement in system performance:

- Thermal mass reduction by minimising the thickness of the test tube walls,
- Reduction of the ligament diameters of the metal support structures to improve the trade-off between thermal conductance and thermal mass
- Prolongation of the desorption part-cycle to allow for adequate material regeneration

11.3 Recommendations for further research

The mathematical model provides a powerful tool for analysing various prospective inserts and channel configurations. It provides an effective way to investigate the effect of reduced ligament diameters and improved thermal contact on the system performance. This can be considered an appropriate next step, together with the validation of the model against improved experimental data. The coherence of the numerical analysis could be improved by refining the pore-scale flow models, especially for the brush type inserts. The addition of an expression to capture heat losses from the air channel to the environment during the regeneration phase might

be a useful extension in order to make the model more representative of the true desiccant wheel process.

Given the identified weaknesses of the investigated structures, the exploration of other test tube designs is recommendable. One interesting alternative could be the use of high density aluminium honeycomb structures made from corrugated thin aluminium sheets, that could serve as micro-flow channels with decent thermal conductivity.

The single tube test rig designed in this work is useful for the small scale testing of prospective tube inserts and channel configurations. The quality of the obtainable experimental results is, however, greatly dependent on the accuracy and response time of the hygrometers used. Due to shipment delays it was not possible to utilise the sensors originally intended for the experimental analysis in this work and it is recommendable to repeat the experimental tests employing improved sensing equipment in order to achieve a satisfactory heat and mass balance and validate the simulation model. Furthermore, an adaptation of the cooling water circuit in order to omit the necessity of a continuous purge air flow would greatly improve the emulation of the actual desiccant wheel process. Finally, in order to facilitate an operation at higher regeneration temperatures, it is necessary to substitute the polystyrene insulation material utilised for the in- and outlet channels with a more temperature resistant material with minimal thermal mass.

A dedicated analysis of the diffusive resistance to the moisture transfer into the desiccant layer would be useful in order to quantify the impact of the coating composition on the moisture transport kinetics.

References

ASHRAE. Standard method for measurement of moist air properties. *Standard 41.6*, 1994.

ASHRAE. *Fundamentals*. ASHRAE, 2005.

Hand Dieter Baehr and Karl Stephan. *Heat and mass transfer*. Springer, 3 edition, 2011.

A. Bejan. Theory of heat transfer from a surface covered with hair. *Journal of Heat Transfer*, 112(3):662–667, 1990.

Adrian Bejan, Ibrahim Dincer, Sylvie Lorente, Antonio F. Miguel, and A. Heitor Reis. *Porous and Complex Flow Structures in Modern Technologies*. Springer, 2004.

A.E. Bergles, R.L. Webb, and G.H. Junkan. Energy conservation via heat transfer enhancement. *Energy*, 4(2):193 – 200, 1979. 1978 Midwest Energy Conference.

A. Bhattacharya, V.V. Calmidi, and R.L. Mahajan. Thermophysical properties of high porosity metal foams. *International Journal of Heat and Mass Transfer*, 45 (5):1017 – 1031, 2002.

Lucio Bonaccorsi, Angelo Freni, Edoardo Proverbio, Giovanni Restuccia, and Fabio Russo. Zeolite coated copper foams for heat pumping applications. *Microporous and Mesoporous Materials*, 91(1-3):7 – 14, 2006.

Constanze Bongs. *Experimentelle und mathematisch-numerische Untersuchung von verdunstungsgekühlten, sorptiv beschichteten Wärmeübertragern für die Luftentfeuchtung und -kühlung*. PhD thesis, Technische Universität Berlin, Berlin, February 2013.

Constanze Bongs, Alexander Morgenstern, Yudhi Lukito, and Hans-Martin Henning. Advanced performance of an open desiccant cycle with internal evaporative cooling. *Solar Energy*, 104:103–114, 2013.

K. Boomsma, D. Poulikakos, and Y. Ventikos. Simulations of flow through open cell metal foams using an idealized periodic cell structure. *International Journal of Heat and Fluid Flow*, 24(6):825 – 834, 2003a.

K. Boomsma, D. Poulikakos, and F. Zwick. Metal foams as compact high performance heat exchangers. *Mechanics of Materials*, 35(12):1161 – 1176, 2003b.

M. Brandemuehl. *Analysis of heat and mass transfer regenerators with time varying or spatially nonuniform inlet conditions*. PhD thesis, University of Wisconsin, Madison, 1982.

T. H. Chilton and A. P. Colburn. Mass transfer (absorption) coefficients: Prediction from data on heat transfer and fluid friction. *Industrial and Engineering Chemistry*, 26(11):1183–1187, 1934.

K. Daou, R.Z. Wang, and Z.Z. Xia. Desiccant cooling air conditioning: a review. *Renewable and Sustainable Energy Reviews*, 10(2):55 – 77, 2006.

J. Deng, R.Z. Wang, and G.Y. Han. A review of thermally activated cooling technologies for combined cooling, heating and power systems. *Progress in Energy and Combustion Science*, 37(2):172 – 203, 2011.

A. Dewan, P. Mahanta, K. Sumithra Raju, and P Suresh Kumar. Review of passive heat transfer augmentation techniques. In *Proceedings of the Institution of Mechanical Engineers, Part A: Journal of Power and Energy*, volume 218, pages 509–527. Institution of Mechanical Engineers, Sage Publications, 2004.

Y.P. Du, Z.G. Qu, C.Y. Zhao, and W.Q. Tao. Numerical study of conjugated heat transfer in metal foam filled double-pipe. *International Journal of Heat and Mass Transfer*, 53(21–22):4899 – 4907, 2010.

Nihad Dukhan and Mohamed Ali. Strong wall and transverse size effects on pressure drop of flow through open-cell metal foam. *International Journal of Thermal Sciences*, 57(0):85 – 91, 2012.

Pietro Finocchiaro and Marco Beccali. Innovative compact solar air conditioner based on fixed and cooled adsorption beds and wet heat exchangers. *Energy Procedia*, 48(0):819 – 827, 2014. Proceedings of the 2nd International Conference on Solar Heating and Cooling for Buildings and Industry (SHC 2013).

J.C. Fischer and K.T. Mescher. Desiccant-coated substrate and method of manufacture, 1996. US Patent 5,496,397.

A.J. Fowler and A. Bejan. Forced convection in banks of inclined cylinders at low reynolds numbers. *International Journal of Heat and Fluid Flow*, 15(2):90 – 99, 1994.

A. Freni, L. Bonaccorsi, E. Proverbio, G. Maggio, and G. Restuccia. Zeolite synthesised on copper foam for adsorption chillers: A mathematical model. *Microporous and Mesoporous Materials*, 120(3):402 – 409, 2009.

T.S. Ge, Y.J. Dai, R.Z. Wang, and Y. Li. Experimental investigation on a one-rotor two-stage rotary desiccant cooling system. *Energy*, 33(12):1807 – 1815, 2008a.

T.S. Ge, Y. Li, R.Z. Wang, and Y.J. Dai. A review of the mathematical models for predicting rotary desiccant wheel. *Renewable and Sustainable Energy Reviews*, 12 (6):1485 – 1528, 2008b.

T.S. Ge, Y. Li, R.Z. Wang, and Y.J. Dai. Experimental study on a two-stage rotary desiccant cooling system. *International Journal of Refrigeration*, 32(3):498 – 508, 2009.

T.S. Ge, Y.J. Dai, R.Z. Wang, and Z.Z. Peng. Experimental comparison and analysis on silica gel and polymer coated fin-tube heat exchangers. *Energy*, 35(7):2893 – 2900, 2010a.

T.S. Ge, Y. Li, Y.J. Dai, and R.Z. Wang. Performance investigation on a novel two-stage solar driven rotary desiccant cooling system using composite desiccant materials. *Solar Energy*, 84(2):157 – 159, 2010b.

T.S. Ge, Y.J. Dai, and R.Z. Wang. Performance study of silica gel coated fin-tube heat exchanger cooling system based on a developed mathematical model. *Energy Conversion and Management*, 52(6):2329 – 2338, 2011. 9th International Conference on Sustainable Energy Technologies (SET 2010).

Indranil Ghosh. Heat transfer correlation for high-porosity open-cell foam. *International Journal of Heat and Mass Transfer*, 52(5–6):1488 – 1494, 2009a.

Indranil Ghosh. How good is open-cell metal foam ans heat transfer surface. *Journal of Heat Transfeer*, 131(10), 2009b.

M. Goldsworthy and S. White. Optimisation of a desiccant cooling system design with indirect evaporative cooler. *International Journal of Refrigeration*, 34(1): 148 – 158, 2011.

M. Goldsworthy and S.D. White. Limiting performance mechanisms in desiccant wheel dehumidification. *Applied Thermal Engineering*, 44(0):21 – 28, 2012.

W.H. Hsieh, J.Y. Wu, W.H. Shih, and W.C. Chiu. Experimental investigation of heat-transfer characteristics of aluminum-foam heat sinks. *International Journal of Heat and Mass Transfer*, 47(23):5149 – 5157, 2004.

C. Hutter and Ph. Rudolf von Rohr D. Büchi, V. Zuber. Heat transfer in metal foams and designed porous media. *Chemical Engineering Science*, 66(17):3806 – 3814, 2011.

Frank P. Incropera and David P. DeWitt. *Fundamentals of Heat and Mass Transfer*. Wiley, 5 edition, 2002.

C.X. Jia, Y.J. Dai, J.Y. Wu, and R.Z. Wang. Experimental comparison of two honeycombed desiccant wheels fabricated with silica gel and composite desiccant material. *Energy Conversion and Management*, 47(15–16):2523 – 2534, 2006.

C.X. Jia, Y.J. Dai, J.Y. Wu, and R.Z. Wang. Use of compound desiccant to develop high performance desiccant cooling system. *International Journal of Refrigeration*, 30(2):345 – 353, 2007.

Hellmut G. Karge and Jens Weitkamp. *Molecular Sieves*, volume 7. Springer, 2008.

Akio Kodama, Tadashi Hirayama, Motonobu Goto, Tsutomu Hirose, and R.E. Critoph. The use of psychrometric charts for the optimisation of a thermal swing desiccant wheel. *Applied Thermal Engineering*, 21(16):1657 – 1674, 2001.

Akio Kodama, Naoki Watanabe, Tsutomu Hirose, Motonobu Goto, and Hiroshi Okano. Performance of a multipass honeycomb adsorber regenerated by a direc hot water heating. *Adsorption*, 11(1):603–608, 2005.

Akio Kodama, A. Sanno, and Y. Osaka. Performance of four-divided adsorbent rotor for desiccant dehumidification. In *International Sorption Heat Pump Conference*, pages 707–714, Padua, Italy, April 2011. IIR/AICARR.

A. Kopanidis, A. Theodorakakos, E. Gavaises, and D. Bouris. 3d numerical simulation of flow and conjugate heat transfer through a pore scale model of high porosity open cell metal foam. *International Journal of Heat and Mass Transfer*, 53(11–12):2539 – 2550, 2010.

D. La, Y.J. Dai, Y. Li, R.Z. Wang, and T.S. Ge. Technical development of rotary desiccant dehumidification and air conditioning: A review. *Renewable and Sustainable Energy Reviews*, 14(1):130 – 147, 2010.

H. Li, Y.J. Dai, Y. Li, D. La, and R.Z. Wang. Experimental investigation on a one-rotor two-stage desiccant cooling/heating system driven by solar air collectors. *Applied Thermal Engineering*, 31(17-18):3677 – 3683, 2011.

H. Li, Y.J. Dai, Y. Li, D. La, and R.Z. Wang. Case study of a two-stage rotary desiccant cooling/heating system driven by evacuated glass tube solar air collectors. *Energy and Buildings*, 47(0):107 – 112, 2012.

Michael Karl Löffler and Hans Martin Henning. Sorptive heat exchanger and related cooled sorption process, January 2007. EU Patent EP1508015.

T.J. Lu, H.A. Stone, and M.F. Ashby. Heat transfer in open-cell metal foams. *Acta Materialia*, 46(10):3619 – 3635, 1998.

W. Lu, C.Y. Zhao, and S.A. Tassou. Thermal analysis on metal-foam filled heat exchangers. part i: Metal-foam filled pipes. *International Journal of Heat and Mass Transfer*, 49(15–16):2751 – 2761, 2006.

Kurt O Lund. Fully developed turbulent flow and heat transfer at fiber-flocked surfaces. *International Journal of Heat and Mass Transfer*, 44(20):3799 – 3810, 2001.

Kurt O. Lund and Timothy R. Knowles. Enhanced laminar-flow heat transfer at fiber-flocked surfaces. *International Journal of Heat and Mass Transfer*, 44(8): 1627 – 1636, 2001.

Simone Mancin, Claudio Zilio, Alberto Cavallini, and Luisa Rossetto. Pressure drop during air flow in aluminum foams. *International Journal of Heat and Mass Transfer*, 53(15–16):3121 – 3130, 2010a.

Simone Mancin, Claudio Zilio, Alberto Cavallini, and Luisa Rossetto. Heat transfer during air flow in aluminum foams. *International Journal of Heat and Mass Transfer*, 53(21–22):4976 – 4984, 2010b.

Simone Mancin, Claudio Zilio, Andrea Diani, and Luisa Rossetto. Air forced convection through metal foams: Experimental results and modeling. *International Journal of Heat and Mass Transfer*, 62(0):112 – 123, 2013.

Alfons Mersmann, Matthias Kind, and Johann Stichlmair. *Thermal Separation Technology*. Springer, 2011.

N. J. Mills. The wet kelvin model for air flow through open-cell polyurethane foams. *Journal of Materials Science*, 40(22):5845–5851, 2005.

Paisarn Naphon and Tanapon Suchana. Heat transfer enhancement and pressure drop of the horizontal concentric tube with twisted wires brush inserts. *International Communications in Heat and Mass Transfer*, 38(2):236 – 241, 2011.

R. Narayanan, W.Y. Saman, S.D. White, and M. Goldsworthy. Comparative study of different desiccant wheel designs. *Applied Thermal Engineering*, 31(10):1613 – 1620, 2011.

Fatemeh Esfandiari Nia, Dolf van Paassen, and Mohamad Hassan Saidi. Modeling and simulation of desiccant wheel for air conditioning. *Energy and Buildings*, 38 (10):1230 – 1239, 2006.

Donald A. Nield and Adrian Bejan. *Convection in Porous Media*. Springer, 3 edition, 2006.

M. Odabaee and K. Hooman. Metal foam heat exchangers for heat transfer augmentation from a tube bank. *Applied Thermal Engineering*, 36(0):456 – 463, 2012.

Ahmad A. Pesaran and Anthony F. Mills. Moisture transport in silica gel packed beds—i.theoretical study. *International Journal of Heat and Mass Transfer*, 30 (6):1037 – 1049, 1987a.

Ahmad A. Pesaran and Anthony F. Mills. Moisture transport in silica gel packed beds—ii. experimental study. *International Journal of Heat and Mass Transfer*, 30(6):1051 – 1060, 1987b.

D.A Reay. Heat transfer enhancement—a review of techniques and their possible impact on energy efficiency in the U.K. *Heat Recovery Systems and CHP*, 11(1): 1 – 40, 1991.

Douglas M. Ruthven. *Principles of Adsorption and Adsorption Processes*. John Wiley and Sons, 1984.

Karl J. Sladek, Edwin R. Gilliland, and Raymond F. Baddour. Diffusion on surfaces. ii. correlation of diffusivities of physically and chemically adsorbed species. *Industrial Engineering Chemistry Fundamentals*, 13(2):100–105, 1974.

L.A. Sphaier and W.M. Worek. The effect of axial diffusion in desiccant and enthalpy wheels. *International Journal of Heat and Mass Transfer*, 49(7–8):1412 – 1419, 2006.

William Thomson. Lxiii. on the division of space with minimum partitional area. *Philosophical Magazine Series 5*, 24(151):503–514, 1887.

E. Van Den Bulck, J.W. Mitchell, and S.A. Klein. Design theory for rotary heat and mass exchangers—ii. effective n ess-number-of-transferunits method for rotary heat and mass exchangers. *International Journal of Heat and Mass Transfer*, 28 (8):1587 – 1595, 1985.

Verein Deutscher Ingenieure. *VDI heat atlas*. Springer, 2 edition, 2010.

D. Weaire and R. Phelan. A counter-example to kelvin's conjecture on minimal surfaces. *Philosophical Magazine Letters*, 69(2):107–110, 1994.

John F. Wendt, John D. Anderson, Joris Degroote, Gérard Degrez, Erik Dick, Roger Grundmann, and Jan Vierendeels. *Computational Fluid Dynamics An Introduction*. Springer, 3 edition, 2009.

Stephen D. White, Mark Goldsworthy, Roger Reece, Thorsten Spillmann, Abdullah Gorur, and Dae-Young Lee. Characterization of desiccant wheels with alternative materials at low regeneration temperatures. *International Journal of Refrigeration*, 34(8):1786 – 1791, 2011.

Weigang Xu, Hongtao Zhang, Zhenming Yang, and Jinsong Zhang. Numerical investigation on the flow characteristics and permeability of three-dimensional reticulated foam materials. *Chemical Engineering Journal*, 140:562 – 569, 2008.

X H Yang, J J Kuang, T J Lu, F S Han, and T Kim. A simplistic analytical unit cell based model for the effective thermal conductivity of high porosity open-cell metal foams. *Journal of Physics D: Applied Physics*, 46(25):255302, 2013.

Li-Zhi Zhang, Huang-Xi Fu, Qi-Rong Yang, and Jian-Chang Xu. Performance comparisons of honeycomb-type adsorbent beds (wheels) for air dehumidification with various desiccant wall materials. *Energy*, 65(0):430 – 440, 2014.

L.Z. Zhang and J.L. Niu. Performance comparisons of desiccant wheels for air dehumidification and enthalpy recovery. *Applied Thermal Engineering*, 22(12): 1347 – 1367, 2002.

C.Y. Zhao. Review on thermal transport in high porosity cellular metal foams with open cells. *International Journal of Heat and Mass Transfer*, 55:3618 – 3632, 2012.

Y. Zhao, T.S. Ge, Y.J. Dai, and R.Z. Wang. Experimental investigation on a desiccant dehumidification unit using fin-tube heat exchanger with silica gel coating. *Applied Thermal Engineering*, 63(1):52 – 58, 2014.

Appendix A

Tables of heat transfer test results

Table A.1: 5PPI metal foam test results

No.	$T_{a,in}$	$T_{w,in}$	ΔT_a	ΔT_w	$\dot{V}_a$	$\dot{V}_w$	$\dot{Q}_a$	$\dot{Q}_w$	T_{lm}	UA
-	°C	°C	°C	°C	l/min	l/min	W	W	°C	W/K
1	47.3	23.8	23.62	0.23	14.95	0.373	7.02	6.01	NaN	NaN
2	49.74	25.18	24.58	0.37	20.51	0.373	10.02	9.52	NaN	NaN
3	49.45	23.91	25.41	0.44	24.48	0.373	12.37	11.36	4.73	2.61
4	49.87	24.06	25.57	0.57	32.02	0.373	16.28	14.85	5.34	3.05
5	53.65	24.2	29.16	0.76	35.1	0.373	20.34	19.66	6.2	3.28
6	49.35	24.25	24.73	0.74	40.44	0.373	19.88	19.24	5.7	3.49
7	47.96	24.57	22.92	0.83	46.31	0.373	21.1	21.42	5.69	3.71
8	46.93	24.25	22.13	0.87	50.64	0.373	22.28	22.43	5.79	3.85
9	51.76	23.31	28.42	0.09	4.9	0.37	2.77	2.28	4.1	0.67
10	53.87	23.68	30.05	0.24	10.73	0.37	6.41	6.13	5.57	1.15
11	51.97	23.97	27.12	1.16	56.59	0.375	30.51	30.28	7.59	4.02
12	51.41	24.37	26.03	1.27	60.96	0.375	31.55	33.08	7.64	4.13
13	50.45	24.09	25.27	1.25	62.83	0.375	31.56	32.48	7.66	4.12

Table A.2: 10PPI metal foam test results

No.	$T_{a,in}$	$T_{w,in}$	ΔT_a	ΔT_w	$\dot{V}_a$	$\dot{V}_w$	$\dot{Q}_a$	$\dot{Q}_w$	T_{lm}	UA
-	°C	°C	°C	°C	l/min	l/min	W	W	°C	W/K
1	27.51	20.92	6.51	0.14	30.36	0.357	3.93	3.44	1.44	2.73
2	42.51	21	20.87	0.81	46.92	0.357	19.47	20.21	5.77	3.38
3	38.99	21.08	17.1	0.73	55.21	0.359	18.76	18.31	5.35	3.51
4	28.06	20.87	7.04	0.19	40.18	0.359	5.62	4.79	1.79	3.14
5	39.15	20.49	18.38	0.52	35.62	0.359	13.01	12.92	4.33	3.01
6	37.85	20.57	16.92	0.55	39.47	0.359	12.9	13.67	4.26	3.03
7	48.98	21.13	26.17	1.26	61.4	0.357	31.95	31.36	9.01	3.54
8	29.57	21.08	8.41	0.16	24.7	0.357	4.13	3.88	1.77	2.33
9	45.08	20.81	24.18	0.36	19.75	0.357	9.49	8.98	4.2	2.26
10	30.46	19.56	10.81	0.22	25.27	0.355	5.43	5.51	2.23	2.43
11	42.39	19.54	22.66	0.45	25.32	0.355	11.4	11.2	4.69	2.43
12	36.89	19.68	17.13	0.18	14.43	0.355	4.91	4.37	3.15	1.56
13	43.29	19.65	23.53	0.15	9.29	0.355	4.35	3.63	4.29	1.01
14	37.54	21.46	15.1	0.68	57.34	0.355	17.21	16.75	5.23	3.29
15	43.45	21.8	21.56	0.39	23.56	0.355	10.1	9.68	3.94	2.56

Table A.3: 20PPI metal foam test results

No.	$T_{a,in}$	$T_{w,in}$	ΔT_a	ΔT_w	$\dot{V}_a$	$\dot{V}_w$	$\dot{Q}_a$	$\dot{Q}_w$	T_{lm}	UA
-	°C	°C	°C	°C	l/min	l/min	W	W	°C	W/K
1	37.65	24.85	12.83	0.1	17.62	0.37	4.5	2.62	NaN	NaN
2	56.81	26.21	30.73	0.3	11.81	0.37	7.21	7.65	NaN	NaN
3	49.36	24.57	24.66	0.56	26.11	0.377	12.8	14.63	4.57	2.8
4	49	24.61	24.34	0.54	26.07	0.377	12.61	14.11	3.87	3.26
5	48.12	27.25	20.74	0.6	37.76	0.377	15.57	15.82	3.97	3.92
6	56.86	24.54	32.63	0.17	4.73	0.368	3.07	4.32	NaN	NaN
7	43.13	26.17	16.98	0.21	19.67	0.368	6.64	5.45	NaN	NaN
8	48.61	27.96	20.32	0.64	46.39	0.368	18.74	16.47	4.79	3.91
9	46.33	27.92	18.02	0.65	50.94	0.4	18.25	18.01	4.55	4.01
10	48.36	23.42	24.11	1.07	56.78	0.373	27.21	27.74	6.87	3.96
11	47.9	23.68	23.21	1.07	59.82	0.373	27.6	27.66	7.07	3.9

Table A.4: Aluminium brush test results

No.	$T_{a,in}$	$T_{w,in}$	ΔT_a	ΔT_w	$\dot{V}_a$	$\dot{V}_w$	$\dot{Q}_a$	$\dot{Q}_w$	T_{lm}	UA
-	°C	°C	°C	°C	l/min	l/min	W	W	°C	W/K
1	61.27	22.5	37.3	0.89	29.78	0.316	22.09	19.51	11.19	1.97
2	62.76	24.31	38.05	0.54	18.69	0.319	14.14	11.9	8.25	1.71
3	60.02	26.21	33.48	0.56	21.05	0.323	14.01	12.44	7.12	1.97
4	47.99	23.41	24.08	0.45	24.76	0.375	11.85	11.62	6.09	1.95
5	55.73	25.69	28.55	0.69	35.99	0.385	20.43	18.47	9.35	2.18
6	58.77	24.29	34.24	1.46	14.81	0.097	10.08	9.86	6.72	1.5
7	50.23	23.75	25.6	1.72	24.06	0.103	12.24	12.29	7.16	1.71
8	58.77	24.29	34.24	1.46	14.81	0.097	10.08	9.86	6.72	1.5
9	48.76	24.26	22.57	2.76	35.21	0.082	15.8	15.73	8.17	1.93
10	47.92	24.05	21.39	3.14	40.59	0.08	17.26	17.53	8.59	2.01
11	47.77	24.15	20.12	3.99	50.41	0.075	20.16	20.77	9.36	2.15
12	49.52	24.74	20.53	4.58	54.82	0.075	22.38	23.76	10.23	2.19

Table A.5: Low density copper brush test results

No.	$T_{a,in}$	$T_{w,in}$	ΔT_a	ΔT_w	$\dot{V}_a$	$\dot{V}_w$	$\dot{Q}_a$	$\dot{Q}_w$	T_{lm}	UA
-	°C	°C	°C	°C	l/min	l/min	W	W	°C	W/K
1	43.79	19.68	21.87	0.51	30.32	0.311	13.18	10.95	9.08	1.45
2	43.76	19.88	21.77	0.51	30.34	0.308	13.13	10.93	8.84	1.49
3	41.06	20.28	20.52	0.21	14.57	0.308	5.94	4.4	4.62	1.29
4	40.58	20.09	20.39	0.11	9.17	0.308	3.72	2.36	3.77	0.99
5	39.97	21.04	16.87	0.44	35.15	0.313	11.79	9.5	7.47	1.58
6	47.33	25.41	21.67	0.28	17.21	0.359	7.42	6.97	4.81	1.54
7	50.66	23.74	25.93	0.51	25.53	0.357	13.16	12.68	7.75	1.7
8	49.43	24.07	23.8	0.55	29.95	0.357	14.17	13.75	8.41	1.69
9	45.42	24.91	19.02	0.47	32.37	0.357	12.24	11.58	7.14	1.71
10	46.09	26.55	17.85	0.48	35.44	0.361	12.58	12.09	7.17	1.76
11	49.58	23.8	25.3	0.39	20.09	0.357	10.11	9.68	6.25	1.62

continued on next page

Table A.5 – continued from previous page

No.	$T_{a,in}$	$T_{w,in}$	ΔT_a	ΔT_w	$\dot{V}_a$	$\dot{V}_w$	$\dot{Q}_a$	$\dot{Q}_w$	T_{lm}	UA
-	°C	°C	°C	°C	l/min	l/min	W	W	°C	W/K
12	49.22	23.84	22.67	0.69	39.59	0.359	17.85	17.34	9.95	1.79
13	49.38	24.77	21.39	0.72	44.45	0.359	18.91	18.1	10.32	1.83

Table A.6: Medium density copper brush test results

No.	$T_{a,in}$	$T_{w,in}$	ΔT_a	ΔT_w	$\dot{V}_a$	$\dot{V}_w$	$\dot{Q}_a$	$\dot{Q}_w$	T_{lm}	UA
-	°C	°C	°C	°C	l/min	l/min	W	W	°C	W/K
1	35.28	24.09	11.15	0.09	12.55	0.359	2.78	2.32	1.93	1.44
2	50.68	25.42	25.22	0.4	20.93	0.359	10.5	10.08	3.88	2.71
3	51.62	23.66	27.82	0.47	24.6	0.357	13.6	11.77	5.14	2.65
4	43.78	23.9	19.66	0.45	32.52	0.357	12.71	11.19	4.27	2.98
5	47.81	25.41	22.16	0.57	35.96	0.368	15.85	14.47	4.79	3.31
6	48.43	25.5	22.56	0.66	41.13	0.37	18.45	16.87	5.32	3.47
7	39.28	24.39	14.85	0.15	13.45	0.357	3.97	3.68	2.46	1.61

Table A.7: Low density carbon brush

No.	$T_{a,in}$	$T_{w,in}$	ΔT_a	ΔT_w	$\dot{V}_a$	$\dot{V}_w$	$\dot{Q}_a$	$\dot{Q}_w$	T_{lm}	UA
-	°C	°C	°C	°C	l/min	l/min	W	W	°C	W/K
1	40.51	24	13.23	0.23	22.15	0.316	5.83	5.1	8.11	0.72
2	43.31	21.42	21.3	0.06	4.36	0.313	1.85	1.24	5.9	0.31
3	47.27	21.68	20.64	0.3	16.83	0.312	6.91	6.46	12.47	0.55
4	53.32	21.78	22.76	0.61	29.68	0.313	13.43	13.37	17.6	0.76
5	44.18	20.19	15.92	0.56	40.96	0.312	12.97	12.18	14.41	0.9

Table A.8: Flocked tube

No.	$T_{a,in}$	$T_{w,in}$	ΔT_a	ΔT_w	$\dot{V}_a$	$\dot{V}_w$	$\dot{Q}_a$	$\dot{Q}_w$	T_{lm}	UA
-	°C	°C	°C	°C	l/min	l/min	W	W	°C	W/K
1	40.63	21.74	4.97	0.18	48.67	0.319	4.81	4.09	16.2	0.3
2	41.74	21.43	6.34	0.14	29.66	0.319	3.74	3.01	16.88	0.22
3	43.62	21.64	8.59	0.05	10.37	0.323	1.77	1.03	17.31	0.1
4	34.23	21.66	4.08	0.07	25.92	0.323	2.1	1.48	10.37	0.2
5	42.73	22.12	6.17	0.15	34.02	0.323	4.17	3.45	17.27	0.24
6	45.01	20.98	13.55	0.06	5.41	0.317	1.46	1.39	16.3	0.09
7	36.45	21.23	5.36	0.11	19.65	0.317	2.09	2.51	12.3	0.17
8	36.52	20.41	4.34	0.28	44.29	0.169	3.82	3.34	13.69	0.28
9	35.19	20.27	4.07	0.12	43.26	0.279	3.5	2.32	12.72	0.28
10	39.34	20.58	6.91	0.06	15.74	0.287	2.16	1.19	15.02	0.14

Table A.9: Empty tube test results

No.	$T_{a,in}$	$T_{w,in}$	ΔT_a	ΔT_w	$\dot{V}_a$	$\dot{V}_w$	$\dot{Q}_a$	$\dot{Q}_w$	T_{lm}	UA
-	°C	°C	°C	°C	l/min	l/min	W	W	°C	W/K
1	30.99	20.28	3.63	0.07	38.13	0.357	2.75	1.85	8.74	0.31
2	31.81	20.43	3.87	0.08	38.07	0.361	2.93	2.02	9.28	0.32
3	32.07	20.52	3.9	0.09	38.41	0.361	2.98	2.15	9.43	0.32
4	32.18	20.47	3.95	0.09	38.38	0.361	3.02	2.2	9.56	0.32
5	36.48	19.81	7.04	0.07	19.42	0.357	2.72	1.82	12.79	0.21
6	38.24	24.72	4.12	0.15	55.28	0.373	4.52	3.97	11.27	0.4
7	36.7	25.07	5.02	0.05	19.27	0.373	1.92	1.3	8.86	0.22
8	30.14	20.42	3.39	0.07	35.21	0.361	2.37	1.64	7.88	0.3
9	37.71	20.34	4.99	0.24	66.36	0.361	6.58	5.99	14.63	0.45
10	46.32	20.2	12.01	0.08	11.54	0.361	2.76	1.91	19.46	0.14
11	46.88	21.01	14.62	0.05	8.08	0.361	2.35	1.33	17.55	0.13
12	45.28	21.05	11.04	0.07	12.66	0.361	2.78	1.85	18.13	0.15
13	43.38	22.7	16.4	0.02	3.05	0.368	0.99	0.61	10.41	0.1
14	46.92	22	16.48	0.04	4.71	0.368	1.54	0.97	15.22	0.1
15	43.87	21.65	16.19	0.02	4.12	0.355	1.33	0.61	12.4	0.11

continued on next page

Table A.9 – continued from previous page

No.	$T_{a,in}$	$T_{w,in}$	ΔT_a	ΔT_w	$\dot{V}_a$	$\dot{V}_w$	$\dot{Q}_a$	$\dot{Q}_w$	T_{lm}	UA
-	°C	°C	°C	°C	l/min	l/min	W	W	°C	W/K
16	53.84	22.09	13.45	0.28	27.58	0.361	7.38	7.11	24.29	0.3
17	50.53	22.24	11.38	0.28	32.1	0.361	7.27	7.06	22	0.33
18	52.09	22.46	11.71	0.31	34.29	0.361	7.98	7.77	23.16	0.34
19	53.72	22.49	13.77	0.25	23.48	0.361	6.43	6.21	23.57	0.27
20	53.75	22.44	15.83	0.16	13.81	0.361	4.35	3.9	22.4	0.19
21	49.27	22.71	12.82	0.16	17.18	0.361	4.38	3.92	19.39	0.23

Appendix B

Material properties used in numerical and experimental analysis

This section summarised the thermal properties and geometrical parameters used in the numerical analyses of this work. The global parameters used in the model setup are summarised in table B.1. The relevant thermal properties of the materials employed are listed in table B.2.

Table B.1: Global modelling parameters

Parameter		metal foam	brush insert
$d_{t,i}$	[mm]	19.7	19
$d_{t,o}$	[mm]	21	20
$l_{t,i}$	[mm]	200	200
l_{inlet}	[mm]	50	50
d_{stem}	[mm]	0	1.905
ζ		1/3	1
f_a		0.7	0.7

Table B.2: Thermal properties of materials in standards units

Thermal property	**value**	**Thermal property**	**value**
alum. foam tubes & matrices		brush tube	
$\rho_{\text{Al 6061-T6}}$	2,700	ρ_{CuNi10}	8,954
$c_{p,\text{Al 6061-T6}}$	900	$c_{p,\text{CuNi10}}$	380
$k_{\text{Al 6061-T6}}$	201	k_{CuNi10}	40
alum. brush matrix		copp. brush matrix	
$\rho_{\text{Al 6061-T6}}$	2,700	ρ_{CuNi10}	8,954
$c_{p,\text{Al 6061-T6}}$	900	$c_{p,\text{CuNi10}}$	380
$k_{\text{Al 6061-T6}}$	201	k_{CuNi10}	40
Silica gel coating		brush base-wire	
ρ_{Si}	800	ρ_{Ss}	7,800
$c_{p,\text{Si}}$	921	$c_{p,\text{Ss}}$	477
k_{Si}	0.2	k_{Ss}	16.9
dry air		water	
M_a	28.9645	M_w	18.01528
$c_{p,a}$	1006	$c_{p,w}$	4,189
ρ_a	1.2	polystyrene insulation	
k_a	0.0255	k_{ins}	$0.035 - 0.045$
μ_a	$1.796 \cdot 10^{-5}$	ρ_{ins}	$25 - 45$
		$c_{p,ins}$	1,500

Appendix C

Thermocouple calibration data

For the thermocouple calibration, a thick hole was drilled inside a brass cube, that was put onto a hot plate for temperature elevation. The numerous thermocouples were placed inside the hole together with a class 1/10 Pt-100 RTD element and submerged in heating oil to ensure a uniform temperature.

The calibration rig is depicted in figure C.1 and the resulting offsets are summarised in table C.1.

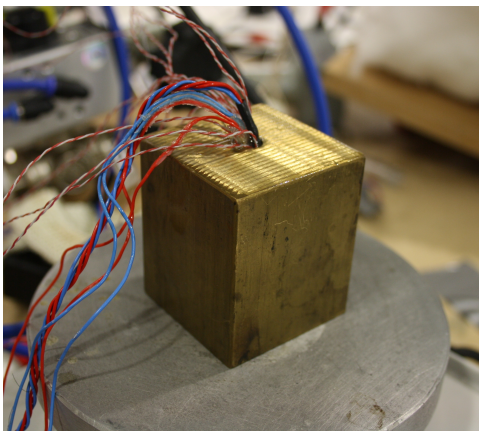

Figure C.1: Thermocouple calibration rig

Table C.1: Thermocouple calibration data

ID	c_1	c_0	ID	c_1	c_0	ID	c_1	c_0
1	1.02	-0.09	5	1.03	-0.09	9	1.00	0.55
2	1.02	0.08	6	1.02	0.02	10	0.99	0.81
3	1.03	-0.14	7	1.03	-0.13	11	1.00	0.65
4	1.02	0.15	8	1.06	-0.68	12	1.01	0.50